Doctoral Dissertation
Doctoral Program in Mechanical Engineering (36^{th}cycle)

Multi-scale multi-fidelity numerical modelling of wave energy converter farms

By

Beatrice Battisti

******

Supervisors:
Prof. Giovanni Bracco, Politecnico di Torino, Supervisor
Dr. Michel Bergmann, Université de Bordeaux,
Co-Supervisor

Doctoral Examination Committee:
Prof. Simone Camarri, Referee, Università di Pisa
Prof. Angelo Iollo, Université de Bordeaux
Prof. Stefano Mauro, Politecnico di Torino
Dr. Vincenzo Nava, Referee, Tecnalia/BCAM
Dr. Angela Scardigli, Optimad Srl

Politecnico di Torino & Université de Bordeaux
2024

One of these days, I'm going to cut you into little pieces.

One of These Days, Pink Floyd

Acknowledgements

I wish to express my gratitude to my supervisors, Michel Bergmann and Giovanni Bracco, for their invaluable guidance over the years. Michel, I am deeply appreciative of your support and foresight, always three steps ahead of each one of my doubts. Your persistent positivity, kindness, and calmness have been invaluable. Giovanni, thank you for your confidence in me, and for offering me a broader perspective on the project. I am grateful for your insightful advice and prompt responsiveness. I cannot thank Angelo Iollo and Giuliana Mattiazzo enough for letting me participate to the cotutelle programme and welcoming me into your research teams. Our open discussions have been precious, and I value your mentorship deeply. Special thanks to Tommaso Taddei for providing me with a space in his office and for sharing our unfortunate transport problems, as well as a lot of other topics. Special thanks also to Giuseppe Giorgi, for your endless guidance and support, in research and beyond, and I consider myself fortunate to have had the opportunity to collaborate with you.

I would like to express my gratitude to Simone Camarri and Vincenzo Nava for dedicating their time and expertise to evaluate my thesis. Your insights and recommendations are immensely appreciated. I am honored to have Stefano Mauro and Angela Scardigli as members of the jury, and I thank you for accepting to evaluate my work.

Participating in a cotutelle programme involves navigating two cities, two institutions, two research groups, and two lives. I am grateful for the opportunity to experience both realities, which can be challenging, but incredibly rewarding. A heartfelt thank you to the members of the MORE Lab, which have been there from the beginning, through the Covid period, many conferences, holidays, and celebrations. Your craziness is infectious, and I have always felt loved, even when far away. I am also deeply appreciative to the Memphis team members, with whom I shared nice adventures, and mathematical challenges. And then, there are the IMB

fellows, who have had the pleasure of seen me only in my best moments. I cherish all the time spent in this Little not-so-little Italy, and the departure will be pretty difficult. I also would like to thank the fellows at Ghent University, who made my brief visit memorable and enjoyable. Special thanks to the Optimad fellows for their hospitality, and for allowing me to occupy their cluster with my simulations.

I extend my gratitude to all the XR fellows across various countries, who have kept me grounded in the real world, with love and rage. To those who had the delight to share a flat with me during those years, enduring the everyday drama and culinary disappointments. To the people that have been there for years, living in my hometown or in many other cities, doing great things, and still willing to talk to me despite my (occasional) lack of responsiveness. To all the people who have crossed paths with me, leaving their mark on my journey, in their own unique way.

Un grande grazie a mamma e papà, che mi supportano e sopportano, anche se probabilmente ancora non sanno cosa faccio, né quando torno. Grazie anche a mia sorella, con cui condivido gioie e dolori, e che mi permette di vestirmi in modo accettabile. Grazie anche a Enzo e Lorenzo, che si ritrovano a dover sopportare innumerevoli ansie, ma lo fanno con il sorriso.

I would like to keep this section brief, not because I lack gratitude, but because words fail to capture the depth of my feelings, and my eyes would probably explode. I hold dear countless memories, conversations, experiences, pleasant and challenging moments. I recognize how fortunate I am to be surrounded by wonderful people, and I sincerely hope this luck will endure beyond the completion of this thesis.

Abstract

The marine sector is increasingly turning to wave energy converters (WECs) for clean energy generation. For commercial-scale production, WEC farm deployment is essential, but requires complex numerical simulations. While high-fidelity models like Computational Fluid Dynamics (CFD) ensure accuracy, their substantial computational demands have prompt interest in model order reduction techniques. Proper Orthogonal Decomposition (POD) projection-based reduced order models have proven effective in monophase flows, yet face stability issues with multiphase flows. A proposed multi-fidelity model integrates CFD for WEC near-field description, and POD for far-field wave propagation. Bidirectional information exchange ensures precise flow reconstruction and floater dynamics description. Testing confirms its efficacy in various scenarios, significantly reducing the computational burden, decisive for tackling WEC farm design and optimization.

Résumé

Le secteur maritime s'oriente de plus en plus vers les convertisseurs d'énergie des vagues (WECs), en particulier vers des fermes de WECs. Cependant, les simulations numériques sont complexes, et bien que les modèles haute fidélité assurent la précision, leurs exigences computationnelles ont stimulé l'intérêt pour les techniques de réduction de modèles. Les modèles à ordre réduit basés sur la Décomposition Orthogonale aux valeurs Propres (POD) sont efficaces dans les écoulements monophasiques, mais rencontrent des problèmes de stabilité avec les écoulements multiphasiques. Un modèle multifidélité intègre la CFD (Computational Fluid Dynamics) pour le champ proche des WECs et la POD pour la propagation des vagues en champ lointain. L'échange d'informations assure une description précise de l'écoulement et de la dynamique des flotteurs. Les tests confirment son efficacité, réduisant significativement la charge computationnelle, cruciale pour aborder l'optimisation des fermes de WECs.

Estratto

Il settore marittimo è sempre più orientato verso i convertitori di energia delle onde (WECs), in particolare verso i parchi di WECs. Tuttavia, le simulazioni numeriche sono complesse e, sebbene i modelli ad alta fedeltà assicurino precisione, i loro requisiti computazionali hanno stimolato l'interesse per le tecniche di riduzione di modello. I modelli a ordine ridotto basati sulla Decomposizione Ortogonale ai valori Propri (POD) sono efficaci per flussi monofase, ma incontrano problemi di stabilità con i flussi multifase. Un modello multifideltà è proposto, che integra la CFD (Computational Fluid Dynamics) per il campo vicino ai WECs e la POD per la propagazione delle onde nel campo lontano. Lo scambio di informazioni assicura una descrizione precisa del flusso e della dinamica dei WECs. I test ne confermano l'efficacia, riducendo significativamente il carico computazionale, cruciale per affrontare l'ottimizzazione dei parchi di WECs.

Long Abstract

In response to the dynamic evolution of the energy landscape toward more sustainable solutions, the marine sector has increasingly turned its focus toward wave energy as a promising avenue for clean energy generation. The deployment of Wave Energy Converters (WECs) in farms holds significant potential for achieving commercial-scale production of renewable energy, but this endeavor necessitates thorough numerical simulations due to the complex hydrodynamics involved. The simulation of WEC farms poses considerable challenges due to their inherently multiscale nature, encompassing the accurate representation of fluid-structure interactions and the interactions among WECs, resulting in near-field effects, and far-field effects, which represent the broader influence of the farm on its surrounding environment. While conventional high-fidelity models, notably Computational Fluid Dynamics (CFD), are indispensable for capturing the complexities of highly nonlinear phenomena in such systems, they come with a high computational price. Model order reduction techniques emerge as a promising approach to mitigate this challenge, aiming to reduce the computational complexity of numerical simulations while maintaining accuracy. Among these techniques, the Proper Orthogonal Decomposition (POD) method stands out as an effective means of deriving a reduced basis in high-dimensional flow systems. Projection-based Reduced Order Models (ROMs) based on POD have demonstrated success in linear and weakly nonlinear model reductions, particularly in monophase flows. However, when dealing with multiphase flows, traditional ROMs obtained via POD and Galerkin projection techniques face several obstacles. These include instability concerns, compatibility issues with model order reduction - evident in the emergence of a fourth-order tensor in the primary dynamical system -, complexities in modeling moving bodies, and difficulties in implementation with commercial codes lacking direct access to the source code. All these considerations lead to the development of a non-intrusive, Galerkin-free approach based on domain decomposition and equipped with sensor

information to account for travelling waves. This multi-fidelity model integrates CFD and POD spatially. The high-fidelity CFD solver is deployed in the near-field around obstacles, where viscous effects and nonlinearities predominate. In contrast, the POD ROM model is tailored for weakly nonlinear regions, focusing on far-field wave propagation. By leveraging a small high-fidelity domain, which represents only a fraction of the original domain used in training the POD modes, the approach achieves significant reductions in CPU costs while preserving precision. Central to this approach is the bidirectional exchange of information between the two models, facilitated by overlapping regions and subdomain boundaries. The simplicity and efficacy of the coupling methodology make it readily applicable to diverse simulations involving moving bodies, including wave energy conversion, allowing for an efficient representation of multiscale properties. This methodology demonstrates accurate flow reconstruction and a comprehensive description of floater dynamics. Extensive validation tests encompass both in-sample simulations, for reproduction configurations, and, more notably, out-of-sample simulations. The latter underscore the accuracy and robustness of the proposed methodology, able to predict solutions for unseen parameters. The efficiency of this hybrid fidelity model empowers the execution of intensive simulations, rendering it suitable for a wide range of applications, including parametric studies, optimization tasks, and multiple-query simulations. By substantially reducing computational costs, the coupled model not only expedites optimization and design processes for wave energy converter farms but also paves the way for enhanced scalability and sustainability in the marine energy sector.

Keywords: Proper Orthogonal Decomposition, Wave Energy, Mathematical Modelling, Reduced-Order Models, Numerical Simulations, Multifidelity models.

Modélisation multi-échelle et multi-fidélité pour des extracteurs d'énergie marine

Résumé étendu

Face à l'évolution de la scène énergétique vers des solutions plus durables, le secteur marin s'intéresse de plus en plus à l'énergie des vagues pour la production d'énergie propre. Le déploiement de convertisseurs d'énergie des vagues (WECs)

dans des fermes offre un potentiel significatif pour une production à grande échelle, mais cela nécessite de simulations numériques approfondies, en raison de la complexité de l'hydrodynamique. La simulation de fermes de WECs pose des défis considérables en raison de leur nature multi-échelle, incluant la représentation précise des interactions fluide-structure et entre les WECs, entraînant des effets de champ proche, et de champ lointain, représentant l'influence plus large de la ferme sur son environnement. Bien que les modèles haute fidélité, comme la CFD (Computational Fluid Dynamics), soient essentiels pour capturer les complexités des phénomènes non linéaires, ils sont accompagnés d'un coût computationnel élevé. Les techniques de réduction de modèles émergent comme une approche prometteuse pour atténuer ce défi, visant à réduire la complexité computationnelle tout en maintenant la précision. Parmi ces techniques, la méthode de Décomposition Orthogonale aux valeurs Propres (POD) se distingue comme un moyen efficace de dériver une base réduite dans les systèmes d'écoulement multidimensionnels. Les Modèles d'Ordre Réduit (ROMs) basés sur la POD ont prouvé leur succès dans les réductions de modèles linéaires et faiblement non linéaires monophasiques. Cependant, les ROMs traditionnels, obtenus par POD et projection de Galerkin, rencontrent plusieurs obstacles dans les écoulements multiphasiques, notamment des problèmes d'instabilité, de compatibilité avec la réduction de modèle, des complexités dans la modélisation des corps en mouvement, et des difficultés dans l'implémentation avec des codes commerciaux ne disposant pas d'un accès direct au code source. Ces considérations ont conduit au développement d'une approche non intrusive et Galerkin-free, basée sur la décomposition de domaine et équipée d'informations de capteurs pour prendre en compte les vagues. Ce modèle multi-fidélité intègre la CFD et la POD spatialement. Le solveur haute fidélité est déployé dans le champ proche où les effets visqueux et non linéaires dominent, tandis que le modèle POD ROM est adapté aux régions faiblement non linéaires, concentré sur la propagation des vagues en champ lointain. En exploitant un petit domaine haute fidélité par rapport au domaine original, cette approche permet des réductions significatives des coûts en CPU, tout en préservant la précision. L'échange bidirectionnel d'informations entre les deux modèles est facilité par des régions de chevauchement et des frontières des sous-domaines. La méthodologie de couplage est facilement applicable à diverses simulations impliquant des corps en mouvement, y compris la conversion d'énergie des vagues, permettant une représentation efficace des propriétés multi-échelles. Cette méthodologie démontre une reconstruction précise de l'écoulement et une

description complète de la dynamique du flotteur. Des tests de validation approfondis comprennent à la fois des simulations in-sample, pour des configurations de reproduction, et, plus notamment, des simulations out-of-sample. Ces dernières soulignent la précision et la robustesse de la méthodologie proposée, capable de prédire des solutions pour des paramètres inconnus. L'efficacité de ce modèle hybride permet des simulations intensives, le rendant adapté à un large éventail d'applications, y compris des études paramétriques, des tâches d'optimisation et des simulations multi-objectif. En réduisant considérablement les coûts computationnels, le modèle couplé non seulement accélère les processus d'optimisation et de conception pour les fermes de convertisseurs d'énergie des vagues, mais ouvre également la voie à une évolutivité et une durabilité accrue dans le secteur de l'énergie marine.

Mots-clés : Décomposition orthogonale aux valeurs propres, Énergie marine, Modélisation mathématique, Modèles réduits, Simulations numériques, Modèles multifidelité.

Modellazione multi-scala et multi-fedeltà per convertitori di energia da moto ondoso

Riassunto esteso

Di fronte all'evoluzione del panorama energetico verso soluzioni più sostenibili, il settore marino sta mostrando un crescente interesse nell'energia da moto ondoso come fonte di energia pulita. La distribuzione di convertitori di energia delle onde (WECs) in parchi offre un notevole potenziale per una produzione su vasta scala, ma richiede altresì simulazioni numeriche approfondite, a causa della complessità dell'idrodinamica. La simulazione di parchi di WECs presenta notevoli sfide a causa della loro natura multi-scala, che include la rappresentazione precisa delle interazioni fluido-struttura e tra i WECs, generando effetti sia nel campo vicino che in quello lontano, il quale rappresenta l'influenza più ampia del parco sull'ambiente circostante.

Sebbene i modelli ad alta fedeltà, come la CFD (Computational Fluid Dynamics), siano essenziali per catturare le complessità dei fenomeni non lineari, presentano un costo computazionale elevato. Le tecniche di riduzione di modello emergono

come un approccio promettente per affrontare questa sfida, mirando a ridurre la complessità computazionale mantenendo al contempo la precisione. Tra queste tecniche, la decomposizione ortogonale ai valori propri (POD) si distingue come un metodo efficace per derivare una base ridotta in sistemi di flusso multidimensionale. I modelli a ordine ridotto (ROMs) basati sulla POD hanno dimostrato il loro successo nelle riduzioni di modelli lineari e debolmente non lineari monofase. Tuttavia, i ROM tradizionali, ottenuti attraverso la POD e la proiezione di Galerkin, incontrano diverse difficoltà nei flussi multifase, tra cui problemi di instabilità, compatibilità con la riduzione del modello, complessità nella modellazione dei corpi in movimento e difficoltà nell'implementazione con codici commerciali che non dispongono di accesso diretto al codice sorgente.

Queste considerazioni hanno portato allo sviluppo di un approccio non intrusivo e Galerkin-free, basato sulla decomposizione del dominio e dotato di informazioni da sensori per tenere conto delle onde. Questo modello multi-fedeltà integra CFD e POD spazialmente. Il solver ad alta fedeltà è utilizzato nel campo vicino, dove gli effetti viscosi e non lineari predominano, mentre il modello POD ROM è adattato alle regioni debolmente non lineari, e concentrato sulla propagazione delle onde in campo lontano. Sfruttando un piccolo dominio ad alta fedeltà rispetto al dominio originale, questo approccio consente significative riduzioni dei costi in termini di CPU, preservando al contempo la precisione. Lo scambio bidirezionale di informazioni tra i due modelli è facilitato da regioni di sovrapposizione e confini dei sotto-domini.

La metodologia di accoppiamento è facilmente applicabile a varie simulazioni che coinvolgono corpi in movimento, compresa la conversione di energia delle onde, consentendo una rappresentazione efficiente delle proprietà multi-scala. Questa metodologia dimostra una ricostruzione precisa del flusso e una descrizione completa della dinamica del WEC. I test di validazione approfonditi includono sia simulazioni in-sample, per la riproduzione della soluzione, sia, e soprattutto, simulazioni out-of-sample. Queste ultime evidenziano la precisione e la robustezza della metodologia proposta, in grado di prevedere soluzioni per parametri sconosciuti. L'efficacia di questo modello ibrido consente simulazioni intensive, rendendolo adatto a una vasta gamma di applicazioni, comprese studi parametrici, attività di ottimizzazione e simulazioni multi-obiettivo. Riducendo notevolmente i costi computazionali, il modello accoppiato non solo accelera i processi di ottimizzazione e progettazione per

i parchi di convertitori di energia delle onde, ma apre anche la strada a una maggiore scalabilità e sostenibilità nel settore dell'energia marina.

Parole chiave: Decomposizione ortogonale ai valori propri, Energia marina, Modellazione matematica, Modelli di ordine ridotto, Simulazioni numeriche, Modelli multifedeltà.

Unité de recherche
UMR 5251 Université, 33000 Bordeaux, France.

Résumé détaillé

Le passage à des énergies renouvelables devient crucial dans un monde où la demande énergétique, en grande partie alimentée par des combustibles fossiles, a des conséquences dévastatrices sur l'environnement. Malgré l'augmentation continue de la consommation d'énergie, des alternatives comme le solaire, l'éolien et l'énergie des vagues offrent des solutions plus durables. Cependant, leur adoption nécessite une modélisation numérique précise pour équilibrer efficacité et coût, ce qui constitue un défi majeur à relever.

Dans le cadre d'un programme de doctorat en cotutelle entre le Politecnico di Torino (Italie) et l'Université de Bordeaux (France), cette thèse aborde la question de l'équilibre entre la précision de la simulation et l'efficacité computationnelle. Pour ce faire, elle combine deux domaines d'expertise différents : l'énergie des vagues et la modélisation numérique. Le laboratoire Marine Offshore Renewable Energy du Politecnico di Torino est spécialisé dans les énergies renouvelables en mer, notamment la conception de convertisseurs d'énergie des vagues (WECs). De son côté, l'Université de Bordeaux, en particulier l'équipe Inria MEMPHIS à l'IMB, excelle dans les techniques de réduction de modèle pour les applications industrielles. Bien que ces techniques permettent de réduire la complexité des simulations tout en maintenant leur précision, leur application à des cas pratiques reste un défi dans ce projet.

Modélisation numérique de fermes de convertisseurs d'énergie des vagues
Un aperçu approfondi de l'énergie des vagues et des technologies associées est nécessaire pour introduire le problème, mettant en avant les convertisseurs d'énergie des vagues et les divers aspects de leur développement, y compris la nécessité de déployer plusieurs WECs dans des fermes. Les fermes de WECs, caractérisées par le placement stratégique de plusieurs dispositifs, visent principalement à réaliser

une compétitivité commerciale à grande échelle par rapport aux autres sources d'énergie renouvelable. Le positionnement stratégique de plusieurs WECs favorise une production d'énergie stable et abondante. L'interaction entre les vagues et les WECs impacte la production d'énergie, avec la proximité entre ces dispositifs offrant un potentiel d'amélioration de la production. En outre, le déploiement de WECs identiques au même endroit présente des avantages opérationnels et des économies de coûts, ce qui se traduit par une réduction des dépenses en capital et en exploitation.

La dynamique des vagues au sein d'une ferme de WECs présente une grande complexité. Une approche de modélisation numérique exhaustive pour une ferme doit prendre en considération divers aspects, tels que les phénomènes dans les champs proche et lointain. Cela implique la description des interactions fluide-structure, des interactions entre les WECs et de l'atténuation des vagues sur de vastes domaines. De plus, les simulations doivent aborder la dynamique de plusieurs WECs, chacun avec plusieurs degrés de liberté, ce qui contribue à la complexité du champ de vagues. Des éléments tels que la turbulence, les systèmes d'amarrage et les stratégies de contrôle ajoutent une couche de complexité supplémentaire au phénomène. En outre, étant donné que les caractéristiques des vagues varient en fonction de l'emplacement choisi pour la ferme, une simulation numérique fiable doit tenir compte de ces variations pour refléter fidèlement la réalité. Répondre à ces exigences représente une tâche très exigeante, nécessitant souvent la séparation des différents éléments et l'utilisation d'hypothèses simplificatrices pour réduire les coûts de calcul.

Quelle que soit la précision déterminée, tout modèle numérique comporte des approximations et des erreurs induites par des hypothèses simplificatrices visant à réduire les coûts de calcul. Il existe une diversité de modèles numériques pour simuler les fermes de WECs, mais les différences entre les phénomènes dans le champ proche et dans le champ lointain peuvent limiter l'efficacité d'un modèle adapté à l'un pour capturer l'autre dans sa totalité. Le choix du modèle implique un compromis entre coût et précision : les modèles rentables peuvent surestimer ou sous-estimer la dynamique, tandis que la précision accrue nécessite davantage de calculs. Outre la simplification traditionnelle du problème, d'autres stratégies alternatives comme les modèles basés sur les données ou les modèles à ordre réduit se concentrent sur la réduction de la taille du problème.

Modèles d'ordre réduit pour les écoulements Les Modèles d'Ordre Réduit (ROM), qui visent à extraire les caractéristiques essentielles et à simplifier la complexité informatique, sont appliqués dans divers domaines, comme la mécanique des fluides. Le développement des ROMs comprend généralement deux phases, appelées offline et online. La phase offline consiste en une phase d'entraînement où des simulations haute fidélité des systèmes cibles sont exécutées pour différents paramètres, et des bases réduites sont construites à partir de snapshots - distributions spatiales de la solution d'une simulation numérique à des occurrences temporelles particulières. Pendant la phase online, le ROM est mis en œuvre en projetant les équations gouvernantes sur les bases réduites.

À la base d'un modèle à ordre réduit, il y a la définition d'une réalisation espace-temps $\mathbf{U}(\mathbf{x},t)$, comme une superposition linéaire de N_r fonctions de base spatiales - ou modes - $\Phi(\mathbf{x})$, et N_r coefficients temporels $\mathbf{a}(t)$, à la différence d'un champ de référence $\overline{\mathbf{U}}(\mathbf{x})$:

$$\mathbf{U}(\mathbf{x},t) = \overline{\mathbf{U}}(\mathbf{x}) + \sum_{i=1}^{N_r} a_i(t)\ \boldsymbol{\Phi}_i(\mathbf{x}). \tag{1}$$

Pour des problèmes linéaires et non linéaires, une méthode fréquemment utilisée pour dériver une base réduite à partir des snapshots est la Décomposition Orthogonale aux valeurs Propres (POD). La POD est un outil robuste pour construire des modèles réduits pour des problèmes de grande dimension et maintient globalement la dynamique non linéaire, même lors de la projection sur des sous-espaces linéaires ou affines. Elle identifie les modes comme étant les fonctions déterministes les plus corrélées, en moyenne, avec les réalisations, ce qui implique de trouver un ensemble de fonctions qui minimisent l'erreur quadratique moyenne entre les réalisations et la superposition linéaire. Cette optimisation énergétique signifie que seul un petit nombre de modes, N_r, peut être nécessaire pour représenter efficacement les réalisations. Lorsque N_r est égal au nombre de snapshots N_s, l'égalité dans l'équation (1) reste valide. Cependant, en choisissant $N_r \ll N_s$, on obtient une approximation, tout en réalisant une réduction cohérente de la taille du problème.

Les ROMs basés sur la POD pour les écoulements multiphasiques manquent de preuves dans la littérature existante. Par conséquent, un POD ROM est introduit pour les écoulements biphases impliquant de l'eau et de l'air. Une approche progressive est adoptée, débutant par une étude de cas bien établie, l'écoulement autour d'un

cylindre, où le modèle ROM basé sur la POD est connu pour être très efficace dans les écoulements monophasiques à faible nombre de Reynolds. La configuration est ensuite progressivement modifiée pour passer à des écoulements biphases à haut nombre de Reynolds, impliquant l'analyse de différents termes des équations de Navier-Stokes et leur effet sur le modèle réduit. Le modèle montre une bonne réduction du problème avec la POD, avec moins de 3% des modes capturant 99% de l'information. Une version asymptotiquement réduite permet d'éviter l'apparition d'un tenseur du quatrième ordre, mais le modèle devient instable lors du traitement de deux fluides distincts et d'une interface entre eux. La version actuelle du modèle POD ROM ne suffit pas pour la réduction des écoulements multiphasiques, nécessitant des recherches supplémentaires. Malgré cela, la réduction permise par la POD est cohérente. Les défis inhérents aux ROMs dans la modélisation précise des corps en mouvement remettent en question leur applicabilité dans la modélisation des WECs, en plus des problèmes d'instabilité, proposant ainsi une approche alternative.

Modélisation multi-fidélité des convertisseurs d'énergie des vagues Une approche multi-fidélité est recommandée pour distinguer les différentes dynamiques et sélectionner le solveur le mieux adapté à chacune d'entre elles. Habituellement, un solveur haute-fidélité est choisi près du WEC, où les non-linéarités et les effets visqueux sont plus prononcés. À l'opposé, un solveur de plus basse fidélité est utilisé pour étendre les solutions sur des domaines plus vastes et doit interagir efficacement avec le solveur haute-fidélité. Un modèle qui maintient la cohérence des variables sur les deux solveurs est une solution pratique. La méthodologie proposée permet cela, s'agissant d'un couplage bidirectionnel entre CFD et POD non intrusif basé sur la décomposition de domaine et une approche Galerkin-free. Cette méthodologie se résume à un problème de minimisation des moindres carrés, permettant son application à des simulations impliquant des corps en mouvement, y compris la conversion de l'énergie des vagues.

Les résultats sont obtenus pour un prototype simple, modélisé comme une sphère (Figure 1), mais la méthodologie peut facilement s'adapter à des WECs plus complexes et à pleine échelle avec plusieurs degrés de liberté. De plus, sans modifier la stratégie de couplage, des détails supplémentaires tels que les systèmes d'amarrage ou de contrôle peuvent être incorporés, améliorant ainsi le réalisme des simulations. Pour le cas considéré, le volume du domaine haute-fidélité est réduit à seulement 0.015% du domaine d'origine, offrant ainsi une énorme économie computationnelle,

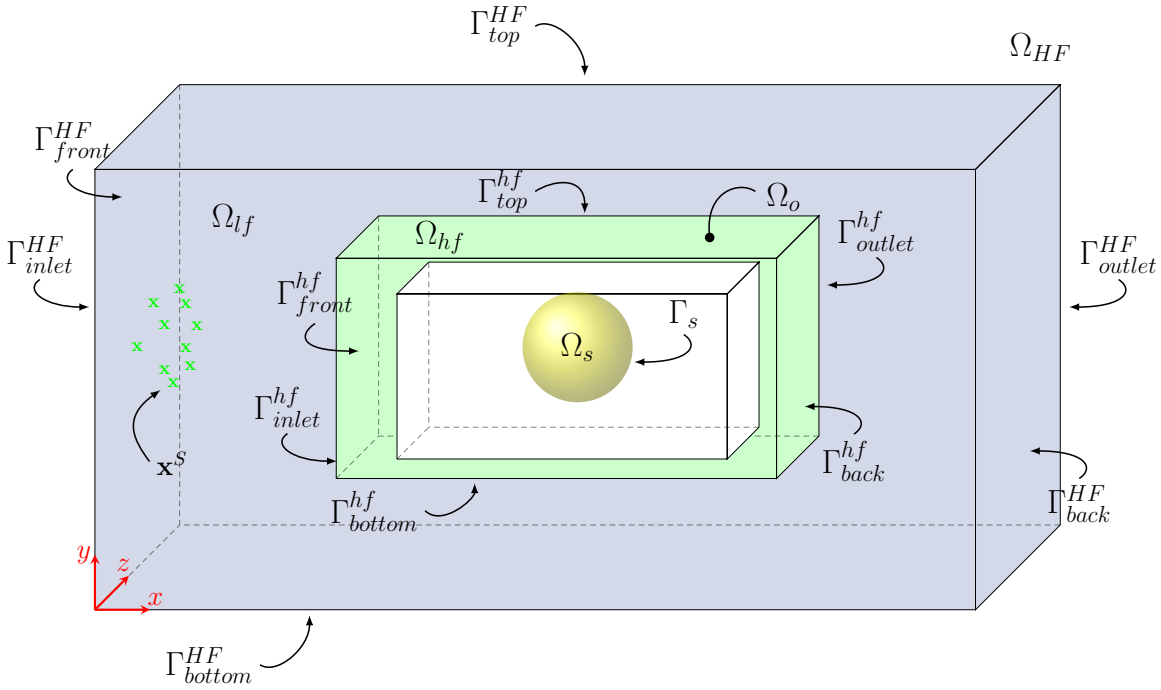

Fig. 1 Esquisse de la décomposition de domaine pour la méthodologie de couplage, avec la définition des différents sous-domaines et des frontières.

tout en maintenant la précision car les erreurs relatives maximales restent inférieures à 0.2%. L'approche donne des résultats satisfaisants pour des cas de reproduction du problème précédemment simulé, mais surtout la méthode démontre également la capacité à prédire des solutions pour des paramètres non connus. Dans ce cas, la précision est conservée et la réduction significative des coûts CPU est poussée encore plus loin, permettant des simulations intensives, adaptées aux tâches d'optimisation et aux simulations multi-objectif.

La recherche de cette thèse pose des questions ouvertes et suggère des pistes pour de futures explorations. La méthodologie de couplage montre des résultats encourageants et une réduction significative de la charge de calcul. Outre la modélisation des fermes de WEC, une gamme étendue d'investigations est envisageable, y compris des configurations hybrides avec d'autres sources d'énergie renouvelable. Bien que cette étude se concentre principalement sur la dynamique des fluides, d'autres aspects tels que les systèmes d'amarrage ou la stratégie de contrôle peuvent nécessiter des approches différentes. La méthodologie de couplage n'exclut pas l'utilisation d'autres modèles. Malgré la complexité, une simulation exhaustive reste essentielle pour obtenir une vision d'ensemble du potentiel des énergie des vagues.

Contents

List of Figures

List of Tables

Nomenclature

Acronyms / Abbreviations

BEM Boundary Element Method

CFD Computational Fluid Dynamics

DMD Dynamic Mode Decomposition

DoF Degree of Freedom

FOM Full Order Model

MOR Model Order Reduction

OSWC Oscillating Surge Wave Converter

OWC Oscillating Water Column

PDE Partial Differential Equation

pMOR Parametric Model Order Reduction

POD Proper Orthogonal Decomposition

PTO Power Take-Off

RANS Reynolds-averaged Navier–Stokes

RIC Relative Information Content

ROM Reduced Order Model

SPH Smoothed-Particle Hydrodynamics

SVD Singular Value Decomposition

TRL Technology Readiness Level

VOF Volume of Fluid

WEC Wave Energy Converter

Chapter 1

Introduction

Any activity demands energy, whether it is commuting to the city center, preparing a meal, watching a video, or turning on the lights. The contemporary lifestyle requires a substantial amount of energy, a demand that has exponentially risen since the Industrial Revolution, as illustrated in Figure 1.1. The share of the energy source displayed in the graph reflects how fossil fuels account for the majority of the world's energy supply. The extensive use of such non-renewable energy sources has catastrophically compromised ecosystems and biodiversity. Moreover, their inherent inability to swiftly regenerate contributes to a gradual depletion of these resources. Despite this, energy consumption continues to grow daily. A transition to renewable energies, albeit more challenging, is imperative. Traditional renewable sources like solar and wind, being well-established, continually evolve towards more efficient solutions. In this context, wave energy emerges as a recent prospect with high potential, but also substantial complexities. The advancements in this field heavily relies on extensive numerical modeling, which, in itself, presents several challenges. The primary difficulty lies in achieving the delicate balance between simulation accuracy and computational cost. Such trade-off is essentially the focus of this work.

Within the framework of a cotutelle PhD programme between Politecnico di Torino (Italy) and Université de Bordeaux (France), this thesis addresses the issue of achieving the equilibrium between simulation precision and computational efficiency. To this end, two different domains of expertise are combined, the wave energy and the numerical modeling. On one side, at Politecnico di Torino, the Marine

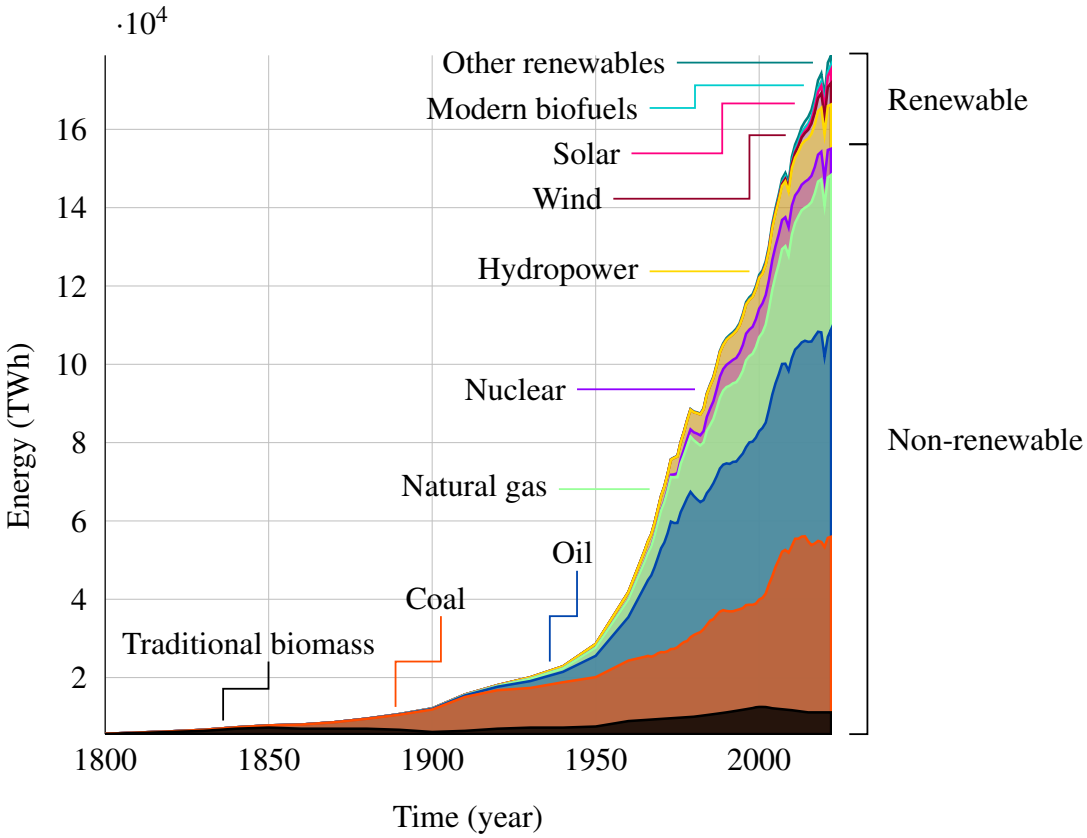

Fig. 1.1 Global primary energy consumption by source, redrawn from [1].

Offshore Renewable Energy Lab boasts extensive knowledge in offshore renewable energies, encompassing all facets of technology development, including Wave Energy Converter (WEC) design. A crucial stage in this process involves arranging multiple WECs in farms to generate power at a commercial scale. Before deploying these devices in real-world settings, thorough numerical simulations are conducted to gain a comprehensive understanding of the underlying phenomena. Depending on the developmental stage, various numerical approaches for WEC farms are available, chosen based on predefined requirements and constraints such as storage and simulation time. On the other side, at Université de Bordeaux, specifically within the Inria MEMPHIS team at IMB (Institut de Mathématiques de Bordeaux), expertise lies in various modeling techniques for industrial applications, including Model Order Reduction (MOR). MOR techniques excel in reducing simulation complexity, thereby lowering computational costs while maintaining high accuracy. Widely employed in various domains, including fluid dynamics, these techniques demonstrate good results in benchmark cases and show promise in real-world applications. However,

the successful application of such mathematical tools to practical cases presents a significant challenge in this project.

The research aims to create an accurate model for multiphase flows and moving bodies, while managing computational demands to align with tight technology development schedules. Given the scarce application of model order reduction to the wave energy domain, outcomes are initially uncertain and the methodology may not be readily clear. Indeed, following unsatisfactory outcomes from an initial implementation of a Reduced-Order Model (ROM) based on Proper Orthogonal Decomposition (POD) for simulating a WEC prototype in regular waves, a methodical approach is adopted, with the surrogate WEC model as the ultimate objective. Beginning with a well-studied problem in model reduction involving a monophase flow, complexities are gradually introduced. Motivated by the absence of evidence for multiphase surrogate models in existing literature, efforts are made to develop a POD ROM model for water and air, but stability issues persist, prompting further investigation. However, an alternative approach involving the coupling of the POD ROM model with a high-fidelity model is pursued and proves successful for numerical simulations of WECs in waves. The algorithm, designed to accommodate multiphase flows and moving rigid bodies, is both straightforward and versatile, effectively reducing computational demands while maintaining accuracy. The findings of this thesis represent cutting-edge advancements that lay the groundwork for accomplishing the more extended objective of modeling WEC farms.

Throughout the leading project, two main short side projects provide opportunities to delve deeper into the numerical modeling of WEC farms, offering valuable insights and alternative perspectives beneficial for the primary project.
A first STSM (Short-Term Scientific Mission) at Ghent University (Belgium) aims at familiarizing with their well-established coupling methodology, and applying it to a small-scale WEC farms. The project allows to appreciate the strength points and limits of such coupling methodology, both mainly related to the fidelity of the implemented numerical models. The experience serves to point the main important nodes in the development of the coupling methodology presented in this work. The other secondment at Optimad Srl in Turin (Italy), in the framework of the ARIA project (Accurate ROMs for Industrial Applications), focuses on exploring the integration of ROMs across various simulations. A notable challenge is the use of commercial softwares, where access to the source code is unavailable, and direct modifications are precluded. The project allows to identify alternative approaches

to directly reduce high-fidelity costs and subsequently applying MOR for learning and predicting solutions. Furthermore, the project has provided access to Optimad's on-premise HPC cluster, instrumental in generating the results presented in this document. Comprising 2 frontend nodes and 8 compute nodes, each node features 2 AMD CPU Epyc 7413 24-core processors, 128GB RAM, and Red Hat OS 8.5.0. Interconnected via Ethernet 10Gbps, the nodes are accessible through a remote GUI facilitated by Nice DCV.

The document is structured into three main chapters, aside from introduction and conclusion.

Chapter 2 delves into the significance of wave energy and provides a non-exhaustive overview of numerical modeling approaches for WEC farms. The chapter aims to:

- Review the fundamental definitions and classifications of WECs to establish a connection between their characteristics and the numerical modeling approach.
- Discuss the key motivations behind developing WEC farms, define the main attributes of a farm, and outline the primary objectives of studies related to WEC farms.
- Explore the diverse range of modeling strategies utilized in WEC farm simulations, considering factors such as desired fidelity levels, computational requirements, and the specific characteristics of WECs and farms targeted.

Additionally, some preliminary results from publications stemming from work conducted at Ghent University are presented, contributing to the advancement of research in numerical modeling of WEC farms.

Chapter 3 provides an introduction to Model Order Reduction (MOR) and Proper Orthogonal Decomposition (POD) techniques, along with an approach for developing a multiphase POD ROM model. Specifically, this chapter covers:

- A brief overview of MOR techniques, emphasizing projection-based ROMs, with a focus on POD and its application to a well-known case for clarity.

- Analysis of the various components comprising the model to understand their impact and how to address them in the context of multiphase flows.
- Presentation of numerical results at each stage to illustrate the challenges encountered.
- Brief introduction of the Dynamic Mode Decomposition (DMD) approach, and comparison with the POD for a specific test case.

This chapter also emphasizes the unsuitability of the presented POD ROM model for multiphase flow simulation, highlighting the importance of sharing unsuccessful attempts to direct future research efforts.

Chapter 4 presents the coupling methodology, covering its definition, implementation, testing, and validation. This chapter includes:

- A brief overview of coupling methodologies in the wave energy and MOR sectors.
- The theoretical framework and algorithmic implementation of the multi-fidelity model.
- Presentation of various tests, along with corresponding numerical results, utilized for refining the methodology.
- Application of the methodology to a case potentially modeling a point absorber WEC type.
- Insights into the algorithm for implementing the WEC farm multi-fidelity model.

The highly accurate results obtained from the coupled model indicate the promising prospects for continued research. Some potential perspectives are provided in the conclusion chapter.

Chapter 2

The Numerical modeling of Wave Energy Converter Farms

This chapter provides an overview of wave energy and the technology associated with it. The primary classifications of Wave Energy Converters (WECs) and the different aspects of technology development are addressed, including the necessity of deploying several WECs in farms (Section 2.1). Within this framework, the key characteristics of a WEC farm are defined in Section 2.2, as well as the main phenomena occurring within such environments, based on current understanding. Additionally, the primary objectives driving studies related to WEC farms are outlined, and some advancements in this field, stemming from dedicated research efforts, are presented. The chapter then explores the various numerical modeling strategies specifically tailored to WEC farm simulation (Section 2.3). Although a wide range of references is available for numerical modeling in wave energy, this chapter mainly covers those related to wave energy converter farms.

2.1 Wave Energy

As the largest global greenhouse gas emissions come from electricity and heat generation, and considering the fragile socio-political scenario of the recent years, a robust expansion of renewable energy is imperative.

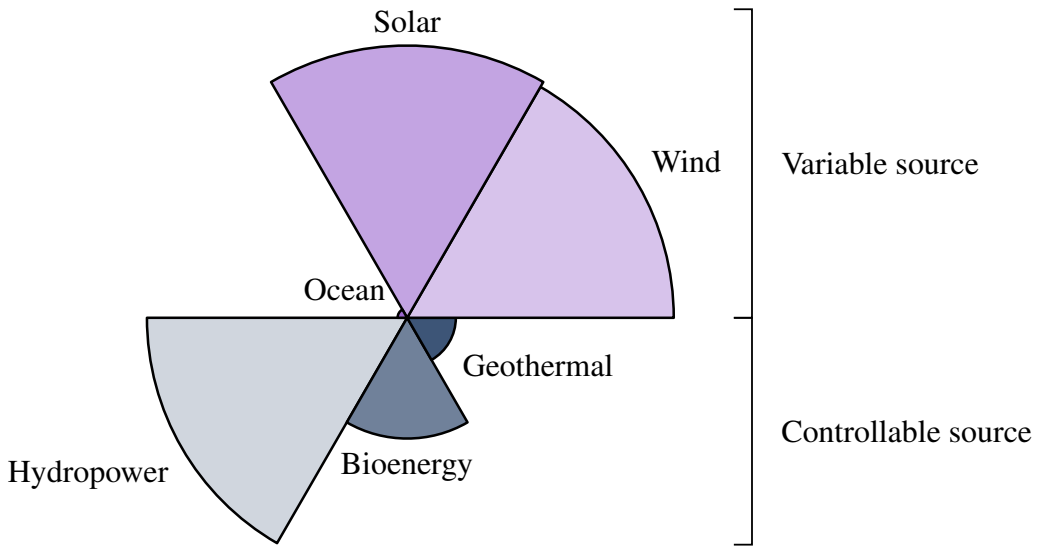

Fig. 2.1 Share of renewable energy source, 2030 forecast [2]. Ocean energy encompasses sources like ocean waves, tidal range, tidal current, ocean current, ocean thermal energy, and salinity gradient.

The International Energy Agency forecast [2] predicts a consistent increase in electricity generation from renewable sources in the coming years, positioning renewables as a primary source of electricity, constituting almost half of the global electricity generation. Figure 2.1 illustrates the share of various renewable energy sources in a polar plot, with the radius proportional to each source's contribution. These sources are categorized as controllable or constant, in contrast to variable or intermittent sources, which are not dispatchable due to their fluctuating nature. While hydropower continues to be a popular renewable energy source, output from variable renewables such as wind and solar is expected to surpass it, benefiting from increasingly lower generation costs, and provided accelerated investments in grids and system flexibility, to ensure a smooth integration in the global power mix. Ocean energy, in particular tidal and wave conversion systems, is expected to contribute significantly in the short to medium term, owing to both local resource availability and technological advancements. Salinity gradient and ocean thermal energy conversion have not reached the same level of maturity. Despite the expected small contribution depicted in Figure 2.1, ocean energy stands out as a consistent and abundant source compared to solar and wind energy [3]. Specifically, wave energy holds huge potential due to its high power density, predictability, and consistency [4]. Waves can travel large distances with little energy loss, and even if they show a

seasonal pattern, they are not intermittent, as wind and solar resources are. Despite leveraging knowledge and infrastructure from the offshore oil sector [5], wave energy technology is still in its early stages compared to wind and solar, lacking cost competitiveness. Research and funding are dispersed across various wave and marine current energy concepts under development, with no technology convergence, unlike the wind energy sector.

The patent literature for wave energy converters features over a thousand patents and over a hundred projects at different stages of development [6]. A wave energy converter (WEC) is a device converting kinetic and potential energy from traveling waves into mechanical or electrical energy. Classification of these technologies can be based on operating principles (rotating mass, overtopping, oscillating water column, oscillating surge converter) [7], deployment location (onshore, nearshore, offshore), orientation (terminator, attenuator, point absorber), installation type (floating, bottom standing, fully submerged) and foundation (attached or moored), or power take-off (PTO) system (self-referenced or seabed referenced, pneumatic, hydro, hydraulic, direct drive) [8]. To delve further into the specifics, some examples are provided, to enhance comprehension of the challenges encountered in the numerical modeling phase of the WECs.

- Point absorber. A structure with dimensions much smaller than the incident wavelength, usually characterized by omnidirectionality. It typically comprises two parts, a floating section, and a fixed structure, exploiting relative motion for energy generation. Primarily capable of heaving or pitching, it results in a numerically straightforward simulation due to the simplification to a single DoF (degree of freedom) and its circular shape. The omnidirectional nature aids in reducing the number of simulations for individual devices but does not hold true for arrays affected by directional waves. Examples include CorPower [9], Powerbuoy [10], and WaveStar [11]. The numerical modeling of point-absorber farms varies from semi-analytical models [12–15] to more detailed attempts, including Computational Fluid Dynamics (CFD) [16], and the farm sizes may range from small to large (up to 100 units).

- Attenuator. Aligned with the predominant wave direction, commonly surface floating, with some submerged designs proposed. Pelamis [17], activating a PTO with motion between adjacent floating structural components, is a floating attenuator example. Simulation of farms of 5 or 10 Pelamis involves using

spectral models like SWAN for assessing, for instance, the environmental impact on the Portuguese coastal environment [18], or using models such as REFDIF based on the mild slope equations [19], and Boussinesq equations [20] for smaller farms. A submerged variant is a rubber tube with elastic walls, known as Anaconda [21], modeled as a farm of few rows in [22] with the MIKE21BW Boussinesq wave propagation model.

- Rotating mass converter. A floating device housing an eccentric mass moved by pitching or rolling motion. Modeling is challenging due to complex geometries, multiple DoFs, intricate mooring systems, and control systems. Examples include ISWEC [23] or PeWEC [24], modeled in farms of up to 3 units, using the Boundary Element Method (BEM) [25–27].

- Terminator. Perpendicular to the wave direction. The most known technology is the overtopping device, which converts wave energy into potential energy, forcing water to be collected into a reservoir above the mean water level and then, with the action of gravity, to be returned to the sea passing through a hydraulic turbine. One example is the Wave Dragon [28], analyzed in a 5-WECs staggered farm by [29] using the MIKE21BW model, and by [30] using MILDwave.

- Oscillating water column. A partially submerged hollow structure exploiting the oscillatory motion of water inside and outside a chamber, driving an air turbine. Some OWCs (Oscillating Water Columns) are onshore, integrated, for example, in breakwaters, as Mutriku, working since 2011 [31]. Other OWCs may be integrated into hybrid platforms as motion suppressors for floating offshore wind turbines [32, 33]. Numerical simulation is challenging due to the need to consider air compressibility. In [34], the linear potential theory is used to model an infinite periodic linear array of OWC, equipped with a linear PTO, so that there is a proportionality relationship between the excess air pressure in the chamber and the air volume flow rate displaced by the interior free surface.

- Oscillating surge wave energy converter. Exploiting the surging motion of a flap moved horizontally by waves, typically designed for near-shore environments and usually attached to the bottom. Simple in shape, the OWSC (Oscillating Surge Wave Converter) is often simplified to one DoF [35, 36].

Prototypes include the WaveRoller [37] and the Oyster [38], with the latter extensively simulated in small to large farms using BEM [39, 27].

Regarding the working principles, the prevalence of point absorber-type WECs is primarily attributed to their simplicity, followed by OWC and OSWC [40]. Single-DoF WECs ideally operate at or near resonance to maximize power absorption. Otherwise, most of the wave energy is stored as reactive power, which cannot be converted into useful power. The strategy to enhance energy absorption involves actively controlling PTO damping to adjust WEC stiffness and mass, at the cost of complicating the technology.

The project's location significantly shapes both the project itself and the numerical modeling of the WEC or WEC farm, in terms of bathymetry and wave climate. In simulations of WEC farms, the bathymetry may undergo substantial changes due to the extensive areas covered, necessitating consideration, as it directly impacts wave behavior. Generally, there are three main categories. Onshore structures, installed directly on land, obviate the need for mooring systems or lengthy cables connecting WECs to the grid. While easily accessible, they exert a substantial environmental impact on nearby communities. Nearshore installations typically reside in shallow waters, with depths less than 40 meters, close to the shoreline. Offshore WECs operate in deep waters, where the depth exceeds half the wavelength of the wave or surpasses 40 meters. Offshore installations, although less visually impactful from land, pose challenges in terms of accessibility and operation costs. Numerical simulations for deep water waves versus shallow water waves differ significantly due to distinct regimes. In offshore areas, the available wave power is often considerably greater than onshore, unaffected by the sea floor, with flow characterized by higher Reynolds numbers. However, frequent extreme events and complex energy extraction, attributed to high wave directionality, complicate the dynamics, especially in the presence of mooring systems, vital for station-keeping in severe storm conditions. Conversely, moving closer to the shore alters the simulation setup, with no mooring system required and changes in wave conditions. As waves approach the shore, they tend to align with it [41], reducing directionality and containing less energy due to interactions with the seabed, where bottom friction dissipates part of the incoming wave energy. Numerical models for these waves must consider wave shoaling, refraction, and wave breaking.

In assessing the wave climate, a comprehensive evaluation of environmental factors influencing WEC power capture is crucial, encompassing not only sea-state but also water depth, strength and direction of marine currents, and wind patterns. Despite oceans covering over 70% of the Earth's surface, not all areas are exploitable. Optimal energy resources are typically found on the western coasts of continents, especially between 30° and 60° latitude in both hemispheres [42]. Moreover, the installation site must be easily accessible from the coast, and underwater cables should not be overly long to prevent excessive power loss. Coastal regions, islands, and archipelagos are particularly noteworthy, presenting significant potential for wave energy due to their location in deep water areas with steep shorelines, enabling the capture of substantial wave energy before dissipation processes occur near the sea bottom. Detailed parameter assessment in a wave area using in situ instruments, especially for offshore regions, is challenging. In such cases, a viable alternative involves considering simulated data from numerical models continually calibrated with measurements from satellite missions, research ships, buoys, and coastal stations. Integrated datasets, such as ERA5, the fifth generation ECMWF (European Centre for Medium-Range Weather Forecasts) reanalysis [43], cover the majority of the global water surface, including oceans, seas, sheltered waters, and calmer seas, presenting interesting locations for wave energy. These datasets boast global availability, no gaps in time series reporting, and are characterized by good spatial and temporal resolution, making them valuable resources for wave energy assessment over extended periods.

Information on the wave climate is crucial for the wave energy extraction process. Control strategies, aimed at optimizing the WEC response by bringing it close to the resonance condition for optimal power production, can be sophisticated. Given the highly complex and nonlinear nature of ocean waves, control strategies mirror these characteristics; consequently, the inclusion of a control system in the numerical simulation of a WEC adds to its complexity.

Another factor to consider in the numerical simulation of a WEC, or WEC farm, is the environmental impact, encompassing aspects like sediment transport, organism movement, pollution dispersal processes, and, on a larger scale, the effects on the benthic zone and coastal communities [44, 45]. For instance, incorporating sediment transportation in the numerical simulation requires the addition of a model to address such dynamics, further complicating the overall model [46]. Other considerations include the materials used for the WEC, along with challenges related to corrosion, fatigue, fouling, impact loading, fracture, and the associated costs of all project

components. While a complete numerical simulation that considers all aspects related to a WEC project would be ideal, it comes with extreme complexity and a prohibitive computational cost. Consequently, each omission or simplification makes the model simpler and more cost-effective, but it may move it further away from reality. The inevitable choice involves striking a trade-off. Moreover, such choices depend also on the level of development of a project. This is normally defined in the Technology Readiness Level (TRL) framework, initially devised by NASA for space technology, adjusted for wave energy technology development. TRL delineates the state of a technology program, typically comprising nine development levels that assess technology maturity through progression. In an effort to establish a standardized development path in wave energy, a five-stage approach has been conceptualized, ranging from small-scale model tests to intermediate stages and concluding with full-scale sea demonstrations [40].

Numerous wave energy converters have been proposed, at different TRL levels, contributing to a lack of convergence in technology and consensus. Varied reasons, including socio-economic and technical factors, such as the diversity of wave climates at different potential wave energy sites, their proximity to the coast, and variations in device operating principles, contribute to this lack of convergence. Despite this diversity in WECs and technology readiness, they all share a common destiny: the deployment of multiple WECs in farms, a mandatory step toward achieving the commercialization of wave energy. This step involves a heavy use of numerical modeling, before experimental and real sea testing and final deployment.

2.2 Wave Energy Converter Farms

Similar to wind and solar energy, wave energy also necessitates the deployment of multiple WECs in farms. These farms can vary in size, with a small group of WECs often referred to as an *array*. An array can be viewed as a block, and when replicated several times, it forms a large WEC farm. Numerical simulations typically focus on small farms, primarily due to computational costs. The behavior of a small block is considered indicative of the overall behavior of an ensemble of such blocks, making it a reasonable assumption, even if some dynamics of large farms may emerge. The concept of farm, involving the strategic placement of multiple WECs, is primarily oriented towards achieving commercial scale and competitiveness compared to other

renewable energies. The arrangement of multiple WECs allows for the capture of a significant amount of energy and ensures stability in power output. As waves travel, consisting of various components moving at different velocities, they interact with the multiple WECs spread across the area in different ways. Each WEC has its own production profile, which is likely independent of others, resulting in a consistent overall power production of the entire farm. Furthermore, proximity among devices may sometimes even boost the power generated by each WEC compared to being isolated. The presence of one WEC can influence the surrounding wave field and impact the dynamics of neighboring WECs if they are situated closely. Furthermore, the deployment of multiple identical WECs simultaneously in the same location enhances the feasibility of shared production, installation, and maintenance operations, including the potential for utilizing common underwater cables and mooring systems. This collective approach serves to minimize both capital (CapEx) and operational (OpEx) expenditures.

To grasp the dynamics of a WEC farm intuitively, the linear potential theory and regular waves can be employed. It is nonetheless important to retain that this model has some limitations, which will be further explained in the next section.

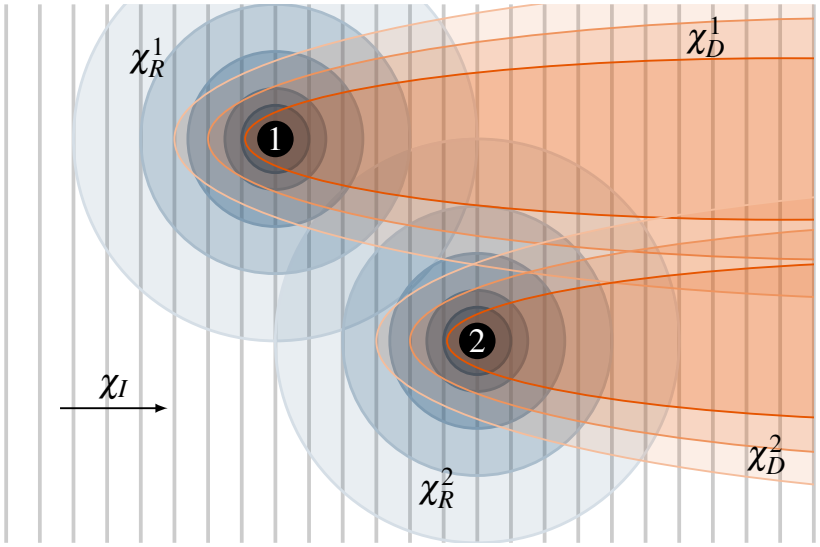

Fig. 2.2 Simplified representation of the different wave fields, incident, radiated and diffracted, for two WECs. The picture is inspired from [47].

According to the linear theory, the wave field passing a WEC can be considered as the superposition of an incident wave χ_I, a diffracted wave χ_D, and a radiated wave χ_R. The incident wave is a plane wave traveling from a distance and impacting

the WEC at a specific direction. The diffracted wave results from the deviation and change in direction of the incident wave due to the presence of a stationary WEC. The radiated wave occurs because of the displacement of water near the WEC, caused by its oscillatory motion in still waters. Figure 2.2 depicts a simplified sketch of the different wave fields, which all sum up to give the perturbed wave field, $\chi_P = \chi_I + \chi_D + \chi_R$. Energy conservation implies that part of the energy carried by the incident wave is redistributed by the diffracted and radiated waves in all other directions, with magnitude decreasing as the distance from the WEC increases. This behavior distinguishes a WEC from a wind turbine, which has a clear wake downstream.

In a WEC farm, the superposition of these elements is complicated by the presence of multiple WECs in close proximity. The diffracted and radiated waves of one WEC impact another WEC in addition to the incident wave. For farms with multiple lines, the rear rows are expected to experience an incident wave with less energy, as part of it has been absorbed by the front rows. This less energetic incident wave is also more perturbed due to the various contributions of diffraction and radiation from the front WECs, which, in turn, experience less disturbed incoming water. When designing a WEC farm, several aspects come into consideration, particularly the positioning of the WECs and the spacing between them in the layout. The former aspect is typically examined through arrays of a few WECs, as demonstrated in [48, 49], where the authors explore inline, triangle, rhombus, and square layouts of point absorbers across various wave climates (see Figure 2.3).

Linear arrays are found to be less efficient in power production, particularly susceptible to wave directionality, whereas square layouts, although more efficient, are also affected. Triangular-based layouts prove to be the most suitable for multidirectional wave climates. The other parameter, the spacing between WECs, significantly impacts the disturbed wave field within the farm and is influenced by technological factors. While closely spaced WECs experience stronger interactions, an optimal farm layout should allow ample space for WEC movement (especially with multiple DoFs and a loose mooring system), and maintenance boat navigation. By defining L as a characteristic length of a general WEC (Figure 2.3), irrespective of its shape and working principle, a general rule suggests maintaining a distance between WECs of at least d = 2L, with a maximum of d = 20L to maintain interactions. Research in [50] indicates that, while interaction decay is slow for regular waves, with a maximum of 10-15% impact on the absorbed power even at a distance of d = 200L,

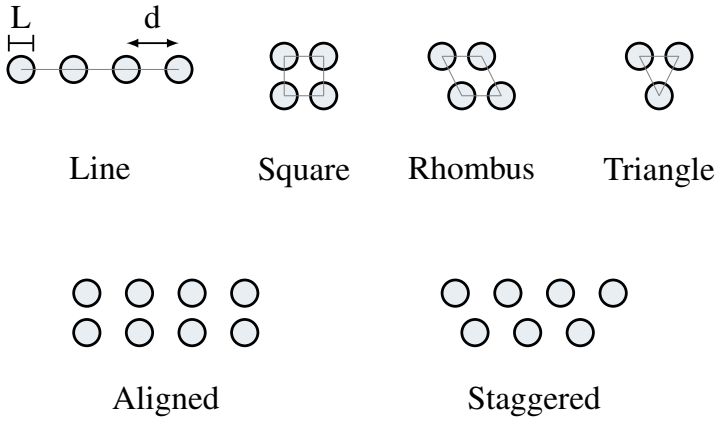

Fig. 2.3 Graphical representation of different WEC farm layouts, for small arrays (top line) and the general nomenclature for larger arrays (bottom line). The picture is inspired from [49].

irregular waves show a faster decrease in absorbed power with distance, with impacts of less than 10% within d = 40L. It should be mentioned that all of those assessments are based on linear potential theory, which ignores viscosity. As a result, interactions are anticipated to be more dispersed in real-world situations. Because of this, a d = 20L cutoff distance appears reasonable; beyond this range, WECs can be regarded as isolated. Nevertheless, the resulting farm would be abnormally large, which would raise expenses - notably for electric cables - and create difficulties for expensive and complex maintenance procedures.

Given the high infrastructure costs associated with WEC technologies, efforts are focused on maximizing power output. Each WEC is equipped with a PTO system, which amplifies interactions and causes an appreciable rise in incident wave cancellation or decrease in wave amplification. The overall energy balance is maintained, causing the wave passing the WEC to possess less energy, and a detectable wake forms in the lee of the WEC. Since the energy from diffraction and radiation decreases with distance, it is likely that WECs that are closer together interact more than those that are farther apart.

Based on these observations, one might anticipate predominantly negative interactions, reducing the overall energy extraction of a WEC farm, compared to an

equivalent number of isolated WECs. However, this assumption is not universally accurate, as positive interactions can also occur.

To quantify the impact of wave interactions on power absorption, the q-factor is defined as

$$\mathrm{q} = \frac{P_{tot}}{n_B P_s}, \tag{2.1}$$

where P_{tot} represents the total power produced by the farm, P_s denotes the power produced by a single, isolated WEC, and n_B is the number of units in the farm. Positive interactions yield $\mathrm{q} > 1$, signifying that placing multiple WECs in a farm layout is advantageous, since the total power surpasses that of isolated WECs. Conversely, if $\mathrm{q} < 1$, negative interactions predominate, resulting in a destructive park effect.

Owing to the fact that the radiated wave is associated with the motion of the WEC, which is influenced by the action of the PTO, a control strategy for the WEC farm is crucial to comprehend its efficiency. Hence, numerous studies delve into the optimization of WEC farm control strategies and related layouts [51–55] to obtain high values of the q-factor.

Most research tend to agree on a few reoccurring components. In most cases, the radiation and diffraction from the other rows help the initial row of a farm absorb more energy. Negative interactions and less energetic waves are seen in succeeding rows. Therefore, it is advisable to keep the number of rows to a minimum, in order to prevent significant losses that might not be compensated by the higher power of the front rows. This tendency is frequently seen both numerically and experimentally, and only one study [56] shows numerical results evidencing an increased power performance in the final row of a large farm of hundreds of WECs. During the experimental campaign of the WECwakes project [57], wave height drop is seen over five rows, in both aligned and staggered layouts (see Figure 2.3 for the definition), starting from the second or third row. Furthermore, for the studied point absorber WECs, characterized by axisymmetric shapes and only heaving motion, favorable interactions are found. Specifically, a marginally positive impact of 3% on the total power absorption for an aligned farm, and up to 16% when testing the staggered arrangement. A point absorber's radiated wave exhibits a circular form, and when it interacts with another such radiated wave, the resulting wave field is

simple. Comparable results might be obtained for OSWCs, which may be simplified to a single DoF as well. Nonetheless, a more elaborate wave field can be expected for more complicated WECs, with several coupled degrees of freedom.

The key objective of all the studies reported thus far is to maximize the power output. The goal is to prevent detrimental interactions as much as possible or, in the event that constructive interference is present, to maximize its benefits by designing an optimal farm layout, in conjunction with a tailored control technique. A popular approach for such a complicated multi-variate problem is to use genetic algorithms, because the dimension of the state vector that needs to be optimized is typically too large for an exhaustive search [58–60]. In [61], a comparison between the genetic algorithm and another optimization approach, the parabolic intersection technique, is conducted for five heaving WECs. The latter method involves defining a set of parabolas, determined by points where scattered or radiated waves are either in phase or out of phase with the ambient incident wave field, with the WECs positioned at the center of these parabolas. Results indicate that while the genetic algorithm yields highly optimal configurations for WEC farms, the parabolic intersection technique offers advantages in terms of simplicity and efficiency, as it quickly identifies points of constructive interference between parabolas for WEC placement.

Strategies for power output maximization are focused on what is known as the "near field," which consists of events that occur within a limited radius surrounding the WEC farm and in close proximity to the WECs. However, a WEC farm is not a closed circle; rather, it is a component of the "far field", a wider system that encompasses coastal populations and marine species. It is usual practice to use the disturbance coefficient K_d to quantify these far-field effects, defined as

$$K_d = \frac{\chi_P}{\chi_I}, \tag{2.2}$$

where χ_P is the total perturbed free surface elevation amplitude, and χ_I is the undisturbed incident wave. This coefficient represents the change in the wave field caused by the presence and action of a WEC or a WEC farm, compared to conditions with only an incident wave. Thus, a $K_d > 1$ corresponds to an increment in the wave field, and $K_d < 1$ symbolizes a wave attenuation. Positive interactions created in the WEC farm typically propagate forward. Conversely, waves that have had part of their energy absorbed by the WECs propagate behind the farm in the form of a wake.

Even if the WEC farm is situated offshore, at a considerable distance from the coast, waves travel long distances with minimal energy loss, potentially impacting coastal territories. In a study carried out as part of the PhD project, a small farm of three PeWECs demonstrates the generation of a wake reaching the coast, at a distance of 700 m (see Figure 2.4) [26].

As these floating WECs possess more than one DoF, interactions may be quite complex. Nevertheless, a visible wake is observed, especially with the action of the PTO, along with a significant area of perturbed wave field in the front. While the effects on local marine fauna in this region are challenging to define, the perturbed wave field reaching the shore can significantly impact the coast and the nearby communities. The wave height attenuation information may be used by sediment transport and morphological models, to predict the coastline evolution [62–64].

Numerous studies explore the effects of a WEC farm on the surrounding area, and for coastal protection purposes, the focus is on minimizing the K_d. Wave attenuation, particularly in regions close to harbors and shores, can be advantageous for mitigating coastal erosion, exacerbated by the effects of the climate crisis [65]. Current solutions for coastal protection, such as groynes, breakwaters, or barriers, may have drawbacks like impacts on marine life, turbidity, lagoon effects, danger to bathers, and visual impact [66]. WECs, especially in the form of farms, have the potential to address some of these issues by extracting energy from waves, resulting in a less energetic wave field in their lee. As investments to adapt to climate crisis effects are expected to be substantial, incorporating WEC farms into coastal protection strategies can lead to reduced wear on existing structures, minimized erosion, and lower associated risks. This cost synergy is crucial in reducing overall expenditure while increasing value, ultimately enhancing the economic viability of WECs [67].

An attempt in this regard is made in [68], where a flap gate system is examined using a semi-analytical approach and it is suggested that wave energy could be extracted from the storm barriers that keep Venice Lagoon from flooding. As a side activity of the PhD project, a multi-query strategy is proposed to balance both the objectives of coastal protection and power production, while also identifying potential synergies [27]. Findings show that maximizing power production causes a small wake because the excited WECs disturb the surrounding wave field significantly. Overall sufficient power can still be achieved by fine-tuning the control mechanism to improve wave attenuation. It is advisable to identify the region with a minimal

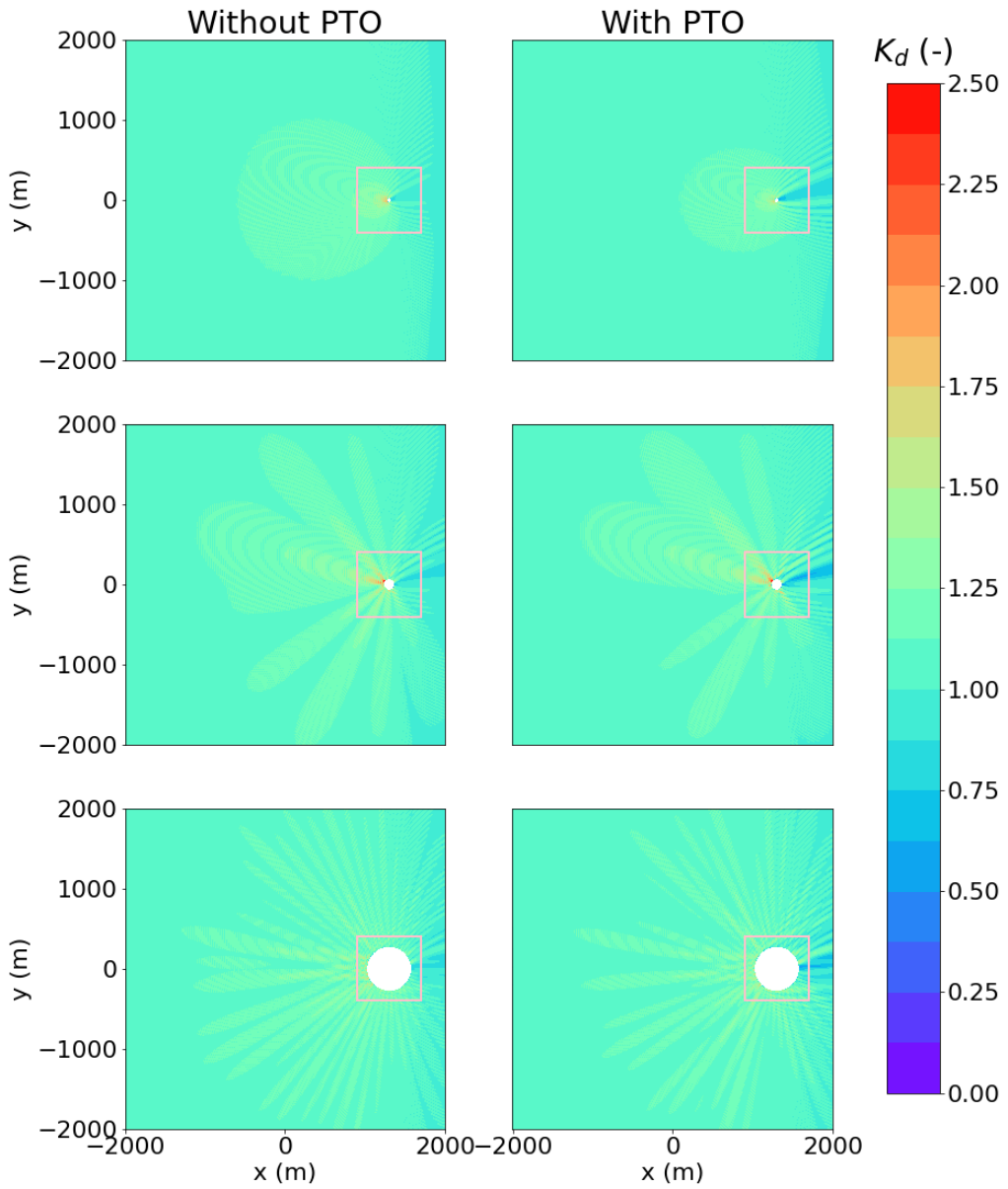

Fig. 2.4 K_d disturbance coefficient for the far-field of a WEC farm, taken from [26]. The comparison is among a single WEC (first row), a 3-WEC farm with separating distance d = 5L (second row), and a 3-WEC farm with separating distance d = 20L (third row). The pink square represents the near-field simulation domain, and the WEC farm is enclosed in the white circle.

wave attenuation of 10% (Figure 2.5) and fine-tuning the PTO to maximize power output. Thus, one can select the best WEC technology and farm structure, adjust the control strategy to meet the requirement, and extract the maximum power, by taking into account a particular sea site and its minimum standards for coastal protection. In this sense, WEC farms turn into an affordable answer that helps the surrounding marine populations, while satisfying demands for clean energy and adaptation.

Typically, analyses of WEC farms prioritize objectives such as power production and coastal protection, as well as finding a balance among the different goals, as mentioned. Secondary effects like desalination, hydrogen production, and photovoltaic panel integration may also be explored, along with co-locating wave-wind farms. Cost minimization serves as the primary driving factor behind these analyses, considering both capital (CapEx) and operational (OpEx) expenditures associated with WECs [69]. Aggregating multiple WECs helps mitigate these costs, reducing the Levelized Cost of Energy (LCOE) overall and enhancing the competitiveness of wave energy with conventional renewable energies. This corroborates the importance of designing and deploying WEC farms, necessitating accurate yet cost-effective numerical simulations at the different stages of the development.

A comprehensive numerical modeling approach for a WEC farm should encompass various aspects, including both the near-field and far-field phenomena. This involves capturing fluid-structure interactions, interactions among WECs, and wave attenuation over large domains. Additionally, simulations must address the dynamics of multiple WECs, each with several DoFs, contributing to the complexity of the wave field. Factors like turbulence, snap loads from mooring systems, and significant motions due to control strategies further complicate the phenomenon. Moreover, since wave characteristics vary based on the chosen site for the farm, a reliable numerical simulation must account for these variations to closely reflect reality. Meeting these requirements is highly challenging, often necessitating the separation of the various elements, and the use of simplifying assumptions to reduce computational costs. In the following section, the different techniques for the numerical simulations of WEC farms are presented. For complete reviews, please refer to [70–73].

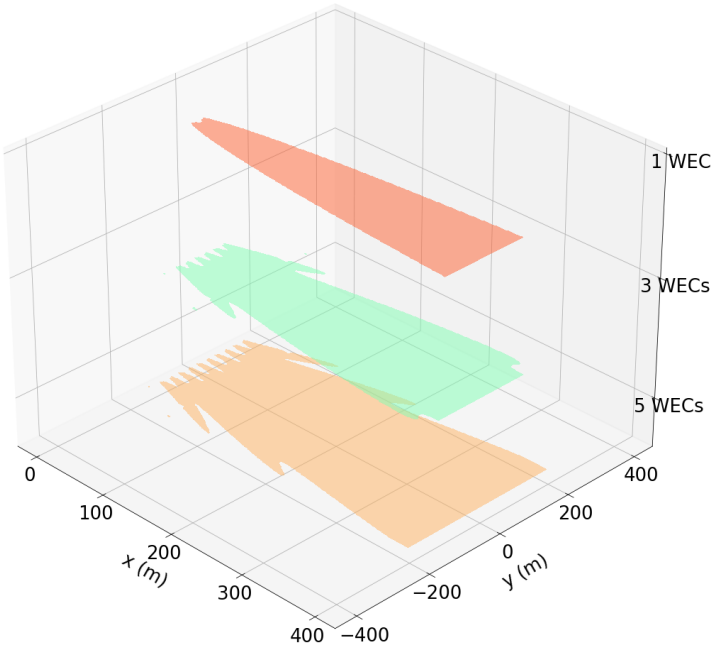

(a) Aligned layout.

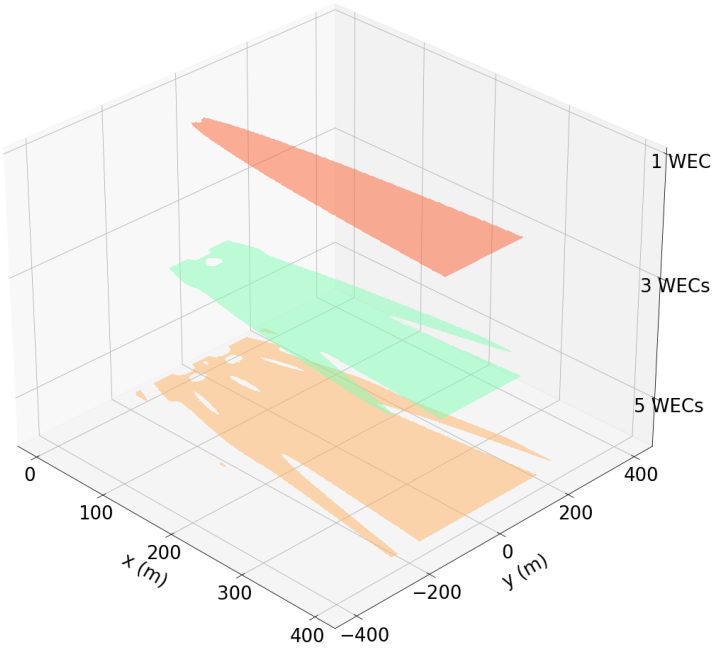

(b) Staggered layout.

Fig. 2.5 Representation of the wake (identified for $K_d < 0.9$) behind the single WEC and the farm of 3 and 5 OSWCs, for the aligned and staggered layouts. The result is in frequency domain and corresponds to the period $T = 6\,\mathrm{s}$, and the presence of the PTO is not considered. The picture is taken from [26].

2.3 Numerical Strategies for WEC Farm Simulations

Early research on numerical modeling of WEC farms dates back over half a century ago [74–76]. Since then, developments in technology have made it possible to perform extremely precise numerical simulations.
Any numerical model, based on a selected accuracy, inevitably incorporates approximations and introduces errors, and further inaccuracies may arise from simplifying assumptions. Such simplifications are usually necessary to reduce the computational cost. Several different numerical models exist for the simulation of WEC farms and are introduced in this section. A graphical representation of the trade-off between accuracy and computational cost of the WEC farm models is shown in Figure 2.6.

Furthermore, differentiating between phenomena in the near-field and in the far-field is essential for a WEC farm analysis. Since such events are different from one another, a model that fits one, may not fully capture the other. The different presented models are classified in Figure 2.7 by the application to the near-field or the far-field, and with the number of WECs modeled.

An accurate description of the dynamics of fluid flows is given by the Navier-Stokes equations, a set of partial differential equations (PDEs) currently lacking an analytical solution. By partitioning the continuum into finite temporal time steps and applying spatial discretization on a mesh or particles, it is possible to approximate these equations numerically. In classical Computational Fluid Dynamics (CFD), the approximate solution is computed at the grid points using an Eulerian technique. Common discretization schemes include the finite difference, finite element, and finite volume approaches. The finite difference method is the most direct approach and uses nodal values of regular grids to estimate derivatives. The finite element method divides the domain into a number of subdomains, and then uses local data to produce local approximations of solutions that are recombined into global approximations of the solution. The finite volume approach builds an approximation of the solution within cells by evaluating an accurate equation for the average value of the solution over a given volume. Finite elements and finite volumes are advantageous for handling intricate geometries and boundaries. Complex WEC geometries and biphase fluids must be taken into consideration by solver algorithms, which need the simultaneous solution of fluid equations in the water and air components. Surface capturing methods, such as Volume of Fluid (VOF) and level set methods, predict the free surface treating it as a sharp boundary and updating it over time, governed by a

pure advection equation without diffusion. The VOF, the most widely implemented in CFD solvers, describes the volume fractions in each cell of the computational grid using a scalar function α. When a cell is full of the tracked phase, $\alpha = 1$, when the cell is completely empty then $\alpha = 0$, else the function takes a value in between, $0 < \alpha < 1$, and in such cells lies the interface. When it comes to water and air, $\alpha = 1$ denotes water, $\alpha = 0$ denotes air, and the $\alpha = 0.5$ isocontour defines the interface. The level set method computes signed distances from the interface, resulting in positive values in the water zone and negative values in the air region. For additional information, see [77]. The most popular commercial and open-source CFD software programs are CFX, Flow3D, Ansys Fluent, OpenFOAM, and StarCCM+, which is the one used in the following studies.
A Lagrangian approach, at the basis of the Smoothed-Particle Hydrodynamics (SPH) technique and integrated into the DualSPHysics software, discretizes the computational region with particles moving at local flow velocities and approximate solutions at the position of each particle. This meshless model is suitable for problems dominated by complex boundary dynamics, such as a free surface, although it usually requires more computing power than grid-based techniques.

The main disadvantage of high-fidelity solvers is undoubtedly their computational expense. Even while Chimera techniques can be used to minimize mesh density, especially near body boundaries and the free surface, some phenomena may require short time steps, leading to excessively long run times. However, these solvers attain very high precision, which allows the addition of turbulence models, compressibility, nonlinear dynamics, and viscous effects. As such, they have a greater affinity for modeling near-field interactions than they do for modeling wave propagation in the far-field. In addition to being unaffordable for large domains, this constraint results from intrinsic mistakes in numerical approximations of the derivatives, which lead to numerical dissipation and diffusion.

As a result, high-fidelity models find extensive use in single WEC simulations but are seldom applied at the scale of a WEC farm. For instance, only two point absorbers are simulated using CFD in [78] for regular waves, and simulations of free decay tests for two and five WECs are conducted in [79]. Another study, [16], performs RANS (Reynolds-Averaged Navier-Stokes) simulations of WEC arrays ranging from two to nine units subjected to regular waves, achieving excellent agreement with experimental data. However, these simulations primarily involve point absorbers with a single DoF, and the use of symmetries, justified by regular waves, helps

reducing computational costs. When dealing with more intricate WEC systems and irregular, multidirectional waves, the simulation may become impractical. Such computational expenses are unaffordable, particularly during design or optimization phases. Therefore, to streamline simulation costs, certain simplifying assumptions become necessary.

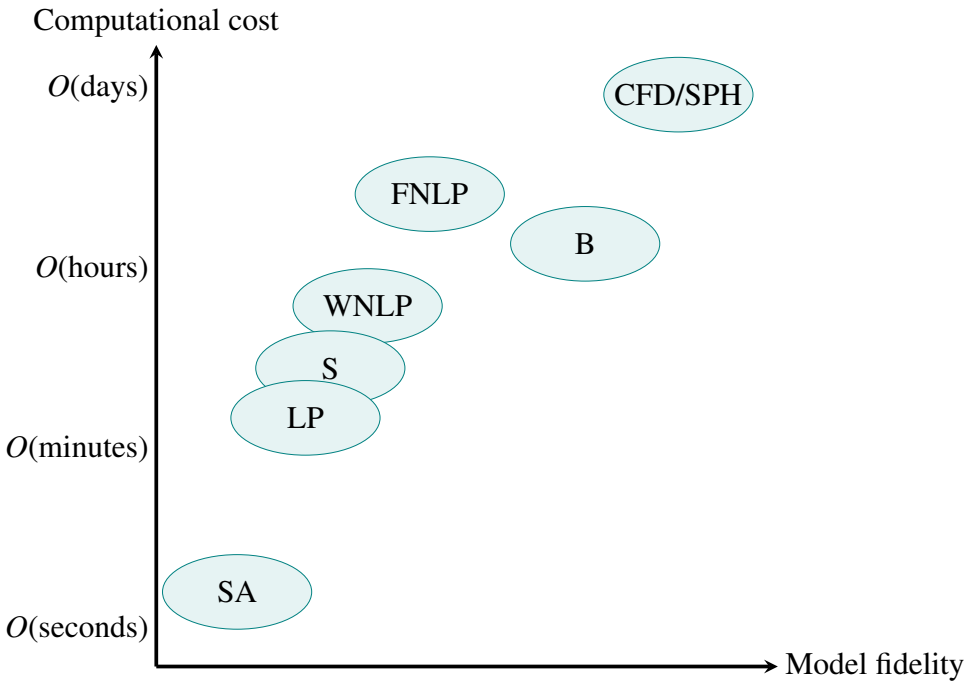

Fig. 2.6 Graphical representation of the various numerical approaches according to their computational cost and their level of fidelity. The plot is inspired from [80], and applied to WEC farms modeling. The following abbreviations for the models are used: SA for semi-analytical, LP for linear potential (with WNLP for weakly nonlinear potential and FNLP for fully nonlinear potential), S for spectral, B for Boussinesq. CFD/SPH are the high-fidelity models.

Assuming incompressibility, which is valid in all situations except for an OWC and the dynamics of the air chamber, is a useful simplification. In other cases, there is very little accuracy loss and while density remains constant, the number of equations reduces. Assuming an inviscid fluid is a more significant simplification, but the Navier-Stokes equations reduce to the Euler equations, once the stress tensor vanishes. By assuming irrotational flow, the Laplace equation is satisfied and velocity can be expressed as the gradient of a potential. Potential flow theory, for

which multiple models are available, is based on those hypotheses. Large-amplitude displacements are allowed in fully nonlinear potential flow models (abbreviated FNLP in Figures 2.6, 2.7), which impose fully nonlinear free-surface and body boundary conditions. A fully nonlinear time-domain method for wave analysis is introduced by Longuet-Higgins and Cokelet [81], using a Mixed Eulerian-Lagrangian method for surface wave modeling, and provide greater precision than RANS models because of smaller numerical dissipation.
Eliminating the vertical dimension is another approach to simplify an equation. This is implemented in shallow water equations, where the vertical velocity component is left out, although the vertical flow structure is, nonetheless, taken into account. Boussinesq-type modeling (B), based on depth-averaged shallow water equations, is used in coastal wave propagation simulation, offering good accuracy in nonlinearity and frequency dispersion [20]. While less suitable for wave-structure interaction problems due to the inability to model the hydrodynamics of a moving device, like for the software MIKE21BW, ongoing efforts aim to extend Boussinesq equations for floating bodies [82–85]. Despite a smaller computational cost compared to CFD models, it remains substantial, requiring additional simplifications, especially in the case of nonlinearity. By treating the incident wave as a driving term and solely accounting for the diffracted and radiated waves, the weakly nonlinear approach (WNLP) simplifies the problem and allows the description of steep nonlinear waves and large amplitude motions of the WEC.

So far in this section, the models have been solvable in the time domain, enabling them to incorporate complex PTO and mooring systems and handle nonlinearities and transient settings. Models based on Cummins equation assume linear hydrodynamics but can account for the nonlinear Froude-Krylov force. However, the Cummins approach has limitations, requiring the introduction of forces as functions of system states or wave properties, necessitating the prior development of empirical formulas for extreme situations. Thus, empirically derived coefficients and/or formulations must inevitably be incorporated at some point (calibration of numerical model against experiments).

In the frequency domain, potential theory assumptions persist, with additional considerations for waves of small amplitude relative to wavelength and small body motions, allowing linearization of the problem and boundary conditions. The superposition principle holds, and the resultant wave field around a WEC is the sum of incident, radiated, and diffracted wave fields. The body is described with an equation

of motion based on Newton's second law, balancing inertial force with external pressure force, wave excitation force, and radiation force. The PTO and mooring systems are linearized in order to preserve the superposition principle's validity. However, these models are limited to linear problems, with reduced accuracy around resonance, lack of consideration for viscous effects, flow separation, vortex shedding, and wave breaking, and an inability to draw conclusions regarding the controllability of WECs due to nonlinear control techniques.

Nonetheless, because of their simplicity, ease of use, and low computational cost, models based on linear potential flow theory (LP) are frequently employed for WEC farm modeling [86–91]. Softwares that implement the Boundary Element Method (BEM) in the frequency domain, including WAMIT, ANSYS Aqwa, Aquaplus, WADAM, NEMOH, and its Python version Capytaine, and Achil3D in the time domain, allow affordable simulations of farms with tens of WECs at a reasonable cost, while taking near-field interactions into consideration. For far-field effects, the linear form of the Boussinesq equations can ensure stability in linear wave propagation over gradually varying bathymetries. Softwares such as MILDwave, which employs mild-slope equations, depict the WEC hydrodynamics as a series of cells with a certain degree of absorption, albeit lacking the modeling of WEC responses and necessitating the fine-tuning of the absorption function using data from other models [92], in addition to being confined to classical linear assumptions. In [93], WECs are implemented in MILDwave using the sponge layer technique and tuning their absorption coefficient separately for each wave period for a given capture ratio.

An alternative approach that simplifies the representation of a WEC is the phase-averaging, spectral wave model (S). Functioning as a probabilistic model, it employs a statistical representation of waves through the energy spectrum. It produces a probabilistic estimate of the WEC response in terms of average power capture by using a transformation function. The evolving variable is the wave action density, governed by a continuity equation, and defined as the wave energy density divided by the wave frequency. A WEC array can be represented by the spectral model at a sub-grid scale, where each WEC is represented at a single computational grid point (as in the software TOMAWAC), or at a supra-grid scale, covering many computational grid points (as in the software SWAN). The input spectrum only gives a partial picture of the near field because it only contains the magnitude of each spectral wave component and lacks phase information [94]. Thus, another model

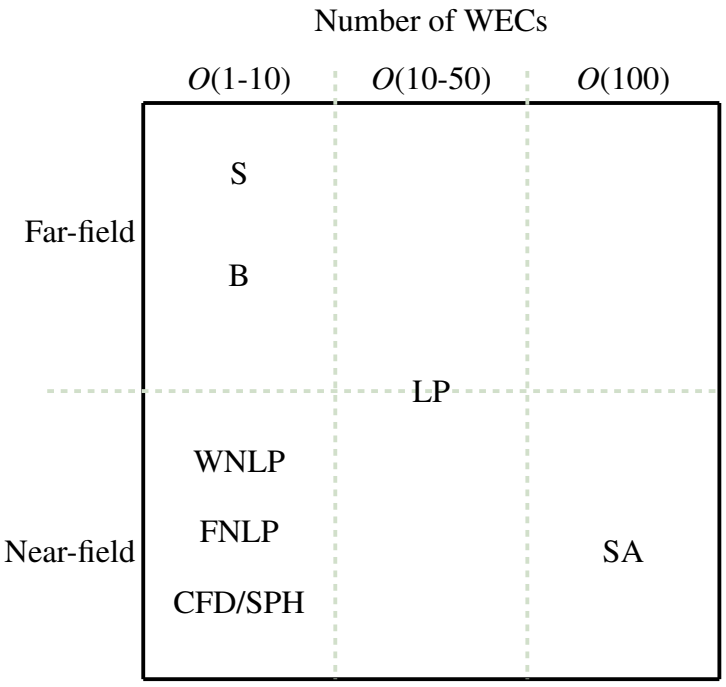

Fig. 2.7 Graphical representation of the various numerical approaches according to their main application, to the near field or far field, and the number of WECs usually modeled. The following abbreviations for the models are used: SA for semi-analytical, LP for linear potential (with WNLP for weakly nonlinear potential and FNLP for fully nonlinear potential), S for spectral, B for Boussinesq. CFD/SPH are the high-fidelity models.

is needed to determine how the WEC modifies the wave action. For instance, the impact of several farm configurations on the nearshore wave climate is examined in [95] using SWAN and each WEC is modeled as an obstacle with a transmission coefficient calculated with a CFD model. In [96], the experimental measurements are used to obtain the absorption coefficients of five point absorbers simulated with SWAN. Nevertheless, spectral models can calculate the effect of large-scale WEC farms, and they are commonly used for far-field effect assessment [97].

Another simplified model, grounded in linear potential flow theory, is the semi-analytical model (SA). Four distinct techniques exist, all sharing common simplifying assumptions, such as identical devices consisting of single, vertically axisymmetric bodies oscillating and absorbing energy in a single heave mode. In the first approach,

the point absorber approximation, the device diameter is small compared to the wavelength and device separation, allowing the radiated wave field of each device to be calculated independently. Another strategy, the plane wave method, considers large spacing between devices relative to the wavelength, treating the diverging wave from one device as a plane wave at another device [98]. The multiple scattering technique, on the other hand, views the diffraction and radiation as a series of separate scattering events [99, 100]. Since each device's escribed cylinder, centered at its origin, must not enclose the origin of any other device, the location of the WECs is crucial [101]. For the fourth strategy, the direct matrix method, the same assumption applies, meaning that the devices' vertical projections cannot cross over. This method finds the solution for the amplitudes of all scattered waves simultaneously using direct matrix inversion, combining the scattering equations and equations of motion into a single matrix. The various techniques use analytical expressions that, in the limit of an infinite series, either approximate or converge to a "exact" answer. They are mainly applied to point absorber types of WEC, from small [102, 103] to large [104] farms. Recent techniques [105] combine multiple scattering and direct matrix theories to describe large farms at a substantially lower computing cost, without imposing geometric constraints on WEC clusters. Since the focus of these methods is on hydrodynamic interaction solutions, body dynamics and power estimations need to be solved independently using a frequency, temporal, or spectral domain model together with derived hydrodynamic parameters. Despite the simplifications, and because of the matrix inversion, as the number of devices increases, the solution's computational demands still rise rapidly. To drastically speed up the simulation time, a modification to the matrix method is described in [56]. An upfront cost is required to compute the hydrodynamic coefficients for each individual WEC, a process conducted only once for identical geometries. Additionally, the total radiation coefficients, force transfer matrix, and diffraction transfer matrix for the entire farm must be established, also a one-time task. Subsequently, the solution to the Boundary Value Problem can be efficiently derived using these hydrodynamic parameters, enabling the calculation of interactions in WEC farms ranging from small to large, encompassing up to a hundred units. The methodology is based on the typical assumptions of linear potential theory, but can be applied to arbitrary geometries and modes of motions [106], and is suitable for optimization tools. The DTOcean tool employs such methodology for calculating and optimizing power absorbed and WEC-WEC interactions in WEC farms of arbitrary size [107]. An

in-depth analysis of a WEC or tidal farm project and its LCOE (Levelized Cost of Energy) variability is provided by the opensource DTOcean software, and takes into account various factors such as farm layout, power calculation, electrical network and station keeping design, installation and infrastructure, lifetime maintenance, and downtime prediction [108].

Irrespective of the chosen technique for modeling a WEC farm, there is a trade-off to consider. The choice of a very cost-effective model frequently entails a strong approximation of reality, which increases the possibility of overestimating or underestimating dynamics, and may provide misleading results, with consequences for decision-makers. Accuracy rises with increasing computational demand. For example, the cost of the BEM increases in proportion to the square of the number of WECs, and the cost of CFD is significantly greater. Traditionally, the main approach has been to simplify the problem being modeled. However, alternative strategies exist, such as employing data-driven models or reduced-order models, focusing on reducing the problem's size.

In the wave energy domain, artificial intelligence methods and data-driven techniques have been predominantly utilized for accurate wave resource characterization, predicting wave parameters, computing missing wave data, estimating wave spectra, and forecasting wave energy flux [109–111]. These methods are also employed for optimizing the shape of WECs or controlling them to enhance performance for single devices [112, 113], hybrid platforms [114], and WEC farms. For additional details, see [115]. In the research by [116], an optimization technique based on the semi-analytical method is integrated with machine learning for the prediction and optimization of a farm with 40 OWSCs arranged in a staggered layout, according to specified bathymetric and spatial limitations. In [117], the authors use and compare different machine learning techniques to predict the net produced power of an optimized farm including 10 offshore wind turbines and 10 WECs. Four adaptive neuro-surrogate optimization methods are investigated for a farm of 16 totally submerged three-tether buoys, in four actual wave Australian climates in [118].
When it comes to Reduced Order Models (ROMs), they may be applied to wave equations, as the parametrized ROM for a wave equation-based FEM (Finite Element Method) system by [119], or the nonlinear ROM suggested in [120], but they are particularly applied to WEC control. For example, a reduced-order wave-to-wire (WTW) model accounting for all elements of wave production for an OWC

(hydrodynamics, aerodynamics, thermodynamics, rotor dynamics, and generator dynamics), is proposed in [121]. By lowering the amount of unknowns in the state space, this model can be used as a time-domain tool to effectively build control systems for single OWCs in various sea states. A reduced electro-visco-elastic PTO for OWC is a further instance, suggested in [122]. Furthermore, a nonlinear model reduction by moment-matching is described in [123, 124] for WEC systems with one DoF, and may be expanded to many degrees of freedom. While reduced-order modeling in the context of wave energy remains relatively limited and focused on specific domains, such as WEC control, its potential application to the numerical simulation of WEC farms, characterized by parametric systems and optimization problems, is evident. This approach addresses the challenges of computational load and complexity associated with the hydrodynamics of WECs and farms, considering near and far field effects and the numerous degrees of freedom involved.

2.4 Conclusion

Ocean energy holds a significant potential to contribute to the low-carbon energy mix in Europe and around the world. However, the early-stage technologies and various financial, environmental, and technical obstacles hinder the advancement and market acceptance of wave energy. Numerical simulations play a crucial role in accelerating the progress of wave energy technologies at all development stages. Yet, the diversity of WEC categories, each with distinct characteristics, and the multitude of prototypes pose significant challenges to the numerical simulations. Simulation fidelity often depends on the complexity of the WEC being modeled, leading to either oversimplified representations or highly approximate numerical methods, particularly for intricate WEC designs. In addition, the multifaceted nature of WEC development introduces further complexities, making it impractical to encompass all aspects into a single simulation. As a result, studies typically focus on a few aspects at a time, limiting the comprehensiveness of multi-query analyses. These challenges extend to WEC farms, which face additional difficulties, such as multi-scale phenomena and complex fluid dynamics. Conventional approaches to WEC farm simulation often trade-off between efficiency and accuracy, with highly efficient but approximate simulations, or prohibitively costly ones. However, achieving minimal accuracy, especially in WEC farm modeling, necessitates a certain level of

computational expense, regardless of the chosen technique. This motivates a change in the strategy and the employment of model order reduction techniques, to reduce problem complexity without resorting to any simplifying assumptions.

Chapter 3

Model Order Reduction for Multiphase Flows

As an alternative to the conventional trade-off between accuracy and efficiency in numerical simulation of WEC farms, data-driven model reduction offers a strategy to extract essential features and reduce computational complexity while preserving accuracy. In this chapter, a Reduced-Order Model (ROM) based on Proper Orthogonal Decomposition (POD) is introduced as a surrogate model for biphase flows involving water and air. Given the significant difference between these fluids and the potentially highly nonlinear phenomenon, a gradual approach is adopted. Starting with a well-established case study, the flow past a cylinder, for which the POD ROM model is known to behave very efficiently in monophase flows at low Reynolds numbers, the setup is progressively modified to transition to biphase flows at high Reynolds numbers. The passage involves analyzing different terms of the Navier-Stokes equations and their effect on the POD ROM model. The model becomes progressively unstable when dealing with two completely distinct fluids, and an interface between them. To address this, a correction term is proposed, and a comparison to a fully data-driven, equation-free, ROM model is presented.
Notably, the non-intrusive nature of the current approach stands out, enabling the construction of a surrogate model without direct reliance on the high-fidelity solver used for generating the snapshots. This strategy avoids the challenges associated with the implementation of ROMs in codes, especially when covered by commercial licenses that prevent access to the source code. Instead, the only requirement is to

provide snapshots on a uniform Cartesian mesh, which can be accomplished with any high-fidelity solver.

The chapter is organized as follows. Section 3.1 introduces the primary motivations behind Model Order Reduction, and Section 3.2 the theoretical aspects of the Proper Orthogonal Decomposition and projection-based Reduced-Order Models. The typical procedure for deriving a POD-ROM model is detailed in Section 3.3 for the case of the monophase flow past a cylinder at low Reynolds numbers. The analyses conducted to develop the multiphase POD ROM are presented in Section 3.4, featuring the biphase flow past a cylinder test case, and a free wave test case.

3.1 Model Order Reduction

Advances in technology have made it possible to perform extremely accurate numerical simulations of multiphysics, complex, and multi-scale phenomena, albeit a high memory and CPU resource cost remains. Nevertheless, it is imperative to lessen the computing load of these simulations in order to make them practically usable. Model reduction appears as a strategy for extracting essential characteristics and reducing computing complexity. Reduced-Order Models (ROMs) find applications across diverse fields, including thermo-acoustics [125], aeroelasticity [126], image processing [127], graphics [128, 129], and fluid flows [130, 131]. In fluid dynamics alone, ROMs are utilized for reactive flows [132, 133], hypersonic flows [134], fluid control [135–138], flow-body interaction [139–141], and turbulence description [142–145], among other areas. Applications for these models can be found in many other fields, ranging from fluid-structure interaction in cardiovascular problems [146] to the numerical simulation of the wake behind a wind turbine [147], and the representation of the dynamics of multiphase flows [148, 149], as also in the case of this study.

Developing ROMs usually comprises two phases, which are referred to as *offline* and *online*. The offline stage consists of a training phase in which high-fidelity simulations of the target systems are run for different parameters, and reduced basis and projections are built on low-dimensional manifolds. During the online stage, the ROM is implemented by projecting the governing equations onto the low-dimensional manifold. This is the case of *intrusive* ROM methods, for which the reduced solutions are determined by solving the reduced order model. Traditionally,

projection-based model reduction is intrusive because it necessitates access to the discretized PDE operators, typically unavailable when working with proprietary software. Conversely, another class of ROMs, known as data-driven or *non-intrusive*, are learned solely from snapshots - numerical approximations or measurements of the dynamical system states - when discretized system operators are not accessible.

Model order reduction methods can be categorized according to the definition and construction of the reduced order basis. Under the *a posteriori* approach, the reduced basis is created during the training phase by either solving the original issue at particular points in time or by solving a modified version of the original problem with new parameters, or a combination of the two. There can be ROMs based on Volterra kernels [150, 151], Harmonic Balance [152, 153], Krylov subspaces [154], Balanced Truncation [155, 156], Proper Orthogonal Decomposition. On the other hand, the *a priori* method enables the approximate calculation of the entire space-time solution without the need for a training phase, meaning that the lower order basis is determined gradually online as the problem is solved. One popular technique is the Proper Generalized Decomposition (PGD) [157].

Snapshots, defined as the spatial distribution of a numerical simulation at particular time occurrences, indicating system dynamics, usually constitute the data set for the ROMs. For both linear and nonlinear problems, a commonly used method for obtaining a reduced basis from these snapshots is the Proper Orthogonal Decomposition (POD). POD is a strong tool for obtaining surrogate models for high-dimensional problems and maintains overall nonlinear dynamics, even when projecting onto linear or affine subspaces. But issues with instability, non-linearity, and intrusiveness persist, frequently necessitating intricate coding changes [158].

Further alleviation of the computational burden is achievable through parametric model order reduction (pMOR) [159].
Many dynamical systems are influenced by parameters, such as material properties, system geometry and configuration, initial and boundary conditions. The usual approach is the computation of the solution for the different parameter values with repeated runs of the Full Order Model (FOM), following the red path in Figure 3.1. As already mentioned, a ROM reduces the computational cost of the FOM, but for parametric studies, the parametric dependence should also be retained in the reduced model, since one cannot afford to create a new reduced model for every change in the parameter values. pMOR enables training the ROM across a narrow parameter

space and computing solutions for several parameter values (the blue path added to the red one in Figure 3.1).

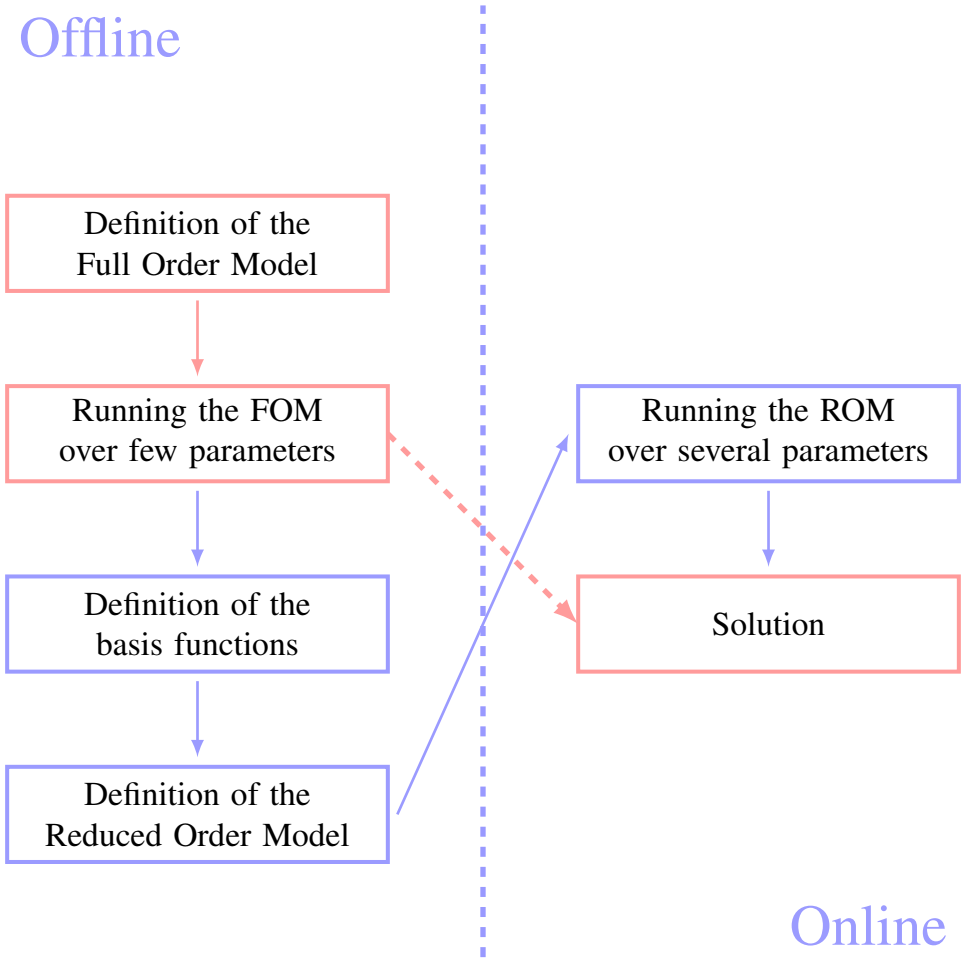

Fig. 3.1 Outline of the steps of a parametric study using the FOM (red path), and using the ROM (red and blue path). The offline stage relates to the training of the pROM, while the online stage concerns the execution of the reduced model.

As in various domains, also in the wave energy sector, applications like design, control, optimization, and uncertainty quantification often entail repeated model evaluations across a wide parameter space. In the context of WEC farms, simulating various wave characteristics, farm layouts, WEC designs, mooring systems, and control strategies is crucial. The computational demand for such comprehensive simulations and extensive parameter spaces is prohibitive. Nonetheless, a well-trained pROM could significantly reduce overall computational costs. To be beneficial, rapid online evaluations should outweigh the upfront offline cost, which can also be

mitigated through various techniques, including hyper-reduction [160] and Empirical Interpolation Method [161], or a combination of the pMOR with ANN (Artificial Neural Network) [162]. However these are intrusive approaches, which are impossible to implement in the context of a commercial software where the sources, and thus the numerical residuals, are not available.

The model order reduction technique proposed in this chapter is non-intrusive, as it can be applied irrespective of the CFD code used, or the numerical scheme chosen, provided that the simulation is well-posed. The basic request is a dataset of snapshots, with information on a consistent Cartesian mesh, at regular time instants. Although not the primary focus of this study, the technique is also suitable for parametric extension.

3.2 MOR Framework

In practical applications, numerical simulations of fluid flows can be highly resource-intensive, often involving thousands or even millions of degrees of freedom. Consequently, there is an increasing demand for reduced order models to provide low-dimensional approximations. Reduction techniques typically involve the definition of reduced basis functions, offering various options, such as Lagrange bases, Hermite bases, Taylor bases, and POD bases. POD basis functions own several characteristics that render them suitable for this specific problem: the reduction of high-fidelity numerical simulations of multiphase flows based on the Navier-Stokes equations. In this scenario, the laminar form of the equations is considered over a computational domain Ω, expressed as:

$$\nabla \cdot \mathbf{u} = 0 \qquad \text{in } \Omega, \tag{3.1a}$$

$$\frac{\partial \mathbf{u}}{\partial t} + (\mathbf{u} \cdot \nabla)\mathbf{u} = -\frac{1}{\rho}\nabla p + \frac{1}{\rho}\nabla \cdot (\mu(\nabla \mathbf{u} + (\nabla \mathbf{u})^T)) + \mathbf{g} \qquad \text{in } \Omega. \tag{3.1b}$$

To the best of the author's knowledge, there is a lack of literature on reduced-order models utilizing POD for multiphase flows. As a result, the study begins with the monophase case, which has been extensively studied in existing literature, and progressively advances to incorporate elements with the intention of developing a

model for water and air, two distinctly different fluids, with a complex and nonlinear interface between them.

3.2.1 Proper Orthogonal Decomposition

Originally introduced for a variety of purposes independently, Proper Orthogonal Decomposition is recognized under different names, such as Karhunen-Loève decomposition or expansion, Principal Component Analysis (PCA), and Singular Value Decomposition (SVD). Historically, the POD was first introduced by Lumley in the context of turbulence [163], one of the main domains of application. Particularly, Lumley defined the so-called *Classical POD*, which is best suited for problems well-defined in time but with limited spatial resolution. However, the problems of interest here exhibit high spatial resolution, due to the large domain and mesh size, along with a moderate time history. In such cases, the *Snapshot POD*, proposed by Sirovich [164], is more appropriate. The study shall hence concentrate on this methodology. For further details on both Classical POD and Snapshot POD, including their distinctions, readers are encouraged to consult [165].

At the basis of a reduced-order model, there is the definition of a space-time realization $\mathbf{U}(\mathbf{x},t)$, defined on a domain $\mathscr{D} : \Omega \times [0,T]$, as a linear superposition of N_r spatial basis functions - or modes - $\Phi(\mathbf{x})$, and N_r temporal coefficients $\mathbf{a}(t)$, at the difference of a reference field $\overline{\mathbf{U}}(\mathbf{x})$:

$$\mathbf{U}(\mathbf{x},t) \approx \widetilde{\mathbf{U}}(\mathbf{x},t) = \overline{\mathbf{U}}(\mathbf{x}) + \sum_{i=1}^{N_r} a_i(t)\ \Phi_i(\mathbf{x}). \tag{3.2}$$

Defining the inner product $(\cdot,\cdot)_\Omega$ between two fields $\boldsymbol{V}$ and $\boldsymbol{W}$ as: $(\boldsymbol{V},\boldsymbol{W})_\Omega = \int_\Omega \boldsymbol{V}\cdot\boldsymbol{W}\,\mathrm{d}\mathbf{x}$, the temporal coefficients in Eq. (3.2) are defined as:

$$a_i(t) = \int_\Omega \left[\mathbf{U}(\mathbf{x},t) - \overline{\mathbf{U}}(\mathbf{x})\right]\ \Phi_i(\mathbf{x})\ \mathrm{d}\mathbf{x} = \left(\left[\mathbf{U}(\mathbf{x},t) - \overline{\mathbf{U}}(\mathbf{x})\right], \Phi_i(\mathbf{x})\right). \tag{3.3}$$

The definition of the basis functions is what distinguishes the POD technique from others. Typically, predetermined functions, such as Chebychev polynomials, Legendre polynomials, or trigonometric functions, are used as $\Phi(\mathbf{x})$. However,

the POD defines modes as the deterministic functions that are best correlated, on average, with the realizations. This involves identifying a set of functions that, on average, minimizes the mean square error between the realizations and the linear superposition:

$$\min_{\{\Phi_j\}_{j=1}^{N_r}} \frac{1}{T}\sum_{i=1}^{T}\left\| \left[\mathbf{U}_i - \overline{\mathbf{U}}\right] - \sum_{j=1}^{N_r}\left(\left[\mathbf{U}_i - \overline{\mathbf{U}}\right], \Phi_j\right)\Phi_j \right\|_2^2, \tag{3.4}$$

or, equivalently, maximizes the projection on the observations:

$$\max_{\{\Phi_j\}_{j=1}^{N_r}} \sum_{j=1}^{N_r}\left[\frac{1}{T}\sum_{i=1}^{T}\left|\left(\left[\mathbf{U}_i - \overline{\mathbf{U}}\right], \Phi_j\right)\right|^2\right]. \tag{3.5}$$

After some passages, the maximization problem can be cast in an equivalent eigenvalue problem, which can be written as a Fredholm equation:

$$\int_0^T C(t,t')\,a_i(t')\mathrm{d}t' = \lambda_i\, a_i(t), \tag{3.6}$$

where an operator, $C(t,t')$, appears, and is defined as:

$$C(t,t') = \frac{1}{T}\left(\left[\mathbf{U}(\mathbf{x},t) - \overline{\mathbf{U}}(\mathbf{x})\right], \left[\mathbf{U}(\mathbf{x},t') - \overline{\mathbf{U}}(\mathbf{x})\right]\right)_\Omega. \tag{3.7}$$

The correlation matrix $C(t,t')$ is symmetric and positive definite, *i.e.* the eigenvalues in Eq. (3.6) are all real and positive, $\lambda_1 \geq \lambda_2 \geq \cdots \geq \lambda_i \geq 0$. According to the definition in Eq. (3.7), if $\mathbf{U}$ contained solely the velocity field, the eigenvalues would be associated to the kinetic energy of the system, which is proportional to the square of the velocity. Although this correspondence may not always hold true, and the λ_i are not strictly speaking energy, they nevertheless indicate the relative significance and contribution of the corresponding modes Φ_i to the information content of the original data.

The POD modes form a complete orthogonal set, and can be chosen mutually orthonormal, so that

$$\int_\Omega \Phi_i(\mathbf{x})\ \Phi_j(\mathbf{x})\ d\mathbf{x} = \delta_{ij}, \tag{3.8}$$

where the Kronecker delta symbol is

$$\delta_{ij} = \begin{cases} 0 & \text{for } i \neq j, \\ 1 & \text{for } i = j. \end{cases}$$

Consequently, and because of their definition (Eq. (3.3)), the coefficients are orthogonal, so the expression

$$\frac{1}{T}\int_0^T a_i(t)a_j(t)\,\mathrm{d}t = \lambda_i \delta_{ij} \tag{3.9}$$

implies that the i-th coefficient only depends on the i-th mode, and not on the others.

Link to the SVD The Singular Value Decomposition of a real matrix $\mathbb{A}$ of dimensions $M \times N_t$ is the factorization

$$\mathbb{A} = \boldsymbol{Q}\Sigma\boldsymbol{Z}^T, \tag{3.10}$$

where $\boldsymbol{Q}$ and $\boldsymbol{Z}$ are non unique unitary matrices of dimensions $M \times M$ and $N_t \times N_t$, respectively, and $\Sigma = diag(\sigma_1, \ldots, \sigma_p)$, with $\sigma_1 \geq \sigma_2 \geq \cdots \geq \sigma_p \geq 0$, $p = \min(M, N_t)$. The eigenvalue problem in Eq. (3.6) can be reformulated in a matrix form as the factorization of Eq. (3.10). In this sense, a link can be found between the POD basis functions Φ and the left eigenfunction matrix $\boldsymbol{Q}$, between the temporal coefficients $\mathbf{a}$ and the right eigenfunction matrix $\boldsymbol{Z}$, and between the eigenvalues set $\Lambda = diag(\lambda_1, \ldots, \lambda_{N_r})$ and Σ.

Reduction POD bases are particularly attractive because of their proven efficiency, being the most energetically optimal bases, among all linear decompositions [165]. This energetic optimality implies that only a small number of modes, N_r, may be required to effectively represent the realizations. When $N_r = \infty$, or in finite dimensions as considered here, when $N_r \equiv N_s$, with N_s the number of original time realizations (the snapshots), the expression in Eq. (3.2) holds true as an equality. However, by choosing $N_r \ll N_s$, an approximation is obtained, while also achieving a consistent reduction in the problem size. To determine the appropriate value of N_r, the following ratio is defined:

$$\text{RIC} = \frac{\sum_{i=1}^{N_r} \lambda_i}{\sum_{i=1}^{N_s} \lambda_i}, \tag{3.11}$$

which indicates the percentage of energy retained in the first N_r modes compared to the total energy of the problem. Truncation occurs at the number of modes that yields a RIC (Relative Information Content) above a predefined percentage.

To significantly diminish the problem's dimensionality, meaning having a small N_r compared to the total N_s, it is essential that the eigenvalues decrease rapidly. In many applications, such as fluid dynamics or heat transfer, an exponential decrease in the eigenvalues is observed, increasing the likelihood of deriving low-order approximate models. However, while POD modes optimally approximate a given dataset in the least squares sense, they are not designed to approximate the dynamics generating the data. Consequently, features with relatively small energy compared to others may be neglected in a reduced model, despite being relevant aspects of the full dynamical system. Additionally, while an increase in the number of POD modes decreases the least squares error, there may be instances where incorporating more POD modes results in a poorer approximation of the full dynamics [166].

3.2.2 POD Reduced-Order Model

Given that the POD technique yields efficient basis functions for representing space-time realizations, there is an interest in utilizing them to build a low-dimensional dynamical system for the computation of the temporal coefficients. A common approach for reducing high-dimensional partial differential equations to a reduced system of ordinary differential equations is the Galerkin or the Petrov-Galerkin projection. The former is the most popular technique, in which the system of equations is projected onto a set of test functions, set to be equal to the trial functions, here the POD basis functions.

A classical system of PDEs, such as the Navier-Stokes equations, may be generally written as:

$$\frac{\mathrm{d}\mathbf{U}}{\mathrm{d}t} = \mathbf{F}(\mathbf{U}) \tag{3.12}$$

over the spatial domain Ω. Here, $\mathbf{F}$ is a differential operator containing only spatial derivatives. The system is completed by the initial conditions, $\mathbf{U}(\mathbf{x}, t=0) = \mathbf{U}_0(\mathbf{x})$, and the boundary conditions, and can be resolved over time. In real-world applications such as flow problems, dealing with numerous degrees of freedom is inevitable, potentially resulting in a system space of significant dimension. In practical computations, this can lead to dimensions on the order of $\mathscr{O}(10^6 - 10^{10})$, necessitating integration over time with likely small time steps.
Evaluating the Galerkin projection of Eq. (3.12) onto the POD subspace of dimension N_r, yields:

$$\left(\frac{\mathrm{d}\mathbf{U}}{\mathrm{d}t}, \boldsymbol{\Phi}_j\right) = \left(\mathbf{F}(\mathbf{U}), \boldsymbol{\Phi}_j\right) \quad \text{with } j = 1, ..., N_r. \tag{3.13}$$

Substituting the definition of Eq. (3.2), after few passages, the following dynamical system is obtained:

$$\frac{\mathrm{d}\mathbf{a}(t)}{\mathrm{d}t} = \boldsymbol{F}(\mathbf{a}(t)), \tag{3.14}$$

where $\boldsymbol{F}$ now may contain quadratic functions of $\mathbf{a}$, because of the convective terms present in the Navier-Stokes equations. The system is completed by initial conditions, that can be directly inferred as $a_i^0 = (\mathbf{U}_0(\mathbf{x}), \boldsymbol{\Phi}_i)$, and boundary conditions. Given that the POD basis functions inherently reflect the flow configurations from which they are derived, the boundary conditions are automatically fulfilled. The dimension of the resulting dynamical system is N_r, and is subsequently integrated over time. As N_r typically falls within the order of magnitude of $\mathscr{O}(10^2)$, the dimensional reduction is substantial.

3.2.3 Definition of the Errors

In this section, the definition of the errors as consistently computed throughout the entire document, is outlined. Let ξ be a variable of interest, namely the velocity $\mathbf{u}$, possibly defined by components, or the Volume of Fluid (VOF) α, the pressure p, the density ρ, the viscosity μ, or any combination of them. Let ξ_{ref} denote the reference value of the variable, usually the high-fidelity target solution, and ξ_{approx} its approximation, possibly obtained from projection, or as solution of the

reduced-order model or the coupling model (presented in the subsequent chapter). The errors are defined over domains or subdomains, each declared by the subscript k in Ω_k. To define the errors, the L2-norm is also introduced, as the distance $\|\xi\|_{\Omega_k} = \sqrt{\int_{\Omega_k}(\xi(\mathbf{x}))^2 \mathrm{d}\mathbf{x}}$.

The errors used in the document are absolute and relative. Absolute errors are defined over time as:

$$\varepsilon_k^{\xi}(t) = \|\xi_{ref}(t) - \xi_{approx}(t)\|_{\Omega_k}. \tag{3.15}$$

Relative errors are considered integrated over time, as:

$$\overline{\varepsilon}_k^{\xi} = \int_T \frac{\|\xi_{ref}(t) - \xi_{approx}(t)\|_{\Omega_k}}{\|\xi_{ref}(t)\|_{\Omega_k}} \mathrm{d}t. \tag{3.16}$$

In general, the variables may be computed on different domains, each with independent spatial discretization. However, it is assumed that they will be discretized at corresponding grid points prior to error calculation, and potentially interpolated, if required. Any adjustment or manipulation of the values will be explicitly stated when presenting the errors.

Throughout the document, various errors are compared, including projection and model errors. The main difference lies in the definition of the temporal coefficients. By defining a_j^{proj} as the POD eigenvectors, the projection error is computed by defining $\xi_{approx} = \overline{\xi} + \sum_{j=1}^{N_r} a_j^{proj} \Phi_j$ across the computational domain of interest. However, when temporal coefficients are computed by solving the dynamical system of Eq. (3.14), or during the coupling methodology implementation as detailed in the subsequent chapter, ξ_{approx} is computed accordingly, and consequently the model error. The projection error reflects the filtering effect of the POD truncation, and quantifies, thus, the error due to the truncated modes. It represents the best achievable approximation of the model with the defined POD basis functions, serving as a lower bound. On the other hand, the model error indicates the actual error, which typically exceeds the projection error, and may increase over time as discrepancies from the truncated information accumulate.

3.3 Monophase POD-ROM

Let a flow be described in a Cartesian coordinate system $\{x,y,z\}$, where the positive x-axis is aligned with the mean flow, the y-axis extends in the vertical direction and the z-axis spans in the transversal direction. Locations are defined by the vector $\mathbf{x} = \{x,y,z\}$, the velocity vector is defined as $\mathbf{u} = \{u,v,w\}$, and the pressure is represented by the scalar p.
In a generic monophase laminar flow, the evolution of the fluid variables is governed by the Navier-Stokes equation of the following form:

$$\nabla \cdot \mathbf{u} = 0 \qquad \text{in } \Omega, \tag{3.17a}$$

$$\frac{\partial \mathbf{u}}{\partial t} + (\mathbf{u}\cdot\nabla)\mathbf{u} = -\frac{1}{\rho}\nabla p + \nu\Delta\mathbf{u} + \mathbf{g} \qquad \text{in } \Omega. \tag{3.17b}$$

with $\mathbf{g}$, a vector of magnitude $|\mathbf{g}| = 9.81\,\mathrm{m/s^2}$ directed negatively along the vertical axis.

For the purpose of discussing the principles of model order reduction, and as an introductory example, the flow past a cylinder is described and simulated. Such a problem serves as a classical illustration in literature, combining a simple geometry with a rich flow dynamics. In three dimensions, an infinite cylinder of diameter d is positioned, at rest, normal to a flow of free stream speed $\mathbf{u}_0 = [u_0,0,0]$. As the fluid can have various characteristics (in terms of density ρ and dynamic viscosity μ), as well as the flow velocity and the cylinder size, the dimensionless Reynolds number is introduced: $Re = \frac{\rho \mathbf{u}_0 d}{\mu}$. Such a parameter represents the ratio between inertial and viscous forces. At very low Reynolds numbers, the flow remains completely laminar and symmetrical upstream and downstream of the cylinder. With increasing Re, a wake develops behind the cylinder, leading to the formation of a flow pattern known as the Karman vortex street. As Re continues to rise, the viscous effects diminish, resulting in instability of the vortex street, development of a boundary layer, and eventual transition to turbulent flow.
The primary focus is not on turbulence description, hence the chapter retains the laminar version of the Navier-Stokes equations throughout. The main interest is to begin with a well-established example, for which the definition of a reduced-order model is manageable, and progressively introduce complexities to ultimately develop

a ROM model for multiphase flows.
As mentioned, since the POD modes can be represented as linear combinations of the realizations, they inherently possess the properties of the snapshots. For instance, in the case of the incompressible Navier-Stokes equations, if the snapshots are divergence free, then the POD modes will also satisfy this condition. Consequently, the continuity equation, Eq. (3.17a), is always satisfied and not considered in the Galerkin projection. Therefore, only the momentum equations, Eq. (3.17b), are considered in the following.

3.3.1 Cylinder at $Re = 200$

At $Re = 200$, the laminar flow exhibits an unsteady, periodic shedding of Karman vortices. Physically, this involves a combination of a mean flow, and the vortex structures. In general, the focus is on the latter phenomenon, hence the mean flow is often computed and subtracted from the snapshots, to better capture the smaller structures.

The snapshots are produced using the commercial software StarCCM+, a Computational Fluid Dynamics (CFD) software based on the finite volume method. Given the incompressibility assumption, the segregated flow solver is employed, where the mass conservation constraint on the velocity field is fulfilled by solving a pressure-correction equation. The SIMPLE algorithm is used to solve the Navier-Stokes equations due to its robust stability independent of the chosen time step. For convection, a second-order upwind discretization scheme is employed in space, with 10 inner iterations for convergence. Additionally, a hybrid Gauss-Least Squares method, with a Venkatakrishnan limiter, is used for the gradients. Regarding the time discretization, a second-order implicit unsteady time scheme, with a constant time step, is chosen. Further details can be found in the StarCCM+ user guide [167].

In terms of numerical setup, the simulation domain spans $\Omega = [24 \times 16 \times 1]\text{m}$, discretized with an octree mesh and refined in the lee of the cylinder. The cylinder has unit diameter, $d = 1\,\text{m}$, its surface Γ_c is modeled as a wall, and is located in a flow with incoming unitary velocity in the longitudinal direction, so $\mathbf{u}_0 = [1,0,0]\text{m/s}$. The Reynolds number is thus easily determined, with the primary focus being on fluid characteristics. Dirichlet boundary conditions are imposed for velocity at the inlet (Γ_{inlet}), top (Γ_{top}) and bottom (Γ_{bottom}) boundaries, while for pressure at

the outlet boundary, Γ_{outlet}. Symmetry planes are employed at the front and back boundaries, Γ_{front} and Γ_{back} respectively, to reduce the computational cost and maintain a manageable domain size (Figure 3.2).

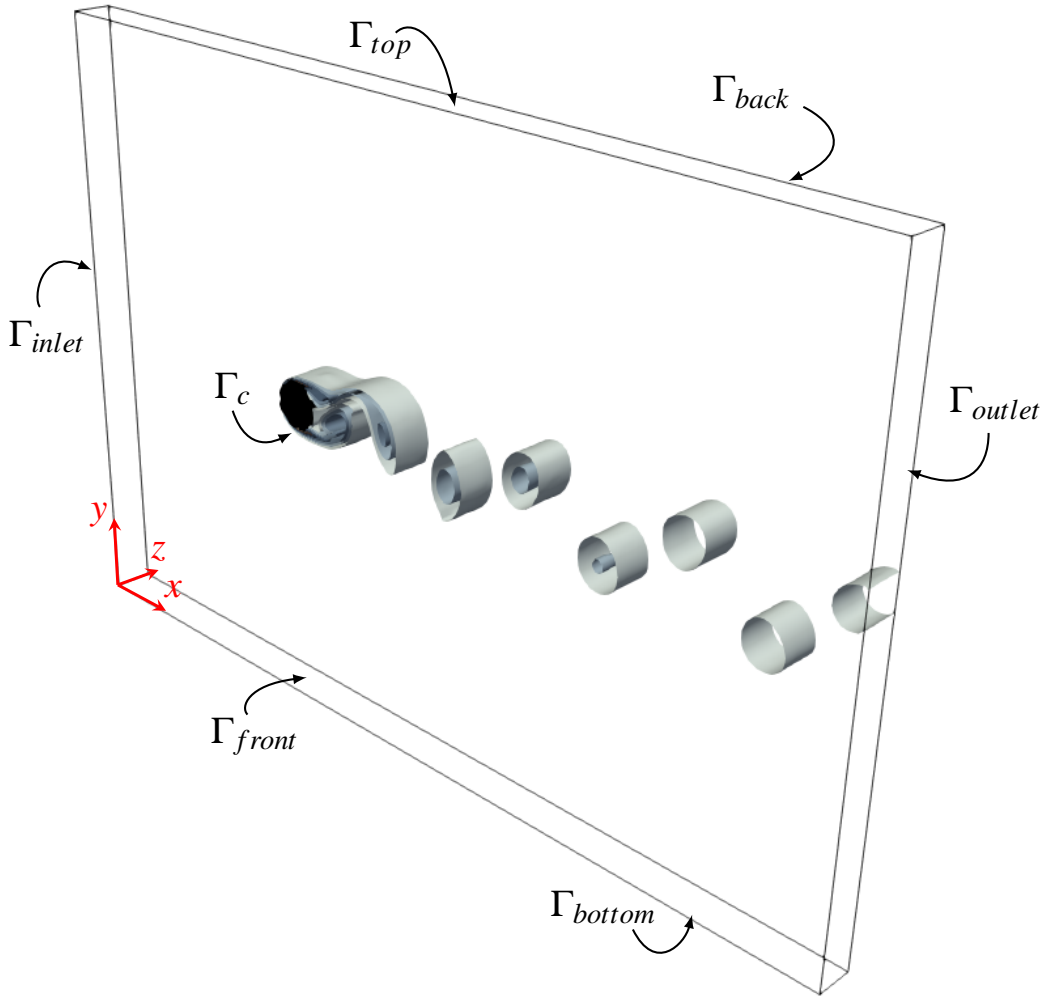

Fig. 3.2 Simulation domain for the monophase flow past a cylinder, with definition of the boundaries. The vorticity is represented to show the Karman vortex street.

Two distinct test cases are defined, each involving different fluids: one with density $\rho = 1\,\mathrm{kg/m^3}$ and another with $\rho = 1000\,\mathrm{kg/m^3}$. The dynamic viscosity is adjusted such that both cases yield $Re = 200$, resulting in $\mu = 0.005\,\mathrm{m^2/s}$ and $\mu = 5\,\mathrm{m^2/s}$, respectively. Although the same Re implies similar dynamics, the effect of gravity is more pronounced for higher density fluids, leading to an expected difference in the pressure field. This difference primarily relates to the static pres-

sure, whose magnitude increases with increasing distance from the reference, since $p_{static} = \rho|\mathbf{g}|y$.

For the numerical results, the simulation is conducted with a fixed time step of $\Delta t = 0.1\,\mathrm{s}$ over the time interval $t_{sim} = [0, 100]\mathrm{s}$, to allow for initial development and stabilization of the dynamics. After all the transients have died out, the solution converges rapidly to a periodic state, and the analysis is focused on the interval $t = [90, 100]\mathrm{s}$, corresponding to a multiple of the vortex shedding period, here of 5 s.

Definition of the snapshot matrix In matrix form, the variables of interest are

$$\mathbf{U} = \begin{pmatrix} \mathbf{u} = \begin{pmatrix} u \\ v \\ w \end{pmatrix} \\ p \end{pmatrix}, \tag{3.18}$$

and their values are collected at predefined time steps, generating the snapshots. The snapshots matrix, hence, is $\mathbf{S} = [\mathbf{U}(\mathbf{x}, t_1)^T \quad \mathbf{U}(\mathbf{x}, t_2)^T \quad \cdots \quad \mathbf{U}(\mathbf{x}, t_{N_s})^T] \in \mathbb{R}^{4n_c \times N_s}$, where n_c is the number of points of the mesh where the solution is collected. In the case of a parametric analysis, with varying parameters η, the snapshot matrix would become $\mathbf{S} = (\mathbf{S}_{\eta_1}, \mathbf{S}_{\eta_2}, \ldots, \mathbf{S}_{\eta_{N_m}})$, with N_m the number of sampling points for parameters η, and each $\mathbf{S}_{\eta_i}$ as the snapshot matrix built with $\eta = \eta_i$, yielding to a total of $N_s := N_s \times N_m$ snapshots. In this chapter, the parametric study is not treated, and the ROM model primary objective is the reproduction of the FOM solution.

Numerically, for the considered case, the snapshots are sampled equidistantly within the time interval, at every time step, which is $\Delta t = 0.1\,\mathrm{s}$, for a total of $N_s = 101$. The variable values are extracted on a Cartesian mesh, with homogeneous spacing in the three directions, $\Delta \mathbf{x} = 0.1\,\mathrm{m}$, so $n_c = 426811$. Therefore, expanding the snapshot matrix, one obtains:

$$\mathbf{S} = \begin{pmatrix} u(\mathbf{x}_1,t_1) & u(\mathbf{x}_1,t_2) & \cdots & u(\mathbf{x}_1,t_{N_s}) \\ \vdots & \vdots & \ddots & \vdots \\ u(\mathbf{x}_{n_c},t_1) & u(\mathbf{x}_{n_c},t_2) & \cdots & u(\mathbf{x}_{n_c},t_{N_s}) \\ v(\mathbf{x}_1,t_1) & v(\mathbf{x}_1,t_2) & \cdots & v(\mathbf{x}_1,t_{N_s}) \\ \vdots & \vdots & \ddots & \vdots \\ v(\mathbf{x}_{n_c},t_1) & v(\mathbf{x}_{n_c},t_2) & \cdots & v(\mathbf{x}_{n_c},t_{N_s}) \\ w(\mathbf{x}_1,t_1) & w(\mathbf{x}_1,t_2) & \cdots & w(\mathbf{x}_1,t_{N_s}) \\ \vdots & \vdots & \ddots & \vdots \\ w(\mathbf{x}_{n_c},t_1) & w(\mathbf{x}_{n_c},t_2) & \cdots & w(\mathbf{x}_{n_c},t_{N_s}) \\ p(\mathbf{x}_1,t_1) & p(\mathbf{x}_1,t_2) & \cdots & p(\mathbf{x}_1,t_{N_s}) \\ \vdots & \vdots & \ddots & \vdots \\ p(\mathbf{x}_{n_c},t_1) & p(\mathbf{x}_{n_c},t_2) & \cdots & p(\mathbf{x}_{n_c},t_{N_s}) \end{pmatrix} \in \mathbb{R}^{4n_c \times N_s}. \tag{3.19}$$

Following (3.2), such variables may be expressed as:

$$\mathbf{U}(\mathbf{x},t) = \overline{\mathbf{U}}(\mathbf{x}) + \sum_{j=1}^{N_r} a_j(t)\Phi_j(\mathbf{x}), \tag{3.20}$$

with the reference value, $\overline{\mathbf{U}}$, as non-null mean value. The mean value is normally computed as the average value of the provided data over time. In finite dimensions, this reduces to calculating the mean value across the total number of snapshots N_s:

$$\overline{\mathbf{U}}(\mathbf{x}) = \frac{1}{N_s}\sum_{i=1}^{N_s} \mathbf{U}(\mathbf{x},t_i). \tag{3.21}$$

Therefore, the mean value can be subtracted from the snapshot matrix, to give $\tilde{\mathbf{S}} = \mathbf{S} - \overline{\mathbf{U}}$.

Choice of the POD basis functions The temporal correlation matrix is computed as

$$\mathbf{R} = \tilde{\mathbf{S}}^T\,\tilde{\mathbf{S}} \in \mathbb{R}^{N_s \times N_s}, \tag{3.22}$$

and the following eigenvalue problem is solved:

$$\mathbf{R}\varphi_i = \lambda_i \varphi_i, \quad i = 1, \cdots, N_s, \tag{3.23}$$

where $\lambda_1 \geq \lambda_2 \geq \cdots \geq \lambda_{N_s} \geq 0$. In a dynamical system, large eigenvalues capture the essential characteristics, while smaller eigenvalues contribute minor perturbations to the overall dynamics. When the mean field is not subtracted, the first POD mode corresponds to it, resulting in a large eigenvalue compared to the others. Consequently, very few modes could account for a high RIC, as most of the energy is concentrated in the first mode. However, this approach would be trivial, since the mean is already known everywhere, and the objective is to reduce the oscillating part.

For the case of interest, the eigenvalue spectrum depicted in Figure 3.3 on a semi-log scale and normalized to the first eigenvalue, shows a rapid decline in information content with increasing mode number. This trend is also conveyed by the RIC, which increases very quickly. Remarkably, the first 10 modes contain over 99.99% of the total kinetic energy, leading to a truncation at $N_r = 10$, which represents the 10% of the total N_s, yielding a substantial reduction. The preference for an even number is due to the "pair by pair" pattern. Such a trend is related to the physics of the problem - a parallel flow with constant-shaped structures moving downstream at a constant speed. In such cases, the eigenvalue problem is degenerate and yields pairs of nearly identical eigenvalues, separated by significant gaps in magnitude from the other pairs. This pairing is less pronounced as N_r increases, corresponding to less energetic modes (see left-hand side of Figure 3.3).

The POD basis functions are defined as:

$$\Phi_i = \frac{1}{\sqrt{\lambda_i}} \tilde{\mathbf{S}} \varphi_i, \quad i = 1, \cdots, N_s, \tag{3.24}$$

with associated POD temporal coefficients $a_i = \frac{\varphi_i}{\sqrt{\lambda_i}}$.
In this case, a unique set of basis functions is defined for all the variables,

$$\Phi = \begin{pmatrix} \boldsymbol{\phi}^{\mathbf{u}} = \begin{pmatrix} \boldsymbol{\phi}^u \\ \boldsymbol{\phi}^v \\ \boldsymbol{\phi}^w \end{pmatrix} \\ \boldsymbol{\phi}^p \end{pmatrix}, \tag{3.25}$$

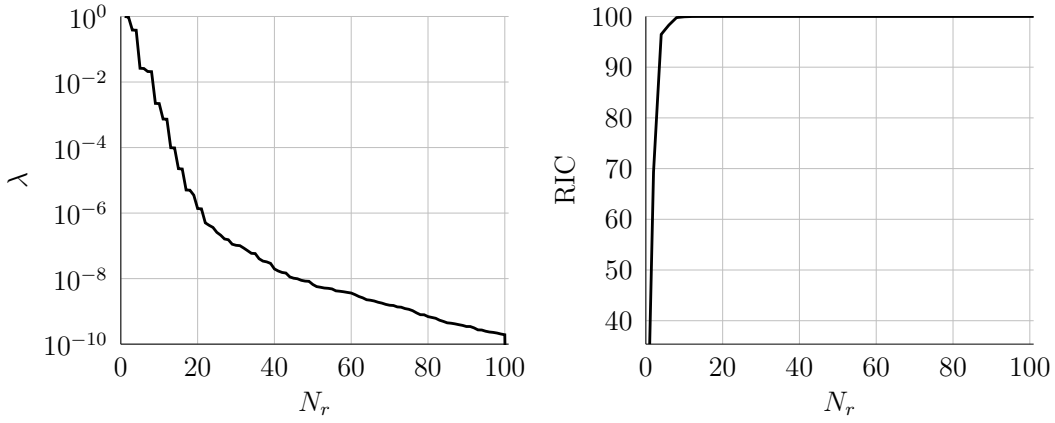

Fig. 3.3 Evolution of the eigenvalues in Eq. (3.23), normalized to the fist eigenvalue (left), and of the RIC (right) with respect to the number of POD modes N_r, for the case of the cylinder at $Re = 200$, with $\rho = 1000\,\mathrm{kg/m^3}$.

which are truncated to N_r, and lead to the following expanded matrix:

$$\Phi = \begin{pmatrix} \phi^u(\mathbf{x}_1,t_1) & \phi^u(\mathbf{x}_1,t_2) & \cdots & \phi^u(\mathbf{x}_1,t_{N_r}) \\ \vdots & \vdots & \ddots & \vdots \\ \phi^u(\mathbf{x}_{n_c},t_1) & \phi^u(\mathbf{x}_{n_c},t_2) & \cdots & \phi^u(\mathbf{x}_{n_c},t_{N_r}) \\ \phi^v(\mathbf{x}_1,t_1) & \phi^v(\mathbf{x}_1,t_2) & \cdots & \phi^v(\mathbf{x}_1,t_{N_r}) \\ \vdots & \vdots & \ddots & \vdots \\ \phi^v(\mathbf{x}_{n_c},t_1) & \phi^v(\mathbf{x}_{n_c},t_2) & \cdots & \phi^v(\mathbf{x}_{n_c},t_{N_r}) \\ \phi^w(\mathbf{x}_1,t_1) & \phi^w(\mathbf{x}_1,t_2) & \cdots & \phi^w(\mathbf{x}_1,t_{N_r}) \\ \vdots & \vdots & \ddots & \vdots \\ \phi^w(\mathbf{x}_{n_c},t_1) & \phi^w(\mathbf{x}_{n_c},t_2) & \cdots & \phi^w(\mathbf{x}_{n_c},t_{N_r}) \\ \phi^p(\mathbf{x}_1,t_1) & \phi^p(\mathbf{x}_1,t_2) & \cdots & \phi^p(\mathbf{x}_1,t_{N_r}) \\ \vdots & \vdots & \ddots & \vdots \\ \phi^p(\mathbf{x}_{n_c},t_1) & \phi^p(\mathbf{x}_{n_c},t_2) & \cdots & \phi^p(\mathbf{x}_{n_c},t_{N_r}) \end{pmatrix} \in \mathbb{R}^{4n_c \times N_r}. \tag{3.26}$$

Since, from Eq. (3.2),

$$\mathbf{U} \simeq \widetilde{\mathbf{U}} = \overline{\mathbf{U}} + \Phi\mathbf{a}, \tag{3.27}$$

with $\mathbf{a} \approx (a_1, a_2, \ldots, a_{N_r})^T$, and defining the sub-matrices

$$\boldsymbol{\phi}^u = \begin{pmatrix} \phi^u(\mathbf{x}_1,t_1) & \cdots & \phi^u(\mathbf{x}_1,t_{N_r}) \\ \vdots & \ddots & \vdots \\ \phi^u(\mathbf{x}_{n_c},t_1) & \cdots & \phi^u(\mathbf{x}_{n_c},t_{N_r}) \end{pmatrix} \in \mathbb{R}^{n_c \times N_r},$$

$$\boldsymbol{\phi}^v = \begin{pmatrix} \phi^v(\mathbf{x}_1,t_1) & \cdots & \phi^v(\mathbf{x}_1,t_{N_r}) \\ \vdots & \ddots & \vdots \\ \phi^v(\mathbf{x}_{n_c},t_1) & \cdots & \phi^v(\mathbf{x}_{n_c},t_{N_r}) \end{pmatrix} \in \mathbb{R}^{n_c \times N_r},$$

$$\boldsymbol{\phi}^w = \begin{pmatrix} \phi^w(\mathbf{x}_1,t_1) & \cdots & \phi^w(\mathbf{x}_1,t_{N_r}) \\ \vdots & \ddots & \vdots \\ \phi^w(\mathbf{x}_{n_c},t_1) & \cdots & \phi^w(\mathbf{x}_{n_c},t_{N_r}) \end{pmatrix} \in \mathbb{R}^{n_c \times N_r},$$

$$\boldsymbol{\phi}^p = \begin{pmatrix} \phi^p(\mathbf{x}_1,t_1) & \cdots & \phi^p(\mathbf{x}_1,t_{N_r}) \\ \vdots & \ddots & \vdots \\ \phi^p(\mathbf{x}_{n_c},t_1) & \cdots & \phi^p(\mathbf{x}_{n_c},t_{N_r}) \end{pmatrix} \in \mathbb{R}^{n_c \times N_r}, \tag{3.28}$$

each physical field can be approximated onto these bases:

$$\begin{aligned} u &\simeq \widetilde{u} = \overline{u} + \boldsymbol{\phi}^u \mathbf{a}, \\ v &\simeq \widetilde{v} = \overline{v} + \boldsymbol{\phi}^v \mathbf{a}, \\ w &\simeq \widetilde{w} = \overline{w} + \boldsymbol{\phi}^w \mathbf{a}, \\ p &\simeq \widetilde{p} = \overline{p} + \boldsymbol{\phi}^p \mathbf{a}. \end{aligned} \tag{3.29}$$

For a clearer idea, in Figures 3.4-3.7 the first four basis functions for all the variables are plotted in a two-dimensional $x-y$ section of the domain, and in Figure 3.8 the first projection coefficients are shown.

For all the modes, oscillations are concentrated behind the cylinder, with little activity occurring before it, where the mean field suffices to replicate the actual simulation. The modes form pairs, such as (Φ_1,Φ_2),(Φ_3,Φ_4), and so forth, exhibiting similar energy and frequency trends, in line with the eigenvalue descent pattern. Each pair essentially represents the same spatial structure, with one element slightly

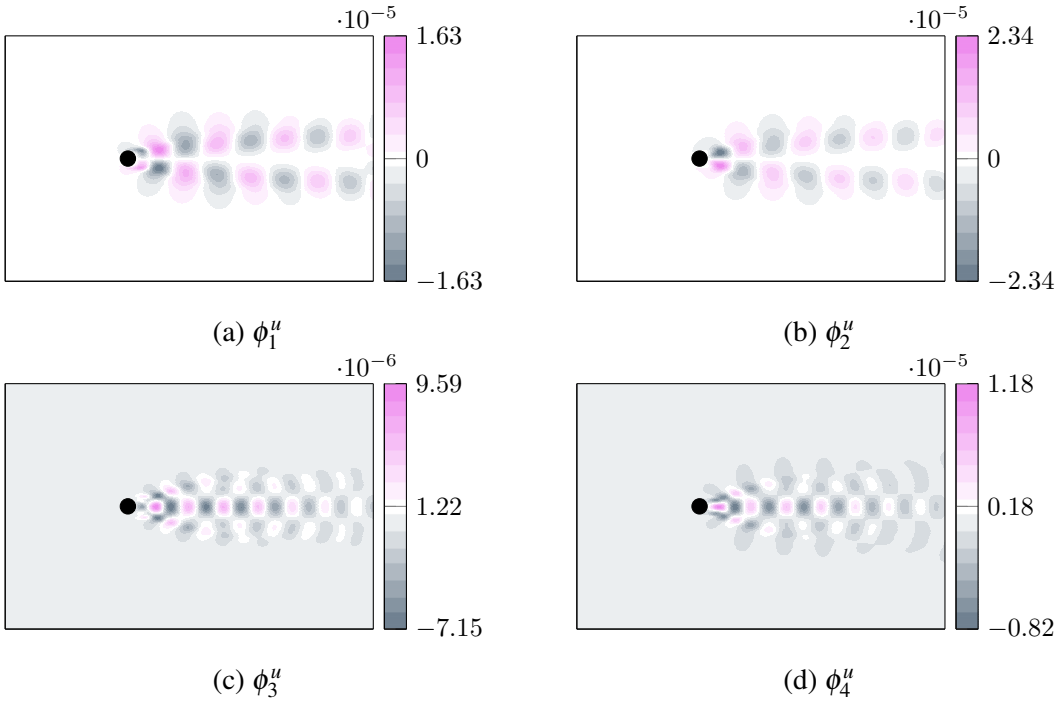

(a) ϕ_1^u (b) ϕ_2^u

(c) ϕ_3^u (d) ϕ_4^u

Fig. 3.4 Spatial evolution on a $x-y$ section of the first four basis functions for the longitudinal velocity, $\boldsymbol{\phi}^u$.

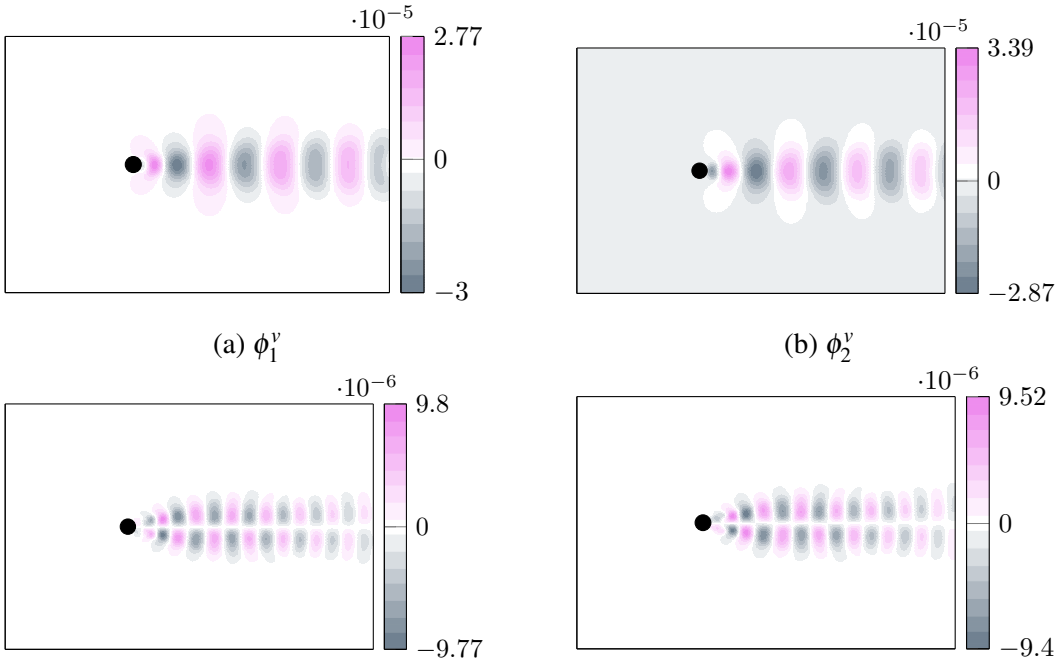

(a) ϕ_1^v (b) ϕ_2^v

(c) ϕ_3^v (d) ϕ_4^v

Fig. 3.5 Spatial evolution on a $x-y$ section of the first four basis functions for the vertical velocity, $\boldsymbol{\phi}^v$.

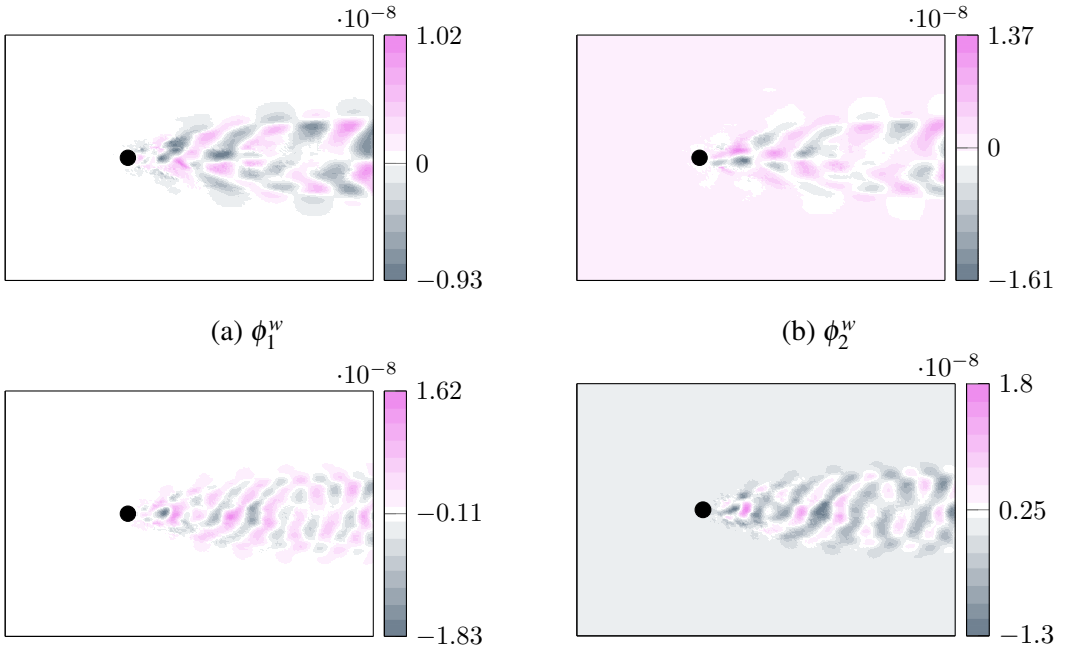

(a) ϕ_1^w (b) ϕ_2^w

(c) ϕ_3^w (d) ϕ_4^w

Fig. 3.6 Spatial evolution on a $x-y$ section of the first four basis functions for the transversal velocity, $\boldsymbol{\phi}^w$.

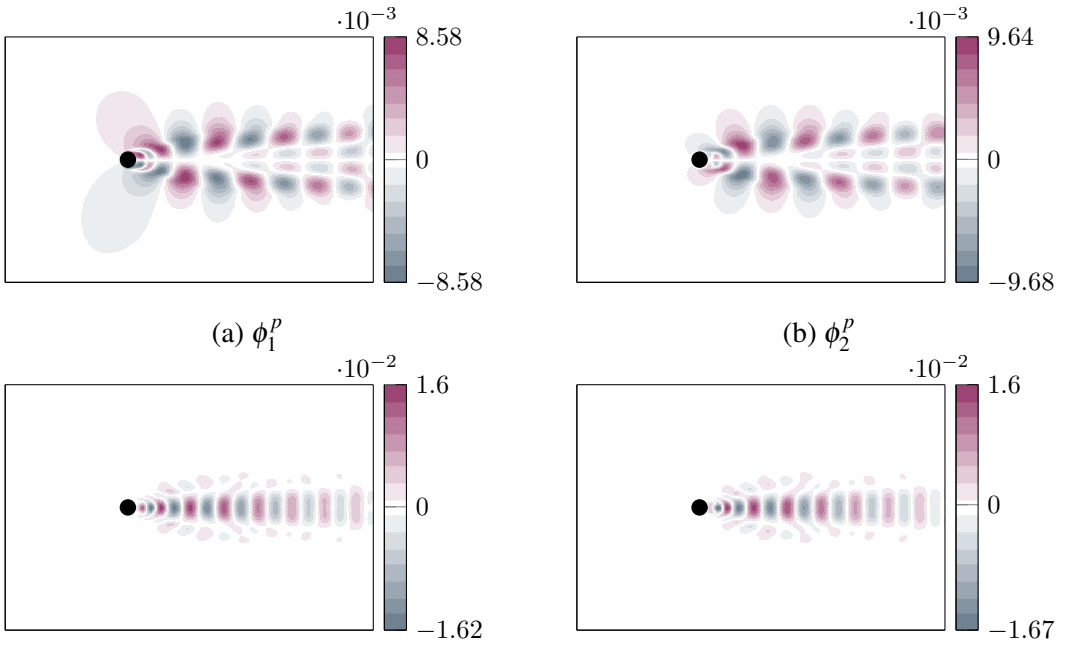

(a) ϕ_1^p (b) ϕ_2^p

(c) ϕ_3^p (d) ϕ_4^p

Fig. 3.7 Spatial evolution on a $x-y$ section of the first four basis functions for the pressure, $\boldsymbol{\phi}^p$.

shifted with respect to the other, in the streamwise direction. This behavior holds true for the basis functions of all the variables. While $\boldsymbol{\phi}^u$ and $\boldsymbol{\phi}^v$ share similar amplitudes but differ in shape, $\boldsymbol{\phi}^w$ presents a much smaller amplitude, and the shape in the chosen section is not very representative. Indeed, although the simulation is in three dimensions, the phenomenon is predominantly two-dimensional, minimizing the contribution of the third direction. The pressure shows a regular shape, similar to velocity, but with larger magnitude in the basis functions. This discrepancy arises from considering velocity and pressure with equal weight in the variable matrix, whereas their difference in magnitude is of the order of $\mathcal{O}(10^5)$. Since the temporal coefficients are the same for the entire basis function set, the modes capture this difference also in their values.

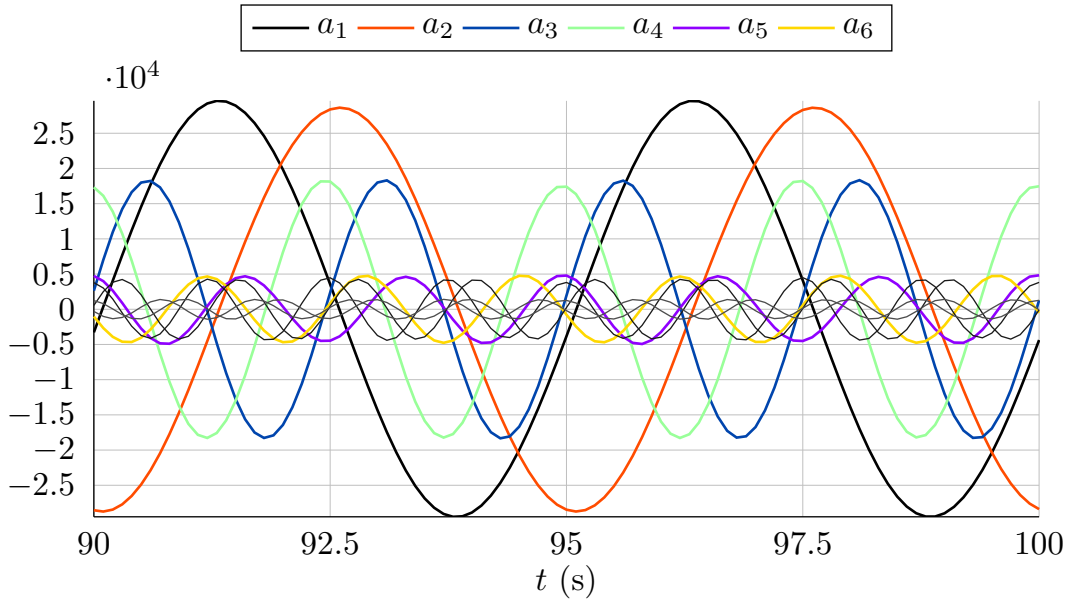

Fig. 3.8 Temporal evolution of the first six projection coefficients (in color). The lines in grey are the other, less energetic, projection coefficients.

However, employing a global POD basis with $\mathbf{U} = (u, v, w, p)^T$ offers the advantage of using the same temporal coefficients $\mathbf{a}$ for each variable. The projection coefficients plotted in Figure 3.8 are representative of a fully developed flow, devoid of transients, and manifesting periodic behavior. The temporal evolution of the first represented coefficients aligns with the energy descent pattern by pair, with the second pair of coefficients, a_3, a_4, having smaller amplitude and half the frequency of the first pair. Each pair also reveals a 90-degree phase shift within the two compo-

nents. Subsequent pairs have smaller amplitudes and higher frequency, following the eigenvalue trend.

Computation of the ROM model As the basis functions inherit the properties of the variables, they directly satisfy the continuity equation. Henceforth, just the momentum equations are considered.

Substituting the definition of the variables (Eq. (3.29)) and doing a Galerkin projection of $\boldsymbol{\phi}^{\mathbf{u}}$ on the Navier-Stokes momentum equations (Eq. (3.17b)), after few passages, the dynamical system looks like:

$$\mathbf{L}\dot{\mathbf{a}} = \mathbf{A} + \mathbf{B}\,\mathbf{a} + \mathbf{a}^T\,\mathbf{C}\,\mathbf{a}, \tag{3.30}$$

that is expanded, using Einstein summation convention, as:

$$\sum_{j=1}^{N_r} L_{ij}\frac{\mathrm{d}a_j}{\mathrm{d}t} = A_i + \sum_{j=1}^{N_r} B_{ij}\,a_j + \sum_{j=1}^{N_r}\sum_{k=1}^{N_r} C_{ijk}\,a_j\,a_k, \tag{3.31}$$

with

$$L_{ij} = +\left(\phi_i^{\mathbf{u}}, \phi_j^{\mathbf{u}}\right) \tag{3.32a}$$

$$A_i = -\left(\phi_i^{\mathbf{u}}, (\bar{\mathbf{u}}\cdot\nabla)\bar{\mathbf{u}}\right) + \nu\left(\phi_i^{\mathbf{u}}, \Delta\bar{\mathbf{u}}\right) - \frac{1}{\rho}\left(\phi_i^{\mathbf{u}}, \nabla\bar{p}\right) + \left(\phi_i^{\mathbf{u}}, \mathbf{g}\right) \tag{3.32b}$$

$$B_{ij} = -\left(\phi_i^{\mathbf{u}}, (\bar{\mathbf{u}}\cdot\nabla)\phi_j^{\mathbf{u}}\right) - \left(\phi_i^{\mathbf{u}}, (\phi_j^{\mathbf{u}}\cdot\nabla)\bar{\mathbf{u}}\right) + \nu\left(\phi_i^{\mathbf{u}}, \Delta\phi_j^{\mathbf{u}}\right) - \frac{1}{\rho}\left(\phi_i^{\mathbf{u}}, \nabla\phi_j^{p}\right) \tag{3.32c}$$

$$C_{ijk} = -\left(\phi_i^{\mathbf{u}}, (\phi_j^{\mathbf{u}}\cdot\nabla)\phi_k^{\mathbf{u}}\right). \tag{3.32d}$$

The tensor $\mathbf{A}$ contains terms associated to the mean field and gravity, given their constant vector nature. Meanwhile, the tensor $\mathbf{B}$ encompasses terms related to convection, diffusion, and pressure gradient effects. The tensor $\mathbf{C}$ contains a term linked specifically to convection. If the modes were built solely on velocity, their orthogonality feature $\left(\phi_i^{\mathbf{u}}, \phi_j^{\mathbf{u}}\right) = \delta_{ij}$, would cause the tensor $\mathbf{L}$ to be the identity matrix. However, when additional variables beyond the velocity field are considered in the mode construction, although the entire set of basis functions remains orthogonal, the projection is performed only on the velocity component of the basis functions, $\boldsymbol{\phi}^{\mathbf{u}}$,

hence $\left(\phi_i^{\mathbf{u}}, \phi_j^{\mathbf{u}}\right) \neq \delta_{ij}$, and $\mathbf{L} \neq \mathbb{I}$.
All those tensors are constant over time, computed once using the POD modes, and used throughout the integration in time. Given the initial condition $\mathbf{a}^0 = \left(\left[\mathbf{U}_0(\mathbf{x}) - \overline{\mathbf{U}}(\mathbf{x})\right], \Phi\right)$, the system of ODE (Eq. (3.30)) is integrated using a fourth-order Runge-Kutta scheme, resulting in a series of predicted time history of the temporal coefficients.

Pressure Term

As the pressure contributes to the definition of the POD modes, it naturally influences the dynamical model, evident in the terms in Eqs. (3.32b), (3.32c). By reverting one step back and considering the Galerking projection onto the pressure term, one can write:

$$-\left(\phi_i^{\mathbf{u}}, \nabla p\right) = \left(\nabla \cdot \phi_i^{\mathbf{u}}, p\right) - \left[\phi_i^{\mathbf{u}}\, p \cdot \mathbf{n}\right]. \tag{3.33}$$

The integration by parts, along with Green's formula, have been employed in this derivation. The round brackets denote the value over the entire computational domain Ω, whereas the square brackets represent the value on the boundary of the computational domain Γ, with $\mathbf{n}$ the normal vector. Due to the divergence-free property of the POD modes, inherited from the snapshots, the first term in Eq. (3.33) vanishes, leaving only the term on the boundary. Moreover, a proper selection of the simulation boundary conditions can potentially eliminate such term. As explained in [168], for many flows, the pressure term is effectively zero (owing to periodic boundary conditions or steady Dirichlet boundary conditions in the wall-normal direction), or nearly so. However, the avoidance of the pressure modeling impedes tracking its evolution, and may introduce significant errors, which cannot be compensated by an increase in the number of modes [169, 170]. Moreover, considering that the ultimate objective is the multiphase flow description, with a possibly substantial pressure jump, and arbitrary boundary conditions, the pressure integral neither vanishes nor can it be disregarded. Consequently, the pressure variable is retained in the ROM model, albeit with a weighting applied. Since the absolute value of the variables may be significantly different between velocity and pressure, normalization of the snapshots is desirable, to ensure equal significance

across all variables. Taking the velocity as normalization reference (thus assigning it a weight of unity), the snapshot matrix assumes the form:

$$\mathbf{U} = \begin{pmatrix} \mathbf{u} = \begin{pmatrix} u \\ v \\ w \end{pmatrix} \\ Q_p\ p \end{pmatrix}, \tag{3.34}$$

where the constant Q_p permits arbitrary weighting of pressure with respect to velocity. While the preceding results are obtained with $Q_p = 1$, comparison with alternative scenarios, such as for $Q_p = 0$ and $Q_p = 10^{-5}$ can be insightful.

Case $Q_p = 0$. In this case, the pressure is excluded from the model, and the basis functions are built only on the velocity field. Consequently, if required, the pressure can be reconstructed a posteriori. In monophase scenarios, this choice is often acceptable.

Case $Q_p = 1$. In this configuration, the pressure is integrated into the model, with the basis functions derived from both velocity and pressure fields. For this specific test case, velocity typically ranges around unity, while the pressure, here the total absolute pressure, tends to be of the order of $\mathscr{O}(10^5)$. Moreover, as previously mentioned, the values and the effect of the pressure may be different when considering different fluids, due to the static pressure, which increases under the effect of gravity. The considerable difference in magnitude between the two variables might influence the construction of basis functions, potentially leading them to be more affected by pressure than velocity.

Case $Q_p = 10^{-5}$. In order to ensure equal importance to both velocity and pressure during the construction of the basis functions, pressure is downweighted significantly by setting $Q_p = 10^{-5}$. This choice aims to normalize all variables around unity or at least within the $\mathscr{O}(1)$ range. Consequently, this weighting is applied consistently across the different density values tested ($\rho = 1\,\mathrm{kg/m^3}$ and $\rho = 1000\,\mathrm{kg/m^3}$), even though higher densities typically result in larger pressure values.

Comparison ROM to FOM

Before comparing the results, the evaluation of the computational effort required for both the FOM and the ROM is essential to grasp the real impact of techniques like the POD. Running the FOM for $t = 10\,\mathrm{s}$ on StarCCM+ takes around 15 minutes using 48 processors on a supercomputer. In contrast, computing the ROM over the same time interval using Matlab only takes around 65 seconds, on a single processor. It is worth noting that such time corresponds to the online phase, while an offline phase, in this case taking approximately 88 seconds to compute, is necessary for computation, excluding a snapshot pre-processing. Comparing the velocity magnitude and the pressure at time $T = 98\,\mathrm{s}$, reveals a very good agreement between the ROM and the FOM, across all values of Q_p. Figure 3.9 shows the FOM and ROM velocity fields at the same instant, showing corresponding results.

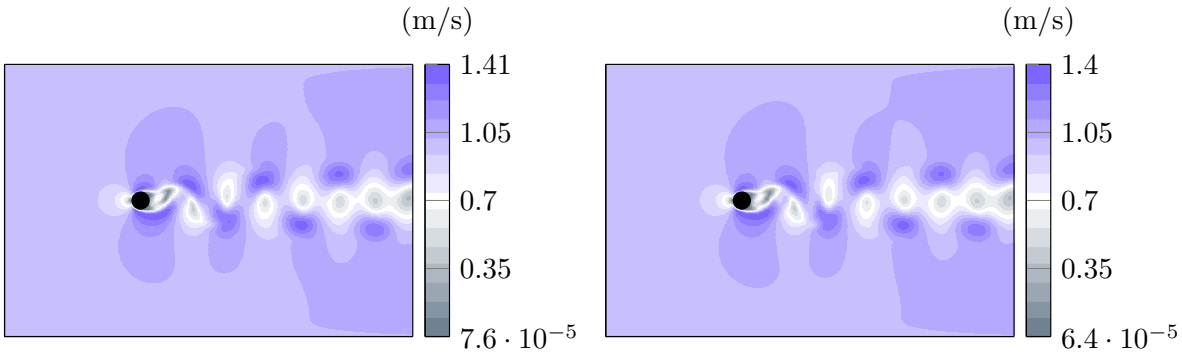

(a) FOM velocity field.

(b) ROM velocity field.

Fig. 3.9 Comparison between FOM and ROM solutions, for the case with $\rho = 1000\,\mathrm{kg/m^3}$ and $Q_p = 10^{-5}$, for the velocity magnitude, on a $x-y$ section, at time $T = 98\,\mathrm{s}$.

A quantitative difference can be appreciated in the absolute difference plots, for both velocity and pressure, of Figure 3.10, simply calculated as $\|\xi_{ref} - \xi_{approx}\|$, with $\xi \equiv \{\mathbf{u}, p\}$. The main discrepancies are localized in the wake of the cylinder, where larger oscillations occur.

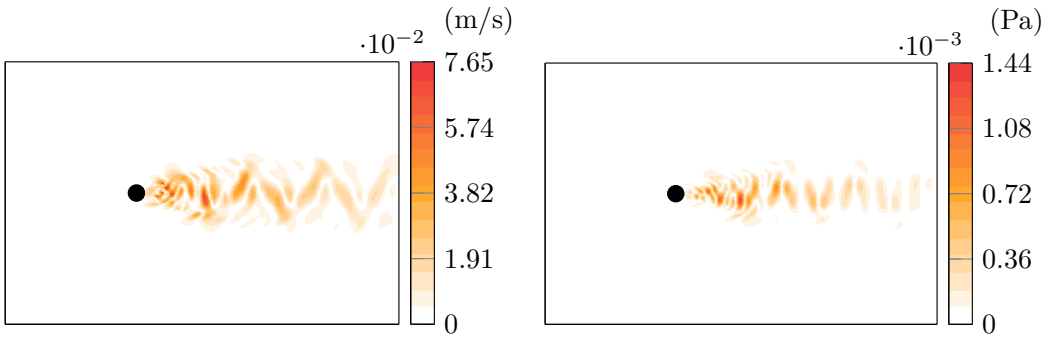

(a) Velocity field.

(b) Pressure field.

Fig. 3.10 Absolute difference between FOM and ROM solutions for the case with $\rho = 1000\,\mathrm{kg/m^3}$ and $Q_p = 10^{-5}$, for the velocity and the pressure magnitudes, on a $x-y$ section, at time $T = 98\,\mathrm{s}$.

Analysis of Figure 3.11 and Table 3.1, indicates consistently small absolute and relative errors, irrespective of density values and pressure weighting in the variable matrix.

	Error	$\rho = 1\,\mathrm{kg/m^3}$			$\rho = 1000\,\mathrm{kg/m^3}$		
		$Q_p = 0$	$Q_p = 1$	$Q_p = 10^{-5}$	$Q_p = 0$	$Q_p = 1$	$Q_p = 10^{-5}$
Projection	$\bar{\varepsilon}^u$	5.10e-6	5.12e-6	5.10e-6	5.10e-6	5.14e-6	5.10e-6
	$\bar{\varepsilon}^v$	5.37e-5	5.38e-5	5.37e-5	5.37e-5	5.40e-5	5.37e-5
	$\bar{\varepsilon}^w$	1.56e-3	1.56e-3	1.56e-3	1.56e-3	1.56e-3	1.56e-3
	$\bar{\varepsilon}^p$	-	1.29e-10	1.30e-10	-	1.17e-7	1.18e-7
ROM	$\bar{\varepsilon}^u$	2.74e-5	3.45e-5	3.45e-5	2.74e-5	3.43e-5	3.44e-5
	$\bar{\varepsilon}^v$	3.79e-4	4.71e-4	4.71e-4	3.79e-4	4.68e-4	4.69e-4
	$\bar{\varepsilon}^w$	3.16e-3	3.66e-3	3.67e-3	3.17e-3	3.67e-3	3.67e-3
	$\bar{\varepsilon}^p$	-	6.97e-10	6.96e-10	-	6.33e-7	6.31e-7

Table 3.1 Relative errors for the velocity and pressure variables, for both fluid cases, $\rho = 1\,\mathrm{kg/m^3}$ and $\rho = 1000\,\mathrm{kg/m^3}$. Projection and model errors are displayed.

Notably, Table 3.1 shows that projection errors remain unchanged regardless of the fluid characteristics or the pressure weighting (except for the pressure itself), which only affect the ROM model errors. As expected, ROM errors surpass projection errors, albeit marginally. Moreover, absolute errors display an increasing trend over time, which is typical as the ROM model approximates the FOM model with a truncation, resulting in error accumulation. Besides, since the problem is three-

dimensional, the w component of the velocity is considered and examined alongside other variables, throughout the entire document. However, given that some problems, such as this one, are predominantly evolving in two dimensions [171], there is limited variation of the solution in the z direction. Consequently, relative errors appear significant due to the division by a velocity field with very small values in that direction.

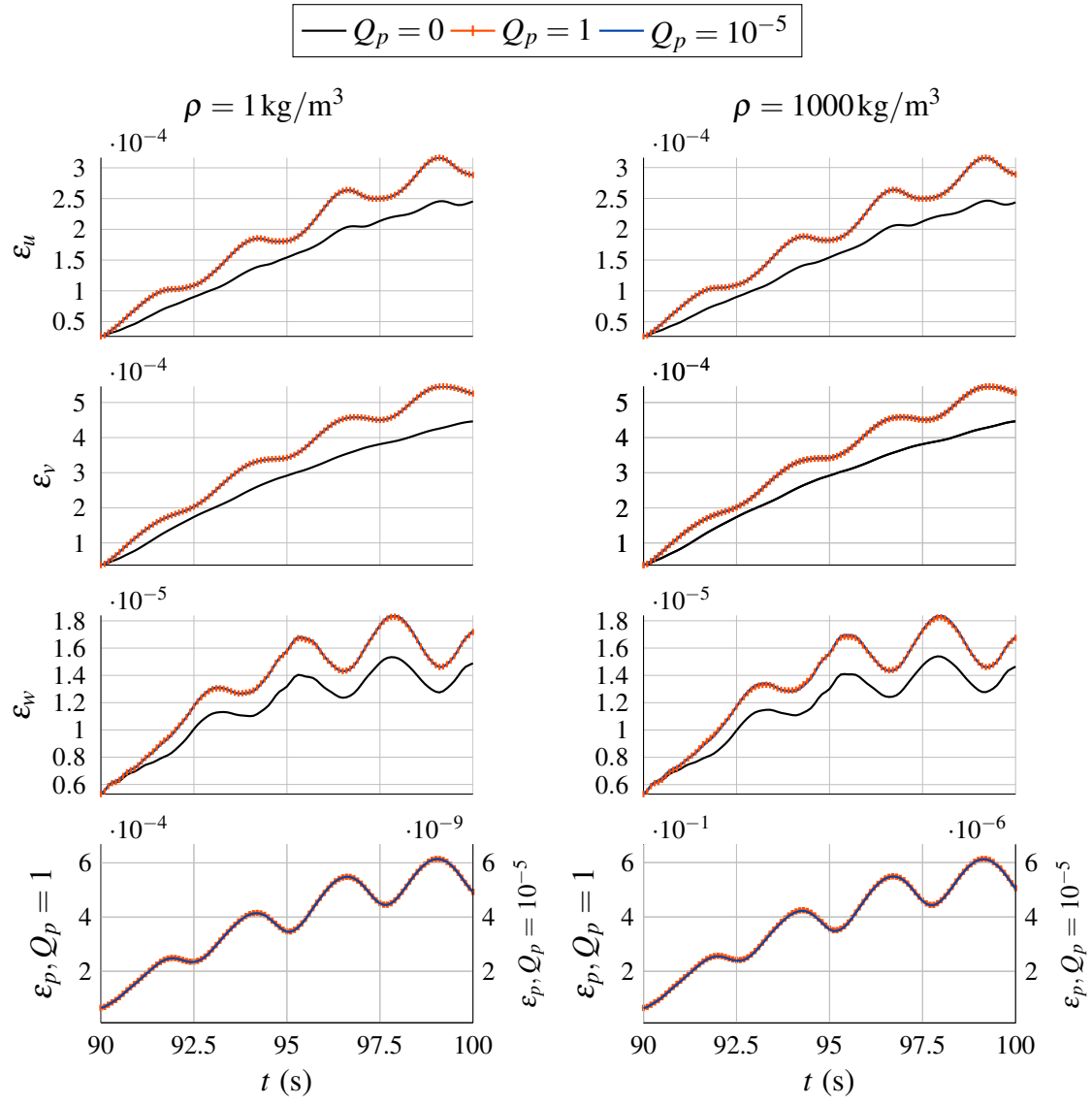

Fig. 3.11 Evolution of the absolute error for velocity and pressure variables over time. Both fluid cases, with $\rho = 1\,\mathrm{kg/m^3}$ (left) and $\rho = 1000\,\mathrm{kg/m^3}$ (right) are displayed.

Upon closer examination, several observations can be made to discern the impact of the pressure weighting and different fluid properties. Firstly, the absolute and relative errors in the velocity field remain consistent across the different fluid characteristics, indicating that the underlying pattern remains unchanged. Relative errors for all the variables are comparable for the different values of Q_p, suggesting minimal sensitivity to pressure weighting. Considering absolute errors allows to detect a subtle difference: using pressure to construct the model marginally deteriorates its performance, irrespective of the weighting value. In terms of the pressure field, the primary distinction lies in magnitude, which decreases with decreasing Q_p. Intuitively, a strong weight (like $Q_p = 10^{-5}$), reduces the pressure values, hence diminishing their difference (and consequently the error). However, the evolution of the absolute error remains unaffected by changes in Q_p. This behavior likely stems from the relatively minor fluctuations in the pressure, mainly driven by the static pressure, with minimal dynamic pressure contributions. This raises questions about the utility of incorporating the scalar pressure into the ROM model. Nonetheless, despite the slight influence of the pressure on the final results, including it in the ROM model ensures a more informative model, allowing also for the reconstruction of this additional value.

Alternatively, one could consider utilizing the pressure gradient, instead of pressure itself, in the ROM model. This approach would mitigate the influence of static pressure, leading to a behavior analogous to the velocity field, characterized by wake oscillations behind the cylinder, as depicted in Figure 3.12. Further analysis of this approach will be undertaken in the context of multiphase flow scenarios.

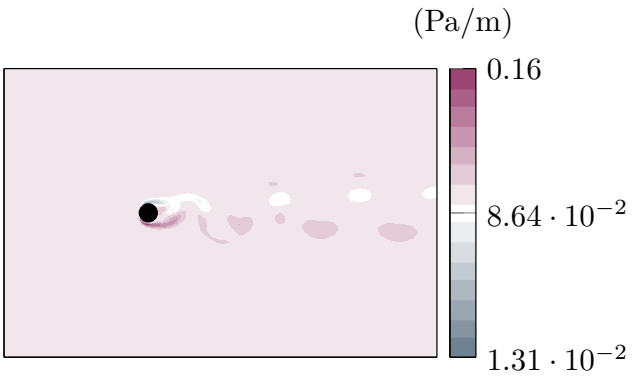

Fig. 3.12 Magnitude of the pressure gradient, on a $x-y$ section, at $T = 98\,\mathrm{s}$, for the case with $\rho = 1000\,\mathrm{kg/m^3}$ and $Q_p = 10^{-5}$.

3.3.2 Cylinder at $Re = 9 \times 10^5$

At low Reynolds numbers, the flow shows periodicity in the vortex street despite its unsteadiness, helping to preserve a manageable problem. Notwithstanding, transitioning towards real-world scenarios, such as those comprising air or water, normally involves higher Reynolds numbers. For instance, using the same cylinder and the same upstream velocity, air density and viscosity induce $Re_a \sim 6.7 \times 10^4$, whether with water characteristics, $Re_w \sim 9 \times 10^5$. Conventionally, Reynolds numbers as high as Re_w in open channels signify flow reaching a turbulent regime. Hence, turbulence modeling becomes imperative for such scenarios, entailing its incorporation into the Navier-Stokes equations.

However, in the context of wave energy applications, a laminar description might be a reasonable assumption, without making any simplification. As argued in [71], the transient nature of the phenomenon - a body and a flow field constantly oscillating - raises doubts about the full development of a boundary layer on the body. Furthermore, the complexity introduced by multiphase problems amplifies the challenges associated with turbulent flow treatment. These considerations, along with examples of laminar CFD simulations of WECs validated against experimental data [172], corroborate the choice of excluding turbulence in the high-fidelity simulations conducted in this study.

Additionally, maintaining the laminar version of the governing equations simplifies the treatment of the problem, avoiding the need to introduce closure terms and other adjustments required for turbulence modeling [142, 170, 173]. Indeed, a ROM based on POD is based on an energy criterion, wherein a turbulent flow tends to dissipate energy in high frequencies corresponding to the less energetic eigenvalues, normally truncated in the ROM. Consequently, the model may fail to represent such dissipation, potentially leading to instability. To recover the effect of the truncated modes, a turbulent coefficient can be added to the model. This can be implemented within the $\mathbf{B}$ tensor, where the third element of B_{ij} (Eq. (3.32c)), containing the kinematic viscosity ν, is modified to $\nu(1+\nu_T)$, with ν_T a constant value, ideally smaller than unity, yet sufficient to introduce artificial dissipation into the reduced model.

Numerical Results

The simulation setup remains unchanged, except for the fluid characteristics, now modeled after water. New snapshots are generated, and the model is built for varying values of ν_T.

From Figure 3.13, the eigenvalue descent is less pronounced compared to the case at $Re = 200$ (Figure 3.3), and the RIC increases with N_r at a slower rate. This implies that a greater number of modes are required to adequately approximate the solution. In this case, a RIC $> 99.99\%$ is attained with $N_r = 48$, indicating that either a higher N_r is necessary for a satisfactory reduction, or maintaining N_r at a reasonable level, for reduction purposes, would result in a lower RIC. Hence, truncation is done at $N_r = 21$, yielding RIC $> 99.00\%$, albeit at the cost of doubling the number of retained modes, compared to the previous case.

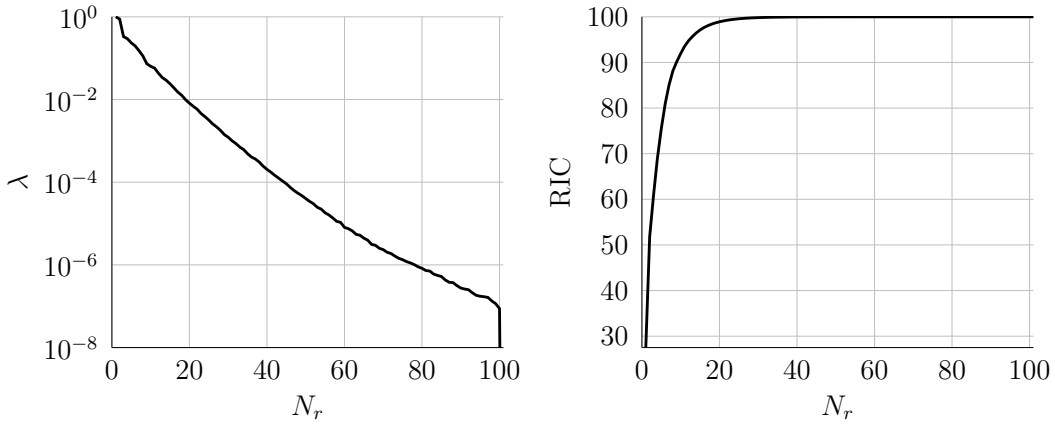

Fig. 3.13 Evolution of the eigenvalues spectrum, normalized to the fist eigenvalue (left), and of the RIC (right) with respect to the number of POD modes N_r, for the case of the cylinder at $Re = 9 \times 10^5$.

Furthermore, the descent by pair observed previously becomes less discernible, as corroborated by the coefficients plotted in Figure 3.14. Although the first two coefficients remain dominant, as evidenced also by the eigenvalue plot, and out of phase, their magnitude decreases with time. Coefficients a_3 and a_4 show a less periodic behavior than expected. The smaller coefficients have significant amplitudes, which also vary over time, and lack ordered frequencies. This overall behavior suggests that the information is scattered across a wider spectrum, necessitating larger N_r to correctly represent the phenomenon.

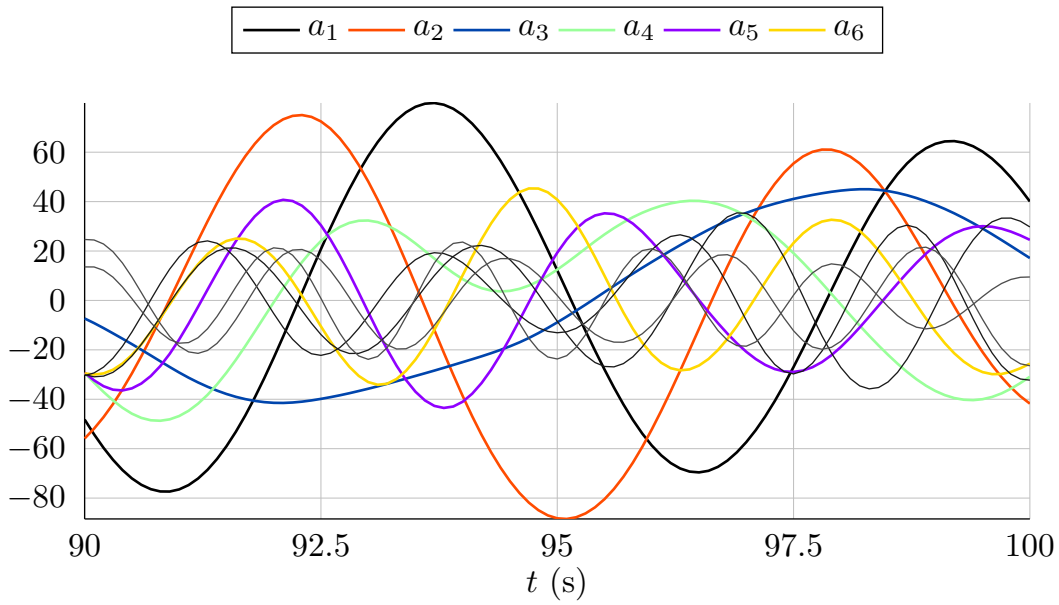

Fig. 3.14 Temporal evolution of the first six projection coefficients (in color). The lines in grey are the projection coefficients for subsequent indices.

The first basis functions depicted in Figures 3.15, 3.16 exhibit a less regular spatial evolution compared to the case of $Re = 200$. Particularly in the velocity field, a subtle difference is still present between the first two modes and the subsequent pair, characterized by higher frequencies and a more disturbed wake. This slight effect is not visible in the pressure field.

The analysis of the modes and coefficients suggests a more difficult flow dynamics, resulting in a correspondingly complex ROM model. Despite this, the computational effort required for the FOM simulation remains consistent with the previous case. The online phase of the ROM now takes around 90 seconds, on a single processor, which is still comparable to the previous case. However, the offline phase of the ROM has increased to 7 minutes due to the larger dimensions of the tensors.

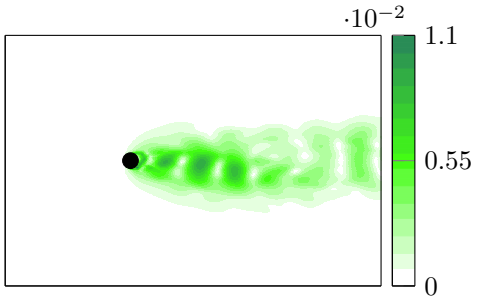

(a) $\phi_1^{\mathbf{u}}$

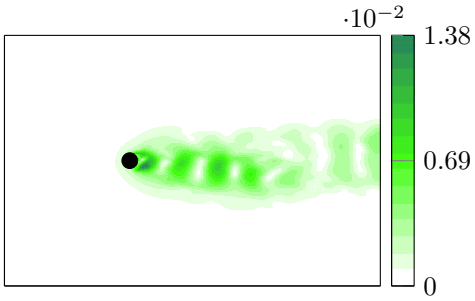

(b) $\phi_2^{\mathbf{u}}$

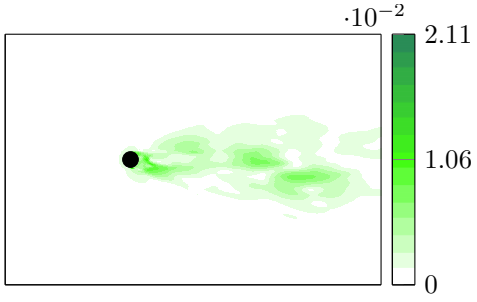

(c) $\phi_3^{\mathbf{u}}$

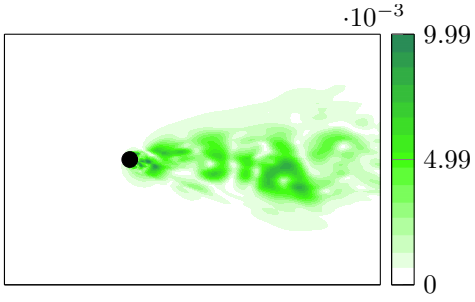

(d) $\phi_4^{\mathbf{u}}$

Fig. 3.15 Spatial evolution on a $x-y$ section of the first four basis functions for the velocity field, $\boldsymbol{\phi}^{\mathbf{u}}$.

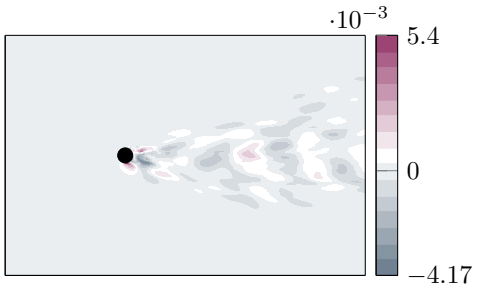

(a) ϕ_1^p

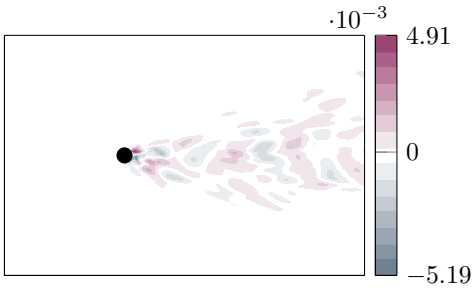

(b) ϕ_2^p

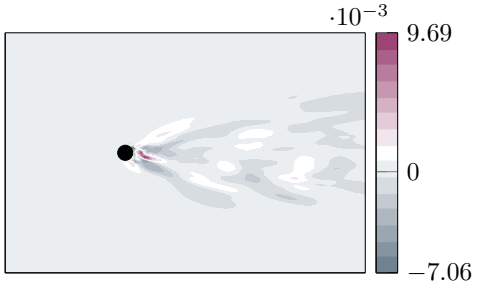

(c) ϕ_3^p

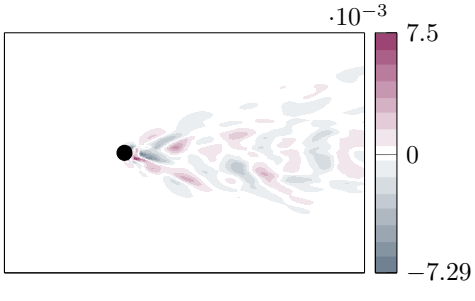

(d) ϕ_4^p

Fig. 3.16 Spatial evolution on a $x-y$ section of the first four basis functions for the pressure field, $\boldsymbol{\phi}^p$.

The reconstruction of the ROM continues to provide a reliable approximation of the FOM, as the relative errors in Table 3.2 remain at most of the order of $\mathcal{O}(10^{-3})$. The addition of the viscosity coefficient ν_T impacts the results by helping reducing the amplification of the coefficients through the introduction of artificial viscosity. Notably, small values of ν_T give smaller errors with respect to the case with $\nu_T = 0$. Excessively large values of the artificial viscosity can have a detrimental effect, resulting in excessive dissipation. This effect is visible in Figure 3.17, especially for the higher frequencies. Nevertheless, the introduction of $\nu_T \neq 0$ primarily affects the amplitude of the temporal coefficients without altering their phase, thus maintaining the slight shift observed between the predicted coefficients and the projection coefficients.

	Error	Turbulent coefficient			
		$\nu_T = 0$	$\nu_T = 0.2$	$\nu_T = 0.6$	$\nu_T = 1.0$
Projection	$\bar{\varepsilon}^u$	8.13e-5	-	-	-
	$\bar{\varepsilon}^v$	7.15e-4	-	-	-
	$\bar{\varepsilon}^w$	1.98e-3	-	-	-
	$\bar{\varepsilon}^p$	1.03e-6	-	-	-
ROM	$\bar{\varepsilon}^u$	3.78e-4	3.34e-4	3.02e-4	3.09e-4
	$\bar{\varepsilon}^v$	3.54e-3	3.17e-3	2.92e-3	3.02e-3
	$\bar{\varepsilon}^w$	6.36e-3	5.56e-3	5.00e-3	5.12e-3
	$\bar{\varepsilon}^p$	3.80e-6	3.35e-6	3.03e-6	3.11e-6

Table 3.2 Relative errors for the velocity and pressure variables, for the cases with varying turbulent coefficient values. Both projection and model errors are displayed.

The findings prove the necessity for a greater number of modes as the Reynolds number increases, reflecting the increased complexity and instability of the flow. Despite the need for a higher amount of information, the reduction is, nonetheless, consistent, even if marginally less effective. The monophase ROM implemented in this section is accurate, with careful consideration required to well represent several fluid conditions. The literature on model order reduction for fluids focuses on monophase flows, with an emphasis on the modeling of turbulence, or compressibility in shock analysis. To the best of the author's knowledge, there is currently limited evidence of a ROM tailored specifically for real multiphase flows in three dimensions. As the application of such multiphase ROM model would potentially be diverse, extending beyond wave energy, further exploration of this subject is needed.

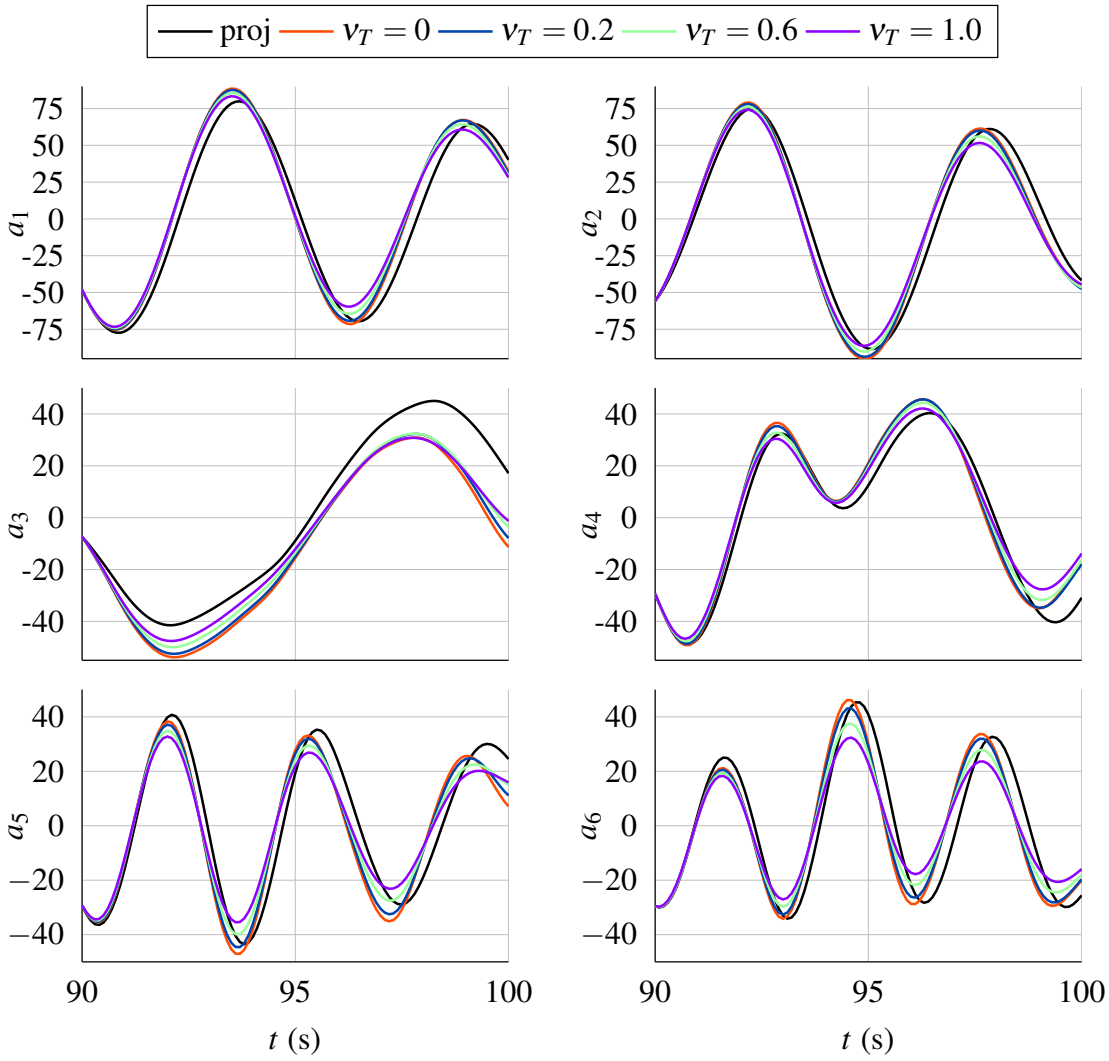

Fig. 3.17 Evolutionf of the first six temporal coefficients, for the varying values of ν_T, in comparison to the projection coefficients, for the case at $Re = 9 \times 10^5$.

3.4 Multiphase POD-ROM

Considering the extensive research conducted on the flow past a cylinder, it serves as an ideal subject for further inquiry. This investigation is prompted by lacking answers in the field of low-dimensional models for multiphase flows. Employing the same simulation framework used so far, a second fluid is introduced, dividing the domain in a *light* (above) fluid with characteristics ρ_l and μ_l, and a *heavy* (below) fluid, characterized by ρ_h and μ_h, as in Figure 3.18.

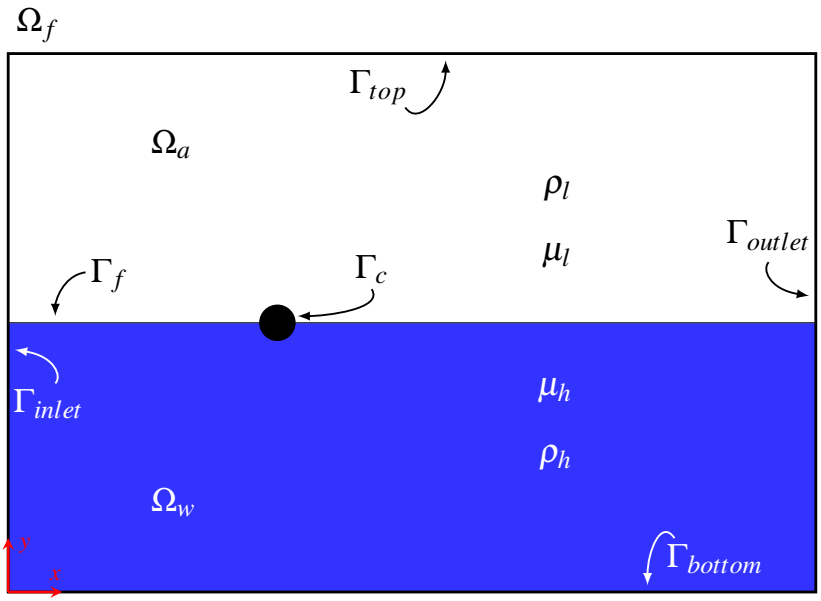

Fig. 3.18 $x-y$ section of the simulation domain for the cylinder in multiphase flows, with definition of the boundaries. In this case, two flows, a light (subscript l) and a heavy one (subscript h), are simulated. The front and back boundaries are not visible, but present in the three-dimensional simulation.

Following the strategy used in the previous section, the starting point is the momentum Navier-Stokes equations, which, for a multiphase, incompressible, laminar flow read as:

$$\frac{\partial \mathbf{u}}{\partial t} + (\mathbf{u}\cdot\nabla)\mathbf{u} = -\frac{1}{\rho}\nabla p + \frac{1}{\rho}\nabla\cdot(\mu(\nabla\mathbf{u} + (\nabla\mathbf{u})^T)) + \mathbf{g}. \tag{3.35}$$

Similar to the monophase scenario, turbulence may be inserted in the equation, and hence in the model. To maintain simplicity and relevance to specific cases of interest, the study is confined to the laminar framework.

Compared to the monophase case, the multiphase setup introduces additional variables into the model: the density and the viscosity, which now evolve, especially across the interface between the two fluids. One approach is to incorporate ρ and μ directly in the model. Alternatively, the Volume of Fluid method can be employed. The variable α assumes unitary values in the heavy fluid, null values in the light fluid, and values $0 < \alpha < 1$ at the interface of the two fluids. The evolution of density and viscosity is then recovered using the expressions $\rho = \rho_l + \alpha(\rho_h - \rho_l)$ and $\mu = \mu_l + \alpha(\mu_h - \mu_l)$. With this strategy, however, an additional equation appears in the system, the one for the transport of α:

$$\frac{\partial \alpha}{\partial t} + \mathbf{u} \cdot \nabla \alpha = 0. \tag{3.36}$$

In StarCCM+, the segregated VOF solver is added to the simulation setup. For an accurate resolution of the interface, the Adaptive Mesh Refinement (AMR) of two levels is triggered at each time step along the free surface, and the HRIC (High Resolution Interface Capturing) scheme is implemented to maintain a sharp interface between the two immiscible fluids. Even though an implicit time scheme is used in the simulation, the HRIC necessitates small values of the CFL (Courant–Friedrichs–Lewy), to be kept below 0.4, to promote convergence. This forces the time step to small values, even though the snapshots are collected at bigger Δt. As in the previous case, Dirichlet boundary conditions for velocity are imposed on Γ_{inlet}, Γ_{top}, and Γ_{bottom}, and for pressure on Γ_{outlet}. Symmetry planes are employed for the transversal boundaries, Γ_{front} and Γ_{back}, and the cylinder boundary Γ_c is modeled as a wall. A new "boundary" appears, Γ_f, the interface between the two fluids, which is initialized as a flat line at the start of the simulation (Figure 3.18).

To preserve the clarity of the study at this stage, the VOF is not integrated into the ROM model, hence avoiding adding an equation to the dynamical system. Even though a solution can be derived, it would be cumbersome, since density and viscosity, both linked to the VOF, appear in the momentum equation. For this reason, the following fluid characteristics are considered in the variable matrix:

$$\mathbf{U} = \begin{pmatrix} \mathbf{u} = \begin{pmatrix} u \\ v \\ w \end{pmatrix} \\ Q_p\, p \\ Q_{1/\rho}\, \frac{1}{\rho} \\ Q_\mu\, \mu \end{pmatrix}, \tag{3.37}$$

where new weighting coefficients, $Q_{1/\rho}$ and Q_μ, appear, to homogenize the values, and have contributions from the different variables normalized with respect to the velocity contribution. The set of basis functions is now:

$$\Phi = \begin{pmatrix} \boldsymbol{\phi}^{\mathbf{u}} = \begin{pmatrix} \boldsymbol{\phi}^{u} \\ \boldsymbol{\phi}^{v} \\ \boldsymbol{\phi}^{w} \end{pmatrix} \\ \boldsymbol{\phi}^{p} \\ \boldsymbol{\phi}^{1/\rho} \\ \boldsymbol{\phi}^{\mu} \end{pmatrix}. \tag{3.38}$$

where $\mathbf{u}$ and p are defined as in Eq. (3.29), and adding

$$\begin{aligned} \frac{1}{\rho}(\mathbf{x},t) &= \frac{1}{\bar{\rho}}(\mathbf{x}) + \sum_{j=1}^{N_r} a_j(t)\phi_j^{1/\rho}(\mathbf{x}), \\ \mu(\mathbf{x},t) &= \bar{\mu}(\mathbf{x}) + \sum_{j=1}^{N_r} a_j(t)\phi_j^{\mu}(\mathbf{x}). \end{aligned} \tag{3.39}$$

The dynamical system deriving from the Galerkin projection looks quite complex:

$$\mathbf{L}\dot{\mathbf{a}} = \mathbf{A} + \mathbf{B}\mathbf{a} + \mathbf{a}^T\mathbf{C}\mathbf{a} + \mathbf{a}^T\left(\mathbf{a}^T\mathbf{D}\mathbf{a}\right), \tag{3.40}$$

with the matrices:

$$L_{ij} = +\left(\phi_i^{\mathbf{u}}, \phi_j^{\mathbf{u}}\right) \tag{3.41a}$$

$$\begin{aligned} A_i = &-\left(\phi_i^{\mathbf{u}}, (\bar{\mathbf{u}}\cdot\nabla)\bar{\mathbf{u}}\right) - \left(\phi_i^{\mathbf{u}}, \frac{1}{\bar{\rho}}\nabla\bar{p}\right) + \left(\phi_i^{\mathbf{u}}, \frac{1}{\bar{\rho}}\nabla\bar{\mu}(\nabla\bar{\mathbf{u}} + (\nabla\bar{\mathbf{u}})^T)\right) + \\ &+ \left(\phi_i^{\mathbf{u}}, \frac{1}{\bar{\rho}}\bar{\mu}\Delta\bar{\mathbf{u}}\right) + \left(\phi_i^{\mathbf{u}}, \mathbf{g}\right) \end{aligned} \tag{3.41b}$$

$$\begin{aligned} B_{ij} = &-\left(\phi_i^{\mathbf{u}}, (\bar{\mathbf{u}}\cdot\nabla)\phi_j^{\mathbf{u}}\right) - \left(\phi_i^{\mathbf{u}}, (\phi_j^{\mathbf{u}}\cdot\nabla)\bar{\mathbf{u}}\right) - \left(\phi_i^{\mathbf{u}}, \frac{1}{\bar{\rho}}\nabla\phi_j^{p}\right) - \left(\phi_i^{\mathbf{u}}, \phi_j^{1/\rho}\nabla\bar{p}\right) + \\ &+ \left(\phi_i^{\mathbf{u}}, \frac{1}{\bar{\rho}}\nabla\bar{\mu}(\nabla\phi_j^{\mathbf{u}} + (\nabla\phi_j^{\mathbf{u}})^T)\right) + \left(\phi_i^{\mathbf{u}}, \frac{1}{\bar{\rho}}\nabla\phi_j^{\mu}(\nabla\bar{\mathbf{u}} + (\nabla\bar{\mathbf{u}})^T)\right) + \\ &+ \left(\phi_i^{\mathbf{u}}, \phi_j^{1/\rho}\nabla\bar{\mu}(\nabla\bar{\mathbf{u}} + (\nabla\bar{\mathbf{u}})^T)\right) + \left(\phi_i^{\mathbf{u}}, \frac{1}{\bar{\rho}}\bar{\mu}\Delta\phi_j^{\mathbf{u}}\right) + \\ &+ \left(\phi_i^{\mathbf{u}}, \frac{1}{\bar{\rho}}\phi_j^{\mu}\Delta\bar{\mathbf{u}}\right) + \left(\phi_i^{\mathbf{u}}, \phi_j^{1/\rho}\bar{\mu}\Delta\bar{\mathbf{u}}\right) \end{aligned} \tag{3.41c}$$

$$\begin{aligned} C_{ijk} = &-\left(\phi_i^{\mathbf{u}}, (\phi_j^{\mathbf{u}}\cdot\nabla)\phi_k^{\mathbf{u}}\right) - \left(\phi_i^{\mathbf{u}}, \phi_j^{1/\rho}\nabla\phi_k^{p}\right) + \left(\phi_i^{\mathbf{u}}, \frac{1}{\bar{\rho}}\nabla\phi_j^{\mu}(\nabla\phi_k^{\mathbf{u}} + (\nabla\phi_k^{\mathbf{u}})^T)\right) + \\ &+ \left(\phi_i^{\mathbf{u}}, \phi_j^{1/\rho}\nabla\bar{\mu}(\nabla\phi_k^{\mathbf{u}} + (\nabla\phi_k^{\mathbf{u}})^T)\right) + \left(\phi_i^{\mathbf{u}}, \phi_j^{1/\rho}\nabla\phi_k^{\mu}(\nabla\bar{\mathbf{u}} + (\nabla\bar{\mathbf{u}})^T)\right) + \\ &+ \left(\phi_i^{\mathbf{u}}, \frac{1}{\bar{\rho}}\phi_j^{\mu}\Delta\phi_k^{\mathbf{u}}\right) + \left(\phi_i^{\mathbf{u}}, \phi_j^{1/\rho}\bar{\mu}\Delta\phi_k^{\mathbf{u}}\right) + \left(\phi_i^{\mathbf{u}}, \phi_j^{1/\rho}\phi_k^{\mu}\Delta\bar{\mathbf{u}}\right) \end{aligned} \tag{3.41d}$$

$$D_{ijkl} = +\left(\phi_i^{\mathbf{u}}, \phi_j^{1/\rho}\nabla\phi_k^{\mu}(\nabla\phi_l^{\mathbf{u}} + (\nabla\phi_l^{\mathbf{u}})^T)\right) + \left(\phi_i^{\mathbf{u}}, \phi_j^{1/\rho}\phi_k^{\mu}\Delta\phi_l^{\mathbf{u}}\right). \tag{3.41e}$$

In this case, the tensor $\mathbf{L}$ remains unchanged with respect to the monophase case, but additional terms appear in $\mathbf{A}$, because of the necessity of incorporating mean fields for density and viscosity. The tensor $\mathbf{B}$ still contains terms for convection, diffusion and pressure gradient, and similarly the tensor $\mathbf{C}$. A new, fourth-order tensor $\mathbf{D}$ emerges in the dynamical system, increasing its complexity. While a solution remains attainable, the computational cost escalates significantly. For instance, considering $N_r = 10$, three-dimensional tensors would have size $10 \times 10 \times 10 = 10^3$, but $\mathbf{D}$ would have size 10^4, posing prohibitive challenges. Not only does the offline phase become more resource-intensive due to tensor construction, but also the online phase faces increased demands as the temporal scheme needs to use large, full tensors at each time step.

In addition to the complexity of the model, the difference between the two fluids of interest, water and air, is substantial, with one fluid exhibiting a density three orders of magnitude greater than the other. Moreover, a traveling wave is a highly complex and nonlinear phenomenon. Those considerations motivate a gradual approach for the development of a ROM for such a multiphase problem. Consequently, all the variables are analyzed for their influence on the model, making exception for the velocity. Despite the light impact of pressure on the monophase case, it might have a more pronounced effect on the multiphase case, particularly when using the gradient instead of the absolute value in the variable matrix. Similarly, the density and the viscosity are analyzed individually. Therefore, initially, the monophase case serves as a starting point, with only viscosity altered, leading to the definition of a simplified ROM model (Section 3.4.1). Subsequently, in Section 3.4.2, density variation is introduced and the simplified ROM model is tested against scenarios with spatially varying interfaces. The influence of density and pressure is further explored in Section 3.4.3, integrated in the variable matrix in different forms. Finally, as the fluid characteristics resemble and meet the water and air ones, the model shows instabilities, that are tackled with correction terms or a different model reduction technique in Section 3.4.4.

3.4.1 Viscosity Term

At this stage, the density is kept constant, and only the viscosity is varied. Focusing on the viscosity term of the Navier-Stokes equations, Eq. (3.35), the gradient can be split in two elements, as:

$$\frac{1}{\rho}\nabla\cdot(\mu(\nabla\mathbf{u}+(\nabla\mathbf{u})^T)) = \frac{1}{\rho}\left[\nabla\mu\ (\nabla\mathbf{u}+(\nabla\mathbf{u})^T)+\mu\Delta\mathbf{u}\right] \tag{3.42}$$

where the first element can be called the *symmetric gradient*, standing from the relationship $\text{sym}\nabla\mathbf{u} = \frac{1}{2}(\nabla\mathbf{u}+(\nabla\mathbf{u})^T)$, and the second element is the *Laplacian*. The variable matrix for this case is:

$$\mathbf{U} = \begin{pmatrix} \mathbf{u} = \begin{pmatrix} u \\ v \\ w \end{pmatrix} \\ Q_p\ p \\ Q_\mu\ \mu \end{pmatrix}, \tag{3.43}$$

where the density is absent, as is kept constant in the entire domain. The related basis functions are:

$$\Phi = \begin{pmatrix} \boldsymbol{\phi} = \begin{pmatrix} \boldsymbol{\phi}^u \\ \boldsymbol{\phi}^v \\ \boldsymbol{\phi}^w \end{pmatrix} \\ \boldsymbol{\phi}^p \\ \boldsymbol{\phi}^\mu \end{pmatrix}. \tag{3.44}$$

The dynamical system remains unchanged with respect to the monophase expression (Eq. (3.30)), but the tensors now have additional elements, because of the modes built on the viscosity, $\boldsymbol{\phi}^\mu$:

$$L_{ij} = +\left(\phi_i^{\mathbf{u}}, \phi_j^{\mathbf{u}}\right) \tag{3.45a}$$

$$\begin{aligned} A_i = &-\left(\phi_i^{\mathbf{u}}, (\bar{\mathbf{u}}\cdot\nabla)\bar{\mathbf{u}}\right) - \frac{1}{\rho}\left(\phi_i^{\mathbf{u}}, \nabla\bar{p}\right) + \frac{1}{\rho}\left(\phi_i^{\mathbf{u}}, \nabla\bar{\mu}(\nabla\bar{\mathbf{u}} + (\nabla\bar{\mathbf{u}})^T)\right) + \\ &+ \frac{1}{\rho}\left(\phi_i^{\mathbf{u}}, \bar{\mu}\Delta\bar{\mathbf{u}}\right) + \left(\phi_i^{\mathbf{u}}, \mathbf{g}\right) \end{aligned} \tag{3.45b}$$

$$\begin{aligned} B_{ij} = &-\left(\phi_i^{\mathbf{u}}, (\bar{\mathbf{u}}\cdot\nabla)\phi_j^{\mathbf{u}}\right) - \left(\phi_i^{\mathbf{u}}, (\phi_j^{\mathbf{u}}\cdot\nabla)\bar{\mathbf{u}}\right) - \frac{1}{\rho}\left(\phi_i^{\mathbf{u}}, \nabla\phi_j^p\right) + \\ &+ \frac{1}{\rho}\left(\phi_i^{\mathbf{u}}, \nabla\bar{\mu}(\nabla\phi_j^{\mathbf{u}} + (\nabla\phi_j^{\mathbf{u}})^T)\right) + \frac{1}{\rho}\left(\phi_i^{\mathbf{u}}, \nabla\phi_j^\mu(\nabla\bar{\mathbf{u}} + (\nabla\bar{\mathbf{u}})^T)\right) + \\ &+ \frac{1}{\rho}\left(\phi_i^{\mathbf{u}}, \bar{\mu}\Delta\phi_j^{\mathbf{u}}\right) + \frac{1}{\rho}\left(\phi_i^{\mathbf{u}}, \phi_j^\mu\Delta\bar{\mathbf{u}}\right) \end{aligned} \tag{3.45c}$$

$$C_{ijk} = -\left(\phi_i^{\mathbf{u}}, (\phi_j^{\mathbf{u}}\cdot\nabla)\phi_k^{\mathbf{u}}\right) + \frac{1}{\rho}\left(\phi_i^{\mathbf{u}}, \nabla\phi_j^\mu(\nabla\phi_k^{\mathbf{u}} + (\nabla\phi_k^{\mathbf{u}})^T)\right) + \frac{1}{\rho}\left(\phi_i^{\mathbf{u}}, \phi_j^\mu\Delta\phi_k^{\mathbf{u}}\right). \tag{3.45d}$$

The separation in two elements of the viscosity term allows to quickly analyze their influence on the model. Three model definitions are considered: one implementing the entire viscosity term, so with both elements, one keeping only the Laplacian term and putting the symmetric gradient equal to zero, and one without the entire viscosity term. The models are called, respectively, *Visc*, *LaplVisc*, and *NoVisc*.

Numerical Results. The problem under study remains the flow past a cylinder, with the introduction of two distinct fluids, separated by an interface. Throughout the domain, the density remains constant to the value $\rho = 1000\,\mathrm{kg/m^3}$, whereas the viscosity varies, thus altering the Reynolds number. The analysis comprises two cases, merged to the model definitions based on the viscosity term, one named *LoRe* because characterized by lower Reynolds numbers with respect to the other case, termed *HiRe*. For each case, specific weighing coefficients for pressure and viscosity variables are defined. To ensure comparability, the number of retained modes is fixed at $N_r = 10$, although the resulting RIC varies slightly, remaining above 99% in both scenarios. The key attributes of the two cases are summarized in Table 3.3.

	LoRe	*HiRe*
μ_l ($\mathrm{m^2/s}$)	1	10^{-3}
μ_h ($\mathrm{m^2/s}$)	5	1
Re_l	10^3	10^6
Re_h	200	10^3
Q_p	10^{-5}	10^{-5}
Q_μ	$1/5$	1
N_r	10	10
RIC (%)	99.72	99.07

Table 3.3 Fluid characteristics and model parameters for the two flow cases analyzed, *LoRe* and *HiRe*.

To have an idea of the free surface evolution, a spatial representation of the VOF field (though not considered as variable in the model), at two different times during the simulation, is depicted in Figure 3.19, for the case *LoRe*. Remarkably, the Karman street presence influences the interface between the two fluids, that, having the same density, strongly mix and yield a highly oscillating wake in the lee of the cylinder.

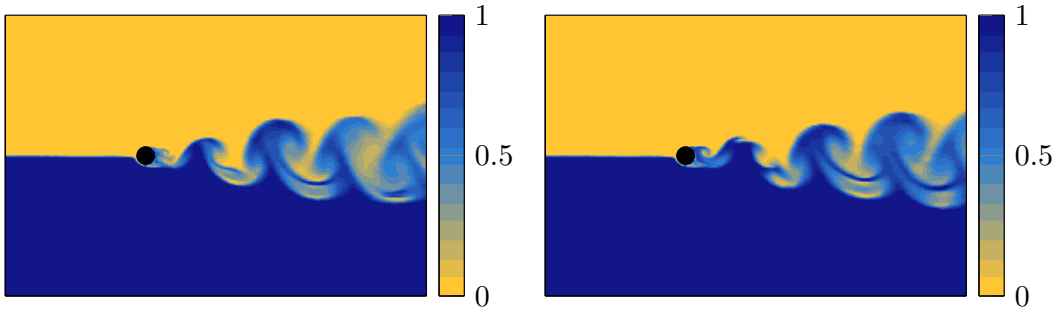

(a) Snapshot at $T = 95\,\text{s}$. (b) Snapshot at $T = 100\,\text{s}$.

Fig. 3.19 Snapshots of the VOF field on a $x-y$ section for the cylinder in the biphase flow with same density and different dynamic viscosity (case *LoRe*).

Nonetheless, the phenomenon retains a periodic nature, as evinced by the first four temporal coefficients plotted in Figures 3.20, 3.21. These figures juxtapose the projection coefficients, as a reference, with the coefficients obtained from the ROM model, for all the cases considered, with different viscosity terms and Reynolds numbers. In the *LoRe* case (Figure 3.20), where the difference between the two fluids is minimal, the variance in the first temporal coefficients for the different viscosity terms is subtle. A slight difference is visible for the smaller amplitude coefficients, a_3 and a_4, where dissipation is less pronounced, resulting in slight phase shift in peaks and troughs, that amplify with time. This behavior is intuitive, recalling that these smaller coefficients primarily drive dissipation. When the viscosity term is absent (model *NoVisc*), coefficients tend to diverge more readily due to the lack of dissipation. As soon as at least one viscosity term is included in the model, this trend relaxes. This effect is more evident in case *HiRe* (Figure 3.21), where the discrepancy between fluids intensifies. Here, the coefficients have higher amplitude and higher frequency than the projection coefficients.

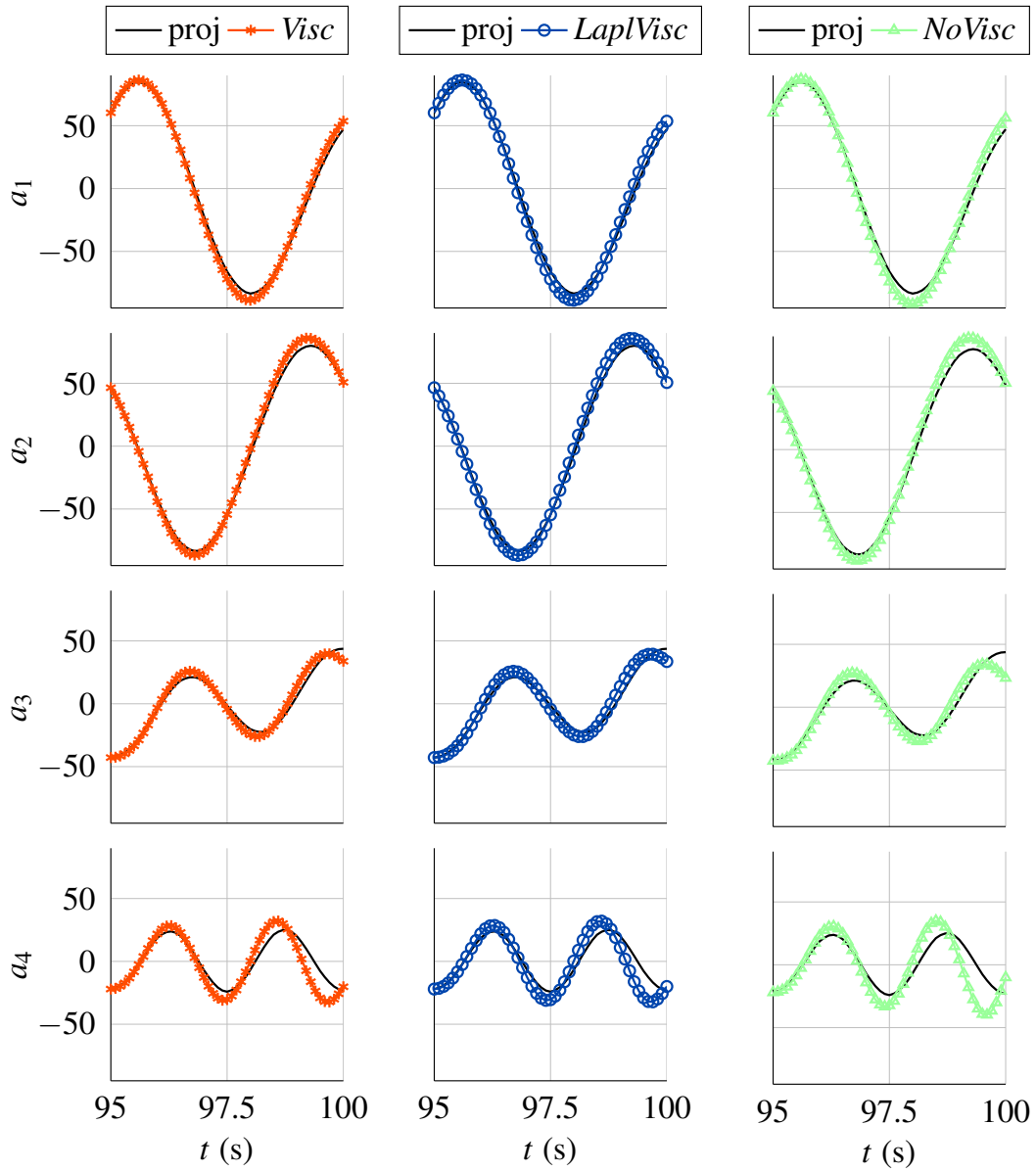

Fig. 3.20 Evolution of the first four projection and model coefficients for the flow case *LoRe*. The three models, *Visc*, *LaplVisc*, and *NoVisc* are compared.

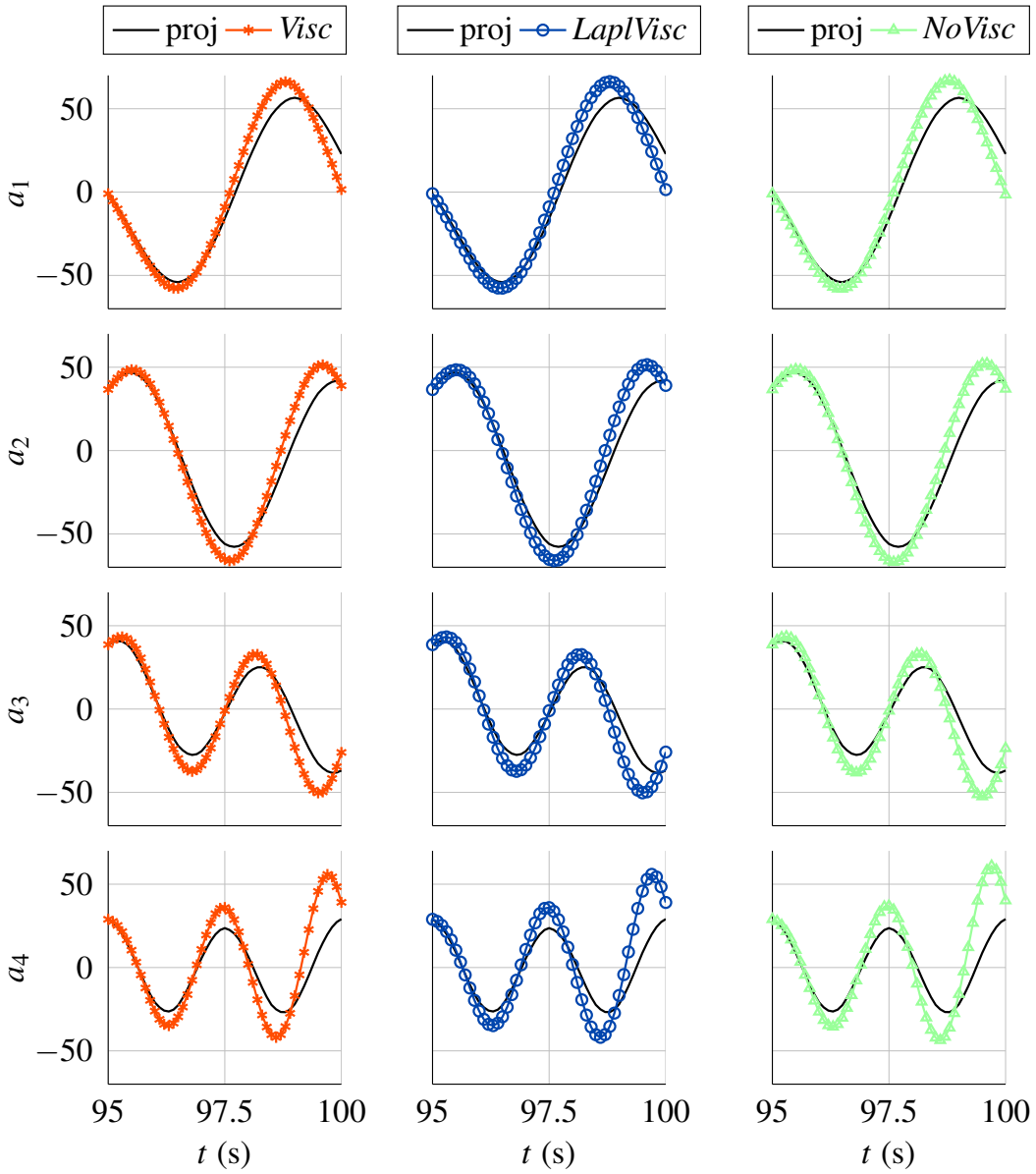

Fig. 3.21 Evolution of the first four projection and model coefficients for the flow case *HiRe*. The three models, *Visc*, *LaplVisc*, and *NoVisc* are compared.

However, the inclusion or exclusion of viscosity in the model appears to have a minor impact, as reflected in the relative errors presented in Table 3.4, where the last column (*NoVisc*) shows slightly larger errors.

	Error	Model		
		Visc	*LaplVisc*	*NoVisc*
LoRe	$\bar{\varepsilon}^u$	2.31e-4	2.33e-4	3.55e-4
	$\bar{\varepsilon}^v$	3.40e-3	3.43e-3	5.28e-3
	$\bar{\varepsilon}^w$	9.58e-3	9.68e-3	1.50e-2
	$\bar{\varepsilon}^p$	7.62e-6	7.66e-6	1.09e-5
	$\bar{\varepsilon}^\mu$	7.29e-4	7.35e-4	1.12e-3
HiRe	$\bar{\varepsilon}^u$	5.35e-4	5.35e-4	6.03e-4
	$\bar{\varepsilon}^v$	9.35e-3	9.35e-3	1.05e-2
	$\bar{\varepsilon}^w$	1.92e-2	1.91e-2	2.17e-2
	$\bar{\varepsilon}^p$	4.35e-6	4.35e-6	4.90e-6
	$\bar{\varepsilon}^\mu$	1.29e-3	1.29e-3	1.45e-3

Table 3.4 Relative errors for the velocity, pressure, and viscosity variables, in both flow cases. The errors for the model accounting for the entire viscosity term (*Visc*), only the Laplacian part (*LaplVisc*), and without viscosity term (*NoVisc*), are compared.

This marginal difference may stem from the similarity of the two fluids, as the densities are identical. Consequently, when dealing with two substantially different fluids, the combined contribution of viscosity and density could exacerbate the divergence from the *Visc/LaplVisc* models. Comparing *Visc* and *LaplVisc*, as the discrepancy between fluids increases, model outputs tend to converge. More clearly, the errors for both *LoRe* and *HiRe* remain largely consistent regardless of whether the symmetric gradient is considered or not (see absolute errors in Figure 3.22).

Examining the viscosity term (Eq. 3.42), some remarks may be suggested. The separation of the viscosity term into two elements allows to analyze their different impacts on the model, and on the problem overall. The Laplacian term, which involves the second derivative of velocity, represents the difference between the velocity at a point and the mean velocity in a small surrounding volume, regarding viscosity as momentum diffusion. The symmetric gradient term is the product of two components: a term representing viscosity jump and another representing the velocity jump. While the jump in viscosity may be significant, it predominantly

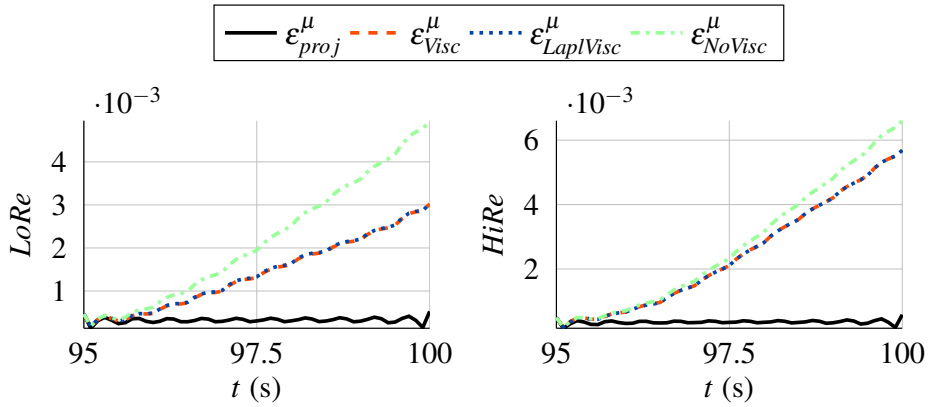

Fig. 3.22 Evolution of the absolute error on μ, for the different cases, compared to the projection error.

occurs at the fluid interface, which constitutes a small portion of the entire domain. Furthermore, abrupt velocity variations are unlikely in incompressible fluids, leading to potentially small overall values. Therefore, such multiplication may result very small, supporting its exclusion from the ROM model.

In any case, this analysis suggests an asymptotic reduction of the reduced-order model, a concept that will be verified afterwards also for cases with different viscosity *and* density.

To assess the reduction in computational workload, the comparison focuses on the time needed to compute tensors **L**, **A**, **B**, **C**, and **D** when present, across the models. The comprehensive *Visc* model demands 17 minutes for these calculations, primarily due to the computational intensity of the fourth-order tensor. In contrast, the *LaplVisc* and *NoVisc* models only require a little over 2 minutes and 1 minute, respectively. Additionally, a slight difference is noticeable in the temporal integration of the dynamical system, with the complete model taking 43 seconds, compared to 35 seconds for the other two models.

3.4.2 Interface

The interface between the two fluids, regardless of it being flat or wavy, mainly spans the horizontal direction, according to the employed reference system. However, its vertical position may also affect the ROM model, as it demarcates specifics volumes for each fluid. For instance, when the interface lies close to the top boundary of

the domain, the heavy fluid predominates, filling most of the domain and exerting a considerable influence on the model. Conversely, positioning the interface close to the bottom boundary favors the amount of light fluid. A balance between the two fluids is achieved as long as the interface is around the midpoint of the domain. Given the different dynamics within each fluid, related to their respective Reynolds numbers, the focus of this section is to examine the impact of varying interface positions. The simulation domain remains unaltered, albeit the two fluids, owning different values for both viscosity and density, being separated by an interface of varying position, and yielding to the cases depicted in Figure 3.23.

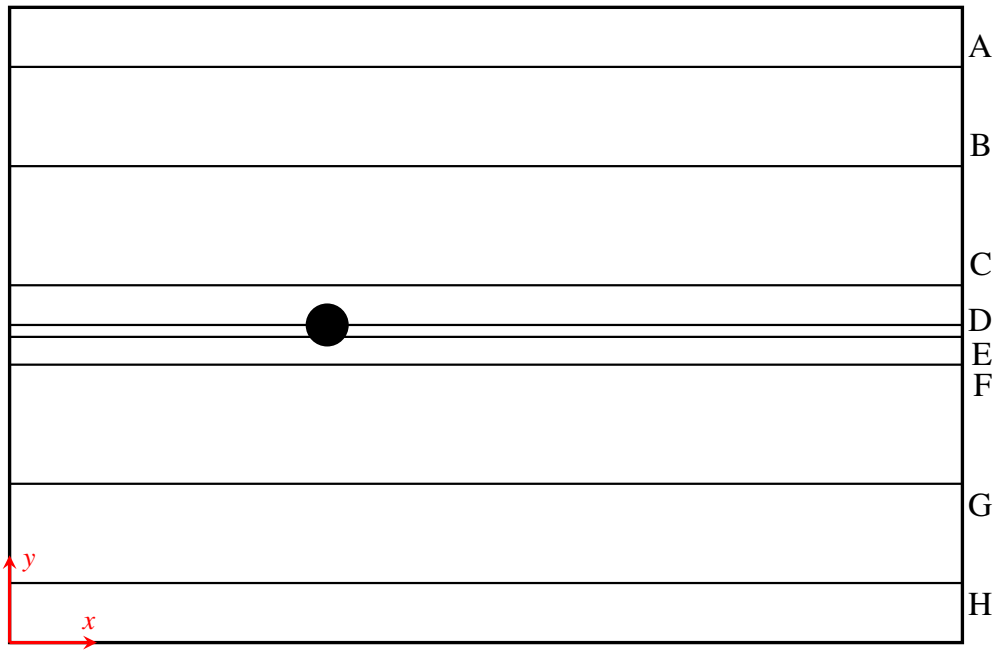

Fig. 3.23 Sketch of the positions of the fluid interface Γ_f yielding the different simulated cases.

The ROM model in the asymptotic reduction form (*LaplVisc*) is used for these tests, so the viscosity is present in the Laplacian term. The variable matrix is defined as follows:

$$\mathbf{U} = \begin{pmatrix} \mathbf{u} = \begin{pmatrix} u \\ v \\ w \end{pmatrix} \\ Q_p \quad p \\ Q_{1/\rho} \quad \frac{1}{\rho} \\ Q_{\mu/\rho} \quad \frac{\mu}{\rho} \end{pmatrix}, \tag{3.46}$$

where the density is also considered. The dynamical system is the same as in Eq. (3.30), with the following expressions for the contributing tensors:

$$L_{ij} = +\left(\phi_i^{\mathbf{u}}, \phi_j^{\mathbf{u}}\right) \tag{3.47a}$$

$$A_i = -\left(\phi_i^{\mathbf{u}}, (\bar{\mathbf{u}}\cdot\nabla)\bar{\mathbf{u}}\right) - \left(\phi_i^{\mathbf{u}}, \frac{1}{\bar{\rho}}\nabla\bar{p}\right) + \left(\phi_i^{\mathbf{u}}, \frac{\bar{\mu}}{\bar{\rho}}\Delta\bar{\mathbf{u}}\right) + \left(\phi_i^{\mathbf{u}}, \mathbf{g}\right) \tag{3.47b}$$

$$\begin{aligned} B_{ij} = &-\left(\phi_i^{\mathbf{u}}, (\bar{\mathbf{u}}\cdot\nabla)\phi_j^{\mathbf{u}}\right) - \left(\phi_i^{\mathbf{u}}, (\phi_j^{\mathbf{u}}\cdot\nabla)\bar{\mathbf{u}}\right) - \left(\phi_i^{\mathbf{u}}, \frac{1}{\bar{\rho}}\nabla\phi_j^{p}\right) + \\ &- \left(\phi_i^{\mathbf{u}}, \phi_j^{1/\rho}\nabla\bar{p}\right) + \left(\phi_i^{\mathbf{u}}, \frac{\bar{\mu}}{\bar{\rho}}\Delta\phi_j^{\mathbf{u}}\right) + \left(\phi_i^{\mathbf{u}}, \phi_j^{\mu/\rho}\Delta\bar{\mathbf{u}}\right) \end{aligned} \tag{3.47c}$$

$$C_{ijk} = -\left(\phi_i^{\mathbf{u}}, (\phi_j^{\mathbf{u}}\cdot\nabla)\phi_k^{\mathbf{u}}\right) - \left(\phi_i^{\mathbf{u}}, \phi_j^{1/\rho}\nabla\phi_k^{p}\right) + \left(\phi_i^{\mathbf{u}}, \phi_j^{\mu/\rho}\Delta\phi_k^{\mathbf{u}}\right). \tag{3.47d}$$

For the numerical implementation, a summary of the main parameters is listed in Table 3.5. The modes are truncated at the same N_r for all the cases, yielding slightly different RICs, but always RIC $> 99\%$.

μ_l (m^2/s)	1.5×10^{-3}
μ_h (m^2/s)	1
ρ_l (kg/m^3)	100
ρ_h (kg/m^3)	1000
Re_l	6.7×10^4
Re_h	10^3
Q_p	10^{-5}
$Q_{1/\rho}$	10^2
$Q_{\mu/\rho}$	1
N_r	12
RIC (%)	A: 99.81 B: 99.78 C: 99.56 D: 99.36 E: 99.17 F: 99.03 G: 99.36 H: 99.31

Table 3.5 Fluid characteristics and model parameters analyzed, for different positions of the interface.

In the following, the first temporal coefficients computed with the ROM model are plotted against the projection coefficients, for the several cases analyzed, organized symmetrically based on the interface position. The main information conveyed by Figures 3.24,3.25 is that as the volume of heavy fluid (where a lower Reynolds number is present) decreases, the stability of the ROM model tends to degrade.

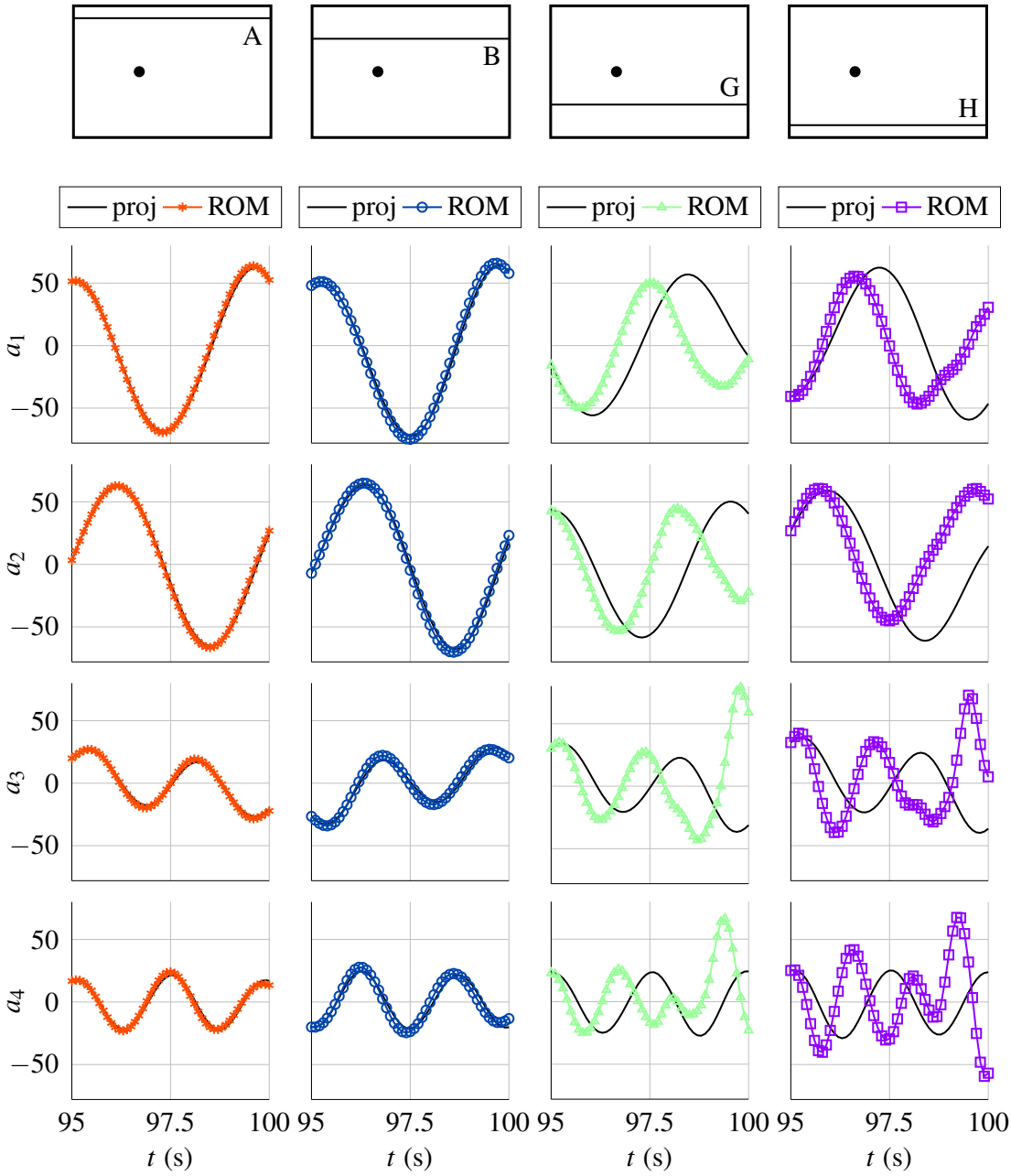

Fig. 3.24 Evolution of the first four projection and ROM coefficients for cases A, B, G, and H, for which the interface is situated at the greatest distance from the cylinder.

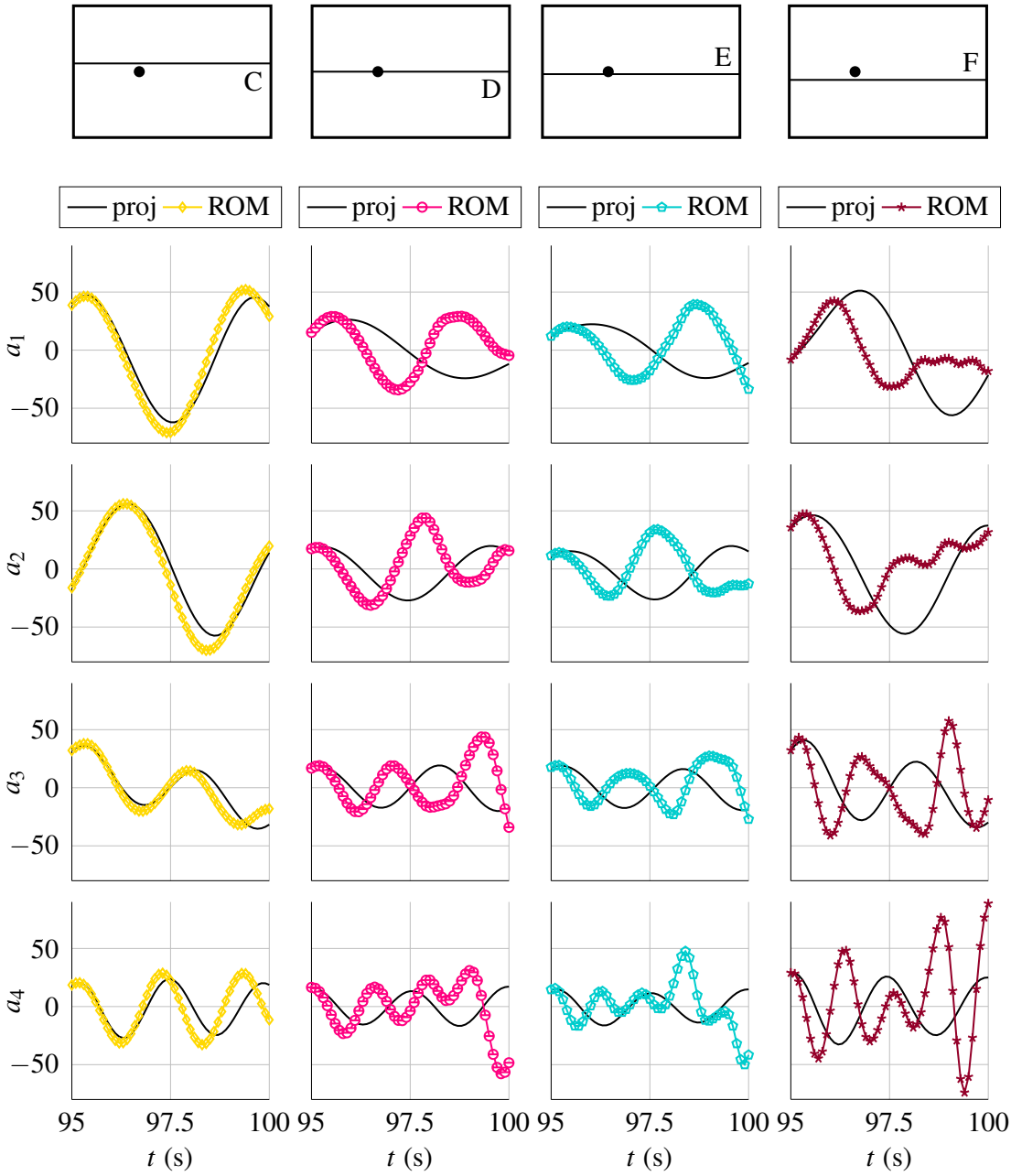

Fig. 3.25 Evolution of the first four projection and ROM coefficients for cases C, D, E, and F, for which the interface is situated close to the cylinder.

The predicted temporal coefficients progressively deviate from the projection coefficients, including the most energetic ones. With the exception of cases D and E, the dynamics behind the cylinder predominantly reside within one fluid. The dynamics and the form of the temporal coefficients vary across cases, evidenced by non-coincident crests and troughs (e.g., comparing a_1 between cases A and H). When the interface approaches the middle of the domain, the wake dynamics is disturbed by the presence of both fluids, with very different characteristics. Cases D and E exhibit similar dynamics, despite the lack of symmetry of case E, resulting in a comparable behavior of the ROM model. In general, the dynamics are inadequately reproduced, with the predicted coefficients having different frequencies with respect to the projection coefficients, and tending towards instability with significant amplitudes.

The error plots in Figure 3.26 do not give a general trend across all variables. Velocity and pressure errors generally escalate as the interface transitions from the top of the domain to the bottom. This result underscores the substantial influence of the heavy fluid volume on the model, despite cases G and H displaying temporal coefficients that closely resemble the target form, compared to cases D and E. However, $\bar{\varepsilon}^{1/\rho}$ and $\bar{\varepsilon}^{\mu/\rho}$ are smaller when the interface is distant from the cylinder, in either direction (cases A, B, G, and H). The interface remains relatively stationary, even for disturbed flows in the lee of the cylinder, potentially due to the substantial difference in the fluids, which prevents the interface from deviating from the flat line. Another possibility for this behavior is related to the cylinder intersecting the interface. Point-by-point differences, during error computation, may introduce inaccuracies around the body, absent when the interface is farther from the cylinder, and generally increasing the errors. Among all cases, case F stands out as the one with the biggest mean errors for almost all variables. Also the right-hand side of Figure 3.25 shows the worst coefficients among all cases analyzed, with a_1 and a_2 losing periodicity after a few seconds.

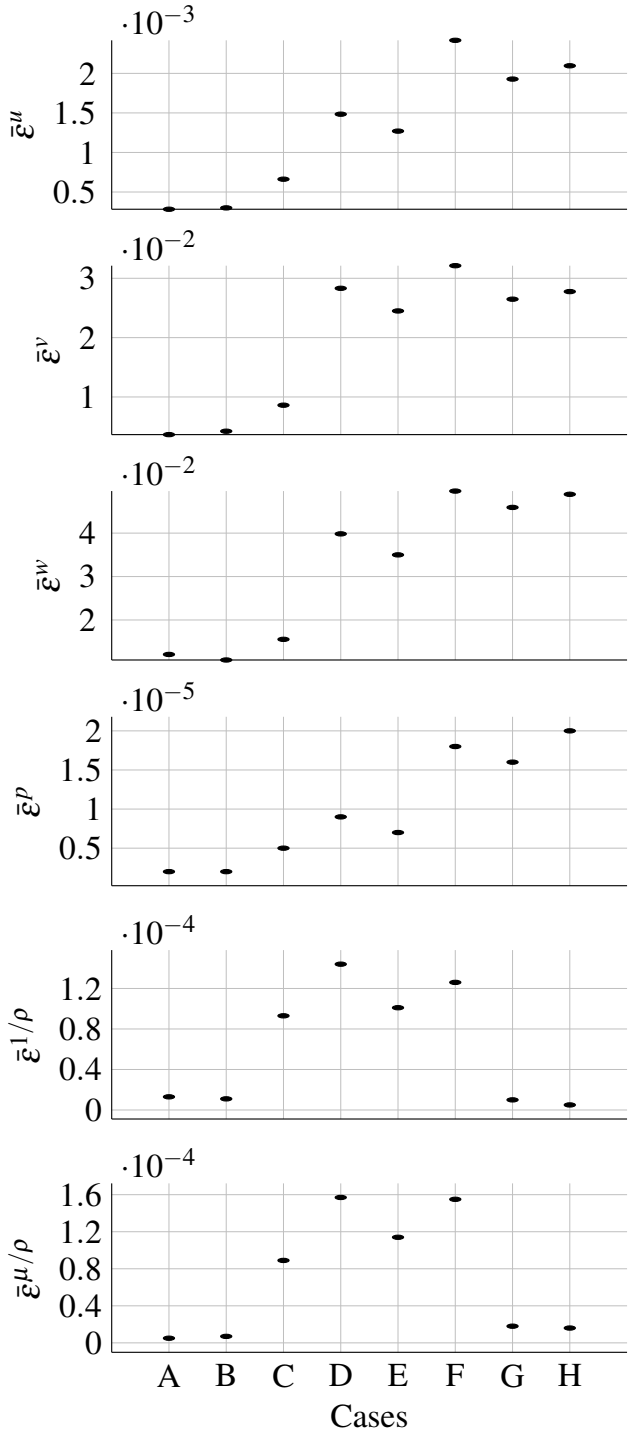

Fig. 3.26 Visual representation of the relative errors for the velocity, pressure, density and viscosity variables, of all the cases analyzed.

The analysis conducted in this section shows the strong influence of the interface position within the domain on the fidelity of the ROM model. Considering the ultimate objective, the simulation of a floating body, some hypotheses might be suggested. In such scenarios, a floating body, with the interface similar to case E, is expected. However, given the disparity in water and air volumes, with the primary interest lying in free surface evolution, body and mooring system forces, considerations typically favor the limitation of the air domain. As a consequence, cases resembling A and B are anticipated. Nonetheless, real-case scenarios entail high Reynolds numbers, a wavy interface, a moving body, an incoming velocity $\mathbf{u}_0$ not confined solely to the horizontal direction.

3.4.3 Density and Pressure Term

The ROM models used in the preceding sections all define the pressure in the variable matrix as a scalar, possibly with a weighing coefficient. However, as pointed out in Section 3.3.1, the pressure is mainly dominated by its static component, suggesting that an alternative form, such as the pressure gradient, may offer a more appropriate description of an evolving flow. In addition, for biphase flows, the density assumes significance as a variable, interlinked with pressure, viscosity and velocity terms in the Navier-Stokes equations. Using the asymptotically reduced version of the ROM model, the variable μ/ρ can be defined. Regarding the pressure term, various options exist, separating or combining pressure and density. In general, the variable matrix may contain diverse variables, in different forms and combinations. One could then introduce space derivatives or even time derivatives of the snapshots, with the result of getting different weights in the correlation and thus different modes [174].

In this study, different models are explored, based on those considerations. The first model, *P*, corresponds to the one used in the previous section, with all the variables separated. Model *gradP* incorporates the gradient of the pressure, in the three dimensions, in the variable matrix, while model *DgradP* combines the pressure gradient and the density together. An overview of those models, in terms of the variable and modes matrices, is provided in Table 3.6.

Model	Variable matrix	Basis functions matrix
P	$\mathbf{U} = \begin{pmatrix} \mathbf{u} = \begin{pmatrix} u \\ v \\ w \end{pmatrix} \\ Q_p \quad p \\ Q_{1/\rho} \ \frac{1}{\rho} \\ Q_{\mu/\rho} \ \frac{\mu}{\rho} \end{pmatrix}$	$\Phi = \begin{pmatrix} \boldsymbol{\phi}^{\mathbf{u}} = \begin{pmatrix} \boldsymbol{\phi}^{u} \\ \boldsymbol{\phi}^{v} \\ \boldsymbol{\phi}^{w} \end{pmatrix} \\ \boldsymbol{\phi}^{p} \\ \boldsymbol{\phi}^{\frac{1}{\rho}} \\ \boldsymbol{\phi}^{\frac{\mu}{\rho}} \end{pmatrix}$
gradP	$\mathbf{U} = \begin{pmatrix} \mathbf{u} = \begin{pmatrix} u \\ v \\ w \end{pmatrix} \\ Q_p \ \nabla p = \begin{pmatrix} \partial_x p \\ \partial_y p \\ \partial_z p \end{pmatrix} \\ Q_{1/\rho} \ \frac{1}{\rho} \\ Q_{\mu/\rho} \ \frac{\mu}{\rho} \end{pmatrix}$	$\Phi = \begin{pmatrix} \boldsymbol{\phi}^{\mathbf{u}} = \begin{pmatrix} \boldsymbol{\phi}^{u} \\ \boldsymbol{\phi}^{v} \\ \boldsymbol{\phi}^{w} \end{pmatrix} \\ \boldsymbol{\phi}^{\mathbf{p}} = \begin{pmatrix} \boldsymbol{\phi}^{px} \\ \boldsymbol{\phi}^{py} \\ \boldsymbol{\phi}^{pz} \end{pmatrix} \\ \boldsymbol{\phi}^{\frac{1}{\rho}} \\ \boldsymbol{\phi}^{\frac{\mu}{\rho}} \end{pmatrix}$
DgradP	$\mathbf{U} = \begin{pmatrix} \mathbf{u} = \begin{pmatrix} u \\ v \\ w \end{pmatrix} \\ Q_p \ \frac{1}{\rho}\nabla p = \begin{pmatrix} \frac{1}{\rho}\partial_x p \\ \frac{1}{\rho}\partial_y p \\ \frac{1}{\rho}\partial_z p \end{pmatrix} \\ Q_{\mu/\rho} \ \frac{\mu}{\rho} \end{pmatrix}$	$\Phi = \begin{pmatrix} \boldsymbol{\phi}^{\mathbf{u}} = \begin{pmatrix} \boldsymbol{\phi}^{u} \\ \boldsymbol{\phi}^{v} \\ \boldsymbol{\phi}^{w} \end{pmatrix} \\ \boldsymbol{\phi}^{\mathbf{p}/\boldsymbol{\rho}} = \begin{pmatrix} \boldsymbol{\phi}^{\frac{px}{\rho}} \\ \boldsymbol{\phi}^{\frac{py}{\rho}} \\ \boldsymbol{\phi}^{\frac{pz}{\rho}} \end{pmatrix} \\ \boldsymbol{\phi}^{\frac{\mu}{\rho}} \end{pmatrix}$

Table 3.6 Definition of the variable matrix and modes matrix for the different defined models.

The resulting dynamical system remains unchanged, as in Eq. (3.30), with slitghly different expressions for the tensors. For model *P*, the expressions in Eq. (3.47a)-(3.47d) hold. For model *gradP*, the main change is the direct expression of the basis functions on the pressure instead of their gradient. Hence, they become:

$$L_{ij} = +\left(\phi_i^{\mathbf{u}}, \phi_j^{\mathbf{u}}\right) \tag{3.48a}$$

$$A_i = -\left(\phi_i^{\mathbf{u}}, (\bar{\mathbf{u}}\cdot\nabla)\bar{\mathbf{u}}\right) - \left(\phi_i^{\mathbf{u}}, \frac{1}{\bar{\rho}}\nabla\bar{p}\right) + \left(\phi_i^{\mathbf{u}}, \frac{\bar{\mu}}{\bar{\rho}}\Delta\bar{\mathbf{u}}\right) + \left(\phi_i^{\mathbf{u}}, \mathbf{g}\right) \tag{3.48b}$$

$$\begin{aligned} B_{ij} = &-\left(\phi_i^{\mathbf{u}}, (\bar{\mathbf{u}}\cdot\nabla)\phi_j^{\mathbf{u}}\right) - \left(\phi_i^{\mathbf{u}}, (\phi_j^{\mathbf{u}}\cdot\nabla)\bar{\mathbf{u}}\right) - \left(\phi_i^{\mathbf{u}}, \frac{1}{\bar{\rho}}\phi_j^{\mathbf{p}}\right) - \left(\phi_i^{\mathbf{u}}, \phi_j^{1/\rho}\nabla\bar{p}\right) + \\ &+ \left(\phi_i^{\mathbf{u}}, \frac{\bar{\mu}}{\bar{\rho}}\Delta\phi_j^{\mathbf{u}}\right) + \left(\phi_i^{\mathbf{u}}, \phi_j^{\mu/\rho}\Delta\bar{\mathbf{u}}\right) \end{aligned} \tag{3.48c}$$

$$C_{ijk} = -\left(\phi_i^{\mathbf{u}}, (\phi_j^{\mathbf{u}}\cdot\nabla)\phi_k^{\mathbf{u}}\right) - \left(\phi_i^{\mathbf{u}}, \phi_j^{1/\rho}\phi_k^{\mathbf{p}}\right) + \left(\phi_i^{\mathbf{u}}, \phi_j^{\mu/\rho}\Delta\phi_k^{\mathbf{u}}\right). \tag{3.48d}$$

Finally, for model *DgradP*, the tensors are:

$$L_{ij} = +\left(\phi_i^{\mathbf{u}}, \phi_j^{\mathbf{u}}\right) \tag{3.49a}$$

$$A_i = -\left(\phi_i^{\mathbf{u}}, (\bar{\mathbf{u}}\cdot\nabla)\bar{\mathbf{u}}\right) - \left(\phi_i^{\mathbf{u}}, \nabla\frac{\bar{p}}{\bar{\rho}}\right) + \left(\phi_i^{\mathbf{u}}, \frac{\bar{\mu}}{\bar{\rho}}\Delta\bar{\mathbf{u}}\right) + \left(\phi_i^{\mathbf{u}}, \mathbf{g}\right) \tag{3.49b}$$

$$\begin{aligned} B_{ij} = &-\left(\phi_i^{\mathbf{u}}, (\bar{\mathbf{u}}\cdot\nabla)\phi_j^{\mathbf{u}}\right) - \left(\phi_i^{\mathbf{u}}, (\phi_j^{\mathbf{u}}\cdot\nabla)\bar{\mathbf{u}}\right) - \left(\phi_i^{\mathbf{u}}, \phi_j^{\mathbf{p}/\boldsymbol{\rho}}\right) \\ &+ \left(\phi_i^{\mathbf{u}}, \frac{\bar{\mu}}{\bar{\rho}}\Delta\phi_j^{\mathbf{u}}\right) + \left(\phi_i^{\mathbf{u}}, \phi_j^{\mu/\rho}\Delta\bar{\mathbf{u}}\right) \end{aligned} \tag{3.49c}$$

$$C_{ijk} = -\left(\phi_i^{\mathbf{u}}, (\phi_j^{\mathbf{u}}\cdot\nabla)\phi_k^{\mathbf{u}}\right) + \left(\phi_i^{\mathbf{u}}, \phi_j^{\mu/\rho}\Delta\phi_k^{\mathbf{u}}\right). \tag{3.49d}$$

Numerical Results

Considering the configuration outlined in case C of Section 3.4.2, with the fluid characteristics listed in Table 3.5, the snapshots are used to build three different ROM models, for the three definitions of the variable matrix proposed. Case C is chosen as a balanced compromise between a relatively equal volume of the two phases and a minimally disruptive interface position, ensuring that the dynamics around the cylinder remain almost undisturbed. Since the variable matrices are

different, and different is the information correlated to build the basis functions, each model inherently carries different information content. For the sake of comparison, truncation is at $N_r = 15$, resulting in nearly identical values of the RIC (see Table 3.7).

	Case P	Case *gradP*	Case *DgradP*
Q_p	10^{-5}	10^{-4}	10^{-1}
$Q_{1/\rho}$	10^2	10^2	-
$Q_{\mu/\rho}$	10^3	10^3	10^3
N_r	15	15	15
RIC (%)	99.87	99.88	99.91

Table 3.7 Fluid characteristics and parameters for the different models.

In this section, alongside the quantitative comparison of the relative errors (Table 3.8), a qualitative assessment of the temporal coefficients (Figure 3.27) is favored for its simplicity.

Variable	Error	Case		
		P	*gradP*	*DgradP*
Velocity	$\bar{\varepsilon}^u$	6.62e-4	4.86e-4	4.94e-4
	$\bar{\varepsilon}^v$	8.61e-3	7.11e-3	6.49e-3
	$\bar{\varepsilon}^w$	1.55e-2	1.12e-2	1.35e-2
Pressure	$\bar{\varepsilon}^p$	5.34e-6	-	-
	$\bar{\varepsilon}^{\partial_x p}$	-	6.47e-3	-
	$\bar{\varepsilon}^{\partial_y p}$	-	1.61e-4	-
	$\bar{\varepsilon}^{\partial_z p}$	-	8.24e-3	-
	$\bar{\varepsilon}^{\frac{1}{\rho}\partial_x p}$	-	-	5.01e-3
	$\bar{\varepsilon}^{\frac{1}{\rho}\partial_y p}$	-	-	1.96e-4
	$\bar{\varepsilon}^{\frac{1}{\rho}\partial_z p}$	-	-	2.88e-3
Density	$\bar{\varepsilon}^{1/\rho}$	9.28e-5	6.84e-5	-
Viscosity	$\bar{\varepsilon}^{\mu/\rho}$	8.93e-5	7.55e-5	6.40e-5

Table 3.8 Relative errors for the velocity, pressure, density and viscosity variables, in the form analyzed for each model.

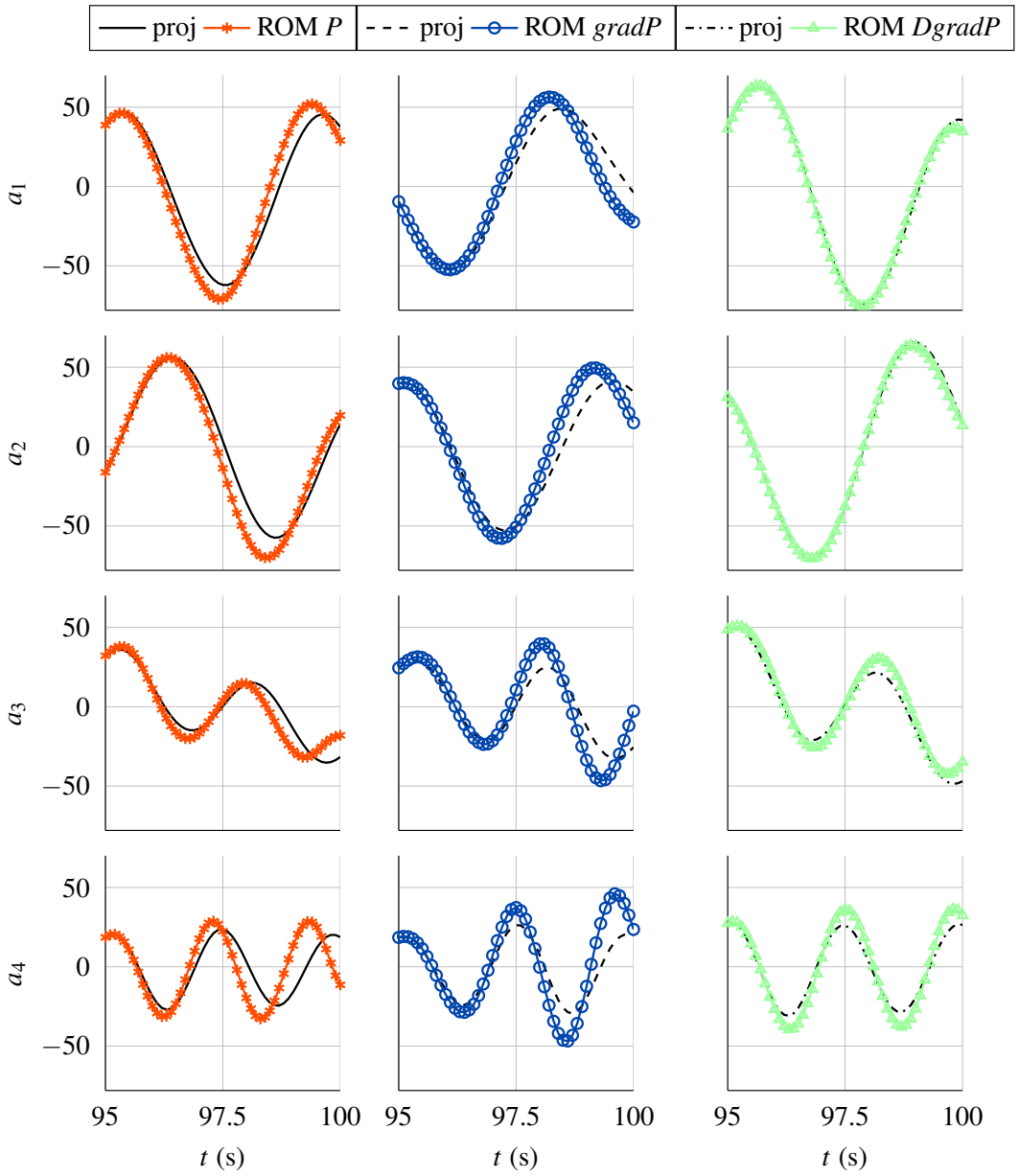

Fig. 3.27 Evolution of the first four projection and ROM coefficients for models *P*, *gradP*, and *DgradP*.

The results show that using the pressure gradient with the density, as in the *DgradP* model, facilitates the accurate reproduction of the temporal coefficients, with minor amplitude discrepancies from the projection coefficients emerging from a_3 onward, and minimal discrepancy in frequency. Conversely, the other two models exhibit reduced accuracy in both amplitude and frequency, evident as early as a_1. However, the errors are generally comparable, although the *P* model gives small errors for the pressure mainly because of the small Q_p value.

Even if the pressure gradient appears more suited for inclusion in the variable matrix, it poses greater complexity as a standalone variable. During the production of the snapshots, the pressure gradient can be stored rather than simply the pressure, or alternatively, the gradient can be calculated a posteriori, independently of the high-fidelity simulation. However, integrating the gradient into a ROM model renders the reconstruction cumbersome for the scalar pressure value, as is typically a preferred output. If, however, the values of the pressure are regarded merely as supplementary information, potentially enhancing the ROM model, this dilemma is avoided.

3.4.4 POD-ROM Instability

Up to this point in the document, the chosen phases for the analysis are fictitious, featuring density and viscosity values that differ significantly, but not excessively, and aligning with, or approaching, real-world Reynolds numbers. However, the final objective is the numerical simulation of real fluids, particularly water and air. These two fluids are very different, with characteristics spanning several orders of magnitude. As a result, the ROM model is expected to behave less efficiently than for the previous cases, likely requiring more modes for an accurate approximation of the variables.

Considering the key parameters for water and air listed in Table 3.9, taking $N_r = 15$ yields a very high RIC. Nevertheless, the free surface, until this point, remains static, as the water is too dense to be influenced by the wake of the cylinder (see the snapshot in Figure 3.28). Despite this, constructing the ROM model is feasible, but executing it becomes problematic. The dynamical system to solve for $\mathbf{a}$ becomes highly unstable, leading to rapid divergence after only a few initial iterations. Adjusting the time step or changing the temporal scheme has no effect on the execution stability [175]. Additionally, using either the asymptotically reduced

μ_a (m^2/s)	1.803×10^{-5}
μ_w (m^2/s)	1.14×10^{-3}
ρ_a (kg/m^3)	1.2
ρ_w (kg/m^3)	1025
Re_a	6.66×10^4
Re_w	8.99×10^5
Q_p	10^{-5}
$Q_{1/\rho}$	1
$Q_{\mu/\rho}$	10^3
N_r	15
RIC (%)	99.68

Table 3.9 Fluid characteristics and model parameters for the water/air tested case.

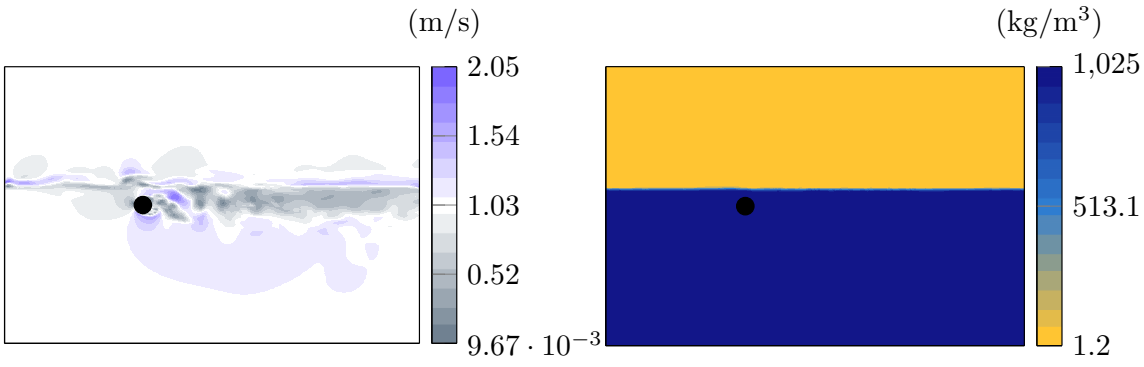

(a) FOM velocity field.

(b) FOM density field.

Fig. 3.28 Snapshot of the FOM velocity and density fields, at $T = 98\,\mathrm{s}$.

ROM, or the complete ROM, yields similar outcomes. The problem is, thus, dig further, changing the test case to accommodate for a moving interface.

Free Wave Test

To have an example that better resembles the simulation of a wave, a different simulation may be tested. Drawing inspiration from the well-known dam break test, an asymmetric initial condition is defined, and allows the free surface to evolve under the influence of gravity, without any body nor wave forcing. The result is a traveling wave, albeit less steep than the wave typically created after the dam break. This approach ensures that the interface between the two phases is evolving without complicated phenomena, such as breaking waves and recirculation.

In this new setup, the simulation domain $\Omega_{HF} = \Omega$ has now size $[L_x \times L_y \times L_z] = [10 \times 6 \times 0.4]$m. The initial position of the water-air interface, Γ_f, is analytically defined by

$$\Gamma_f^0 = H_w e^{-\frac{1}{2}\left(x+\frac{3}{2}y\right)^2} + H_s, \tag{3.50}$$

where the parameter H_w defines the height of the initial wave relative to the sea level H_s, at $x \to \pm\infty$. H_s can be adjusted to reach a desired water volume in the computational domain, but is set to $H_s = 0\,\text{m}$ for the moment. Similarly, the initial condition is set to $H_w = 0.6\,\text{m}$ to obtain a smooth wave (see Figure 3.29).

No-slip boundary conditions, $\mathbf{u} = [0,0,0]\text{m/s}$, are now imposed at the inlet (Γ_{inlet}), outlet (Γ_{outlet}), bottom (Γ_{bottom}), and top (Γ_{top}) boundaries. The front and back boundaries, Γ_{front} and Γ_{back} (not represented in Figure 3.29), remain symmetry planes, as before, to maintain the computational domain small. The spatial discretization and the temporal discretization schemes remain consistent with the previous simulations. The snapshots are exported on a homogeneous Cartesian mesh with $\Delta\mathbf{x} = 0.05\,\text{m}$, at multiples of the simulation time step, $\Delta t = 0.002\,\text{s}$. The simulation duration spans only $t = [0,3]\text{s}$, as, beyond that time, the free surface stabilizes and reaches an equilibrium position. This evolution differentiates the test from the flow past a cylinder case, because, here, the focus is on reproducing the transitional phase, with no expectation of any periodicity in the solution.

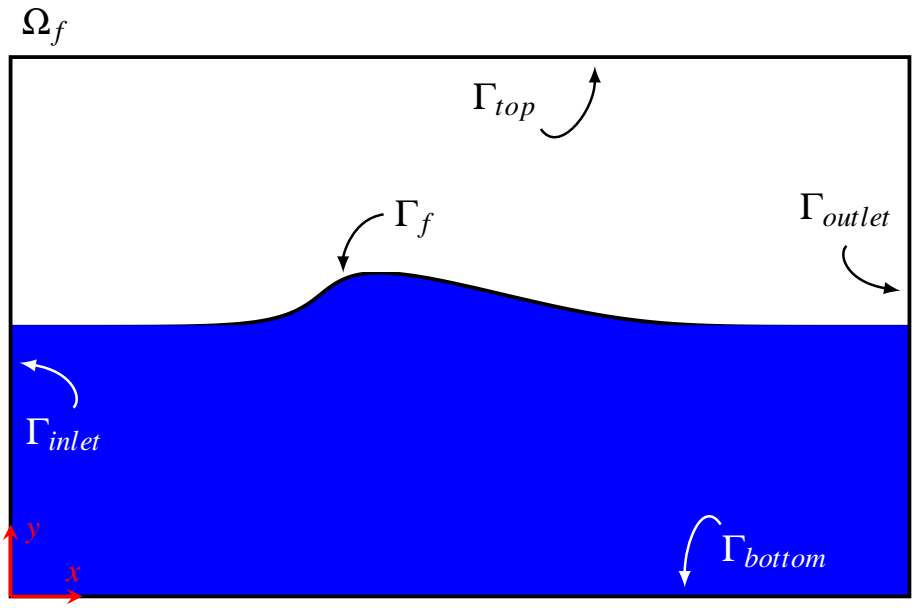

Fig. 3.29 Sketch of the flow configuration of the free wave test, and definition of the boundaries. The initial condition (Eq. (3.50)) for $H_w = 0.6\,\text{m}$ and $H_s = 0\,\text{m}$ is plotted. The front and back boundaries are not visible, but present in the three-dimensional simulation.

Correction Term

Similar to the monofluid case discussed in Section 3.3.2, a possible explanation for the instability of the ROM model may be related to inadequate dissipation. In the case of multiple flows, this issue could be exacerbated due to the complexity introduced by the interaction between different phases, potentially resulting in insufficient dissipation to prevent the uncontrolled growth of the temporal coefficients and their frequencies. As previously demonstrated, incorporating a fictitious viscosity term into the ROM model helps in restraining the amplitude of coefficients, although no effect is noticeable on their frequency.

In the monofluid scenario, the implementation of the numerical dissipation involves adding a portion of the kinematic viscosity, as a constant. In the bifluid case, this adjustment translates to assigning a weight τ, greater than unity, to viscosity-related terms in the expressions of Eqs. (3.47a)-(3.47d). Various cases are explored, considering the substantial complexity of the target bifluid flow, due to the significant disparity between water and air properties. The two fluids are, in a first moment, chosen with slightly different characteristics, to maintain small Reynolds numbers,

with an approach similar to the cylinder test. The configurations are distinguished by their density ratio, denoted as $R_\rho = \rho_h/\rho_l$. Considered cases present a modest difference, $R_\rho = 2$, an intermediate difference, $R_\rho = 10$, and then the more extreme, water/air configuration, which is $R_\rho = w/a \sim 854$. The snapshots are collected each $\Delta t = 0.004\,\mathrm{s}$. The number of modes is adjusted to ensure RIC $\geq 99\%$, resulting in considerable variation across cases (Table 3.10).

	$R_\rho = 2$	$R_\rho = 10$	$R_\rho = w/a$
μ_l (m^2/s)	2.5	1.5×10^{-3}	1.803×10^{-5}
μ_h (m^2/s)	1	1	1.14×10^{-3}
ρ_l (kg/m^3)	500	100	1.2
ρ_h (kg/m^3)	1000	1000	1025
Re_l	2×10^2	6.66×10^4	6.66×10^4
Re_h	10^3	10^3	8.99×10^5
Q_p	10^{-6}	10^{-6}	10^{-5}
$Q_{1/\rho}$	10^2	10^2	1
$Q_{\mu/\rho}$	10^2	10^3	10^5
N_r	7	17	20
RIC (%)	99.09	99.05	99.01

Table 3.10 Fluid characteristics and model parameters for the different density ratio cases analyzed.

Except for $R_\rho = 2$, the other cases exhibit instability, where the integration of the temporal coefficients over time becomes highly unpredictable, leading to excessively high coefficient values after few time steps. This instability manifests more rapidly with higher R_ρ values, reflecting the greater disparity between the fluids. Although reducing the time step size may seem a potential solution, it fails to mitigate the issue, resulting in coefficients with either excessively high or low values. Therefore, a correction term is introduced to amplify the weight on viscosity terms, thereby enhancing dissipation. For the case $R_\rho = 2$, satisfactory results (see Figure 3.30) are achieved without correction terms, owing to the smaller difference between the fluids and the relatively low Reynolds number.

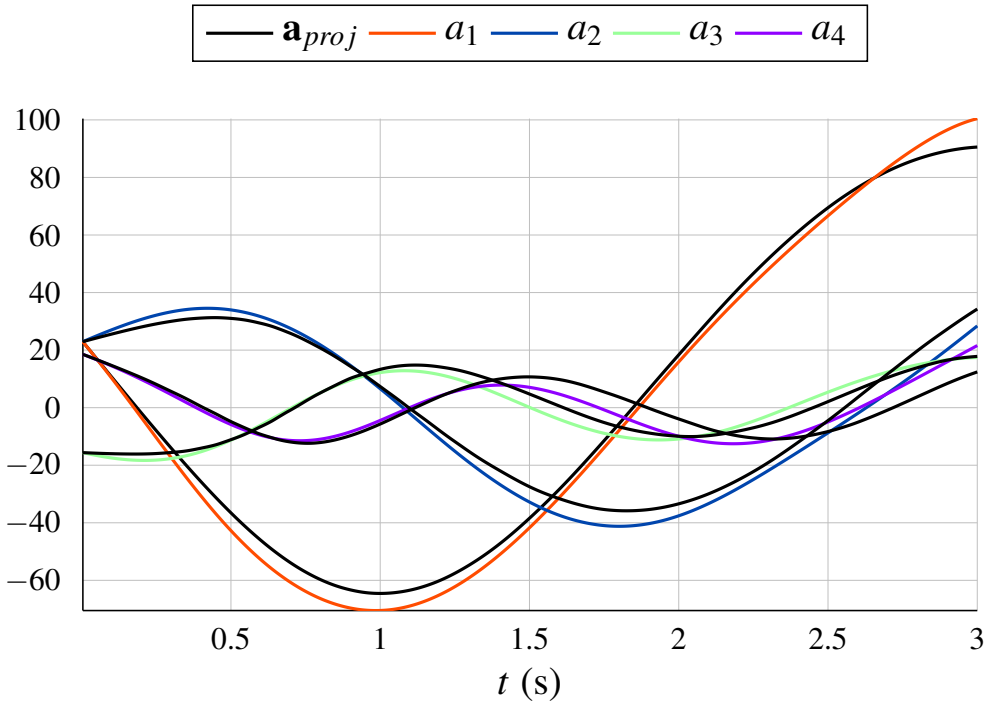

Fig. 3.30 Evolution of the first four temporal coefficients (in color) for case $R_\rho = 2$, compared to their respective projection coefficients (in black).

However, when passing to $R_\rho = 10$, the model shows instability, and the correction term proves effective in stabilizing the system. The correction action is evident in Figure 3.31, for various values of τ. The complete model, comprising both the symmetric gradient and the Laplacian terms (*Visc*), is tested to validate that the problem is not solely attributable to the simplifications of an asymptotic reduction.

While the correction term effectively prevents instabilities from accumulating and causing the model to fail catastrophically, it also kills any temporal evolution of the solution. Therefore, if the model fails and explodes, it also fails when all the temporal coefficients remain constant throughout the entire time lapse. In addition, with higher R_ρ values, the correction term has limited efficacy, and the instability persists.

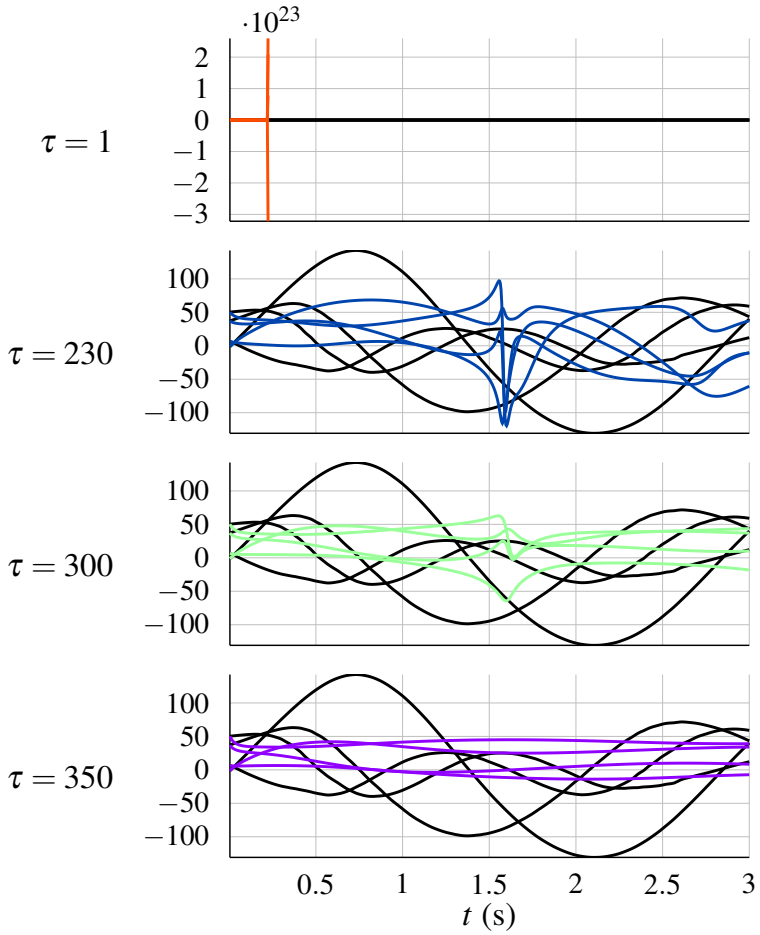

Fig. 3.31 Evolution of the first four temporal coefficients (in color) for case $R_\rho = 10$, compared to the projection coefficients (in black). The effect of various values of τ is represented. For $\tau < 230$, the model is still unstable, for $\tau > 350$ the coefficients are not evolving. Thus, results for such ranges are not displayed.

The POD ROM model, in its current form, is evidently ill-suited for bifluid flows. The reasons may extend beyond viscosity alone, and comprise factors such as the potential onset of a turbulent regime at high Reynolds numbers, whereas the current model assumes a laminar flow. Another reason may be related to the use of a limited number of modes, discarding higher-frequency modes, crucial for preventing instability. However, increasing the number of retained modes contradicts the objective of reducing model complexity and computational cost. Another possibility may be linked to the interpolation process required to extract the snapshots. The CFD model is based on finite volumes, and on a Cartesian octree mesh, with local refinements in regions such as the free surface, or around a body. However, results

are extracted on a uniform Cartesian mesh, corresponding to the coarsest level of the original CFD mesh. This discrepancy could introduce inaccuracies in the snapshot data passed to the model, affecting its fidelity to the Navier-Stokes equations, at the basis of the reduced model. For instance, interpolation errors might compromise the divergence-free property of the basis functions, upon which the ROM model relies. Additionally, lower amplitude modes are susceptible to bring numerical noise to the model and to cause loss of orthogonality [176]. Such inaccuracies may not be perceptible when plotting the basis functions, as in Figures 3.32, 3.33.

Alternatively, a completely data-driven model, that abstains from equations and relies solely on reproducing provided information, shall be tested, to explore whether the data are reconstructible. Dynamic Mode Decomposition offers a promising approach, maintaining the notion of defining a physical field through spatial basis functions and temporal coefficients. This approach stands in contrast to machine learning-based data-driven models, which lack explicit modeling of underlying physical principles.

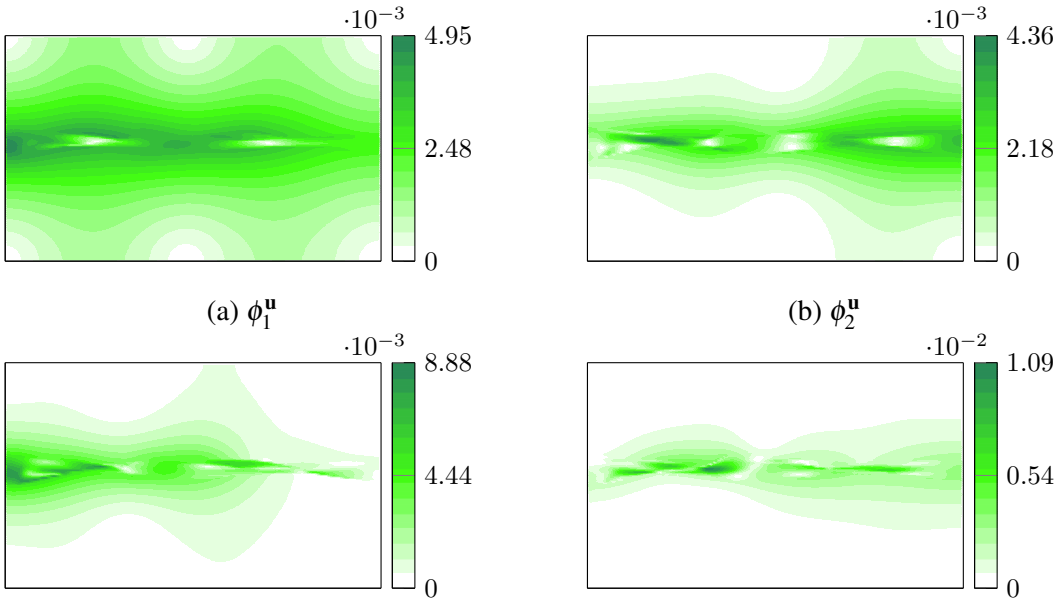

(a) $\phi_1^{\mathbf{u}}$ (b) $\phi_2^{\mathbf{u}}$

(c) $\phi_3^{\mathbf{u}}$ (d) $\phi_4^{\mathbf{u}}$

Fig. 3.32 Spatial evolution on a $x-y$ section of the first four basis functions of the velocity field, $\boldsymbol{\phi}^{\mathbf{u}}$.

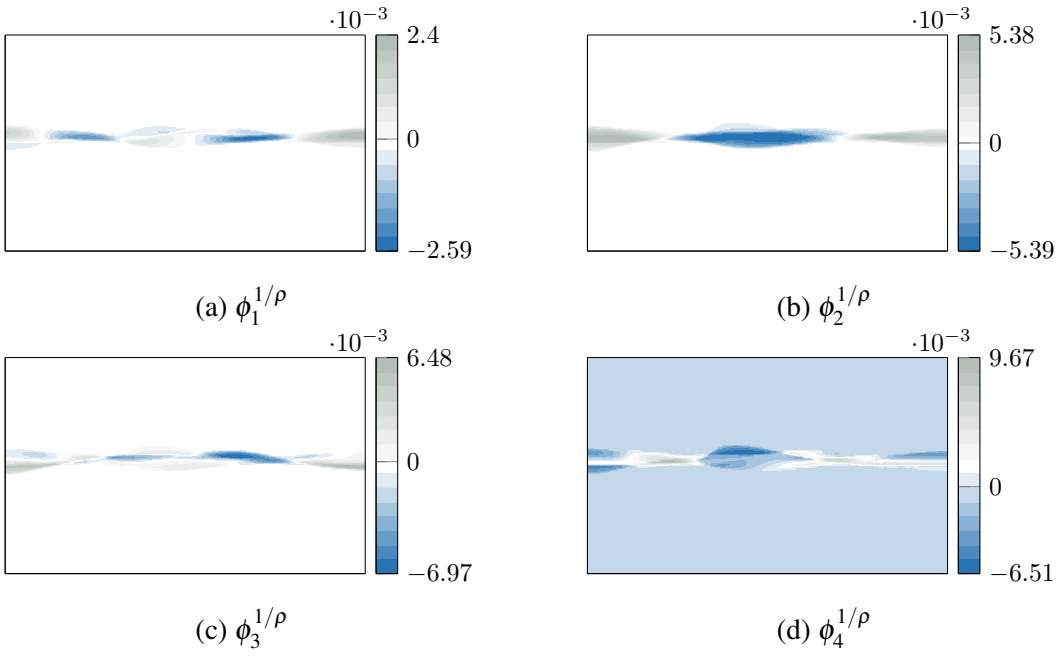

(a) $\phi_1^{1/\rho}$ (b) $\phi_2^{1/\rho}$

(c) $\phi_3^{1/\rho}$ (d) $\phi_4^{1/\rho}$

Fig. 3.33 Spatial evolution on a $x-y$ section of the first four basis functions of the density field, $\boldsymbol{\phi}^{1/\rho}$.

Dynamical Mode Decomposition

As the ROM based on the POD fails to describe the evolution of a biphase flow with water and air, one may explore alternative techniques for problem reduction. While the POD basis functions demonstrate proficiency in reducing the problem, and yielding minimal projection errors, the primary issue appears to come from the construction of the dynamical system. This issue is, thus, related to the Galerkin projection and, by extension, the Navier-Stokes equations. A different approach would, then, be to discard any physics-informed stage, and rely solely on data. A data-driven technique not based on machine learning methods, yet sharing similarities with a basis function-based approach like the POD, is the Dynamical Mode Decomposition (DMD). DMD finds application in several domains, among which fluid dynamics, and can be used with both numerical and experimental data [177]. The following discussion of the theory underlying the DMD is not exhaustive, yet aims to provide a fundamental comprehension of the application of such technique. For further details, information may be found in [178–180].

The main objective remains the reduction of a dynamical system potentially governed by a system of PDEs, such as before, in Eq. (3.12). Contrary to POD, DMD adopts an equation-free perspective, assuming that the right-hand side of the system, $\mathbf{F}$, is unknown. The assumption is that any problem may be approximated by a linear dynamical system such as:

$$\frac{\mathrm{d}\mathbf{U}}{\mathrm{d}t} = \mathbb{B}\,\mathbf{U}, \tag{3.51}$$

which has initial conditions $\mathbf{U}(\mathbf{x}, t=0) = \mathbf{U}_0(\mathbf{x})$, and solution of the form

$$\mathbf{U}(\mathbf{x},t) = \mathbf{b}\Psi(\mathbf{x})\exp(\Upsilon t) = \sum_{i=1}^{N_r} b_i \psi_i(\mathbf{x})\exp(\upsilon_i t). \tag{3.52}$$

Here, Ψ are the eigenvectors and Υ the eigenvalues of the matrix $\mathbb{B}$, and $\mathbf{b}$ are the projection coefficients associated to $\mathbf{U}_0$, giving the initial amplitude of each mode. The discrete expression of Eq. (3.51) read as

$$\mathbf{U}(\mathbf{x}, t_{i+1}) = \widetilde{\mathbb{B}}\,\mathbf{U}(\mathbf{x}, t_i), \tag{3.53}$$

which means that the flow field at time t_i is connected to the subsequent flow field, at time t_{i+1}. In Eq. (3.53), $\widetilde{\mathbb{B}} = \exp(\mathbb{B}\Delta t)$ is the discrete form of the continuous $\mathbb{B}$, with a time discretization of Δt. The idea of the DMD is to produce a low-rank eigendecomposition of $\widetilde{\mathbb{B}}$, that optimally fits the realizations for all the i considered, so it can be seen as a minimization of

$$\left\| \mathbf{U}(\mathbf{x}, t_{i+1}) - \widetilde{\mathbb{B}}\mathbf{U}(\mathbf{x}, t_i) \right\|_2, \tag{3.54}$$

in a least squares sense.

From a numerical point of view, there is, once again, a snapshot matrix $\mathbf{S}$, with the space-time values of the variables of interest over N_s time instances, as in Eq. (3.19). Since the linear mapping is assumed to be approximately the same over all the snapshots, one can rewrite the snapshot matrix as
$\mathbf{S} = [\mathbf{U}(\mathbf{x}, t_1)^T \quad \widetilde{\mathbb{B}}\mathbf{U}(\mathbf{x}, t_1)^T \quad \widetilde{\mathbb{B}}^2\mathbf{U}(\mathbf{x}, t_1)^T \quad \cdots \quad \widetilde{\mathbb{B}}^{Ns-1}\mathbf{U}(\mathbf{x}, t_1)^T]$. For linear processes, assuming a constant mapping does not result in any approximation. However, in the context of nonlinear processes, it corresponds to a linear tangent approximation.

The objective is the derivation of the dynamic properties of the process described by $\widetilde{\mathbb{B}}$, using the sequence $\mathbf{S}$. To do so, two data matrices are defined, shifted in time,

$$\mathbf{S}_1 = [\mathbf{U}(\mathbf{x}, t_1)^T \quad \mathbf{U}(\mathbf{x}, t_2)^T \quad \cdots \quad \mathbf{U}(\mathbf{x}, t_{N_s-1})^T]$$

and

$$\mathbf{S}_2 = [\mathbf{U}(\mathbf{x}, t_2)^T \quad \mathbf{U}(\mathbf{x}, t_3)^T \quad \cdots \quad \mathbf{U}(\mathbf{x}, t_{N_s})^T],$$

and based on Eq. (3.53), the following expression holds:

$$\mathbf{S}_2 = \widetilde{\mathbb{B}}\mathbf{S}_1. \tag{3.55}$$

When the size of the process is large, dealing with $\widetilde{\mathbb{B}}$ may become intractable, so a rank-reduced representation, in terms of a POD-projected approximation $\hat{\mathbb{B}}$, is preferred. First, the SVD of $\mathbf{S}_1$ is computed, with reference to the notation in Eq. (3.10), as $\mathbf{S}_1 = \boldsymbol{Q}\Sigma\boldsymbol{Z}^T$, where the matrices are truncated to a certain level N_r. Then, it can be demonstrated with only few passages, that the approximation can be computed as:

$$\hat{\mathbb{B}} = \boldsymbol{Q}^T \mathbf{S}_2 \boldsymbol{Z} \Sigma^{-1}. \tag{3.56}$$

Computing the eigendecomposition of $\hat{\mathbb{B}}$,

$$\hat{\mathbb{B}} \boldsymbol{V} = \Lambda \boldsymbol{V}, \tag{3.57}$$

allows to reconstruct the eigendecomposition of $\widetilde{\mathbb{B}}$ with the eigenvalues Λ and the eigenvectors as $\Psi = S_2 \boldsymbol{Z} \Sigma^{-1} \boldsymbol{V}$. By defining $\Upsilon = \ln(\Lambda)/\Delta t$ and having the initial coefficients $\mathbf{b}$ from the expression $\mathbf{U}_0 = \Psi \mathbf{b}$, the solution is then approximated as:

$$\mathbf{U}(\mathbf{x},t) \simeq \sum_{i=1}^{N_r} b_i \psi_i(\mathbf{x}) \exp(\upsilon_i t) = \mathbf{b} \Psi(\mathbf{x}) \exp(\Upsilon t). \tag{3.58}$$

The technique is tested on the same scenario as in the previous section, the free wave test, directly using the characteristics of water and air, denoted as case $R_\rho = w/a$. No weighting coefficients are necessary in the snapshot matrix to balance the contribution of the different variables. For the sake of comparison with the POD, the eigenvalues of the SVD, Σ, and a RIC computed on such values, can be plotted in Figure 3.34, showing that only a few modes contain the majority of the information.

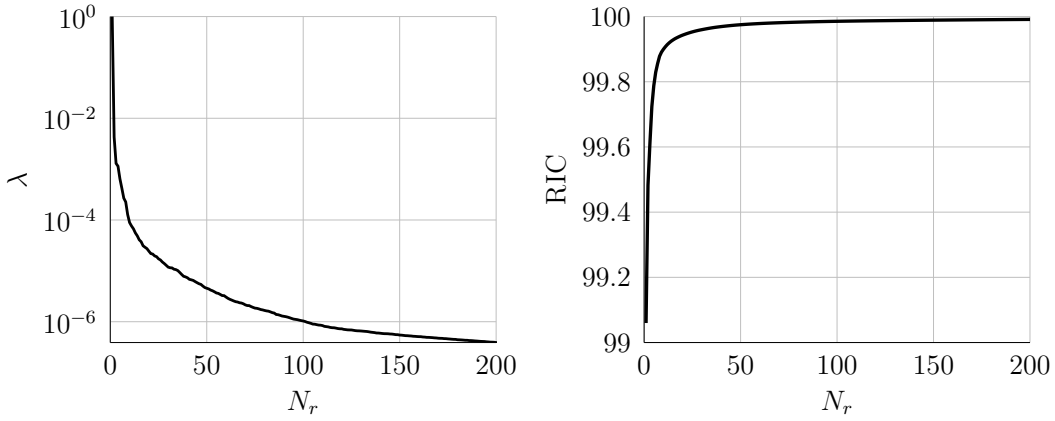

Fig. 3.34 Evolution of the eigenvalues spectrum, normalized to the fist eigenvalue (left), and of the RIC (right) with respect to the number of DMD modes N_r. The plots show only the first 200 modes.

Unlike POD, DMD not only provides modes Ψ, but also a set of associated eigenvalues, that determine a low-dimensional dynamical system, governing the

evolution of the mode amplitudes in time, $\hat{\mathbf{b}} = \mathbf{b}\exp(\Upsilon t)$. To gain insight into how basis functions and coefficients appear in the DMD technique, refer to Figures 3.35-3.37, and Figure 3.38, respectively.

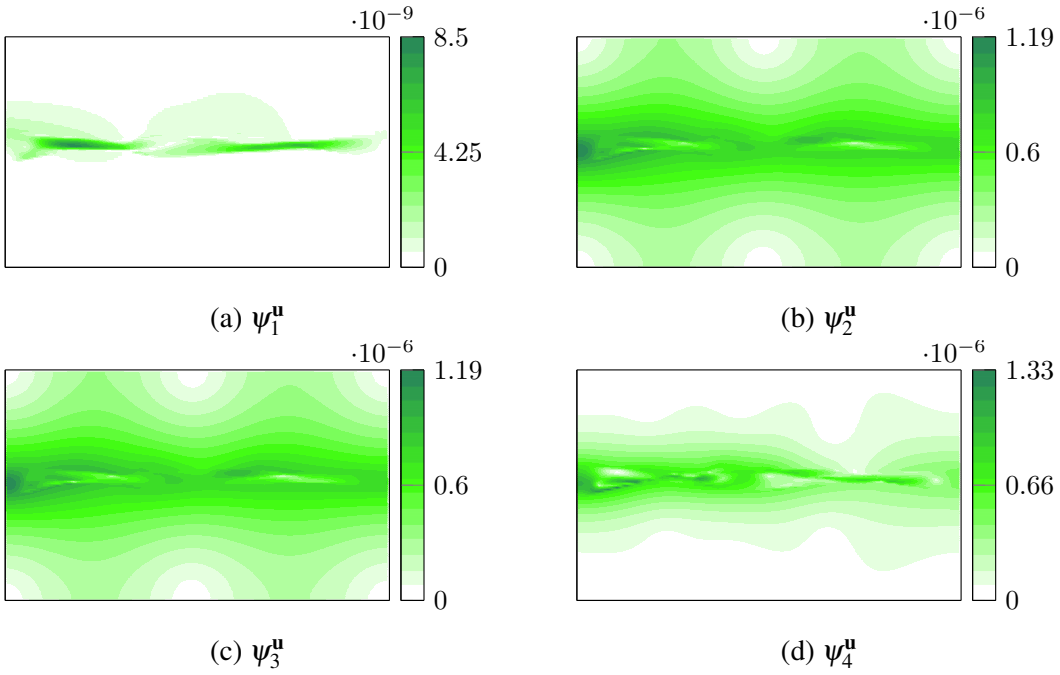

(a) $\psi_1^{\mathbf{u}}$ (b) $\psi_2^{\mathbf{u}}$

(c) $\psi_3^{\mathbf{u}}$ (d) $\psi_4^{\mathbf{u}}$

Fig. 3.35 Spatial evolution on a $x-y$ section of the first four basis functions of the velocity field (in absolute value), $\boldsymbol{\psi}^{\mathbf{u}}$, for $N_r = 5$.

As the modes are complex, the absolute value is represented in Figures 3.35-3.37 for the first four basis functions, when $N_r = 5$. Across all variables, ψ_1 shows a small absolute value (with the exception of pressure) and minimal variation, while subsequent basis functions are coupled, displaying corresponding absolute values. The basis functions for μ/ρ are not depicted, being very similar to the basis functions for $1/\rho$, but with smaller absolute values, on the order of $\mathcal{O}(10^{-11})$, due to the absence of weighting coefficients on the snapshots.

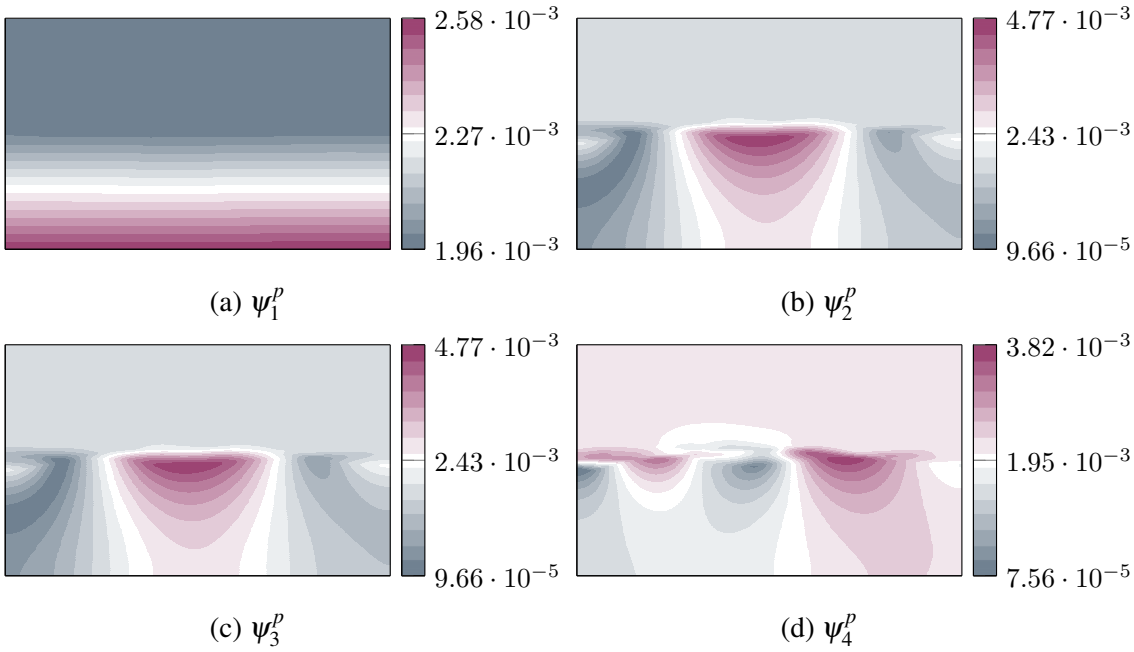

(a) ψ_1^p (b) ψ_2^p

(c) ψ_3^p (d) ψ_4^p

Fig. 3.36 Spatial evolution on a $x-y$ section of the first four basis functions of the pressure field (in absolute value), $\boldsymbol{\psi}^p$, for $N_r = 5$.

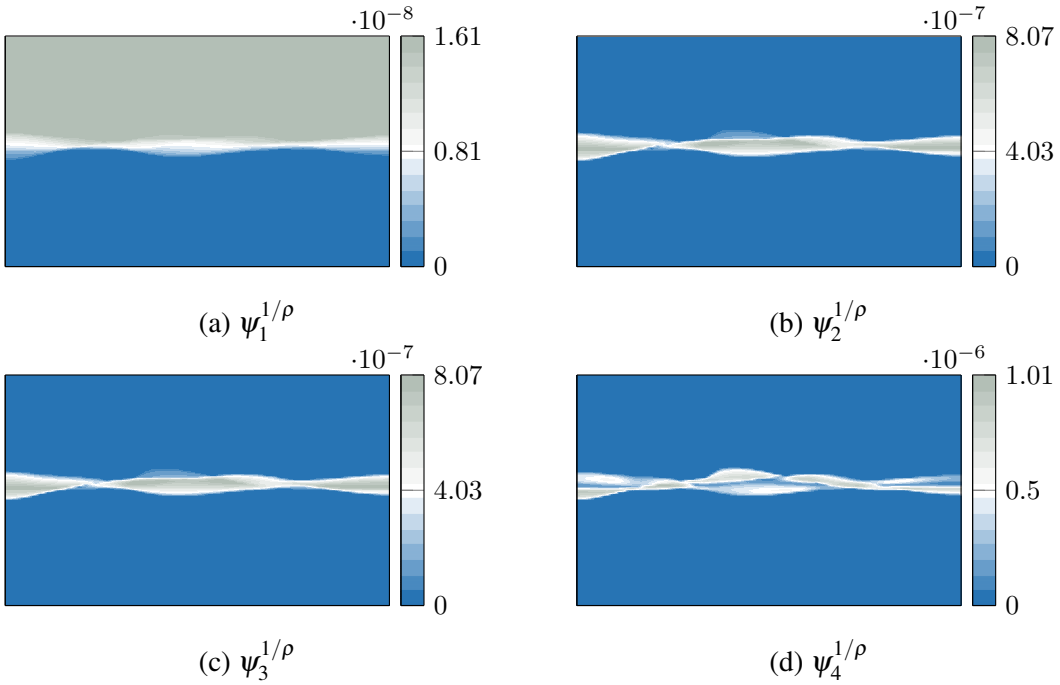

(a) $\psi_1^{1/\rho}$ (b) $\psi_2^{1/\rho}$

(c) $\psi_3^{1/\rho}$ (d) $\psi_4^{1/\rho}$

Fig. 3.37 Spatial evolution on a $x-y$ section of the first four basis functions for the density field (in absolute value), $\boldsymbol{\psi}^{1/\rho}$, for $N_r = 5$.

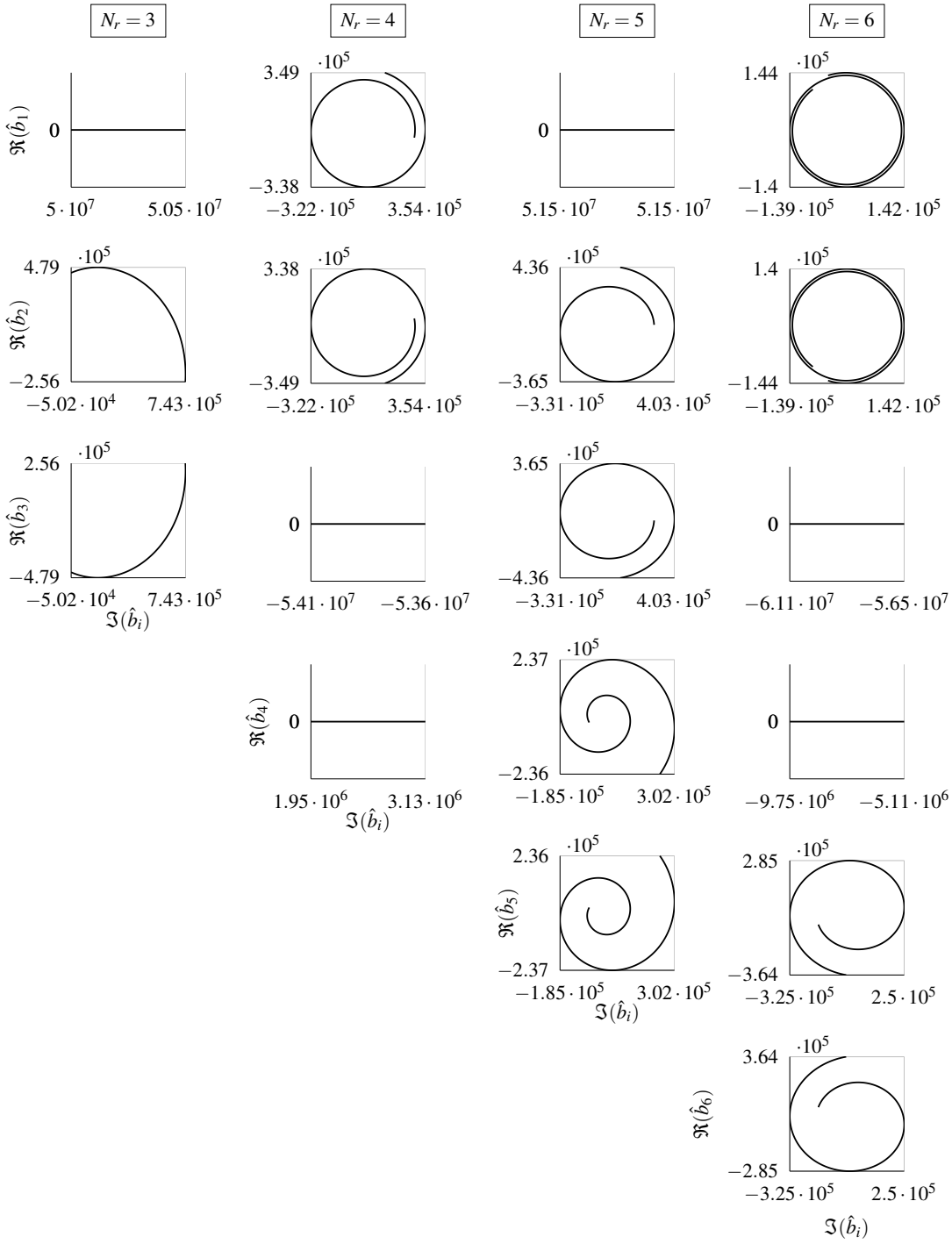

Fig. 3.38 Representation of the DMD temporal coefficients, plotted over real and imaginary components, for $N_r = 3, 4, 5, 6$.

For the temporal coefficients, various truncations are explored, $N_r = 3,4,5,6$. The DMD exhibits distinct ordering in the coefficients (compare corresponding lines in Figure 3.38), in contrast to the POD, which has corresponding coefficients with increasing index, regardless of the truncation. Moreover, unlike POD, the mean is not subtracted from the data in the DMD calculation, so one mode corresponds to a background mode that remains unchanged (i.e., it has zero eigenvalue), not necessarily the first one. Specifically, when truncating at an odd number of modes, this background mode appears as a single mode (e.g. first line, first and third columns in Figure 3.38), and the rest are paired modes. On the other hand, when N_r is even, two background modes exist, as visible in the third and fourth lines, second and fourth columns of Fig 3.38. The remaining modes are paired as well, with opposite phase.

The results show excellent agreement with the original snapshots (despite few peak values, as visible in Figures 3.39-3.41), proving the suitability of the DMD in the reproduction of the data.

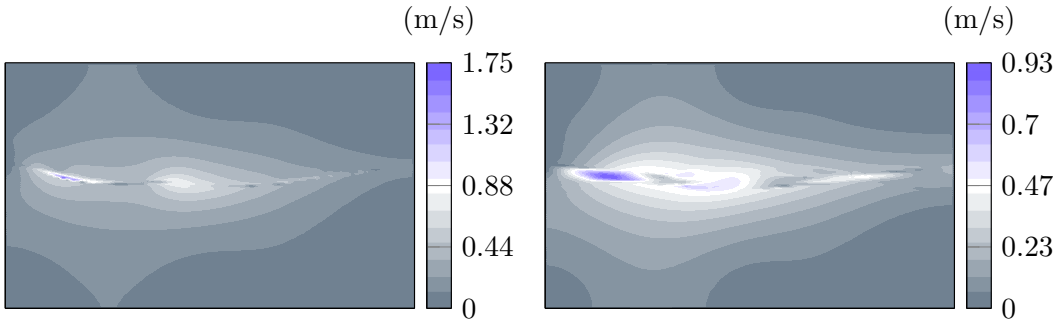

(a) FOM velocity field.

(b) ROM velocity field.

Fig. 3.39 Comparison between FOM and ROM solutions with $N_r = 5$, for the velocity magnitude, on a $x-y$ section, at time $T = 1.5\,\mathrm{s}$.

Different N_r, leading to different levels of compression of the information are tested, and the relative errors are listed in Table 3.11. The errors decrease with increasing N_r, as expected. However, while the errors halve between $N_r = 5$ and $N_r = 10$, they only slightly decrease when passing to $N_r = 20$. This suggests that, for the test case considered, the main information is condensed in a few modes. In terms of computational workload, constructing the various matrices offline takes a maximum of 4 and a half minutes, while the online phase takes less than 3 minutes, regardless of N_r. This duration, on a single processor, is significantly less with respect to the

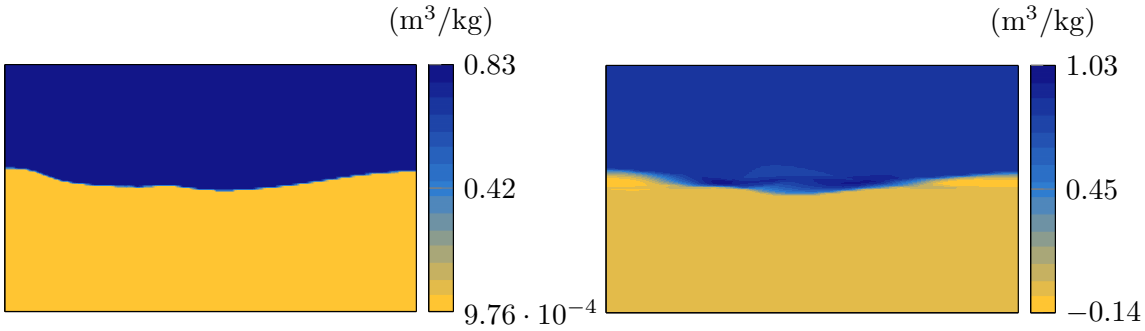

(a) FOM density field.

(b) ROM density field.

Fig. 3.40 Comparison between FOM and ROM solutions with $N_r = 5$, for the density (the inverse), on a $x-y$ section, at time $T = 1.5\,\mathrm{s}$.

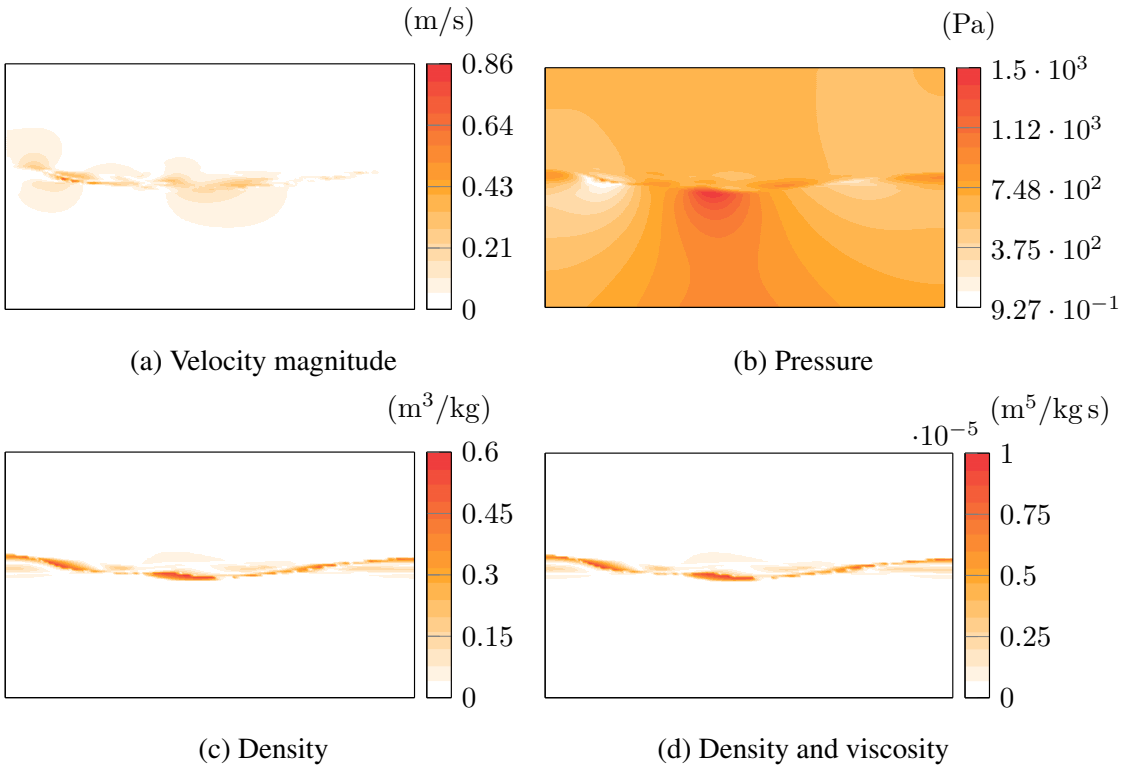

(a) Velocity magnitude

(b) Pressure

(c) Density

(d) Density and viscosity

Fig. 3.41 Absolute difference between FOM and ROM solutions with $N_r = 5$, for the different variables (in absolute value), on a $x-y$ section, at time $T = 1.5\,\mathrm{s}$.

one and a half hours required for the original CFD simulation to run on 48 processors. Regarding the POD ROM for cases where the dynamical system remains stable, computational times are slightly larger, but comparable.

Error	Case		
	$N_r = 5$	$N_r = 10$	$N_r = 20$
$\bar{\varepsilon}^u$	4.58e-4	2.32e-4	2.24e-4
$\bar{\varepsilon}^v$	3.62e-4	1.18e-4	1.06e-4
$\bar{\varepsilon}^w$	1.16e-3	1.01e-3	1.19e-3
$\bar{\varepsilon}^p$	5.79e-6	1.97e-6	2.66e-6
$\bar{\varepsilon}^{1/\rho}$	1.15e-4	6.94e-5	7.77e-5
$\bar{\varepsilon}^{\mu/\rho}$	1.07e-4	6.42e-5	7.18e-5

Table 3.11 Relative errors for the velocity, pressure, density, and viscosity variables for different values of N_r.

The described DMD algorithm exploits the low dimensionality in the data to provide a low-rank approximation of the linear mapping that best approximates the nonlinear dynamics of the original collected data [181]. Based on the available data, the DMD is able to predict future states of the system. Differing from the POD Galerkin method, which requires solving a low-rank set of dynamical quantities to forecast the future state, predicting future states with DMD simply involves plugging the desired future time into the approximation equation, requiring no additional computational effort.

However, handling dynamical evolution with a data-fit model is challenging and typically results in a loss of flexibility in the surrogate model. This limitation arises from a sensitivity to changes in the data distribution, which can lead to inaccurate predictions and reduced performance in out-of-sample scenarios. Contrary to POD, DMD modes contain distinct frequency information and are derived from uniformly sampled time-resolved datasets [182]. As the DMD directly operates on the given data, the order is important, as indicated by the definitions of $\mathbf{S}_1$ and $\mathbf{S}_2$. Consequently, when the dynamics of the system change, DMD may struggle to effectively capture these alterations. In contrast, the frequency-independent nature of POD enables it to simulate various conditions within its range of applicability, hence proving more robust in out-of-sample studies. At the core of the definition of the POD basis lies a correlation matrix $\mathbf{R}$, where snapshots corresponding to different dynamics can be introduced. Thus, POD focuses on capturing the dominant modes of variation in the data, allowing for better generalization to new or unseen data.

3.5 Conclusion

In this chapter, building upon an established model, a surrogate model is derived for a more intricate problem: a POD ROM model for three-dimensional multiphase flows. The POD ROM applied to the monophase flow past a cylinder at $Re = 200$ demonstrates promising results, with a maximum relative error of 0.4%, and significantly reduced simulation time compared to the FOM. However, real-world simulations of WECs normally involve higher Reynolds numbers. As the Reynolds number increases, the viscous effects decrease and the flow could be considered inviscid, and for small amplitude waves and body motions, several simplifications may be accepted, as explained in the previous chapter. Nevertheless, such assumptions do not hold for real WECs, which present nonlinearities, and, in such cases, viscous effects become large. Higher Reynolds numbers must necessarily be tested, and the viscosity terms in the Navier-Stokes equations must be handled carefully. A detailed analysis of the different terms of the governing equations, and their effects on the ROM model, gives insights on the versatility of the model, and the various forms it can take. An encouraging outcome is the asymptotic reduction of the POD ROM, offering a more manageable model. Simplifying the ROM model by considering only the Laplacian term of the viscosity maintains results, without excessive complexity. However, complete or asymptotically reduced ROM models encounter instability issues when dealing with very different fluids. Some attempts to tackle the problem yield only mediocre results. To ascertain whether the issue stems from the Galerkin projection step, a comparison with a purely data-driven model reduction technique such as DMD is necessary. While DMD proves effective for a water/air problem, it inherently exhibits limitations, especially concerning out-of-sample scenarios of interest. The present version of the POD ROM model does not suffice for the multiphase flow reduction, demanding further research. Given the source of the problem, a deeper exploration of the Galerkin projection is warranted. Exploring dissipation in this scheme [183], and considering the potential of a nonlinear Galerkin method [184] are options worth exploring. Additionally, integrating other reduction techniques [185], or employing machine learning-based methods, along with using closure terms to prevent instabilities, could be viable paths.

While this chapter concludes with the acknowledgment that a ROM based on POD for multiphase flows remains an open question, the versatility of POD itself remains evident throughout. This robustness offers hope for its application in the

specific domain of interest. Furthermore, the challenges ROMs inherently face in accurately modeling moving bodies raise doubts about their applicability in WEC modeling, even before addressing instability issues. While research in that direction would be valuable, an alternative approach may offer a more direct solution, as presented and implemented in the next chapter.

Chapter 4

Multi-fidelity modeling of Wave Energy Converters

The objective of this chapter is to develop a three-dimensional numerical model for a WEC interacting with sea waves, in a bifluid environment consisting of air and water. The primary aim is to devise an efficient computational tool that addresses two key challenges: reducing the computational time associated with high-fidelity models, and curing the lack of accuracy of low-fidelity reduced-order models in regions affected by viscous and highly nonlinear effects. To achieve these objectives, a multi-fidelity model is proposed, based on domain decomposition. This approach combines a high-fidelity CFD solver, which accurately captures the behavior in viscous and nonlinear regions, with a Galerkin-free POD ROM model, tailored for weakly nonlinear regions. By spatially integrating these components, the dynamics of a floating body is simulated within a unified framework. Numerical simulations implementing the coupled model, not only provide a good approximation of the solution in several test cases, but also alleviate the computational burden both in terms of memory storage and speedup.

Following the introductory Section 4.1 on coupling methodologies for fluid flows, the chapter proceeds to describe the multi-fidelity model and its implementation, in Section 4.2. Subsequently, several tests are conducted to refine and tune the coupled model (Section 4.3), leading to the application in wave energy simulations, in Section 4.4.

4.1 Coupling Methodologies

As outlined in Chapter 2, numerical modeling of WEC farms presents significant challenges due to their multi-scale nature, necessitating the representation of both near-field and far-field effects. However, these scales correspond to distinct phenomena with different behaviors. The author of [50] notes that near-field wave perturbations decay inversely with distance from the generating body, while far-field effects decay with the square root of such distance. Additionally, far-field domains can be extensive due to the long-distance propagation of waves. Typically, a single modeling technique cannot effectively capture both near and far fields simultaneously due to cost constraints, approximation issues, or suitability concerns. Therefore, a common approach is to employ two separate solvers, one for each problem, coupled using domain decomposition. This methodology, utilized in various domains, among which ship hydrodynamics [186] and external aerodynamics [187], has also been adapted for wave energy applications, with several coupled models proposed recently. Coupled models generally fall into two categories: one-way coupling, where information flows from one solver to another, and two-way coupling, where information exchange occurs bidirectionally at each time step, ensuring a continuous balance between near-field and far-field influences.

A well-established one-way coupling technique has been developed at Ghent University, and extensively used for simulating WEC farms [188, 189, 26], as well as farm clusters [190], and assessing their impact on the surrounding environment. For the near field, the wave-structure interaction solver is NEMOH, which utilizes Boundary Element Method (BEM), while the wave propagation solver is MILDwave, based on mild-slope equations. The former is responsible for the calculation of the radiated and diffracted wave fields inside a circular domain enclosing the entire farm, while the latter propagates the total wave field, given by the superposition of the incident and the BEM wave fields, from the circular boundary around the farm to the limits of the large domain. The methodology is tested on regular and irregular waves, for mildly varying bathymetries, and is also validated against experimental data [191]. The main discrepancies found between numerical and experimental results are linked to the nonlinearities, that are not considered in the coupled model. The far-field calculation cost is fixed to the order of tens of minutes, regardless of the number of WECs present. However, the computational expense of the BEM is sensitive to the number of WECs, since the number of panels increases proportionally

[192]. Additionally, irregular waves are computed as superposition of regular waves, thus the computational cost increases with the frequency discretization of the wave spectrum.

Another coupling method employing BEM for the near field is presented in [193]. However, in this case, each WEC is modeled separately, and then the interactions and the far field are modeled using the plane wave approximation. The coupling is two-way, as the contributions of the different WECs is iteratively updated. This decomposition approach helps to reduce the computational burden for the near field, enabling the modeling of farms with up to 50 WECs, which would otherwise be prohibitively expensive with a standard BEM approach. Similar methodologies can be found in other works [194, 195], where a potential flow model is coupled with a wave model. However, as noted by the author in [196], the linearity of WEC dynamics presents limitations, requiring empirical tuning for accurate predictions, particularly near WEC resonance. Consequently, several coupled models have been proposed, integrating high-fidelity solvers for wave-structure interactions and low-fidelity solvers for wave propagation. The high-fidelity solver allows for the consideration of all nonlinearities related to WECs, including viscosity effects.

Defining appropriate boundary conditions for such subdomains remains a significant challenge, typically addressed through a two-way approach. A study presented in [197] introduces a nested approach where the RANS solver OpenFOAM is integrated with the fully nonlinear potential flow solver OceanWave3D, and primarily focuses on wave propagation scenarios. The authors identify certain limitations, such as the challenging parallelization of computations due to OceanWave3D constraints, and the necessity of filtering VOF information during the exchange phase between solvers on overlapping subdomains.
Another instance of coupling involves the same wave propagation solver, in conjunction with the SPH solver DualSPHysics through open boundaries [198]. The information is exchanged on a buffer zone, filled with layers of SPH buffer particles, on which the boundary conditions are imposed. The SPH subdomain only has an inlet and an outlet, and it develops for the entire water depth. Such a design is chosen usually for application to offshore wind turbines [199, 200], but would be computationally non-optimal for WECs floating in deep water. The communication between the two solvers, with potentially different time steps, is regulated by an intermediate Python program, either in a one-way, or two-way fashion. The one-way coupled model is found to be four times faster than the fully high-fidelity model. The

two-way coupling approach necessitates accurate and stable boundary conditions, posing challenges for non-uniform velocities and surface elevations in the transversal direction, especially in completely three-dimensional simulations involving multidirectional waves.
A further example is a coupling methodology combining a CFD solver with a high-order spectral model, tested on propagating waves and fixed structures [201]. In this case, the spectral wave model limits the simulated waves to non-breaking, and constant water depth, and the air field is modeled in a non-physical manner. As for the other models, also in this case, the communication is made over an overlapping subdomain, using the relaxation zone technique [202] to prevent wave reflections at the computational domain boundaries. In the relaxation zones, the solution of one solver is gradually attenuated to zero, and the solution information of the other solver gradually risen. More insights on other similar coupling methodologies [203, 204] can be found in [71], but they all share a common feature. Indeed, the passage from the high-fidelity solver variables to the low-fidelity solver variables may not be direct. For instance, the velocity, which is known as a vector in all the points of the domain (or else particles), needs to be expressed as the gradient of the velocity potential, a scalar field, for which irrotationality must be satisfied. Similarly, to track a wave, one must passe from a VOF expression to a free surface elevation function, where the air is not accounted. This intermediate passage may be source of inaccuracies and instabilities. In this sense, the POD allows the methodology to simplify, discarding the intermediate variable conversion. Additionally, enhancing accuracy at the boundaries allows for a reduction in the size of the high-fidelity subdomain without concerns about spurious reflections.

In the context of model order reduction, Domain Decomposition, or Component-based techniques find widespread application. Domain decomposition methods involve partitioning the computational domain into subdomains, which may overlap, and reformulating the original problem into smaller subproblems, coupled through the solution values at subdomain interfaces. Such zonal, multi-domain approaches also allow for the use of different numerical schemes and equations within different subdomains, accommodating diverse physical behaviors, and making them effective for handling multiple-scale problems [205, 206]. For instance, in [207], authors decompose a network of pipes, which could be representing arteries or veins, construct a reduced basis for the generic parts, and then combine them together for the solution on the entire domain. An analogous approach is implemented in [208], where

several non-overlapping subdomains, distinguished by different characteristics, such as material and thermal conductivity, are nested in the modeling of a thermal fin. In [209], the behavior of an entire compressor is modeled incorporating low-order models of blade row unsteady aerodynamics. In [210] and [211], parametric ROMs are built for nonlinear elasticity problems, and thermo-hydro-mechanical systems for radioactive waste disposal, respectively. Other domains of application may be elastic-plastic structural problems [212], or neutron transport [213], or digital twin technologies [214].

The idea of coupling FOM and ROM using domain decomposition is not new [215]. In [216], POD and a Galerkin-free algorithm are used for the modeling of two-dimensional high-speed flows with moving shock waves. Two domain decomposition approaches are tested. One approach combines the FOM around the shock wave, with the ROM elsewhere, and gives better results than the approach using ROM also for the shock wave, which is not robust and accurate enough. For incompressible Navier-Stokes equations, the research in [217] demonstrates the improvement in the ROM performance in flow configurations that are not present in the training snapshots set, by integrating the FOM into the component-based modeling framework.

The coupled model developed here adopts the same hybrid approach, dividing the domain into a high-fidelity subdomain, and a reduced subdomain. In the context of a WEC farm, this methodology is modular, with multiple high-fidelity subdomains, connected to the reduced subdomain. A conceptual illustration is provided in Figure 4.1, and further elaboration will be provided later in the chapter.

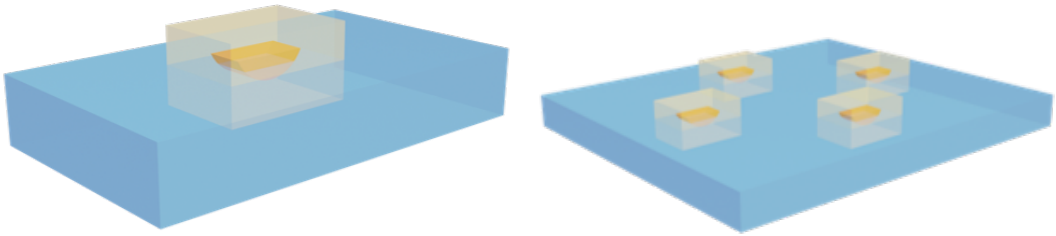

(a) Domain decomposition for a single WEC. (b) Domain decomposition for a WEC farm.

Fig. 4.1 Sketch of the domain decomposition of a single WEC and a WEC farm. The white subdomains represent the high-fidelity areas, each embedding a yellow generic WEC. The blue subdomain the where the POD is applied.

In terms of the domain decomposition techniques in ROMs, our coupling methodology could be defined as a non-overlapping, one-shot Schwarz alternating method.

In the high-fidelity subdomain, the commercial software StarCCM+ is used to obtain the accurate solution of the hydrodynamics of a WEC and the surrounding flow dynamics. In the other subdomain, a non-intrusive ROM approach is used, where POD is employed in a Galerkin-free manner. The methodology operates independently of the original physical system, requiring only the ability to export the evolution of the primary variables involved in the problem from the simulation code. By incorporating POD in the model, no simplifying assumptions about the problem are necessary. Before testing the coupling methodology on floating structures, a free flow evolution is chosen for simplicity. This allows to test and tune the model, in terms of dimensions of the subdomains, sensitivity of the POD, definition of the parameter space. All those aspects are treated in Section 4.3, following the mathematical presentation in Section 4.2. The objective is to obtain an accurate description of the evolution of the velocity field and the water surface, at a reduced computational cost, when compared to the results of the high-fidelity simulations, set as reference. Finally, Section 4 shows the application test of the floating body.

4.2 Multi-fidelity Model

The multi-fidelity model is defined for a generalized biphase simulation, which may involve moving bodies and traveling waves, although these features are not compulsory. The model is described in a generic setup, acknowledging the potential presence of a body, and will be evaluated across different cases. Representing a floating body as a sphere, the domain is now defined as in Figure 4.2. The air and water characteristics are recalled: $\rho_a = 1.2\,\mathrm{kg/m^3}$ and $\mu_a = 1.803 \times 10^{-5}\,\mathrm{m^2/s}$, and $\rho_w = 1025\,\mathrm{kg/m^3}$ and $\mu_w = 1.14 \times 10^{-3}\,\mathrm{m^2/s}$, respectively. The floating structure has density $\rho_a < \rho_s < \rho_w$, and may have several degrees of freedom. Similar to the previous chapter, the fluid domain Ω_f is separated into two domains, Ω_a for air and Ω_w for water, separated by the interface Γ_f.

Both high-fidelity and low-fidelity models involved in the coupling methodology have already been detailed in the previous chapter. In the following, they are recalled to provide additional information related to the coupling approach.

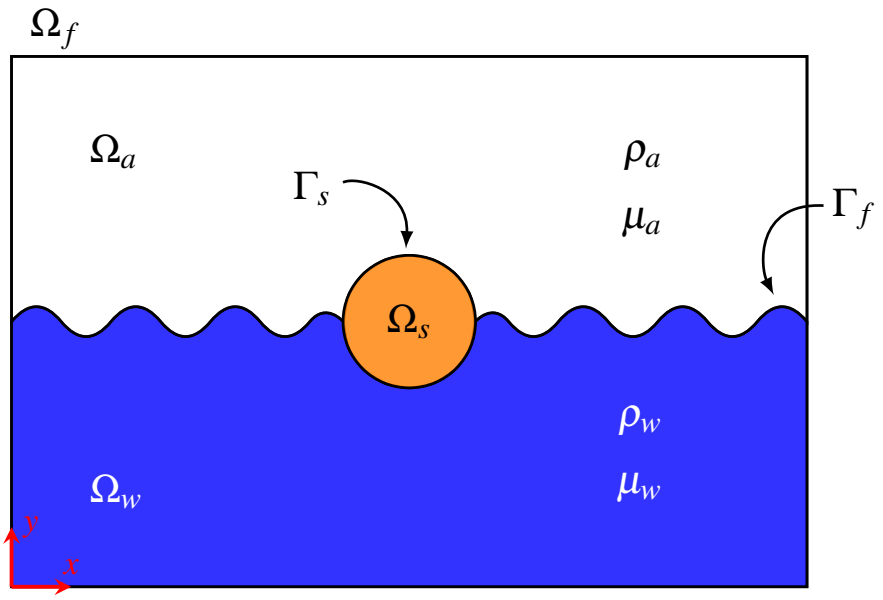

Fig. 4.2 Sketch of the flow configuration, and definition of the subdomains. The front and back boundaries are not visible, but present in the three-dimensional simulation.

4.2.1 High-Fidelity Model

The flow is modeled by the two-phase incompressible, laminar, Navier-Stokes equations (Eq. (3.1a), (3.1b)), with the VOF transport equation (Eq. (3.36)), over the fluid domain $\Omega_f = \Omega_a \cup \Omega_w$, completed with initial, and boundary conditions. Additional equations are necessary to model the motion of the rigid body, based on Newton's law:

$$m\frac{\mathrm{d}\overline{\mathbf{u}}}{\mathrm{d}t} = \boldsymbol{F}_{ext}, \tag{4.1}$$

$$\frac{\mathrm{d}J\boldsymbol{\omega}}{\mathrm{d}t} = \boldsymbol{M}_{ext}, \tag{4.2}$$

where m and J are the mass and inertia matrix of the body, and $\overline{\mathbf{u}}$ and $\boldsymbol{\omega}$ denote the linear and angular velocities. The forces and torques are computed by:

$$\boldsymbol{F}_{ext} = -\int_{\Gamma_s} \mathbb{T}(\mathbf{u}, p)\,\mathbf{n}\,\mathrm{d}\mathbf{x} + \boldsymbol{g}, \tag{4.3}$$

$$\boldsymbol{M}_{ext} = -\int_{\Gamma_s} \boldsymbol{r} \wedge \mathbb{T}(\mathbf{u}, p)\,\mathbf{n}\,\mathrm{d}\mathbf{x}, \tag{4.4}$$

where $\mathbb{T}(\mathbf{u}, p) = -p\mathbb{I} + \mu(\nabla\mathbf{u} + \nabla\mathbf{u}^T)$ is the stress tensor, $\mathbf{n}$ is the unit outward vector to Γ_s, and $\boldsymbol{r} = \mathbf{x} - \mathbf{x}_G$ with $\mathbf{x}_G$ representing the body center of mass.

To correctly follow the dynamics of the body, a body-fitted overset mesh is superposed to the background octree mesh, presenting a two-level refinement around the free surface. An example of the computational mesh is depicted in Figure 4.3.

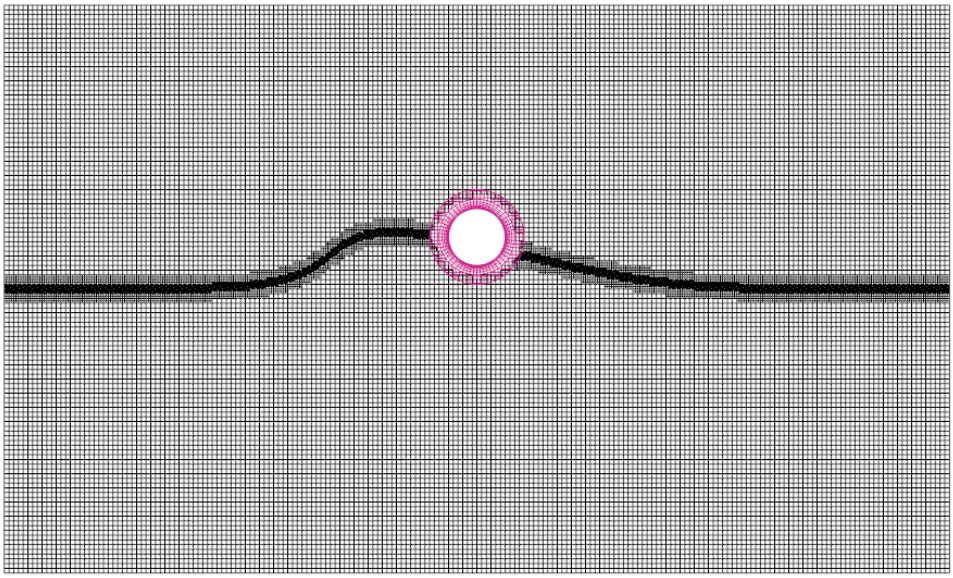

Fig. 4.3 Sketch of the computational mesh for a body moving with an evolving wave. The rose part represents the overset mesh. The depicted mesh is used for the simulation in Section 4.4.1.

4.2.2 Low-fidelity Model

For the low-fidelity modeling, the POD is employed to derive global basis functions from a precomputed snapshot dataset. The key distinction from the model described in the preceding chapter lies in the Galerkin-free approach. While the computation of the POD basis functions remains consistent, the temporal coefficients are not

obtained through the resolution of the dynamical system derived after the Galerkin projection. Instead, a least squares method is preferred, inspired from [218], and presented in Section 4.2.3.

The variables selected for this model include the velocity components and the Volume of Fluid (VOF), hence $\mathbf{U} = (u, v, w, \alpha)^T$. As previously done, other variables may be considered, such as pressure, density, and viscosity. Unlike the POD ROM model, where the variable selection is mainly influenced by the interest in reproducing specific variables, and the form of the governing equations and the Galerkin projection, the current choice is mainly guided by the definition of the boundary conditions in StarCCM+. Within the software, several types of boundary conditions are available, with Dirichlet boundary conditions appearing to be the most suitable for this approach. They allow to specify the values required along the domain boundary. In StarCCM+, such conditions can be imposed either on velocity or pressure, and on VOF. Consequently, density and viscosity are omitted, as the VOF offers a more straightforward approach. Additionally, velocity is prioritized over pressure, given that pressure is mainly represented by its hydrostatic component, while velocity is the primary variable in the original POD treatment. Another consideration involves whether to define a single set of basis functions for all variables, separate sets for different variables, or a combination of them. In this case, the first option is selected, offering the advantage of computing only one set of temporal coefficients that connect all variables, albeit an alternative is tested in Section 4.3.3. Therefore, the variables are hereafter approximated as:

$$\begin{aligned} u &\simeq \widetilde{u} = \overline{u} + \boldsymbol{\phi}^u \mathbf{a}, \\ v &\simeq \widetilde{v} = \overline{v} + \boldsymbol{\phi}^v \mathbf{a}, \\ w &\simeq \widetilde{w} = \overline{w} + \boldsymbol{\phi}^w \mathbf{a}, \\ \alpha &\simeq \widetilde{\alpha} = \overline{\alpha} + \boldsymbol{\phi}^\alpha \mathbf{a}. \end{aligned} \tag{4.5}$$

A potential drawback of such approach is that the same number of modes is considered for both the velocity field and the VOF, despite their potentially differing behaviors and requirements, in terms of N_r, for accurate representation. This may lead to a sub-optimal data compression.

4.2.3 Hybrid Model

Each model involved in the multi-fidelity model is well-defined, thus the most challenging aspect of the coupling methodology lies in their communication. This is achieved through overlapping regions or boundary conditions, positioned along sections separating the different subdomains. The approach used here is a modified and extended version of the method introduced in [218]. The critical aspect of the methodology is ensuring the correct boundary conditions definition for the high-fidelity model. Imposing appropriate boundary conditions remains one of the primary challenges in Computational Fluid Dynamics (CFD).

Numerical Approach

Before describing the coupling methodology, the decomposition of the computational domain must be introduced (Figure 4.4).

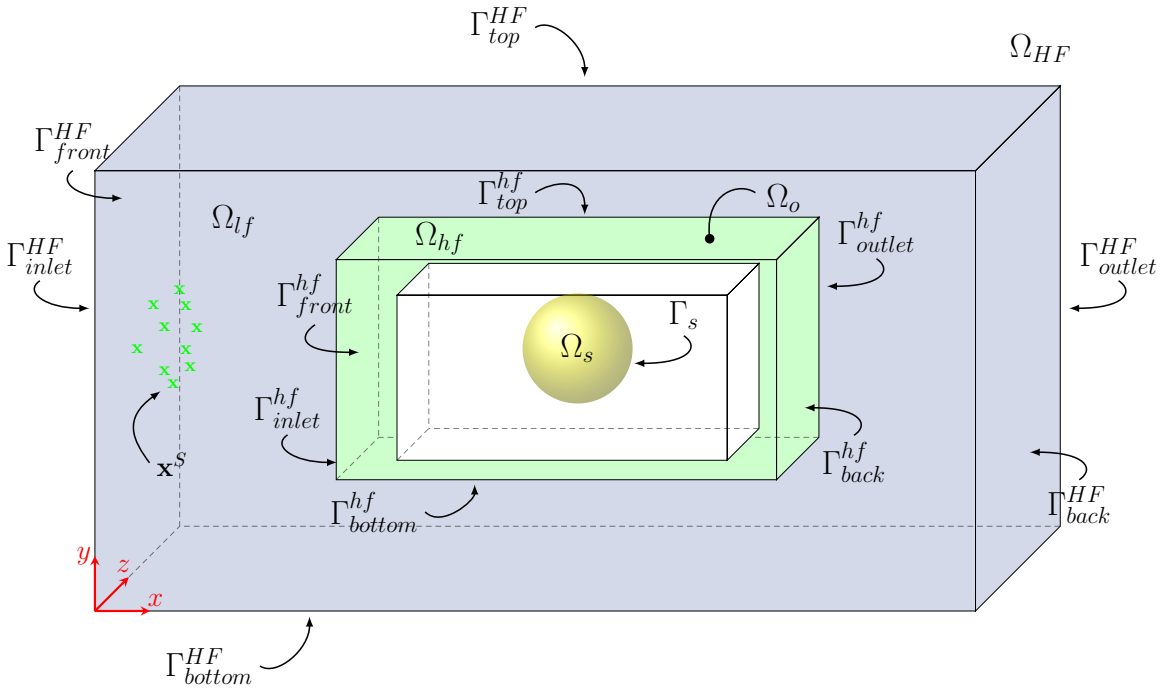

Fig. 4.4 Sketch of the domain decomposition for the coupling methodology, with definition of the different subdomains and boundaries.

Let Ω_{HF} be the entire computational domain, with boundaries $\Gamma_{HF} = \Gamma^{HF}_{top} \cup \Gamma^{HF}_{bottom} \cup \Gamma^{HF}_{inlet} \cup \Gamma^{HF}_{outlet} \cup \Gamma^{HF}_{front} \cup \Gamma^{HF}_{back}$. Now Ω_{HF} corresponds to Ω_f of Figure 4.2, and

is divided into two main subdomains, Ω_{hf} and Ω_{lf}. The high-fidelity model is employed in Ω_{hf}, represented by the white and the green parts in Figure 4.4, with boundaries $\Gamma_{hf} = \Gamma^{hf}_{top} \cup \Gamma^{hf}_{bottom} \cup \Gamma^{hf}_{inlet} \cup \Gamma^{hf}_{outlet} \cup \Gamma^{hf}_{front} \cup \Gamma^{hf}_{back}$. The low-fidelity model is defined in Ω_{lf}, which comprises the blue and the green parts in Figure 4.4. Intuitively, the green part is an overlapping region $\Omega_o = \Omega_{hf} \cap \Omega_{lf}$, where both the models are defined. Finally, M sensors are located at $\{\mathbf{x}^S_i\}^M_{i=1}$, where the information $\widehat{\mathbf{U}}_i = (\widehat{u}_i, \widehat{v}_i, \widehat{w}_i, \widehat{\alpha}_i)^T$ is known, or part of it. As described later, those sensors are important when there is a flow traveling in a certain direction. In this case, waves are traveling from Γ^{HF}_{inlet} to Γ^{HF}_{outlet}, so the sensors are typically located close to the wave source. In some applications, $M = 0$, as in the case of the free wave test.

The high-fidelity domain is localized around the floating body, where the main nonlinearities are located (fluid-structure interactions, mooring and control systems effects), and where the POD fails at giving an accurate representation. The size of such domain must be large enough to account for the movements of the body, which may have many degrees of freedom and the possibility to slightly shift in space, for example if a loose mooring system is modeled. However, since it represents the most computationally expensive part of the simulation, the high-fidelity domain should be as small as possible, to minimize the computational burden. Moreover, it should consist of at least $N_r - M$ discrete points, to obtain a well-posed minimization problem for $\{a_i\}^{N_r}_{i=1}$, as will be explained in the following.
The main requirements for the low-fidelity domain include an effective reduction of the complexity of the problem while preserving the accuracy, and the possibility of reconstructing the solution, at least on the overlapping region, and on the boundaries of Ω_{hf}, Γ_{hf}.

The objective of the coupling methodology is to find the temporal coefficients $\mathbf{a}^* = (a^*_1, a^*_2, \cdots, a^*_{N_r})^T$ such that the reduced solution $\widetilde{\mathbf{U}} = \overline{\mathbf{U}} + \Phi\mathbf{a}$ is as close as possible to the high-fidelity solution $\mathbf{U}^{hf}$ on the overlapping domain Ω_o, while also being close to the observed (and possibly imposed) values $\{\widehat{\mathbf{U}}_i\}^M_{i=1}$ at the M sensor points. Similarly to data $\widehat{\mathbf{U}}$, also the field $\widetilde{\mathbf{U}}$ evaluated at point-wise locations $\mathbf{x}_i$ is denoted $\widetilde{\mathbf{U}}_i$.

Mathematically, at a given time t, the temporal coefficients satisfy:

$$\mathbf{a}^* = \arg\min_{\mathbf{a}} \left(\frac{1}{|\Omega_o|} \int_{\Omega_o} \left(\mathbf{U}^{hf} - \widetilde{\mathbf{U}} \right)^2 \mathrm{d}\mathbf{x} + \frac{\beta}{M} \sum_{i=1}^{M} \left(\widehat{\mathbf{U}}_i - \widetilde{\mathbf{U}}_i \right)^2 \right), \quad \text{with} \quad \widetilde{\mathbf{U}} = \overline{\mathbf{U}} + \boldsymbol{\Phi}\mathbf{a}, \tag{4.6}$$

where the parameter β is used to weight the sensor contributions. For low values of β, the ROM approximation is mostly influenced by the FOM solution $\mathbf{U}^{hf}$. For large values of β, the ROM is mostly influenced by the sensor data $\widehat{\mathbf{U}}$, thus providing new information to the FOM. Values in between, $\beta \approx 1$, offer a compromise between FOM and sensor data contributions. With respect to these choices, the optimal POD field is then $\widetilde{\mathbf{U}} = \overline{\mathbf{U}} + \boldsymbol{\Phi}\mathbf{a}^*$.

The minimization problem may be defined over the entire set of variables or focus on specific ones, depending on the emphasis desired. Some tests, including the one discussed in Sec 4.3.3, indicate that using both the velocity field and the VOF leads to poorer coupling results, compared to solely using the VOF, or assigning it a higher weight. Moreover, some interpolations are necessary for data exchange between CFD and POD, potentially introducing errors. Combining velocity and VOF variables in the minimization problem may amplify the errors, while using only one variable could mitigate such issues. In addition, prioritizing the VOF aligns with the objective of monitoring the evolution of the free surface and, in any case, the velocity is inherently linked to the VOF through the transport equation (Eq. (3.36)) in the high-fidelity model. Based on those considerations, the minimization problem becomes:

$$\mathbf{a}^* = \arg\min_{\mathbf{a}} \left(\frac{1}{|\Omega_o|} \int_{\Omega_o} \left(\alpha^{hf} - \widetilde{\alpha} \right)^2 \mathrm{d}\mathbf{x} + \frac{\beta}{M} \sum_{i=1}^{M} \left(\widehat{\mathbf{U}}_i - \widetilde{\mathbf{U}}_i \right)^2 \right). \tag{4.7}$$

The M sensors represent measurement locations within experimental setups, open sea areas, or specific points on a computational grid. In any case, these sensors may provide data on several variables, either directly (velocity and VOF in this case) or indirectly. Considering that the first term of Eq. (4.7) is now exclusively reliant on the VOF, and that water elevation is readily measurable, both in experimental and numerical environments, the second term is also computed on VOF. The final version of the minimization problem is:

$$\mathbf{a}^* = \arg\min_{\mathbf{a}} \left(\frac{1}{|\Omega_o|} \int_{\Omega_o} \left(\alpha^{hf} - \widetilde{\alpha} \right)^2 \mathrm{d}\mathbf{x} + \frac{\beta}{M} \sum_{i=1}^{M} (\widehat{\alpha}_i - \widetilde{\alpha}_i)^2 \right). \tag{4.8}$$

Each physical field used in the POD snapshots can, then, be approximated as:

$$\begin{aligned} \widetilde{u} &= \overline{u} + \boldsymbol{\phi}^u \mathbf{a}^*, \\ \widetilde{v} &= \overline{v} + \boldsymbol{\phi}^v \mathbf{a}^*, \\ \widetilde{w} &= \overline{w} + \boldsymbol{\phi}^w \mathbf{a}^*, \\ \widetilde{\alpha} &= \overline{\alpha} + \boldsymbol{\phi}^\alpha \mathbf{a}^*. \end{aligned} \tag{4.9}$$

Coupled Model

As the POD serves as the low-fidelity model, a division into offline and online stages remains essential, accounting for the training of the POD basis functions. In contrast to the depiction of the POD ROM description in Figure 3.1, two components are slightly altered and highlighted in green in Figure 4.5: the definition of the ROM model, now the coupled CFD/POD-ROM, and the operational phase.

For the first green block, the multi-fidelity model writes:

$$\frac{\partial \mathbf{u}}{\partial t} + (\mathbf{u} \cdot \nabla)\mathbf{u} = -\frac{1}{\rho}\nabla p + \frac{1}{\rho}\nabla \cdot (\mu(\nabla \mathbf{u} + (\nabla \mathbf{u})^T)) + \mathbf{g} \qquad \text{in } \Omega_{hf}, \tag{4.10a}$$

$$\nabla \cdot \mathbf{u} = 0 \qquad \text{in } \Omega_{hf}, \tag{4.10b}$$

$$\frac{\partial \alpha}{\partial t} + \nabla \cdot (\alpha \mathbf{u}) = 0 \qquad \text{in } \Omega_{hf}, \tag{4.10c}$$

$$\mathbf{u} = \widetilde{\mathbf{u}} = \overline{\mathbf{u}} + \boldsymbol{\phi}^{\mathbf{u}} \mathbf{a}^* \qquad \text{on } \Gamma_{hf}, \tag{4.10d}$$

$$\alpha = \widetilde{\alpha} = \overline{\alpha} + \boldsymbol{\phi}^\alpha \mathbf{a}^* \qquad \text{on } \Gamma_{hf}, \tag{4.10e}$$

$$\mathbf{a}^* = \arg\min_{\mathbf{a}} \left(\frac{1}{|\Omega_o|} \int_{\Omega_o} \left(\alpha^{hf} - \widetilde{\alpha} \right)^2 \mathrm{d}\mathbf{x} + \frac{\beta}{M} \sum_{i=1}^{M} (\widehat{\alpha}_i - \widetilde{\alpha}_i)^2 \right), \quad \text{with } \widetilde{\alpha} = \overline{\alpha} + \boldsymbol{\phi}^\alpha \mathbf{a}. \tag{4.10f}$$

Here, Dirichlet boundary conditions are used for both velocity and VOF fields. Moreover, since the basis functions are defined over Ω_{lf}, which also includes Γ_{hf},

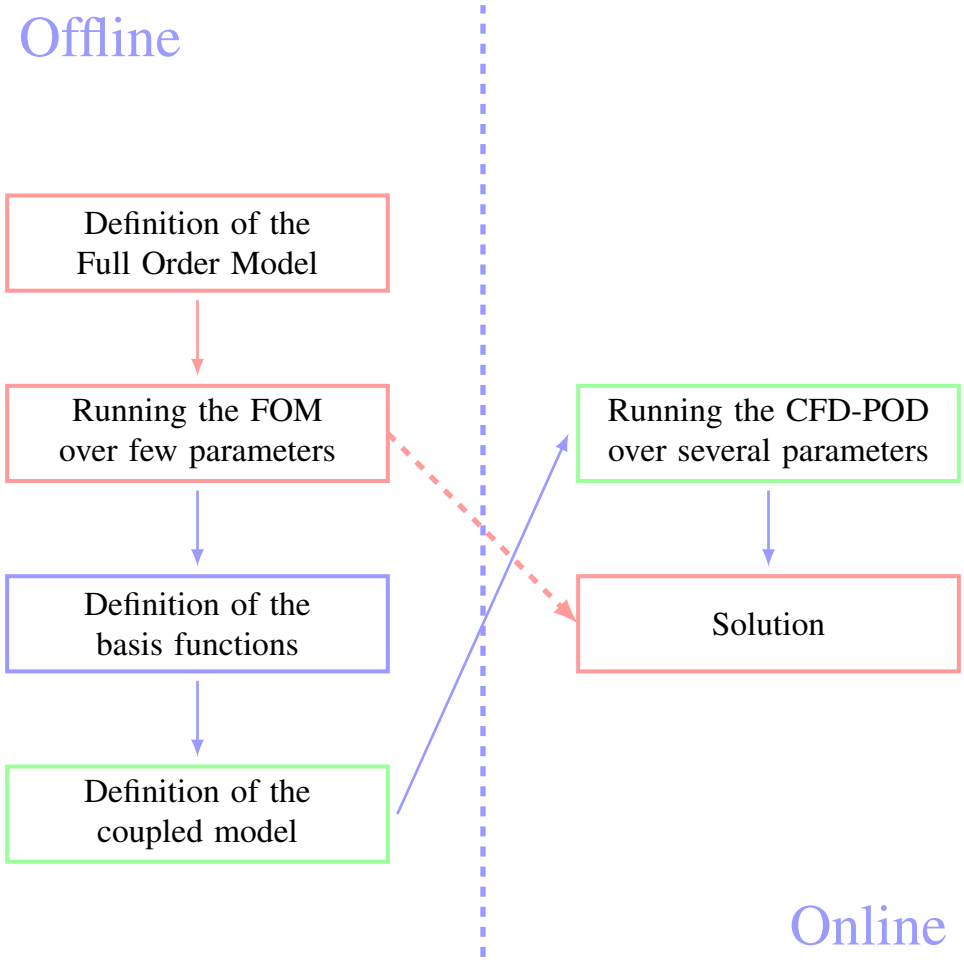

Fig. 4.5 Outline of the steps in a parametric study using the coupled CFD/POD-ROM model (red, blue, and green path). The comparison is still with the FOM model (red path), as in Figure 3.1.

the reconstruction of the fields in Eqs. (4.10d), (4.10e) is available in the low-fidelity domain, and acts as a propagation model.

For a clear overview of the coupling methodology during runtime, represented by the second green box in Figure 4.5, it must be recalled that the high-fidelity simulation is run on a commercial software, StarCCM+. This not only influences the way the boundary conditions are imposed, but also affects the coupling algorithm, and its implementation. Specifically, communication with the software occurs via CSV (Comma Separated Values) tables, for importing and exporting variable values. Moreover, to interact with the application and instruct the program on the tasks to

execute, Java macro files are essential. Consequently, the coupling methodology needs to be implemented into such Java macros.

The workflow of the coupling methodology is the following. First of all, few FOM simulations are conducted on Ω_{HF}, sampling the parameter space. Snapshots are collected for the variables of interest $\mathbf{U}(\mathbf{x},t;\eta) = (u, v, w, \alpha)^T$, and used to build the snapshot matrix $\mathbf{S} = (\mathbf{S}_{\eta_1}, \mathbf{S}_{\eta_2}, \ldots, \mathbf{S}_{\eta_{N_m}})$. Following the methodology outlined in the previous chapter, the POD basis functions $\Phi = (\boldsymbol{\phi}^{\mathbf{u}}, \boldsymbol{\phi}^{\alpha})^T$ are defined, and truncated to a number N_r yielding $\mathrm{RIC}(N_r) \geq \delta$, for a predefined δ. In this offline phase, StarCCM+ is used for the CFD simulations and snapshot generation, while the data processing is implemented in Matlab, though could be coded in any other programming language. The online phase occurs concurrently within StarCCM+ for the simulation in Ω_{hf}, and within the Java macro for the computation necessary to update the boundary conditions on Γ_{hf}. More in detail, the simulation is initiated on Ω_{hf}, with the imposition of initial conditions and boundary conditions of the target setup. A single time step is computed with the CFD solver, solving Eqs. (4.10a), (4.10b), (4.10c). The solution $\mathbf{U}^{hf}$ over Ω_{hf} is then exported from StarCCM+, and read into the Java macro. Subsequently, these results are used in the minimization problem described by Eq. (4.10f) over Ω_o, along with the precomputed basis functions known in the domain Ω_{lf}, which also includes the overlapping region. The temporal coefficients $\mathbf{a}^*$ for the current time step are computed and applied in Eqs. (4.10d), (4.10e), to determine the variable values on the boundary Γ_{hf}. Such boundary conditions are then transmitted back to StarCCM+, enabling it to proceed with the next time step. The iterative process continues until the simulation is completed. It should be noted that, once that the temporal coefficients $\mathbf{a}^*$ are computed, the solution is automatically known in the entire Ω_{lf} subdomain. However, this calculation can also be done a posteriori, during the post-processing. The choice is driven by the potential necessity of having the solution available across the entire simulation domain, particularly if it is required for other model couplings, such as nesting multiple coupled models to create a WEC farm. Finally, post-processing tasks are implemented in Matlab, primarily involving the importation of the solution, and computation of errors.

A more condensed version of the coupling algorithm is given in the following. It should be noted that the boundary conditions are imposed in an explicit manner, at $t = t_n$, even though the time scheme, in the CFD solver, is implicit. This particular is addressed in the next section.

Offline Phase

Snapshots for $\mathbf{U}(\mathbf{x},t;\eta) = (u, v, w, \alpha)^T \leftarrow$ FOM in Ω_{HF}
Definition of the basis functions set $\Phi = (\boldsymbol{\phi}^{\mathbf{u}}, \boldsymbol{\phi}^{\alpha})^T \leftarrow$ Snapshot matrix $\mathbf{S}$

Online Phase

At $t = t_n$
Impose boundary conditions on $\Gamma_{hf} \leftarrow \widetilde{\mathbf{U}}$ ▷ Eqs. (4.10d), (4.10e)

Do a time step in $\Omega_{hf} \rightarrow$ Compute $\mathbf{U}^{hf}$ ▷ Eqs. (4.10a), (4.10b), (4.10c)
At $t = t_{n+1}$
Compute $\mathbf{a}^* \leftarrow$ Minimization problem in Ω_o ▷ Eq. (4.10f)
return $\widetilde{\mathbf{U}}$ ▷ Eqs. (4.10d), (4.10e)
goto *top of online phase*.

Definition of the Interpolations

In general, the high-fidelity and the low-fidelity solutions can be computed on different meshes. However, they require a common framework for communication. The high-fidelity model implements a finite volume method on an octree grid, which is refined near the interface, and may include an overset grid when considering moving bodies. On the other hand, the low-fidelity solution is computed on the points of a uniform Cartesian grid, corresponding to the coarser cell size present in the high-fidelity mesh. Moreover, StarCCM+ exports the results on defined Cartesian coordinates, chosen here as the coarser meshgrid of the high-fidelity model, in the form of CSV tables. Consequently, an interpolation step is necessary, to transition from a finite volume approach to a finite difference one. The CFD software uses a default zeroth order interpolation method, meaning that no interpolation is actually performed on the data. The points in the table are considered unordered, and each point is assigned the value from the closest face or cell available, following a nearest neighbor approach. The same strategy is employed in reverse, when a table is imported in StarCCM+, to impose, for example, the boundary conditions on the boundary surfaces of the simulation domain.

In this study, the minimization on the overlapping domain is conducted on the low-fidelity Cartesian mesh for simplicity reasons, but one can opt to minimize on the high-fidelity octree mesh. Regardless of the choice, interpolations are required when information between subdomains is exchanged. For this reason, two interpolation functions are introduced, $\mathscr{I}_{\downarrow}$ and $\mathscr{I}_{\uparrow}$. The former represents the interpolation from the high-fidelity octree mesh, possibly with local refinements, to the low-fidelity mesh, which is the Cartesian uniform mesh of the coarser level (the background mesh). This interpolation is used to export the Ω_{hf} results, and to obtain the POD coefficients $\mathbf{a}^*$ in Ω_o. The latter represents the interpolation needed to impose the Dirichlet boundary conditions on Γ_{hf}, thus transitioning from the low-fidelity to the high-fidelity meshes. Then, for the Eqs. (4.10d), (4.10e), the values of $\mathbf{u}$ and α imposed as boundary conditions are actually

$$u = \mathscr{I}_{\uparrow}(\widetilde{u}) \quad v = \mathscr{I}_{\uparrow}(\widetilde{v}) \quad w = \mathscr{I}_{\uparrow}(\widetilde{w}) \quad \alpha = \mathscr{I}_{\uparrow}(\widetilde{\alpha}) \quad \text{on} \quad \Gamma_{hf}. \tag{4.11}$$

One may wish the property $\mathscr{I}_{\uparrow} = \mathscr{I}_{\downarrow}^{-1}$ to hold, but it might be not satisfied in the numerical standpoint.

Another interpolator is required when $M \neq 0$ sensors are employed in the coupling methodology. In such cases, $\mathscr{I}_S$ represents the interpolation from low-fidelity Cartesian mesh to the sensor locations $\mathbf{x}_i^S \in \Omega_{lf}$. Given that the sensor locations are typically static, and their number M is likely small, directly interpolating the POD modes onto $\{\mathbf{x}_i^S\}_{i=1}^M$ is the most straightforward and accurate approach, compared to the inverse. Since, here, only the VOF is considered at the sensors, $\alpha_i = \mathscr{I}_S(\alpha)$, and Eq. (4.10f) becomes

$$\mathbf{a}^* = \arg\min_{\mathbf{a}} \left(\frac{1}{|\Omega_o|} \int_{\Omega_o} \left(\mathscr{I}_{\downarrow}(\alpha^{hf}) - \widetilde{\alpha} \right)^2 \mathrm{d}\mathbf{x} + \frac{\beta}{M} \sum_{i=1}^{M} (\widehat{\alpha}_i - \mathscr{I}_S(\widetilde{\alpha}))^2 \right). \tag{4.12}$$

Interpolators also allow to compute errors on corresponding meshes. Therefore, Eqs. (3.15), (3.16) undergo slight modifications, as ξ_{ref} becomes $\mathscr{I}_{\downarrow}(\xi_{ref})$, and ξ_{approx} changes accordingly if it relates to the CFD solution; otherwise, no interpolation is needed, when relative to the POD reconstruction. However, interpolators inevitably introduce interpolation errors, which cannot be eliminated. There exists,

thus, a lower bound for the error that must be considered, and errors arising from the coupling methodology accumulate on this unavoidable value. Interpolation errors can also accumulate, for example when interpolating the high-fidelity solution from Ω_{hf}, and interpolating back the updated boundary conditions on Γ_{hf}. In that case, there is a combination of the form: $\widetilde{\mathbf{U}}_{\Gamma_{hf}} = \mathscr{I}_{\downarrow}(\mathbf{U}^{hf}) \circ \mathscr{I}_{\uparrow}(\widetilde{\mathbf{U}})$. Although efforts have been made to enhance the order of the interpolations, notable improvements have not been achieved.

4.3 Coupled Model Sensitivity Analysis

After the definition of the coupling methodology, and its implementation, several tests are needed to evaluate accuracy, robustness, and efficiency of the multi-fidelity model. Different setups are considered, with or without a moving body, with or without incoming waves, and variations in spatial and temporal domains. The main objective is the accurate reconstruction of the solution, the so-called *in-sample* test, but some prediction, or *out-of-sample*, tests are conducted as well.

For this analysis, the free wave test introduced at the end of the previous chapter is used, omitting any body presence or incoming wave, so $M = 0$. This test case is computationally affordable, and allows for in-depth parameter sensitivity analysis. While other flow configurations may yield different optimal parameter values, this study serves to identify the parameters crucial to the coupling strategy.
The big domain Ω_{HF} extends for $[L_x^{HF} \times L_y^{HF} \times L_z^{HF}] = [10 \times 6 \times 0.4]$m. Now, the high-fidelity subdomain is defined with default size $[L_x^{hf} \times L_y^{hf} \times L_z^{hf}] = [4 \times 2.5 \times 0.4]$m, yielding a reduction of 6 in volume (the R6 case in Section 4.3.5). The small size of $L_z^{HF} \equiv L_z^{hf}$ ensures reasonable computational costs. Maintaining the same domain size in the z direction, for both domains, establishes a simplified condition where the boundary conditions of the high-fidelity model are only four, in the x and y direction. With reference to Figure 4.4, the boundary conditions Γ_{HF} for the large domain used for the snapshots, Ω_{HF}, are all modeled as no-slip wall conditions, resulting in zero fluid velocity. Exceptions are Γ_{front}^{HF} and Γ_{back}^{HF}, defined as symmetry planes, where the normal velocity and the normal gradient of the variables are zero, resulting in zero flux across the plane. The same conditions are imposed on Γ_{front}^{hf} and Γ_{back}^{hf} for the high-fidelity subdomain. On the other boundaries, Γ_{inlet}^{hf}, Γ_{outlet}^{hf}, Γ_{top}^{hf}, and Γ_{bottom}^{hf}, Dirichlet conditions are applied to velocity and VOF. Pressure

is inferred using the value at the interior of the domain and cannot be controlled externally, for the well-posedness of the system to be solved numerically. Finally, in the initial part of the sensitivity analysis, the overlapping region extends over the entire high-fidelity subdomain, so $\Omega_o \equiv \Omega_{hf}$. The initial condition is defined by Eq. (3.50), with $H_w = 0.6\,\mathrm{m}$ and $H_s = 0\,\mathrm{m}$. The overall configuration is depicted in Figure 4.6.

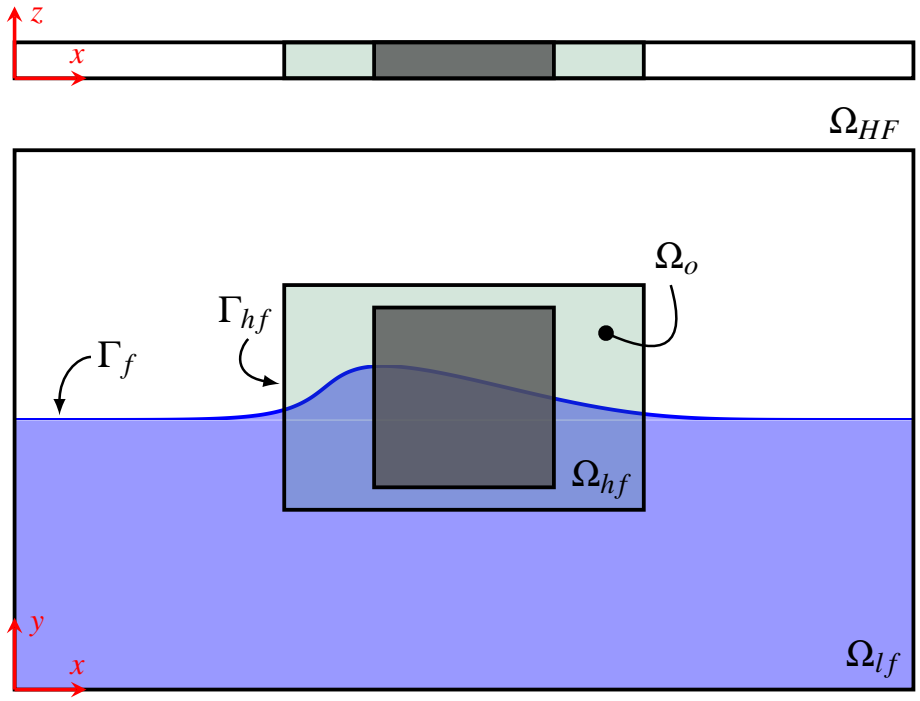

Fig. 4.6 Sketch of the flow configuration with definition of the subdomains. The initial condition (Eq. (3.50)), with $H_w = 0.6\,\mathrm{m}$ and $H_s = 0\,\mathrm{m}$ is shown.

Once the numerical setup is established, the sensitivity analysis can commence. The analysis delves into various physical and numerical parameters, each independently varied, while holding the others constant. To minimize potential biases, ideal scenarios will be considered for fixing the remaining parameters. The numerical sensitivity mostly pertains to the discretization of the mesh of the FOM model (Section 4.3.1), and the coupling temporal scheme (Section 4.3.2), as well as the definition of the POD (Section 4.3.3), and its sensitivity (Section 4.3.4), divided in the number of truncated modes and the number of snapshots used. Geometrical sensitivity relates to the sizes of the subdomains, so of the small high-fidelity Ω_{hf} (Section 4.3.5), and the overlapping region Ω_o (Section 4.3.5). Physical sensitivity

may be defined for the out-of-sample analysis (Section 4.3.6), with different heights of the initial wave condition, and the analysis of the information over time, towards clustering (Section 4.3.7).

4.3.1 Mesh Sensitivity

The first step in the coupling methodology involves the computation of the FOM solution for the definition of the basis functions. To have a correct numerical simulation of the phenomenon of interest, the FOM simulation has to be correctly defined and give accurate snapshots. In the setup of the FOM model, an important role is played by the spatial discretization, based on an Eulerian frame of reference. A hierarchical Cartesian (octree) mesh is used throughout the entire study, requiring careful definition to correctly discretize the evolving free surface, and, if applicable, the motion of a rigid body. To this aim, local refinements are defined, to balance computational cost and accuracy of the solution. The background mesh is uniform in all the directions, so the discretization is constant $\Delta x = \Delta y = \Delta z = h$, and the value of h may vary. Larger values of h result in a coarse mesh, that is lightweight but may provide inaccurate results. Conversely, smaller h values lead to precise discretizations, but at the expense of increased computational burden. To strike the right balance, four different meshes $\{\mathscr{M}_i\}_{i=1}^4$ are tested, for different h values, as listed in Table 4.1. The initial number of cells n_c^i, for mesh $\mathscr{M}_i$, is also provided, with $n_c^1 > n_c^2 > n_c^3 > n_c^4$. Each mesh incorporates two levels of refinement near the air-water interface, causing the number of mesh cells to evolve slightly over time, as the air-water interface moves. To evaluate mesh performance, comparisons are made using the finest $\mathscr{M}_1$ as reference, computing relative errors on the coarsest grid, $\mathscr{M}_4$. The total simulation is run up to $T = 3\,\text{s}$, with a constant time step of $\Delta t = 0.002$ s. Following the error definition in Section 3.2.3, $\xi_{ref} \equiv \xi_{\mathscr{M}_1}$, $\xi_{approx} \equiv \xi_{\mathscr{M}_i}, i = \{2, 3, 4\}$, and $\Omega_k \equiv \Omega_{HF}$. The errors are computed on velocity, VOF and pressure, and are displayed also in Table 4.1. For each quantity (u, v, w, α, and p), a first-order behavior is observed.

Mesh	h(m)	n_c	$\overline{\varepsilon}^u_{mesh}$	$\overline{\varepsilon}^v_{mesh}$	$\overline{\varepsilon}^w_{mesh}$	$\overline{\varepsilon}^\alpha_{mesh}$	$\overline{\varepsilon}^p_{mesh}$
$\mathscr{M}_4$	0.2	1.8×10^4	1.7e-3	6.6e-4	3.9e-2	1.8e-4	2.1e-5
$\mathscr{M}_3$	0.1	8.5×10^4	1.0e-3	3.3e-4	1.5e-2	1.1e-4	1.0e-5
$\mathscr{M}_2$	0.05	4.4×10^5	5.2e-4	1.7e-4	8.6e-3	5.0e-5	3.5e-6
$\mathscr{M}_1$	0.025	2.5×10^6	-	-	-	-	-

Table 4.1 Mesh characteristics and relative errors with respect to the finest mesh $\mathscr{M}_1$.

In Figure 4.7, a snapshot illustrating the position of the free surface, identified at $\alpha = 0.5$, is presented for the various $\mathscr{M}_i$ meshes. Coarser grids exhibit less precise resolution, suggesting a need to increase the number of local refinement levels. However, during the solution export, interpolations become necessary, and could potentially lose information, if the background is overly coarse. Among the meshes, $\mathscr{M}_2$, with $h = 0.05\,$m, represents a favorable trade-off between computational efficiency and accuracy, making it the chosen configuration for both Ω_{HF} and Ω_{hf} simulation setups. Moreover, when exporting the CFD solution in both cases, interpolation is performed onto a uniform Cartesian mesh with $\mathscr{M}_2$ characteristics, without local refinements, to ensure computation consistency. The same framework is retained for POD calculations, including the definition of the basis functions, and the resolution of the minimization problem during coupling.

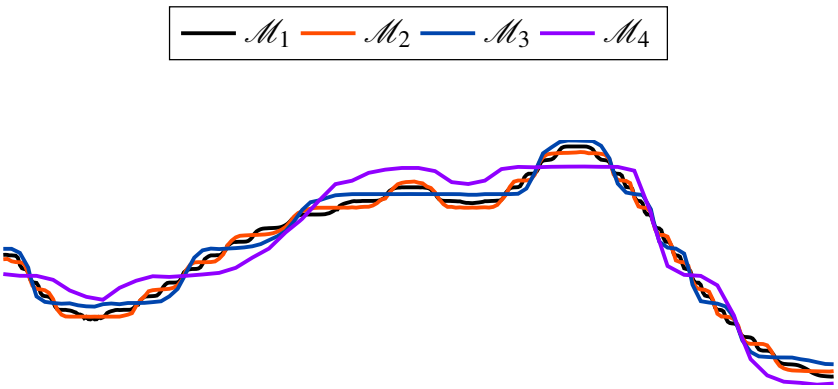

Fig. 4.7 Outline of the free surface (located at $\alpha = 0.5$), for the different mesh discretizations $\mathscr{M}_i$.

4.3.2 Coupling Algorithm Sensitivity

Once the CFD solution is obtained on the $\mathscr{M}_2$ mesh over Ω_{HF}, the POD basis functions can be computed, and the coupling model executed. However, a remark raised in the previous section must be addressed before proceeding. The discretization of the Navier-Stokes equations in the CFD software employs an implicit temporal scheme, chosen for stability considerations, when simulating traveling waves. In the coupling algorithm, the boundary conditions (4.10d), (4.10e) are imposed at time t_n, while they should be, more correctly, applied at time t_{n+1}. If the latter was the case, the minimization problem would become a fully coupled non-linear problem, where all equations (4.10a)-(4.10f) must be solved at the same time, *i.e.* the solution $U = (u, v, w, \alpha)$ and POD coefficients $\mathbf{a}^*$ must be solved simultaneously. Such non-linear minimization can be expensive in the numerical viewpoint, whereas an explicit coupling reduces to a least squares problem, where the POD coefficients $\mathbf{a}^*$ are computed from the known solution $\mathbf{U}^{hf}$ obtained from the previous time step. The goal is, thus, to investigate whether an explicit coupling approach might be acceptable, instead of an implicit one. To assess this, a comparison between the two approaches is conducted within a "fake" coupling setup. This means that, in order to avoid truncation errors due to the POD expansion ($N_r \leq N_s$), the boundary conditions imposed on Γ_{hf} are simply the high-fidelity solution $\widetilde{\mathbf{U}} = \mathbf{U}_{HF}$, pre-computed on the large domain for the same physical configuration. Essentially, this is equivalent to considering all the POD modes built from snapshots, computed at all times, without any truncation. So, in the implicit version, boundary conditions on Γ_{hf} are imposed using $\widetilde{\mathbf{U}}^{n+1} = \mathbf{U}_{HF}^{n+1}$, while in the explicit version, using $\widetilde{\mathbf{U}}^{n} = \mathbf{U}_{HF}^{n}$. In both versions, due to the export and import passages with the CFD software, interpolations are performed, so the real boundary conditions that are imposed are $\mathbf{U}^{n+1} = \mathscr{I}_{\uparrow} \circ \mathscr{I}_{\downarrow}(\mathbf{U}_{HF}^{n+1})$ and $\mathbf{U}^{n} = \mathscr{I}_{\uparrow} \circ \mathscr{I}_{\downarrow}(\mathbf{U}_{HF}^{n})$. One may expect to obtain null errors, at least in the implicit case. However, since $\mathscr{I}_{\downarrow} = \mathscr{I}_{\uparrow}^{-1}$ is not numerically verified, this is not the case. Moreover, due to interpolation on the velocity fields, the mass conservation may be violated, possibly leading to some pressure oscillations. Errors, both absolute and relative, are computed for two cases: one with a time step $\Delta t = 0.002\,\mathrm{s}$, and another with a bigger time step, $\Delta t = 0.004\,\mathrm{s}$. The original high-fidelity simulation on Ω_{HF} is computed for $t = [0, 3]\mathrm{s}$, with $\Delta t = 0.002\,\mathrm{s}$ for stability reasons in the VOF computation. However, the coupling simulation could have, in principle, a different time step, provided it preserves the same constraints of the original simulation. In

this case, doubling the time step also doubles the CFL, potentially compromising the accuracy of the HRIC scheme. Nevertheless, since the exchange of information occurs on a constant Cartesian mesh, the values of the free surface, refined during the CFD simulation, are interpolated, inevitably leading to some loss of accuracy in any case. Table 4.2 shows the relative errors on the subdomain Ω_{hf}, with ξ_{approx} given by the results from the CFD solver during coupling runtime.

	Case		$\bar{\varepsilon}^u$	$\bar{\varepsilon}^v$	$\bar{\varepsilon}^w$	$\bar{\varepsilon}^\alpha$	$\bar{\varepsilon}^p$
Ω_{hf}	Implicit	$dt = 0.002\,\mathrm{s}$	2.60e-5	1.69e-5	1.89e-3	5.78e-6	2.06e-6
		$dt = 0.004\,\mathrm{s}$	7.15e-5	5.13e-5	3.19e-3	1.49e-5	4.89e-6
	Explicit	$dt = 0.002\,\mathrm{s}$	2.98e-5	1.91e-5	1.94e-3	7.58e-6	2.37e-6
		$dt = 0.004\,\mathrm{s}$	8.67e-5	5.93e-5	3.28e-3	2.23e-5	6.00e-6

Table 4.2 Relative errors of the coupling approach with two time steps, for explicit and implicit "fake" coupling.

As Table 4.2 and Figure 4.8 show, the errors are comparable for all the cases, for implicit, explicit, and both the time steps, with a constant evolution over time. Therefore, for sake of simplicity and efficiency, the explicit version with $\Delta t = 0.004\,\mathrm{s}$ is adopted in the coupling methodology. During in-sample test, *i.e.* where the same parameters in Eq. (3.50) are used in both Ω_{HF} and Ω_{hf}, the errors computed with exact explicit boundary conditions establish a lower bound for the coupling methodology. The exact boundary conditions can be equivalently computed by POD with $N_r = N_s = N_i$, with N_i the number of temporal iterations required by the high-fidelity solution. Extra errors will thus inevitably be added when considering reduced basis with $N_r \ll N_s \leq N_i$, as presented in Section 4.3.4.

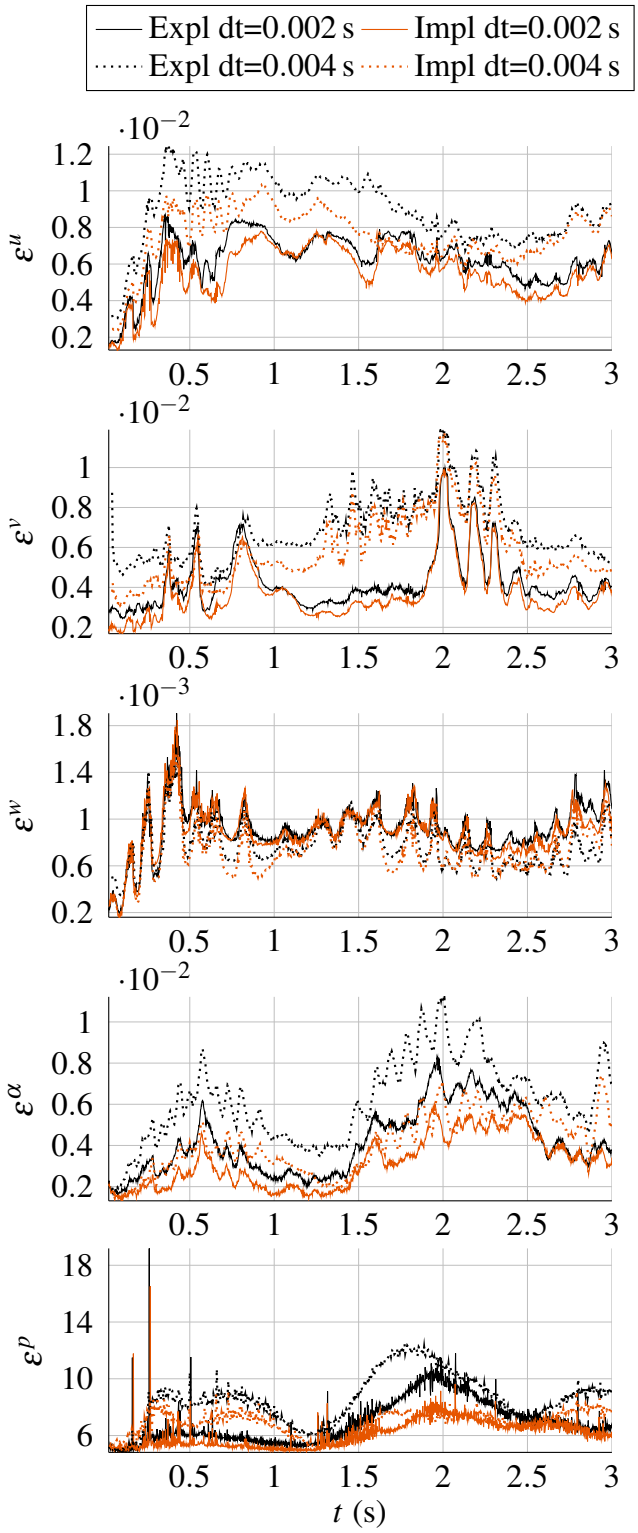

Fig. 4.8 Evolution of the absolute errors for the velocity, VOF and pressure variables over time, for the different coupling approaches tested.

4.3.3 Definition of the POD basis functions set

After establishing the mesh and the coupling algorithm, the analysis can move to the low-fidelity component. Here, decisions must be taken regarding the strategy for defining the basis functions, as well as determining the appropriate number of modes and snapshots.

Throughout the document, a single set of basis functions is employed, for simplicity of the related model, and for the better results generally obtained. However, exploring alternative approaches could potentially yield even more favorable outcomes. In this section, an approach where the basis functions are constructed separately for the velocity and the VOF, is introduced.

While the reference approach defines the basis functions as $\Phi = (\boldsymbol{\phi}^{\mathbf{u}}, \boldsymbol{\phi}^{\alpha})^T$, this approach considers velocity and VOF having separated basis functions: $\Phi = (\boldsymbol{\zeta}^{\mathbf{u}}, \boldsymbol{\vartheta}^{\alpha})^T$. Consequently, the minimization problem undergoes a transformation, as it is now formulated for both velocity *and* VOF. Hence, Eq. (4.6) is split into two expressions, one for velocity and one for VOF:

$$\begin{aligned}
\mathbf{c}_{\mathbf{u}}^{*} &= \arg\min_{\mathbf{c}_{\mathbf{u}}} \left(\frac{1}{|\Omega_o|} \int_{\Omega_o} \left(\mathbf{u}^{hf} - \widetilde{\mathbf{u}} \right)^2 \mathrm{d}\mathbf{x} + \frac{\beta}{M} \sum_{i=1}^{M} (\widehat{\mathbf{u}}_i - \widetilde{\mathbf{u}}_i)^2 \right), \quad \text{with} \quad \widetilde{\mathbf{u}} = \overline{\mathbf{u}} + \boldsymbol{\zeta}^{\mathbf{u}} \mathbf{c}_{\mathbf{u}}, \\
\mathbf{c}_{\alpha}^{*} &= \arg\min_{\mathbf{c}_{\alpha}} \left(\frac{1}{|\Omega_o|} \int_{\Omega_o} \left(\alpha^{hf} - \widetilde{\alpha} \right)^2 \mathrm{d}\mathbf{x} + \frac{\beta}{M} \sum_{i=1}^{M} (\widehat{\alpha}_i - \widetilde{\alpha}_i)^2 \right), \quad \text{with} \quad \widetilde{\alpha} = \overline{\alpha} + \boldsymbol{\vartheta}^{\alpha} \mathbf{c}_{\alpha}.
\end{aligned} \tag{4.13}$$

The physical fields are now approximated as:

$$\begin{aligned}
\widetilde{u} &= \overline{u} + \boldsymbol{\zeta}^{u} \mathbf{c}_{\mathbf{u}}^{*}, \\
\widetilde{v} &= \overline{v} + \boldsymbol{\zeta}^{v} \mathbf{c}_{\mathbf{u}}^{*}, \\
\widetilde{w} &= \overline{w} + \boldsymbol{\zeta}^{w} \mathbf{c}_{\mathbf{u}}^{*}, \\
\widetilde{\alpha} &= \overline{\alpha} + \boldsymbol{\vartheta}^{\alpha} \mathbf{c}_{\alpha}^{*}.
\end{aligned} \tag{4.14}$$

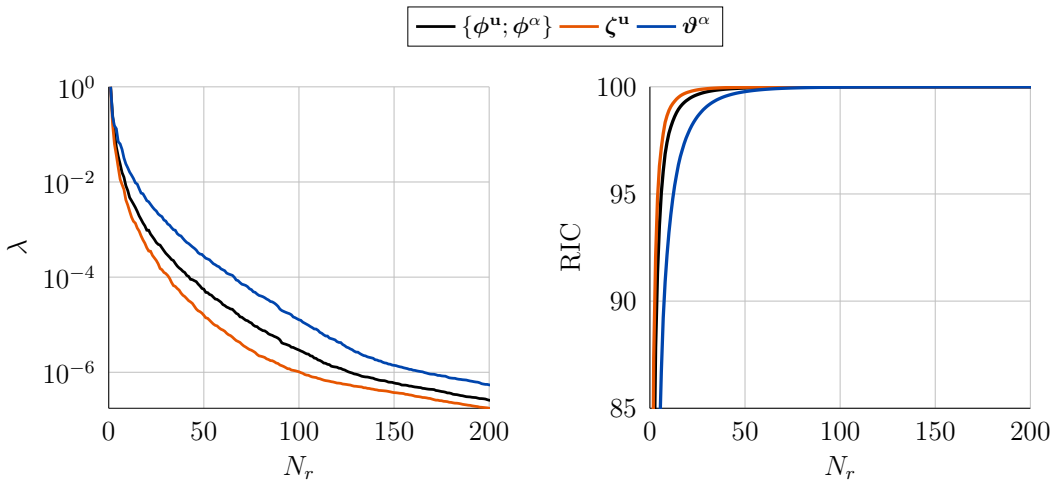

Fig. 4.9 Evolution of the eigenvalues spectrum, normalized to the fist eigenvalue (left), and of the RIC (right) with respect to the number of POD modes N_r, for the two approaches for the definition of the basis functions. The plots show only values for the first 200 modes.

The POD (normalized) eigenvalue spectrum $\{\lambda_i/\lambda_1\}_{i=1}^{N_s}$ and relative information content $\text{RIC}(N_r) = \sum_{i=1}^{N_r}\lambda_i/\sum_{i=1}^{N_s}\lambda_i$ are plotted in Figure 4.9, for the two different approaches. Separating the two physical fields yields to a different compression of the information, evident in the varying rates in the eigenvalue descent for velocity and VOF, and conversely, increase in the RIC. In general, velocity and VOF information may exhibit slight variations in their evolution, despite their close correlation, as also visible in the first projection coefficients in Figure 4.10. This discrepancies suggest the potential for selecting different N_r values for each field, achieving optimal information compression. However, as visible from Eq. (4.13), the minimization problem doubles, necessitating two distinct coefficient sets, and increasing runtime demands, albeit not representing the most computationally costly step of the coupling methodology. Moreover, if $M \neq 0$, integrating sensor data information on the velocity becomes imperative, posing potential challenges if such data are not readily available.

In any case, holding $N_s = 750$ and $N_r = 30$ for all physical fields, in both approaches, allows for comparison of results from the coupled model. Outcomes obtained from the coupled model, as detailed in Table 4.3, show the advantage of using the same basis functions set for all considered physical fields, resulting in errors reduced by up to one order of magnitude. Such a result could potentially be attributed, once more, to the interpolation procedures, which might undermine any enhancement in accuracy, when utilizing separate basis functions. Additionally, simultaneously

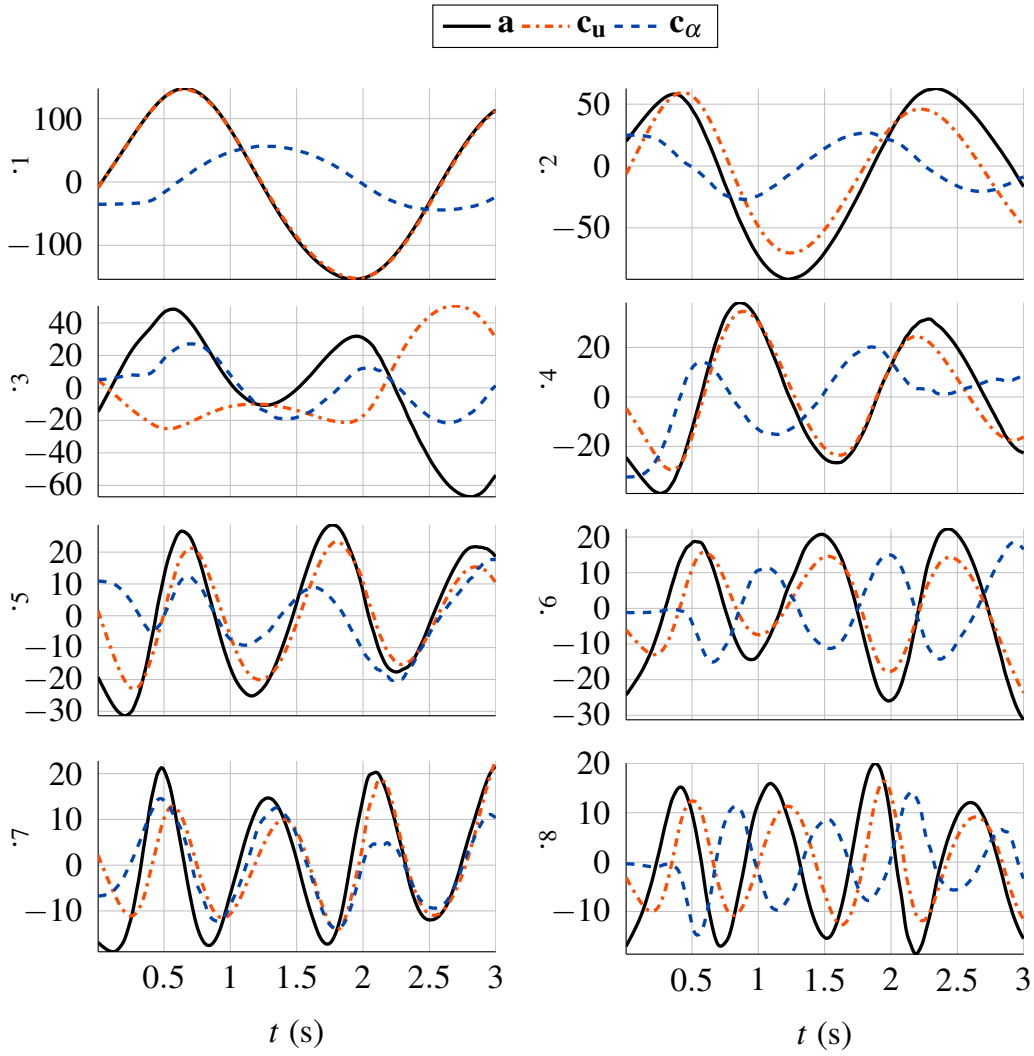

Fig. 4.10 First eight projection coefficients for the two approaches for the definition of the basis functions.

	Case	$\bar{\varepsilon}^u$	$\bar{\varepsilon}^v$	$\bar{\varepsilon}^w$	$\bar{\varepsilon}^\alpha$
$\Omega_{lf} \setminus \Omega_o$	$\Phi = (\boldsymbol{\zeta}^{\mathbf{u}}, \boldsymbol{\vartheta}^{\alpha})^T$	6.61e-4	5.26e-4	1.78e-3	1.47e-4
	$\Phi = (\boldsymbol{\phi}^{\mathbf{u}}, \boldsymbol{\phi}^{\alpha})^T$	7.63e-5	5.35e-5	7.09e-4	1.86e-5
Ω_{hf}	$\Phi = (\boldsymbol{\zeta}^{\mathbf{u}}, \boldsymbol{\vartheta}^{\alpha})^T$	1.17e-3	6.88e-4	4.19e-2	3.70e-4
	$\Phi = (\boldsymbol{\phi}^{\mathbf{u}}, \boldsymbol{\phi}^{\alpha})^T$	1.91e-4	1.32e-4	1.08e-2	2.63e-5

Table 4.3 Relative errors over the high-fidelity domain Ω_{hf} and over the remaining low-fidelity domain $\Omega_{lf} \setminus \Omega_o$, for the two approaches for the definition of the basis functions.

minimizing both velocity and VOF could intuitively yield optimal results. However, when applying boundary conditions to the CFD model, ensuring consistency in variable values is crucial, given their close numerical relationship. The simultaneous minimization might not always makes such consistency achievable numerically.
In any case, these findings corroborate the decision to adopt a simple model, which provides a single set of temporal coefficients, a choice maintained throughout the chapter. Although alternative strategies might promise even better results, the current approach is deemed satisfactory for the present analysis.

4.3.4 POD Sensitivity

Being the POD strategy defined at this point, a sensitivity analysis on the number of modes N_r, and of snapshots N_s, can be conducted. The evolution of the eigenvalues and the RIC is recalled, for the POD strategy considered, in Figure 4.11.

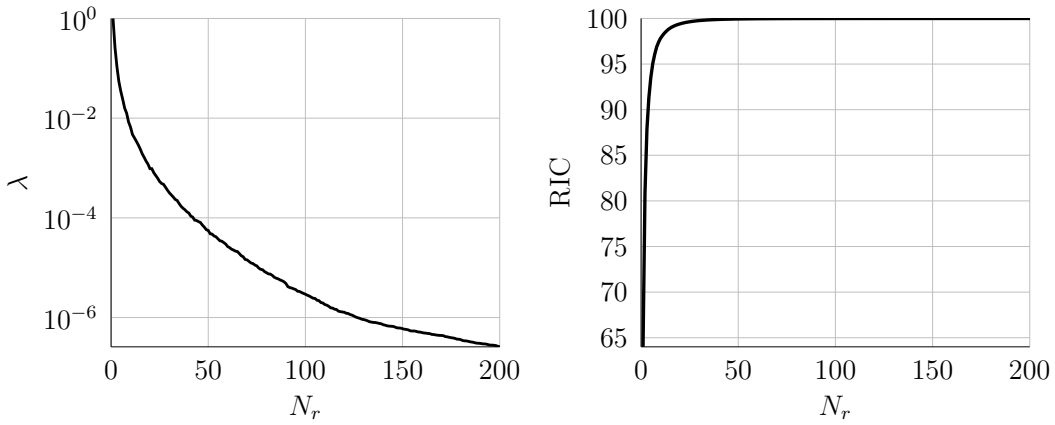

Fig. 4.11 Evolution of the eigenvalues spectrum, normalized to the fist eigenvalue (left), and of the RIC (right) with respect to the number of POD modes N_r. The plots show only values for the first 200 modes.

In a first moment, in both N_r and N_s sensitivity analyses, the projection errors are examined, for varying N_r and N_s, computed following the definition in Section 3.2.3. Here, $\xi_{ref} \equiv \xi_{HF}$, $\xi_{approx} \equiv \overline{\xi} + \sum_{k=1}^{N_r} a_k^{proj}(t_i)\boldsymbol{\phi}_k^{\xi}$ for $i = 1,\ldots,N_i$. The projection coefficients are computed as $a_k^{proj}(t_i) = \mathscr{I}_{\downarrow}(\mathbf{U}_{HF}(t_i))^T \cdot \boldsymbol{\Phi}_k$. Subsequently, the results of the coupled model are produced for few values of N_r and N_s, and compared to the high-fidelity reference solution. Errors are computed in subdomains Ω_{hf}, and $\Omega_{lf} \setminus \Omega_o$, and in this test case, the overlapping region is still considered $\Omega_o \equiv \Omega_{hf}$.

The dual objective of the hybrid fidelity coupling is recalled. Firstly, the POD reduced order solution $\widetilde{\mathbf{U}} = \overline{\mathbf{U}} + \Phi\mathbf{a}^*$, with the optimized coefficients $\mathbf{a}^*$, is used to provide appropriate boundary conditions for the small high-fidelity domain Ω_{hf}. Secondly, it propagates information through the large domain, $\Omega_{lf} \setminus \Omega_o = \Omega_{HF} \setminus \Omega_{hf}$. Particularly, the ξ_{approx} is determined by the CFD solution computed on Ω_{hf} during runtime, or by the POD reconstruction over $\Omega_{lf} \setminus \Omega_o$, using the basis functions and the temporal coefficients $\mathbf{a}^*$, at each time step.

Sensitivity of the number of modes

The sensitivity of the number of modes N_r is studied keeping constant the number of snapshots $N_s = 750$, across the entire domain Ω_{HF}. For an effective reduction, one wishes to minimize N_r as much as possible. The trend of the errors plotted in Figure 4.12 aligns with the trend of the POD eigenvalues in Figure 4.11: errors decrease as the number of POD modes increases. Although in principle, N_r could exceed 100, one can already foresee, from Figure 4.12, the projection errors reaching a plateau, thus showing marginal improvement beyond this point. Moreover, the computational time increases with the number of POD modes retained, hence, it should be limited as much as possible.

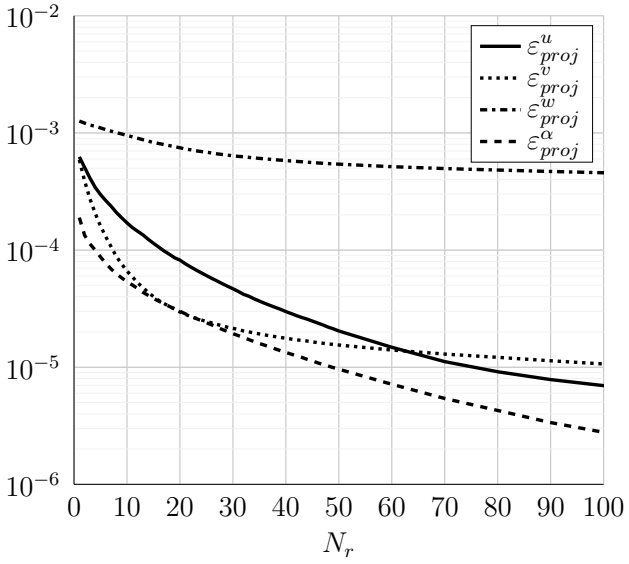

Fig. 4.12 Evolution of the projection errors for the velocity and the VOF fields, with respect to the number of POD modes N_r. The plots show only values for the first 100 modes.

From Table 4.4, the coupled model proves a similar trend, albeit with larger errors compared to the projection, summing the approximations associated to model reduction, to the lower bound related to interpolation. Furthermore, errors in the high-fidelity subdomain generally surpass those of the low-fidelity reconstruction. This discrepancy likely arises because in Ω_{lf}, the solution is filtered by the POD basis functions defined across the large domain, employing a coarse mesh scale, while the CFD model accurately resolves the Navier-Stokes equations in each cell of the mesh.

	Case	$\bar{\varepsilon}^u$	$\bar{\varepsilon}^v$	$\bar{\varepsilon}^w$	$\bar{\varepsilon}^\alpha$
$\Omega_{lf} \setminus \Omega_o$	$N_r = 5$	7.28e-4	6.53e-4	1.25e-3	1.10e-4
	$N_r = 10$	2.57e-4	1.88e-4	9.98e-4	4.75e-5
	$N_r = 20$	1.17e-4	8.09e-5	7.98e-4	2.60e-5
	$N_r = 30$	7.63e-5	5.35e-5	7.09e-4	1.86e-5
	$N_r = 50$	6.01e-5	4.61e-5	6.33e-4	1.28e-5
	$N_r = 100$	5.71e-5	4.68e-5	5.95e-4	1.11e-5
Ω_{hf}	$N_r = 5$	1.36e-3	1.10e-3	1.06e-1	2.61e-4
	$N_r = 10$	4.42e-4	3.21e-4	2.11e-2	6.55e-5
	$N_r = 20$	3.34e-4	2.27e-4	2.91e-2	2.58e-5
	$N_r = 30$	1.91e-4	1.32e-4	1.08e-2	2.63e-5
	$N_r = 50$	1.49e-4	1.08e-4	7.81e-3	2.65e-5
	$N_r = 100$	1.16e-4	8.40e-5	4.86e-3	2.73e-5

Table 4.4 Relative errors over the high-fidelity domain Ω_{hf} and over the remaining low-fidelity domain $\Omega_{lf} \setminus \Omega_o$, for the model based on different numbers of POD modes.

Table 4.4 also shows that starting from $N_r = 20$, the VOF error is almost constant in the domain Ω_{hf}. The higher VOF POD modes are probably being filtered by the interpolator $\mathscr{I}_\uparrow$ used to impose the boundary conditions. Since all the other errors are still decreasing with N_r, a slightly larger value, $N_r = 30$ is arbitrarily chosen, which still accounts for only 4% of the total size of the problem.

Finally, a qualitative comparison of the temporal evolution of the first five POD coefficients $\mathbf{a}_{proj}(t)$ obtained by projection (eigenvectors of the POD) and by the coupling strategy $\mathbf{a}^*(t)$, is given in Figure 4.13. The close agreement observed validates the reduced order model obtained with the Galerkin-free coupling strategy.

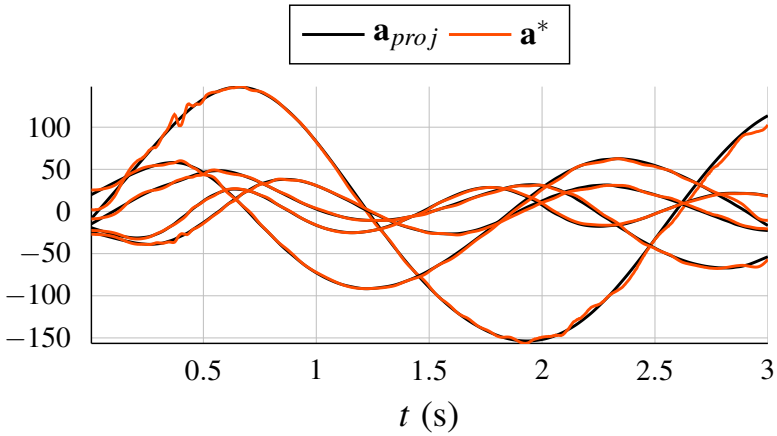

Fig. 4.13 Comparison of the POD temporal coefficients obtained by projection (in black) and by the coupling strategy (in orange).

Sensitivity of the number of snapshots

As observed earlier, the number of temporal iterations N_i for the original high-fidelity simulation does not necessarily correspond to the number of snapshots N_s collected to build the snapshot matrix $\mathbf{S}$. For several reasons, the original simulation may require numerous iterations, but only fewer $N_s \leq N_i$ could suffice to correctly capture the right evolution of the phenomenon. Therefore, varying N_s can potentially reduce the cost of the offline phase. In the studied scenario, the original time step is $\Delta t = 0.002\,\text{s}$, resulting in $N_i = 1500$, whereas the coupling model time step is $\Delta t = 0.004\,\text{s}$, yielding $N_i = 750$ for the reproduction of the same temporal evolution $t = [0,3]\text{s}$. Holding the number of POD basis functions constant to $N_r = 30$ and the higher N_s bound fixed to 750, different multiples of Δt are explored, yielding smaller values for N_s. Figure 4.14 illustrates that the projection errors slightly decrease with an increasing amount of snapshots considered, showing a mild trend. The relative errors presented in Table 4.5 reinforce the notion that the impact of N_s is limited. The RIC decreases with increasing N_s, because the reduction increases, or, equivalently, N_r/N_s decreases. However, this increase in N_s does not necessarily translate to largely smaller errors, as demonstrated. Those considerations, along with the anticipation of the following sensitivity analyses (Section 4.3.6 and Section 4.3.7), where the snapshots dataset will undergo substantial changes, motivate the choice of setting $N_s = 250$ in what follows.

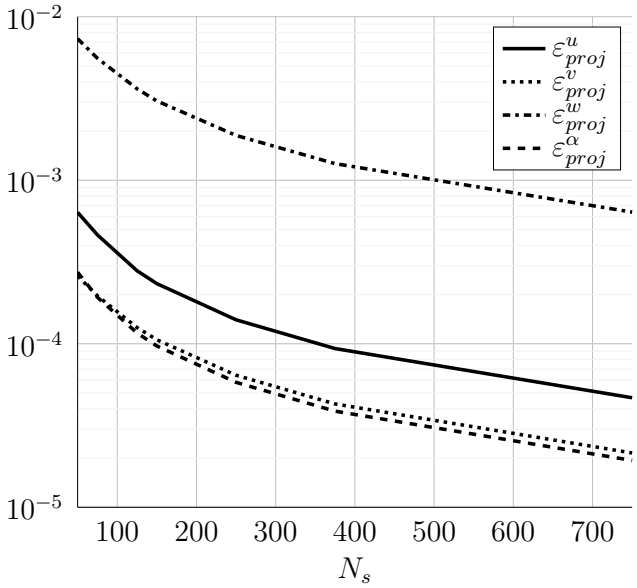

Fig. 4.14 Evolution of the projection errors for the velocity and the VOF fields, with respect to the number of snapshots N_s.

N_s	Multiple of Δt	RIC (%)	$\bar{\varepsilon}^u_{proj}$	$\bar{\varepsilon}^v_{proj}$	$\bar{\varepsilon}^w_{proj}$	$\bar{\varepsilon}^\alpha_{proj}$
50	15	99.80	6.4e-4	2.6e-4	7.3e-3	2.7e-4
75	10	99.78	4.6e-4	2.0e-4	5.6e-3	1.9e-4
150	5	99.77	2.3e-4	1.1e-4	3.1e-3	9.7e-5
250	3	99.77	1.4e-4	6.4e-5	1.9e-3	5.8e-5
750	1	99.77	4.7e-5	2.1e-5	6.4e-4	1.9e-5

Table 4.5 Characteristics and projection errors of velocity and VOF fields, for various number of snapshots N_s.

Finally, the ultimate configuration is $N_r = 30$ and $N_s = 750$. Such a configuration produces absolute errors evolving with time as plotted in Figure 4.15.

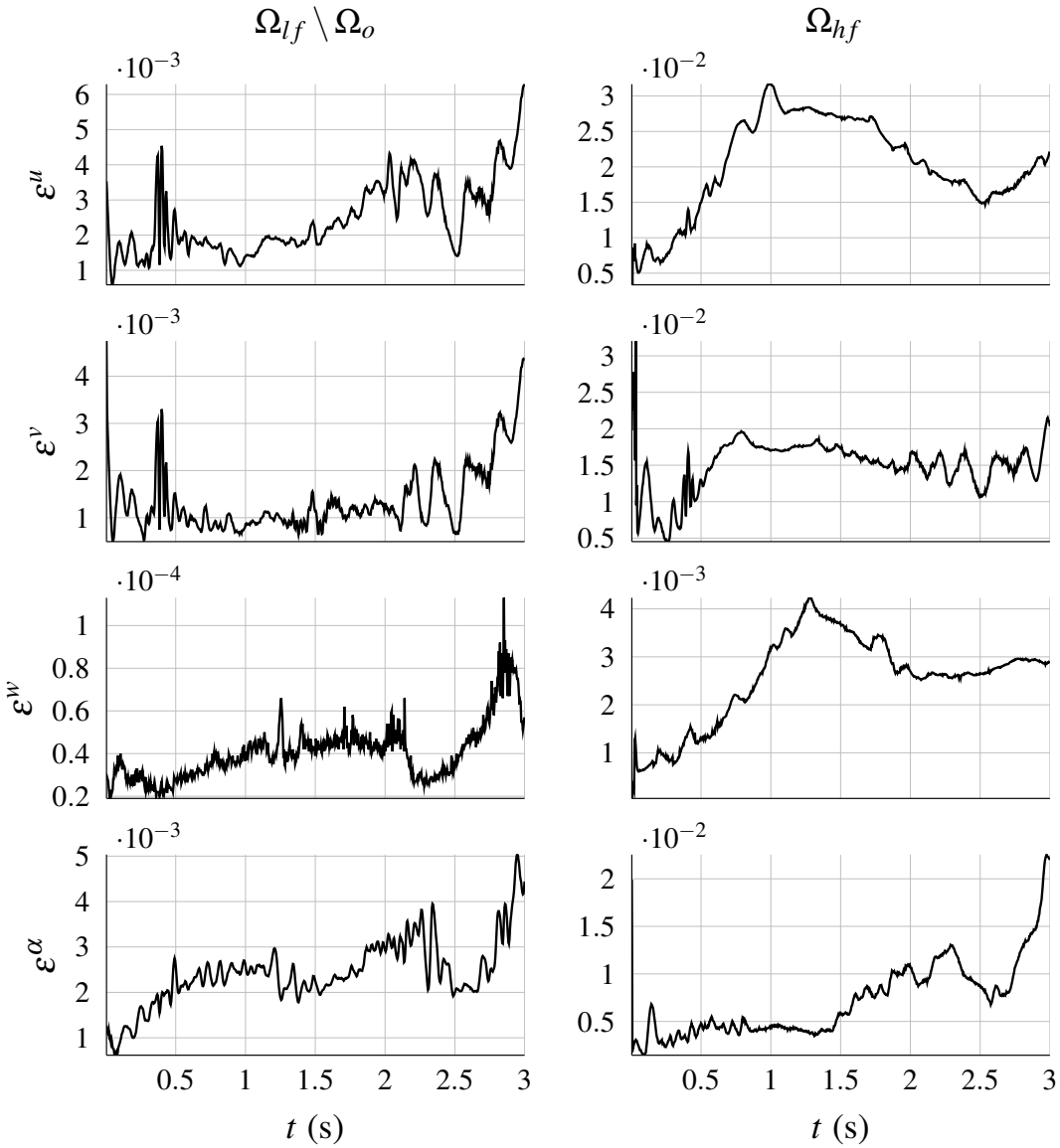

Fig. 4.15 Evolution of the absolute errors for the velocity and VOF fields over time, over the high-fidelity domain Ω_{hf} and over the remaining low-fidelity domain $\Omega_{lf} \setminus \Omega_o$. The POD ROM model is built with $N_r = 30$ and $N_s = 750$.

4.3.5 Subdomains Size Sensitivity

The selection of the size of the subdomains does not directly affect the coupling methodology, but does impact the outcomes of the coupled model. Variations in the size of the high-fidelity subdomain yield corresponding fluctuations in model errors, with an opposite effect on computational costs. Similarly, alterations in the dimensions of the overlapping region, Ω_o, currently encompassing the entire Ω_{hf}, impact both the computational burden of the minimization problem for $\mathbf{a}^*$, and the accuracy of such resolution. The two sensitivity analyses are treated independently, holding the other parameter constant.

Sensitivity of the size of high-fidelity domain

At this stage, the overlapping region is still held $\Omega_o \equiv \Omega_{hf}$. A large Ω_{hf} is expected to result in more accurate outcomes, compared to smaller subdomain sizes, since a larger portion of the entire Ω_{HF} is simulated with the high-fidelity solver, leaving only a small portion for approximation by the low-fidelity solver. To investigate this, three different sizes are considered, denoting each configuration R_D, with parametrization via the volume ratio $D = \frac{|\Omega_{HF}|}{|\Omega_{hf}|}$. All the simulations previously shown use R_6. Two other sizes, namely a larger one with R_3, and a smaller one with R_8 are now simulated as well. The three cases are outlined in Figure 4.16 and Table 4.6 shows the ratio of the number of mesh cells at initialization, $R_{n_{cells}} = \frac{n_{cells}^{\Omega_{HF}}}{n_{cells}^{\Omega_{hf}}}$. The relationship is not linear, but rather depends on the shape and position of Ω_{hf}, especially considering that the majority of the cells are concentrated around the free surface, where adaptive mesh refinement is employed.

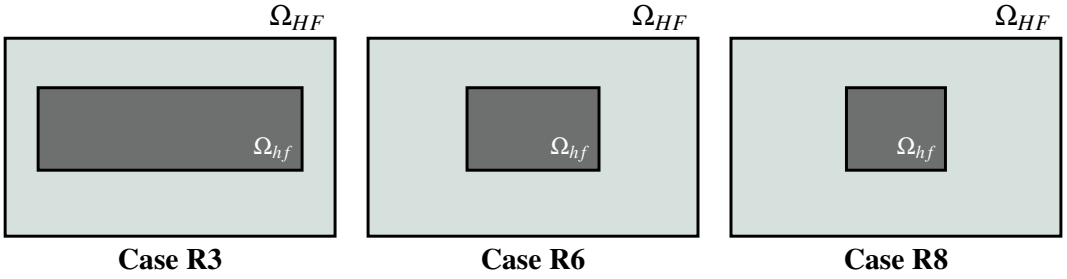

Fig. 4.16 Outline of the high-fidelity subdomain Ω_{hf} with varying size, yielding the different test cases.

Case	R_D	$R_{n_{cells}}$
R_3	3	1.69
R_6	6	3.38
R_8	8	4.50

Table 4.6 Volume ratio R_D and number of mesh cells ratio $R_{n_{cells}}$ for the the three test cases analyzed.

From Table 4.7, the errors obtained for the R_3 and R_6 cases are almost the same, while the error for the R_8 case is larger. A good trade-off between computational time and accuracy seems to be the R_6 case. This case has been chosen in the previous sections and will, thus, continue to be used in what follows.

	Case	$\bar{\varepsilon}^u$	$\bar{\varepsilon}^v$	$\bar{\varepsilon}^w$	$\bar{\varepsilon}^\alpha$
$\Omega_{lf} \setminus \Omega_o$	R_3	6.77e-5	3.92e-5	7.38e-4	1.42e-5
	R_6	7.63e-5	5.35e-5	7.09e-4	1.86e-5
	R_8	1.34e-4	1.20e-4	7.86e-4	2.52e-5
Ω_{hf}	R_3	1.44e-4	1.41e-4	9.69e-3	2.08e-5
	R_6	1.91e-4	1.32e-4	1.08e-2	2.63e-5
	R_8	6.31e-4	3.09e-4	2.27e-2	4.88e-5

Table 4.7 Relative errors over the high-fidelity domain Ω_{hf} and over the remaining low-fidelity domain $\Omega_{lf} \setminus \Omega_o$, for the test cases with varying high-fidelity domain size.

The modest size of the computational domain selected for the sensitivity analysis enables a straightforward comparison of computational times. Both the original CFD simulation on Ω_{HF} and the coupled model are executed on the same computer, using 6 processors. In the R_6 scenario, alongside a high-fidelity mesh cell reduction of over 3 (as indicated in Table 4.6), a speedup factor of 4.35 is achieved.

Sensitivity of the size of the overlapping domain

In the previous analysis, the overlapping region is considered $\Omega_o \equiv \Omega_{hf}$ for simplicity, and corresponds hereafter to the reference, case 0. Three other frame-shaped domains Ω_o are also considered, and presented in Figure 4.17.

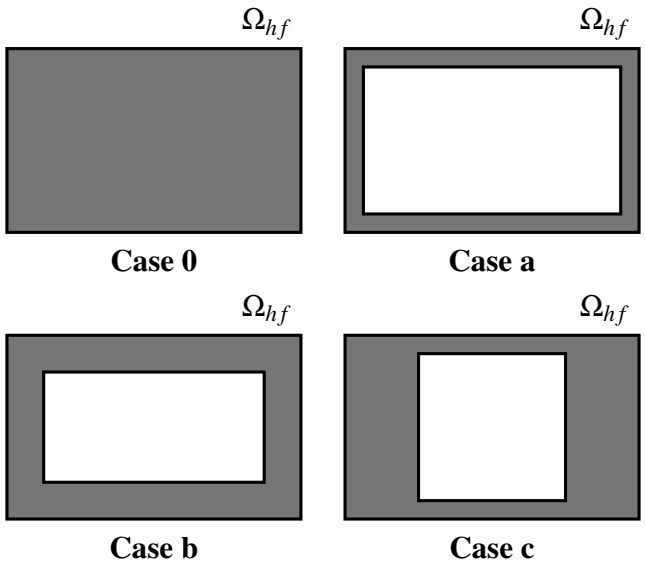

Fig. 4.17 Outline of the overlapping subdomain Ω_o with varying size, yielding the different test cases.

If no sensors are considered ($M = 0$), the minimization problem for $\mathbf{a}^*$ is well-posed if the number of mesh cells N_e included in Ω_o is $N_e \geq N_r$. Each configuration tested here satisfies this requirement. The cases (a), (b), and (c) all present hollow overlapping regions, embedding the region where a rigid body is supposed to be moving. In general, as mentioned, POD encounters challenges when applied to systems involving moving bodies. This difficulty primarily arises because POD basis functions are spatially defined on fixed points, possibly on a mesh grid. However, the movement of a body, whether followed through a deforming mesh or an overset mesh, can disrupt the position or availability of values at these points. To mitigate these issues, one could opt for the implementation of more intricate methods [219, 220]. Alternatively, a simple strategy would be to exclude the portion of the domain where the body is expected to move. This last approach is implemented in the proposed coupling methodology, and ensures that the POD basis functions remain appropriately defined on a consistent mesh.

Case 0, embedding the majority of points for the minimization problem, is expected to give the most accurate outcomes. However, for the reason just explained, it is not a suitable choice for simulations involving moving bodies. On the other hand, cases (a) and (b) feature uniformly shaped overlapping regions, extending 5 and 10 grid elements from the boundaries, respectively. A non-uniform overlapping

region is considered for case (c), with fewer elements above and below the body area, primarily extending longitudinally along the zone containing the free surface.

	Case	$\bar{\varepsilon}^u$	$\bar{\varepsilon}^v$	$\bar{\varepsilon}^w$	$\bar{\varepsilon}^\alpha$
$\Omega_{lf} \setminus \Omega_o$	0	7.61e-5	5.33e-5	7.22e-4	1.86e-5
	a	2.23e-3	1.98e-3	4.45e-3	2.92e-4
	b	1.81e-3	1.80e-3	2.47e-3	2.59e-4
	c	2.30e-4	2.06e-4	8.05e-4	2.83e-5
Ω_{hf}	0	1.85e-4	1.29e-4	1.14e-2	2.61e-5
	a	3.50e-3	3.63e-3	4.28e-1	3.67e-4
	b	2.48e-3	2.32e-3	1.39e-1	5.12e-4
	c	3.09e-4	2.49e-4	1.17e-2	4.73e-5

Table 4.8 Relative errors over the high-fidelity domain Ω_{hf} and over the remaining low-fidelity domain $\Omega_{lf} \setminus \Omega_o$, for the test cases with varying overlapping domain size.

The relative errors computed in the small high-fidelity domain Ω_{hf} and in the low-fidelity domain $\Omega_{lf} \setminus \Omega_o$ are reported in Table 4.8. The errors obtained in case (c) are quite close to those obtained in case 0, while the errors obtained in cases (a) and (b) are one order of magnitude higher. Indeed, the most sensitive boundary conditions for Ω_{hf} are the lateral ones (left and right) where appropriate conditions have to be imposed, especially for the water level, numerically imposed by the VOF α. A large overlapping zone is thus required in this region, case (c) satisfies this requirement, and will be thus used in what follows.

4.3.6 Prediction Sensitivity

Until this section, the data collected from the original high-fidelity simulation, with initial conditions using $H_w = 0.60\,\text{m}$ and $H_s = 0\,\text{m}$, are used to build the POD basis functions for the coupled model, that reproduces the simulation for the same initial conditions. In other words, what is performed is an in-sample test, also called a reproduction problem. In this section, data from simulations based on different initial conditions H_w are collected and used in the training phase, and the coupling algorithm is evaluated for the simulation initialized with $H_w = 0.60\,\text{m}$ (here case 0), which is *not* included in the database. Several training sets are considered (see Figure 4.18), combining different H_w. The chosen H_w are progressively farther

from the target initial conditions (cases A, B, C, and D), or are all collected in a large dataset (case E). In either case, the various initial conditions are all defined symmetrically with respect to the target value, $H_w = 0.60\,\text{m}$. This selection ensures the most challenging prediction scenario. Any other H_w value would be closer to at least one of the solutions present in the trained dataset, making it easier to predict than $H_w = 0.60\,\text{m}$, which maintains the same distance from all solutions in the datasets constructed in this section.

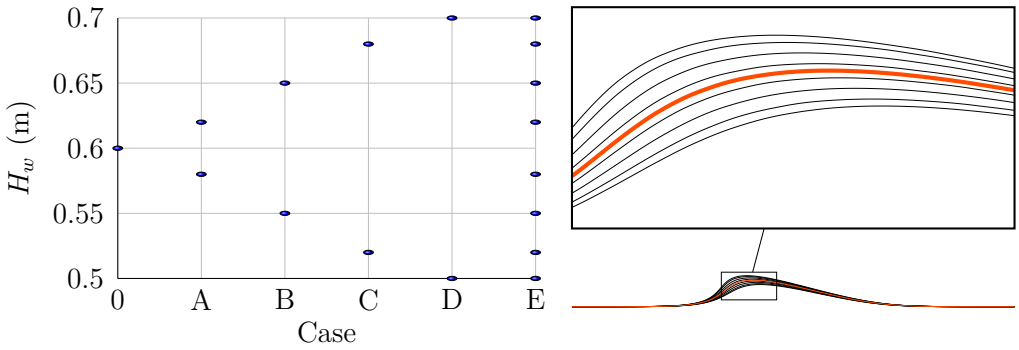

Fig. 4.18 Quantitative (left) and graphical (right) definition of the varying parameter, H_w, for the out-of-sample tests. Case 0 represents the in-sample test, taken as reference. Case E groups the snapshots from all the other cases, except case 0.

The main parameters are recalled. For each case, $N_r = 30$ POD modes are considered. The number of snapshots for each H_w is $N_s = 250$, so cases A, B, C, and D have a dataset of $N_s = 500$ elements, and case E has a large dataset with $N_s = 2000$.

The relative errors, both projection (Table 4.9) and coupled model (tabular representation in Table 4.10, and in graphical representation in Figure 4.19) ones, show the same trend. The solution for the baseline configuration (case 0) can be well approximated using training sets that do not contain the in-sample snapshots. In particular, datasets from initial conditions closer to the target (case A) give good results. The relative errors increase when the training points are farther from the baseline configuration (cases B, C, and D). The large dataset (case E) provides good results, with an expected better robustness than the other cases A-D.

Case	H_w (m)	RIC (%)	$\bar{\varepsilon}^u_{proj}$	$\bar{\varepsilon}^v_{proj}$	$\bar{\varepsilon}^w_{proj}$	$\bar{\varepsilon}^\alpha_{proj}$
0	0.60	99.97	4.90e-5	2.20e-5	6.57e-4	2.02e-5
A	0.58, 0.62	99.92	7.21e-5	3.89e-5	1.19e-3	2.61e-5
B	0.55, 0.65	99.86	1.41e-4	8.08e-5	1.24e-3	4.36e-5
C	0.52, 0.68	99.85	2.00e-4	1.03e-4	1.33e-3	5.82e-5
D	0.50, 0.70	99.84	2.39e-4	1.17e-4	1.35e-3	6.80e-5
E	0.58, 0.62 0.55, 0.65 0.52, 0.68 0.50, 0.70	99.79	1.53e-4	7.44e-5	1.17e-3	4.71e-5

Table 4.9 Characteristics and projection errors of velocity and VOF fields, for various combinations of initial condition parameter H_w.

	Case	$\bar{\varepsilon}^u$	$\bar{\varepsilon}^v$	$\bar{\varepsilon}^w$	$\bar{\varepsilon}^\alpha$
$\Omega_{lf} \setminus \Omega_o$	0	6.29e-5	4.23e-5	7.09e-4	1.74e-5
	A	1.09e-4	8.57e-5	1.27e-3	2.41e-5
	B	2.68e-4	2.32e-4	1.43e-3	4.84e-5
	C	3.54e-4	2.82e-4	1.47e-3	6.75e-5
	D	6.76e-4	5.56e-4	1.57e-3	1.18e-4
	E	3.21e-4	2.68e-4	1.30e-3	5.83e-5
Ω_{hf}	0	1.72e-4	1.19e-4	1.26e-2	1.37e-5
	A	3.43e-4	2.14e-4	2.29e-2	1.95e-5
	B	3.64e-4	2.48e-4	2.11e-2	5.14e-5
	C	4.50e-4	2.98e-4	1.66e-2	5.97e-5
	D	6.18e-4	4.94e-4	2.26e-2	2.02e-4
	E	4.58e-4	2.96e-4	2.04e-2	7.12e-5

Table 4.10 Relative errors over the high-fidelity domain Ω_{hf} and over the remaining low-fidelity domain $\Omega_{lf} \setminus \Omega_o$ for the different sampling test cases.

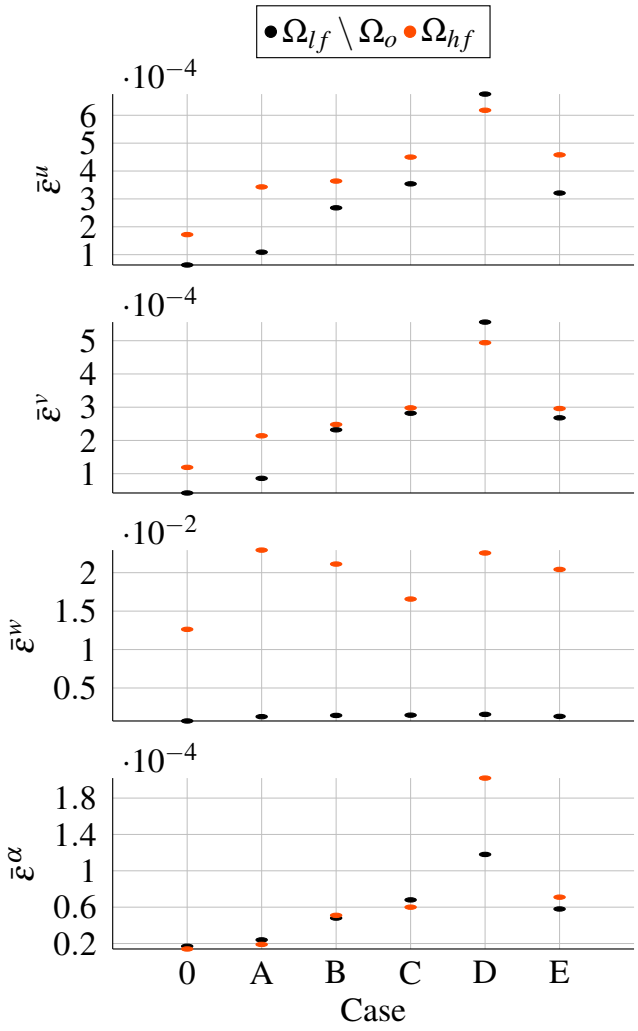

Fig. 4.19 Visual representation of the relative errors for the velocity and VOF fields over the high-fidelity domain Ω_{hf} and over the remaining low-fidelity domain $\Omega_{lf} \setminus \Omega_o$, of all the cases analyzed.

Examining Figure 4.19, case D stands out showing large errors compared to the other cases, as the solutions contained in the dataset are the farthest from the target H_w. When the dataset is trained on solutions with initial conditions that are too distant from the target, and N_r is maintained constant, the model's performance degrades. Indeed, tests can be extended to larger ranges of H_w. For demonstration purposes, another case, case F, is added to the analysis. The dataset comprises solutions from simulations with initial conditions $H_w = \{0.40, 0.80\}$m. Truncation is consistently set at $N_r = 30$, yielding RIC $= 99.82\%$, comparable to the other cases (refer to Table 4.9). The relative errors are detailed in Table 4.11, and graphically depicted in Figure 4.20, compared to the reference, case 0, and case D, the worst case in the previous comparison.

	$\bar{\varepsilon}^u$	$\bar{\varepsilon}^v$	$\bar{\varepsilon}^w$	$\bar{\varepsilon}^\alpha$
Projection	3.87e-4	1.90e-4	5.93e-3	1.05e-4
$\Omega_{lf} \setminus \Omega_o$	1.67e-3	1.62e-3	8.88e-3	2.05e-4
Ω_{hf}	1.54e-3	1.62e-3	5.67e-2	4.13e-4

Table 4.11 Relative errors, obtained from projection and from the coupled model over the high-fidelity domain Ω_{hf} and over the remaining low-fidelity domain $\Omega_{lf} \setminus \Omega_o$ for case F.

As anticipated, the errors progressively escalate to significant magnitudes. Moreover, upon examination of the solution computed by the CFD model in Ω_{hf}, inaccuracies generate, as depicted in the snapshot in Figure 4.21. The free surface and the velocity begin to manifest instabilities, with observable breaking waves. Not only does this outcome deviate from the desired result, but it also lacks physical accuracy, a critical concern. The issue with such data far from the target lies in the model's inability to extract useful information from this dataset for its reconstruction. A smaller H_w leads to a simulation with a tiny wave, with the free surface undergoing slight temporal evolution. On the contrary, a higher H_w generates a steep wave, with substantial water movement within the domain. Both behaviors strongly differ from the evolution of the free surface initiated at $H_w = 0.6$m, and thus are not useful for its accurate modeling. Truncating at a larger N_r may ameliorate results, but would go against reduction principles. Thus, the careful definition of the training set is imperative, and heavily dependent on the specific problem at hand. Improved sampling strategies, such as employing clustering techniques, could be explored. Nonetheless, this

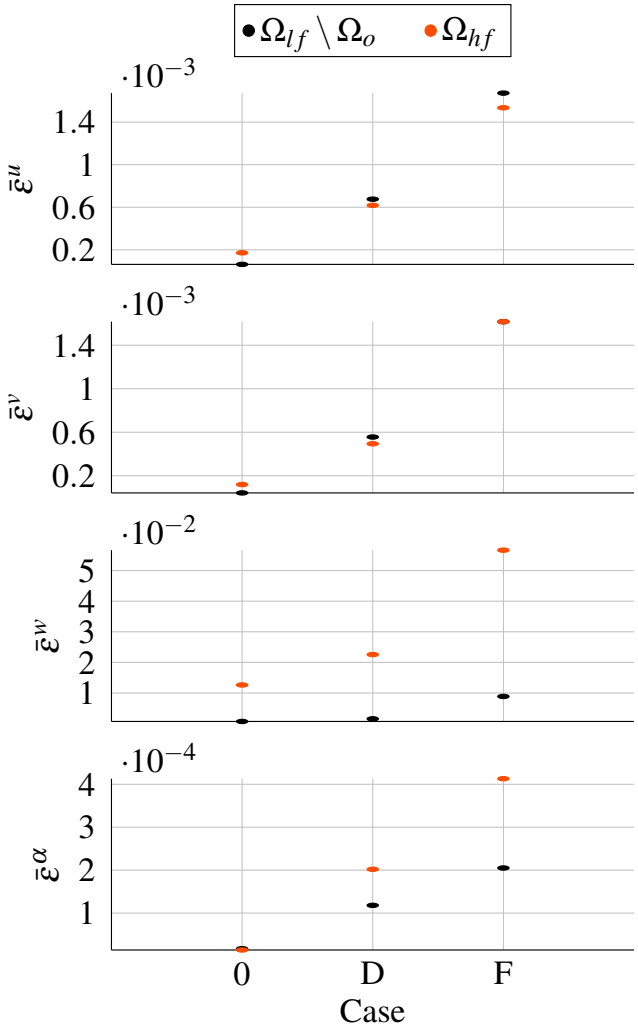

Fig. 4.20 Visual representation of the relative errors for the velocity and VOF fields over the high-fidelity domain Ω_{hf} and over the remaining low-fidelity domain $\Omega_{lf} \setminus \Omega_o$, of the farthest cases (D and F) from the target (case 0), plotted for comparison.

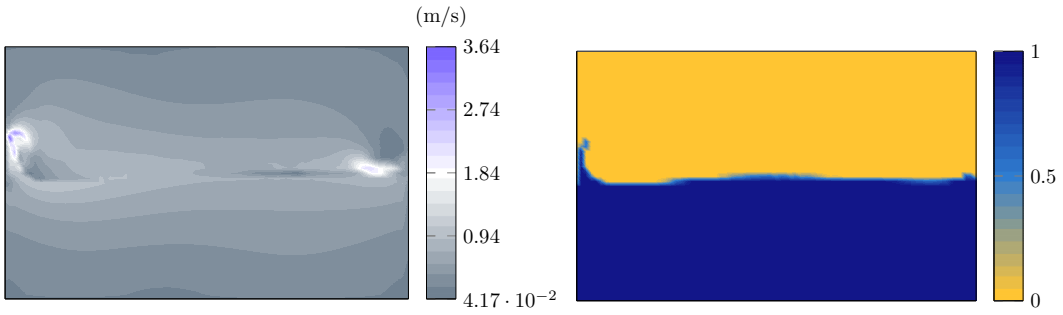

(a) FOM velocity field. (b) FOM VOF field.

Fig. 4.21 Snapshot of the high-fidelity solution on Ω_{hf} during coupling, for case F. Both velocity and VOF fields are represented, on a $x-y$ section, at $T = 0.5\,\mathrm{s}$.

section proves the ability of the coupling methodology for parametric investigations, where the varying parameter, here, is the initial wave height, while other parameters could be similarly explored.

4.3.7 Clustering Sensitivity

As the simulation progresses, the absolute error has a general upward trend (see Figure 4.15), primarily due to the accumulation of approximations introduced by the reduced-order model. While this trend is less pronounced in the low-fidelity subdomain, it exhibits a gradual increase over time. In the high-fidelity subdomain, the velocity error initially increases within the first few seconds before stabilizing. This stabilization can be attributed to the nature of the test case, rapidly transitioning to a state of calm water surface, where the approximation becomes more straightforward, after the initial period. The VOF, however, continues to exhibit a consistent upward trend.

Clustering presents a potential strategy to mitigate error growth. Clustering involves partitioning a vast dataset into smaller, more manageable, groups, by reducing the dimensionality of each group for analysis purposes. While clustering techniques are commonly employed to pattern recognition or classification problems, they have also found application in addressing data compression and model order reduction challenges [221]. The existing literature of model order reduction contains considerable number of clustering techniques, and the K-means stands out as a common strategy applied when the number of clusters is predetermined. K-means is a technique that aims to minimize the average squared distance between points within the same

cluster [222]. In this case study, the dataset $\mathbf{S}$ comprises the snapshots $\mathbf{U}(\mathbf{x},t;\eta)$, and the interest is in selecting arbitrarily K centers $\{q_1,\ldots,q_K\}$, to minimize the total squared distances between each point and its nearest center. Typically, the Euclidean distance serves as the deviation measure, so one must solve, for each group:

$$\sum_{\mathbf{U}\in\mathbf{S}} \min_{q\in\mathscr{Q}} \|\mathbf{U}(\mathbf{x},t;\eta)-q\|^2. \tag{4.15}$$

This implies that for each $i\in 1,\ldots,K$, the cluster $\mathscr{Q}_i$ comprises the data in $\mathbf{S}$ that are closer to q_i than to any other q_j, with $j\neq i$. Subsequently, the center of mass q_i of all the data in the cluster $\mathscr{Q}_i$ is computed as $q_i=\frac{1}{\mathscr{Q}_i}\sum_{\mathbf{U}\in\mathscr{Q}_i}\mathbf{U}(\mathbf{x},t;\eta)$. This iterative procedure, which involves sorting the elements of $\mathbf{S}$, and recomputing the cluster center based on any new addition, continues until $\mathscr{Q}$ remains unchanged. While K-Means lacks accuracy guarantees, its simplicity and computational efficiency make it highly appealing for practical applications. In this case, $\eta=0$, and the only variable parameter is the time. Applying the `kmeans` function in Matlab to the current snapshots dataset provides a first insight into how the 250 snapshots could be partitioned. By requesting $K=2$, $K=3$, or $K=6$ clusters, the algorithm gives the results shown in Figure 4.22.

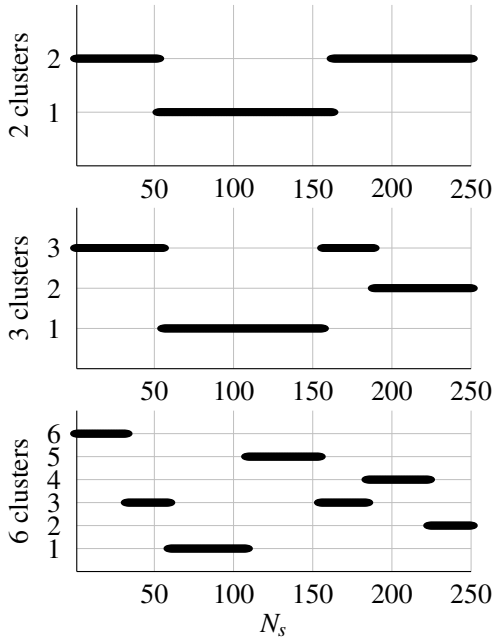

Fig. 4.22 Division of the snapshots in clusters, according to the `kmeans` function in Matlab.

There is a nearly consistent division corresponding to the time evolution, with snapshots distributed fairly evenly across each cluster. The case being studied appears to be relatively straightforward, motivating the division of the entire dataset into distinct clusters, effectively based on time evolution. The division is, thus, unambiguous. The approach involves segmenting the complete simulation time into several intervals, and defining different sets of basis functions based on the snapshots corresponding to each interval, as illustrated in Figure 4.23. Given that the simulation time spans $t = [0,3]$s, three scenarios are compared, dividing into $K = 2,3,6$ intervals, yielding cases $T_{1/K}$.

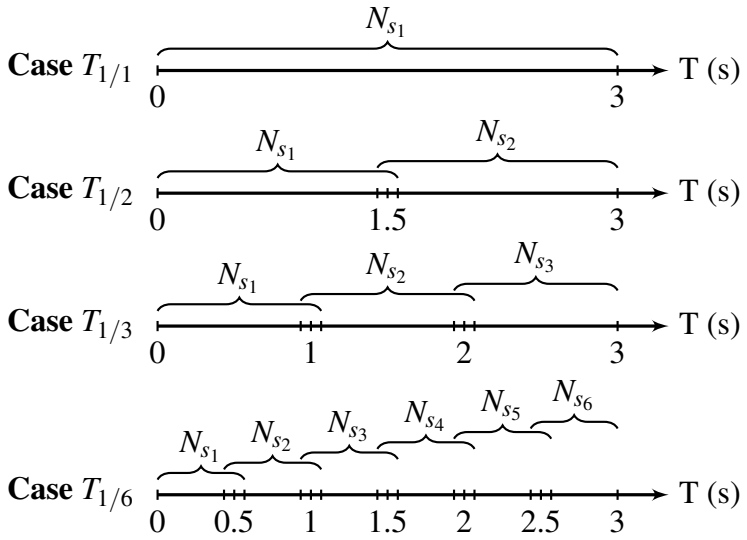

Fig. 4.23 Outline of the cluster separation of the snapshots, yielding to various test cases. The total time is divided in $K = 2,3,6$ clusters, compared to the reference case $T_{1/1}$ (no clustering, with $K = 1$).

Contrary to the K-means algorithm, no centers nor distances need to be computed, since the clusters are defined solely on time. Furthermore, during the coupling process, instead of selecting the closest cluster to the solution at each time step, a simple switch between consecutive clusters is required, when their respective range of applicability ends. As visible in Figure 4.23, the clusters are partially overlapping, incorporating a few snapshots from the nearest cluster, to prevent abrupt shifts in the solutions. However, the transition between clusters occurs precisely at the designated time, so at $T = 1$ s and $T = 2$ s in case $T_{1/3}$, for example. The number of snapshots in each cluster, for the test cases considered, along with their respective RIC, are listed in Table 4.12. The number of modes is held constant across all cases, set to $N_r = 30$.

Case	N_{s_K}	N_s	RIC (%)
$T_{1/1}$	N_{s_1}	250	99.77
$T_{1/2}$	N_{s_1}	142	99.94
	N_{s_2}	143	99.94
$T_{1/3}$	N_{s_1}	100	99.96
	N_{s_2}	119	99.96
	N_{s_3}	101	99.98
$T_{1/6}$	N_{s_1}	59	99.99
	N_{s_2}	76	99.98
	N_{s_3}	77	99.99
	N_{s_4}	77	99.97
	N_{s_5}	76	99.99
	N_{s_6}	60	100

Table 4.12 Characteristics of the test cases considered. N_{S_K} represents the number of snapshots in the K-th cluster.

The absolute errors plotted in Figure 4.24 demonstrate the potential improvement in the approximation of the solution using the clustering technique, controlling the error to a nearly constant value over time. This is particularly noticeable for the velocity in the high-fidelity subdomain Ω_{hf}, although less remarkable for the VOF, and for the low-fidelity reconstruction. The reason for the VOF error trend may lie in the fact that the chosen case lacks significant evolution of the free surface. Regarding the low-fidelity error, on the left-hand side of Figure 4.24, the mild upward trend of errors for the basic simulation suggests that clustering may not bring significant improvements. Additionally, the interpolation process may be, once again, responsible for filtering out any potential improvement during runtime.
As also the relative errors in Table 4.13 highlight, increasing the number of clusters does not necessarily lead to improved solutions. Indeed, for this particular test case, two clusters are enough, and larger K gives comparable, or even worse, solutions, as observed for case $T_{1/6}$. Alternatively, one could continue dividing the simulation time into smaller time intervals, although a minimum number of snapshots for each subset would need to be ensured. Nevertheless, excessively small clusters might fail to accurately capture the simulation dynamics, and could prove detrimental.

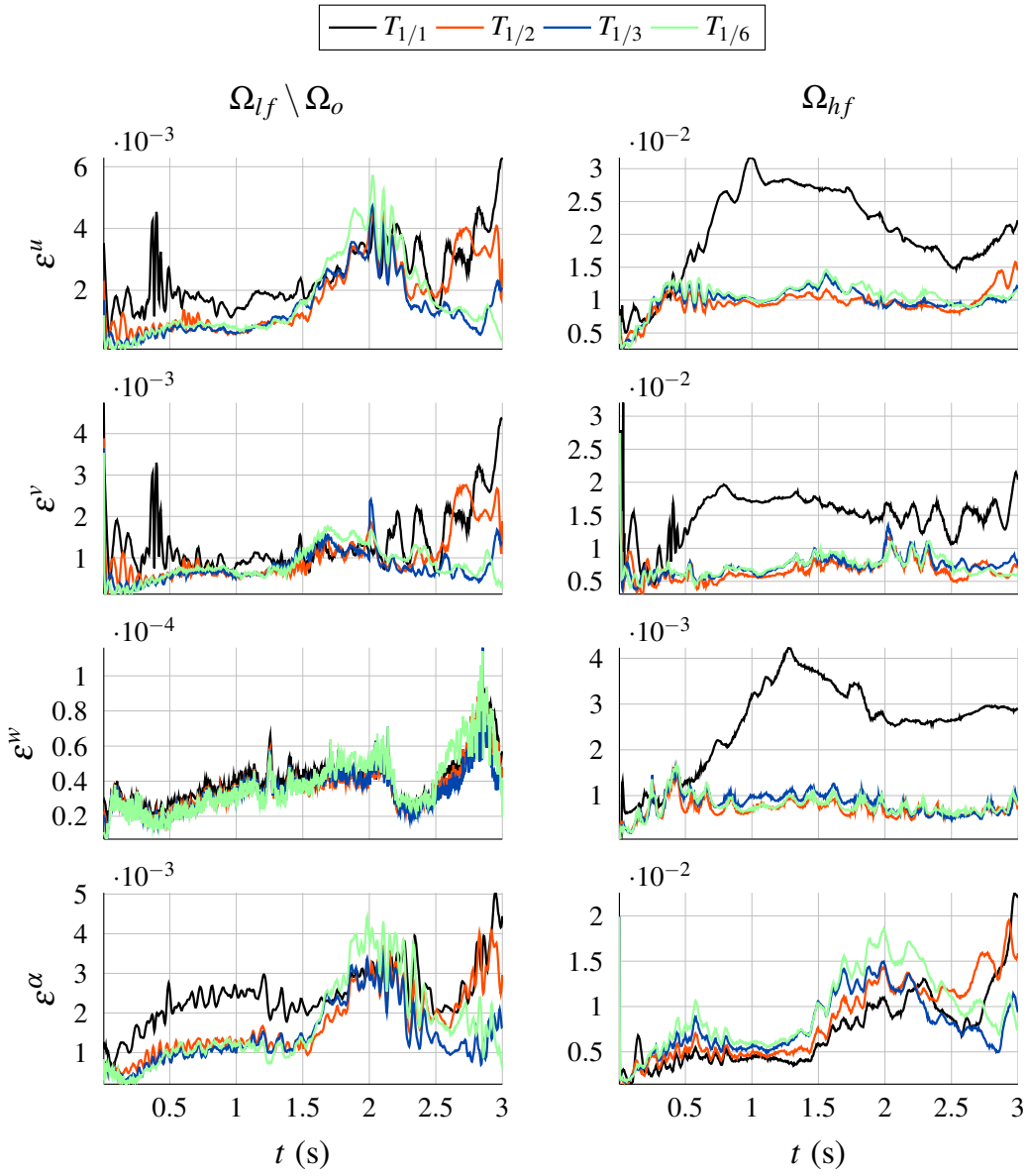

Fig. 4.24 Evolution of the absolute errors for velocity and VOF fields over time. Both errors over the high-fidelity domain Ω_{hf} and over the remaining low-fidelity domain $\Omega_{lf} \setminus \Omega_o$ are plotted for the different clustering test cases.

	Case	$\bar{\varepsilon}^u$	$\bar{\varepsilon}^v$	$\bar{\varepsilon}^w$	$\bar{\varepsilon}^\alpha$
$\Omega_{lf} \setminus \Omega_o$	$T_{1/1}$	2.28e-4	1.60e-4	2.16e-3	5.58e-5
	$T_{1/2}$	5.61e-5	3.99e-5	6.62e-4	1.32e-5
	$T_{1/3}$	4.67e-5	3.20e-5	6.26e-4	1.09e-5
	$T_{1/6}$	5.58e-5	3.52e-5	7.00e-4	1.28e-5
Ω_{hf}	$T_{1/1}$	1.85e-4	1.29e-4	1.14e-2	2.61e-5
	$T_{1/2}$	8.92e-5	5.67e-5	3.09e-3	3.08e-5
	$T_{1/3}$	9.52e-5	6.28e-5	3.62e-3	2.85e-5
	$T_{1/6}$	1.01e-4	6.26e-5	3.34e-3	3.41e-5

Table 4.13 Relative errors for velocity and VOF fields over the high-fidelity domain Ω_{hf} and over the remaining low-fidelity domain $\Omega_{lf} \setminus \Omega_o$, for the different clustering test cases.

4.4 Wave Energy Converter

At this stage, the simulation of a wave energy converter with the coupled model might seem intimidating. Actually, it should be more manageable than one might think. Indeed, the moving body is only modeled within the high-fidelity subdomain, a region that remains outside the coupling methodology, and can be simulated using CFD solvers and overset meshes tailored to the situation. To prove this, an infinite cylinder is first inserted in the simulation, holding all other variable or parameter as defined until this point (Section 4.4.1). Subsequently, a sphere is simulated with an incoming wave, increasing the complexity, with a fully three-dimensional problem and simulation, and a distinct free surface evolution (Section 4.4.2). As the coupling methodology proves its efficiency, an algorithm is proposed for the simulation of a WEC farm, in Section 4.4.3.

4.4.1 Floating Cylinder

The selected body for this study is a cylinder with horizontal axis and a radius of 0.3 m, extending across the entire domain in the z direction. The mass of the body is 10 kg, and it has only one degree of freedom, the heave (Figure 4.25).

Consistent with previous decisions, the size of the high-fidelity subdomain matches case R6, and the overlapping region matches case (c), of Section 4.3.5. The

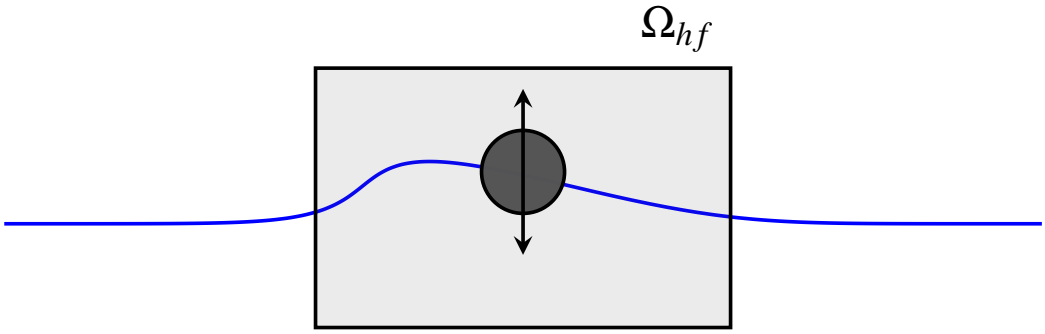

Fig. 4.25 Simulation setup for the modeling of a cylinder, moving in heave (according to the arrow), and floating on water with free surface initial condition plotted in blue.

number of modes retained is $N_r = 30$, and two cases are simulated: one without clustering, called Body $T_{1/1}$, and another with three clusters, labelled Body $T_{1/3}$. The clustering characteristics remain unchanged from the previous section, and the comparison aims to assess the impact of the temporal clustering technique in scenarios involving a moving body, a factor not previously considered. The relative errors in Table 4.14 show a general decreasing trend using clustering, albeit at a rate smaller than in cases without a moving body. For the subsequent test, no clustering will be implemented. However, in the case of a parametric study, with $\eta \neq 0$, a clustering would likely prove more beneficial.

	Case	$\bar{\varepsilon}^u$	$\bar{\varepsilon}^v$	$\bar{\varepsilon}^w$	$\bar{\varepsilon}^\alpha$
$\Omega_{lf} \setminus \Omega_o$	Body $T_{1/1}$	7.96e-5	5.64e-5	6.43e-4	1.89e-5
	Body $T_{1/3}$	4.57e-5	3.46e-5	5.68e-4	1.10e-5
Ω_{hf}	Body $T_{1/1}$	2.29e-4	1.81e-4	2.82e-3	3.87e-5
	Body $T_{1/3}$	1.62e-4	1.19e-4	1.91e-3	4.11e-5

Table 4.14 Relative errors for velocity and VOF fields over the high-fidelity domain Ω_{hf} and over the remaining low-fidelity domain $\Omega_{lf} \setminus \Omega_o$, in the cases with and without clustering.

Moreover, there is a minimal degradation of the solution in the coupled model with the presence of a body, compared to the case with only the wave (see, for example,

Table 4.13). In addition to error assessment, a comparison of the vertical translation motion, and the force exerted on the body, is conducted to understand whether the coupled model can adequately capture the evolution of the body performance. Figure 4.26 corroborates the results, and highlights the suitability of the coupled model for the simulation of the dynamics of a body in a multiphase flow.

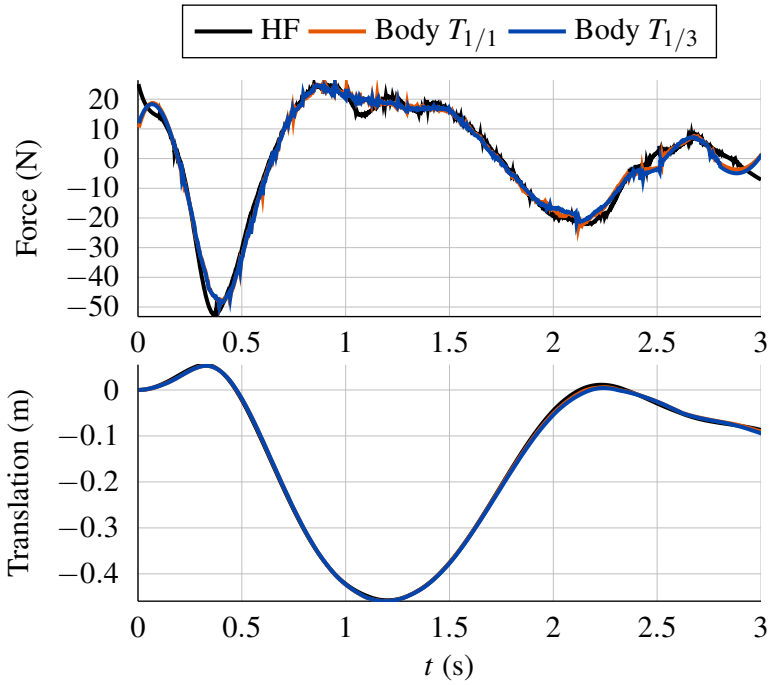

Fig. 4.26 Evolution of the force acting on the body and the heave motion of the body over time. The solutions from the coupled model are compared to the high-fidelity simulation solution over Ω_{HF} used to build the basis functions (HF).

4.4.2 Point Absorber with Incoming Wave

The goal is to numerically model a class of wave energy converters, where the energy harvesting devices are floating bodies, with rigid motions, driven by sea waves. Floating wave energy converters are typically deployed in deep waters, ideally located far from the shoreline. These devices are equipped with a mooring system and harness the oscillatory motion generated by the waves to produce energy. Here, a sphere floating on sea waves is considered. The floating body could easily approximate a point absorber WEC type, i.e., the only degree of freedom is in the y direction (aligned with gravity). The sphere modeled here has radius 0.3 m and mass

20 kg. The incoming wave is imposed by $M > 0$ sensors in the coupling strategy. The objective is to predict the wave behavior and the motion of the floating body, subjected to an imposed wave. The wave is defined with some characteristics (period, height, and wavelength), defined later in the section.

Compared to the previous case of the floating cylinder, in addition to the presence of an incoming wave, the domain also slightly changes. The original computational domain, noted Ω_{sim}, expands to $[85 \times 45 \times 10]$m, see Figure 4.27.

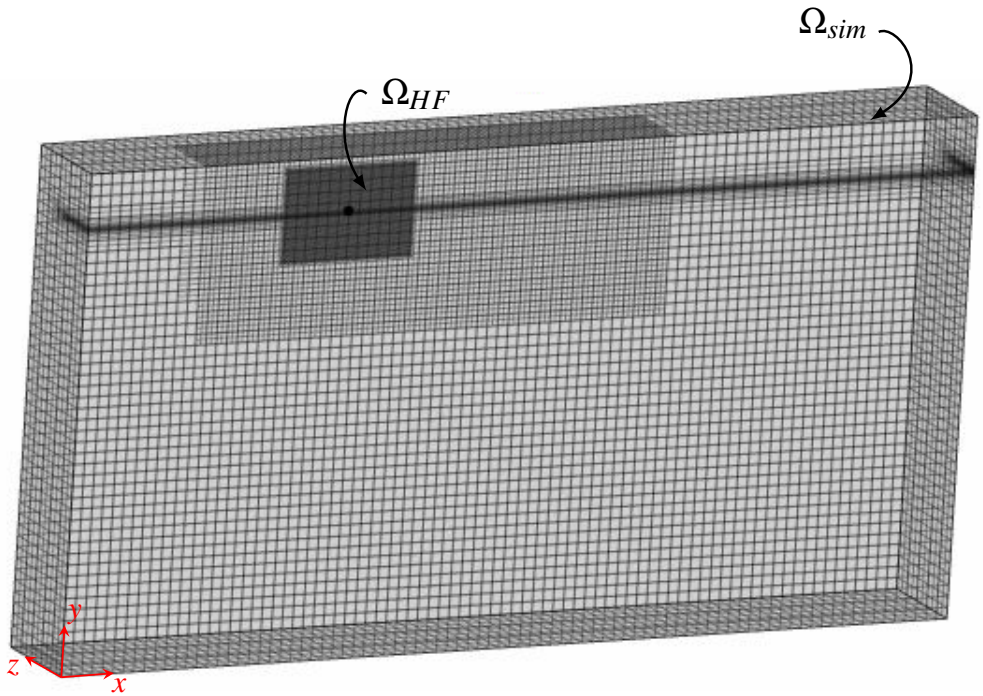

Fig. 4.27 Representation of the original computational domain Ω_{sim}, with the different local mesh refinements.

The large size of this domain is necessary to take into account the water depth, the multiple wavelengths, and artificial forcing zones that avoid spurious reflections. For this simulation, a mesh with several refinements is used, to have at least 13 cells per wave height, and an aspect ratio of 2, in the longitudinal direction, in the area of main interest around the free surface. A coarser background mesh is used for the areas where the computation is less complex, or the solution is imposed. For example, wave forcing and damping is employed to avoid waves that could be reflected back into the domain, and affect the simulation's results. Wave forcing is used to ensure specified wave shapes, and is applied for 3 wavelengths from the inlet

boundary, and one wavelength from the back boundary, where Dirichlet conditions are applied on the velocity. Wave damping, introducing vertical resistance to vertical motion, allows to numerically reduce wave amplitude, and is used for 3 wavelengths from the outlet, where Dirichlet boundary conditions are imposed on pressure. Also at the top boundary, Dirichlet conditions are applied on the pressure. All those considerations allow to have a simulation of a traveling wave which is accurate. Tests are conducted to check that the resulting wave corresponds to the theoretical wave inserted in the model. Subsequently, the floating body is inserted, modeled with the Dynamic Fluid Body Interaction (DFBI) in StarCCM+, which allows to predict dynamic 6-DoFs motion of bodies, due to fluid forces, and potentially constraining them in any direction. In this case, the only degree of freedom is the translation along the y direction, and all the other motions are constrained. This choice is for sake of simplicity, velocity of simulation, and validation of the methodology, but a complete 6-DoFs body, with a mooring system, and a control strategy, could potentially be simulated.
As long as the CFD solver is able to deal with such nonlinearities, the coupling method is not affected. Also, without loss of generality, a smaller domain, $\Omega_{HF} \subset \Omega_{sim}$, is considered to reduce the memory footprint and CPU costs for POD basis functions. Even though it is necessary to compute the actual solution on Ω_{sim}, its trace is considered only on Ω_{HF}. Similar to the previous test case, the domain Ω_{HF} is $[10 \times 6 \times 0.8]$m. This allows to consider more than one wavelength in the domain. The domain Ω_{hf} is $[4 \times 2.5 \times 0.6]$m, which represents 0.015% of the volume of the real simulation domain ($\frac{|\Omega_{sim}|}{|\Omega_{hf}|} = 6375$).

The sketch of the domain decomposition is depicted in Figure 4.28. The change in the domains, for this section, is mainly driven by the need to pass to a completely three-dimensional simulation. Indeed, a sphere is now simulated, and even though the incoming waves are all unidirectional, the fluid-structure interactions may induce oscillations in transversal directions. Therefore, as visible in the top of Figure 4.28, the boundary Γ^{hf}_{back} is added to Γ_{hf}, where the boundary conditions are imposed during the coupling process. For Γ^{hf}_{front}, however, a symmetry condition is still used to reduce the computational burden of the FOM simulation, and is also kept in the coupled model. This is possible as long as the incoming waves are unidirectional, and the floating body is axisymmetrical. When considering multidirectional waves and more complex WEC types, or WEC farms, where the flow dynamics is very

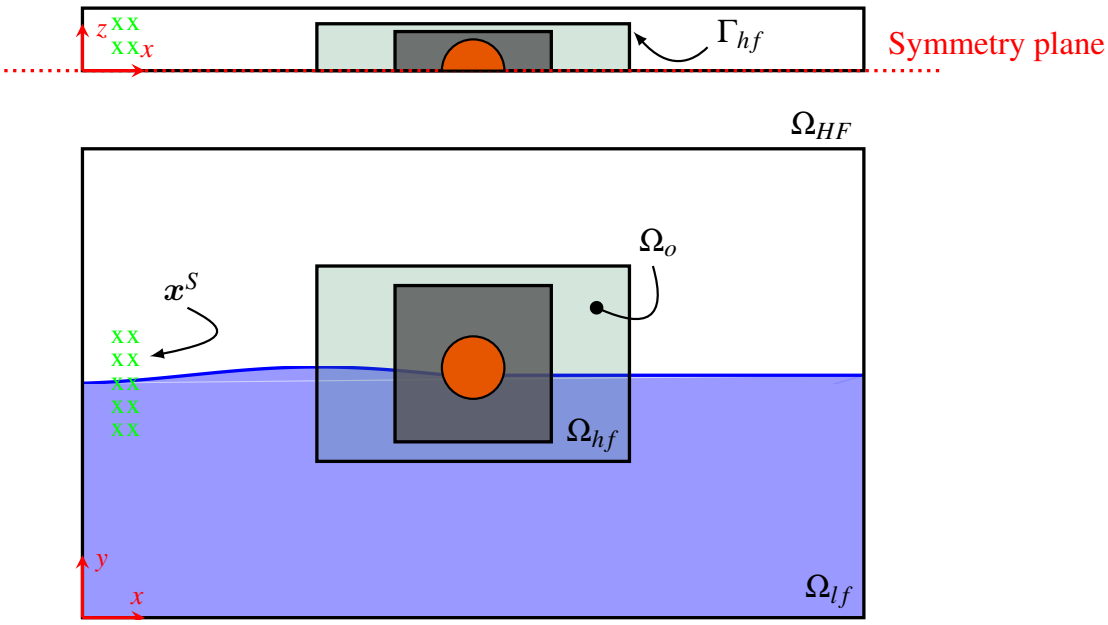

Fig. 4.28 Sketch of the domain for the simulation of the spherical point absorber, with definition of the subdomains and boundaries.

complex in all directions, then, no symmetry planes can be used, and the boundary conditions are imposed in all six boundaries of Γ_{hf}.

An overset mesh is used for the sphere in the whole domain Ω_{sim}, and in the small domain Ω_{hf}. These domains become unsteady, and computing the POD basis functions onto an unsteady domain is challenging. The solution previously implemented is to remove a subdomain including all the possible motions of the floating body. The choices of domains Ω_{hf} and Ω_o are made accordingly to the previous sections, inspired from *R*6 (c), and satisfy the previous requirement, i.e., all possible body locations are in $\Omega_{hf} \setminus \Omega_o$. The POD basis functions are only computed on $\Omega_{lf} = \Omega_o \cup (\Omega_{HF} \setminus \Omega_{hf})$. Particularly, the overlapping region conserves the same size in the x and y directions, from the test case (c) presented in the dedicated section, but a new area is added in the z direction. With the new dimensions, the volume ratio between Ω_{HF} and Ω_{hf} becomes 8, yielding a bigger reduction with respect to the test case used in the sensitivity analysis. Numerically, Ω_{HF} is composed of 413457 cells, Ω_{hf} is composed of 53703 cells, and Ω_o is composed of 38493 cells. For simplicity reasons, $M = 3482$ sensors are used, covering a domain of dimension $[0.2 \times 2 \times 0.8]$m, see Figure 4.31.

With this test case, two analyses are carried out: an in-sample reconstruction, and an out-of-sample prediction. IS denotes the in-sample case where the POD basis is computed with a database from the baseline condition $W0$, and OOS denotes the out-of-sample case, where the POD basis is computed with a database from conditions $W1$ and $W2$. Waves $W0$, $W1$ and $W2$ are defined in Table 4.15, and plotted in Figure 4.29. All the waves have low steepness to be sure to avoid breaking waves. All three waves differ both in wave height and wavelength, so the parameter space has two dimensions, although not very populated for now.

Wave	Wave period (s)	Wave height (m)	Wavelength (m)
$W0$	2	0.4	6.25
$W1$	1.95	0.36	5.94
$W2$	2.05	0.44	6.56

Table 4.15 Characteristics of the tested waves.

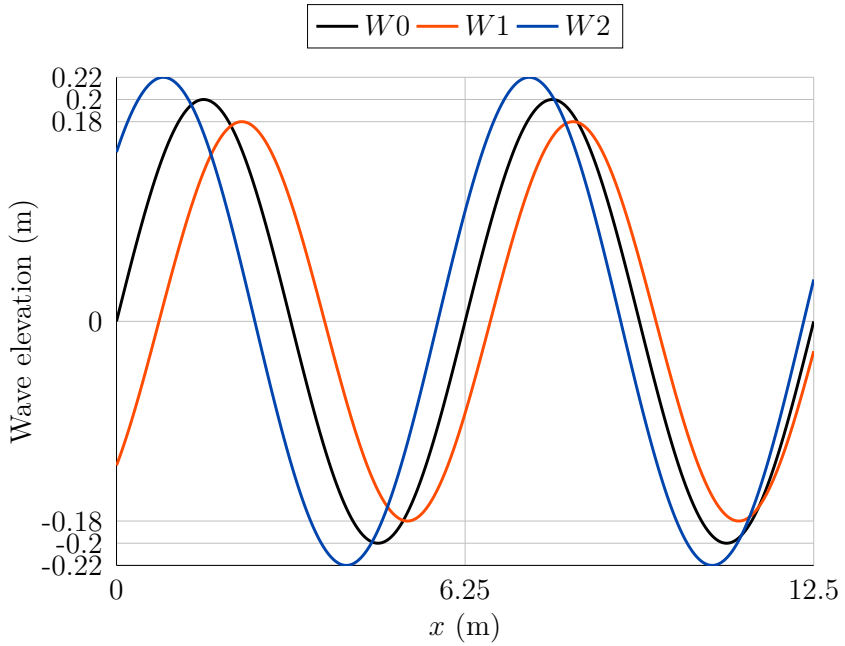

Fig. 4.29 Visualization of the tested waves. The target wave, $W0$, has characteristics (wave height and wave period) equal to the mean of the characteristics of the other two waves, $W1$ and $W2$, used for the out-of-sample test.

The number of POD modes is always $N_r = 30$. Each simulation lasts until $T = 6$ s, allowing an incoming wave to impact the floater. The snapshots are collected at $\Delta t = 0.012$ s, for a total of $N_S = 500$ for each simulation.

	Case	$\bar{\varepsilon}^u$	$\bar{\varepsilon}^v$	$\bar{\varepsilon}^w$	$\bar{\varepsilon}^\alpha$
$\Omega_{lf} \setminus \Omega_o$	IS	2.40e-4	1.67e-4	4.35e-4	3.02e-5
	OOS	4.74e-4	3.39e-4	1.09e-3	5.23e-5
Ω_{hf}	IS	4.35e-4	3.08e-4	1.59e-3	4.38e-5
	OOS	4.80e-4	3.87e-4	1.62e-3	7.77e-5

Table 4.16 Relative errors for velocity and VOF fields over the high-fidelity domain Ω_{hf} and over the remaining low-fidelity domain $\Omega_{lf} \setminus \Omega_o$, for In-Sample (IS) and Out-Of-Sample (OOS) tests.

The computed errors are reported in Table 4.16. The errors obtained in the out-of-sample (OOS) case are slightly larger than in the in-sample (IS) case, but they are comparable. The evolution of the vertical translation of the body and the vertical force acting on it are plotted in Figure 4.30.

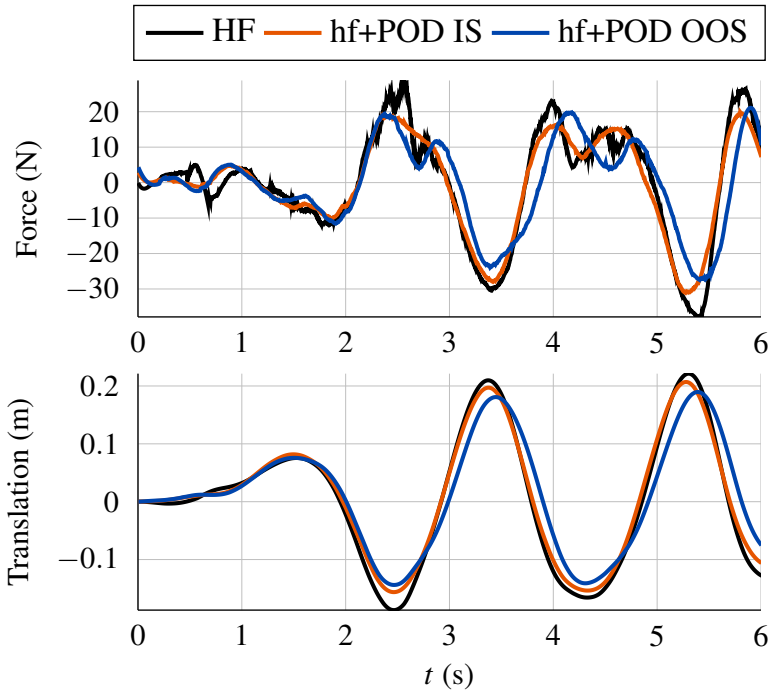

Fig. 4.30 Evolution of the force acting on the sphere and the heave motion over time. The solutions from the coupled model (hf+POD) are compared to the high-fidelity simulation solution over Ω_{HF} used to build the basis functions (HF).

For the IS case, the temporal evolution of the force and the position of the body is very close to the reference one (HF), with a small dissipation, visible at the peaks

and troughs. For the OOS case, the difference between the predicted solution and the reference one is slightly larger, but the overall behavior is good. In this case, in addition to a higher dissipation, maybe also linked to the chosen time step, a phase shift is visible. This is most probably related to the fact that the training dataset contains different wave periods from the target one, and some difficulties have already been pointed out in the phase reconstruction by the POD. The comparison of the force on the body and its translation is kept graphical, since an error, considering such a phase shift, would not be representative. An error based on a Wasserstein distance might be more appropriate than the L2 norm, for example. Anyway, to limit the phase shift, a clustering technique could be a good approach, starting from a larger dataset than the one available here, and letting the model find the closer cluster at each time step. In any case, these first results show that it is possible to obtain good predictions for out-of-sample cases with large CPU gains. Indeed, recalling that $\frac{|\Omega_{hf}|}{|\Omega_{sim}|} = 0.015\%$ points out the significant CPU savings.

In terms of computational times, a direct comparison is not feasible, as the original CFD simulation on Ω_{sim} and the coupled model are executed on different computers. However, certain observations can still be made. A single high-fidelity simulation on Ω_{sim}, using a set of wave characteristics outlined in Table 4.15, requires approximately 10 hours and 30 minutes, with 48 processors. In contrast, the coupled model delivers results in less than 4 hours, using 6 processors. Although the speedup achieved is already significant, it does not mirror the storage gain ratio, since the computational bottleneck, implementing the DFBI model, and the overset mesh for the moving body, is present in both high-fidelity simulations, whether in Ω_{sim} or Ω_{hf}. Furthermore, despite the necessary expense of the offline training phase, which entails running costly simulations for a few parameter values (here $W1$ and $W2$), it enables the generation of a wide array of new solutions, for numerous other parameter values (where $W0$ only represents one example, and the most distant in terms of parameter values), at the reduced cost afforded by the coupled model.

Finally, a snapshot of the air-water interface (from the VOF variable α) with the spherical point absorber, obtained with the multi-fidelity model, is given in Figure 4.31. The air-water interface is continuous across the whole domain, with little spurious effects being observed near the overlapping zone.

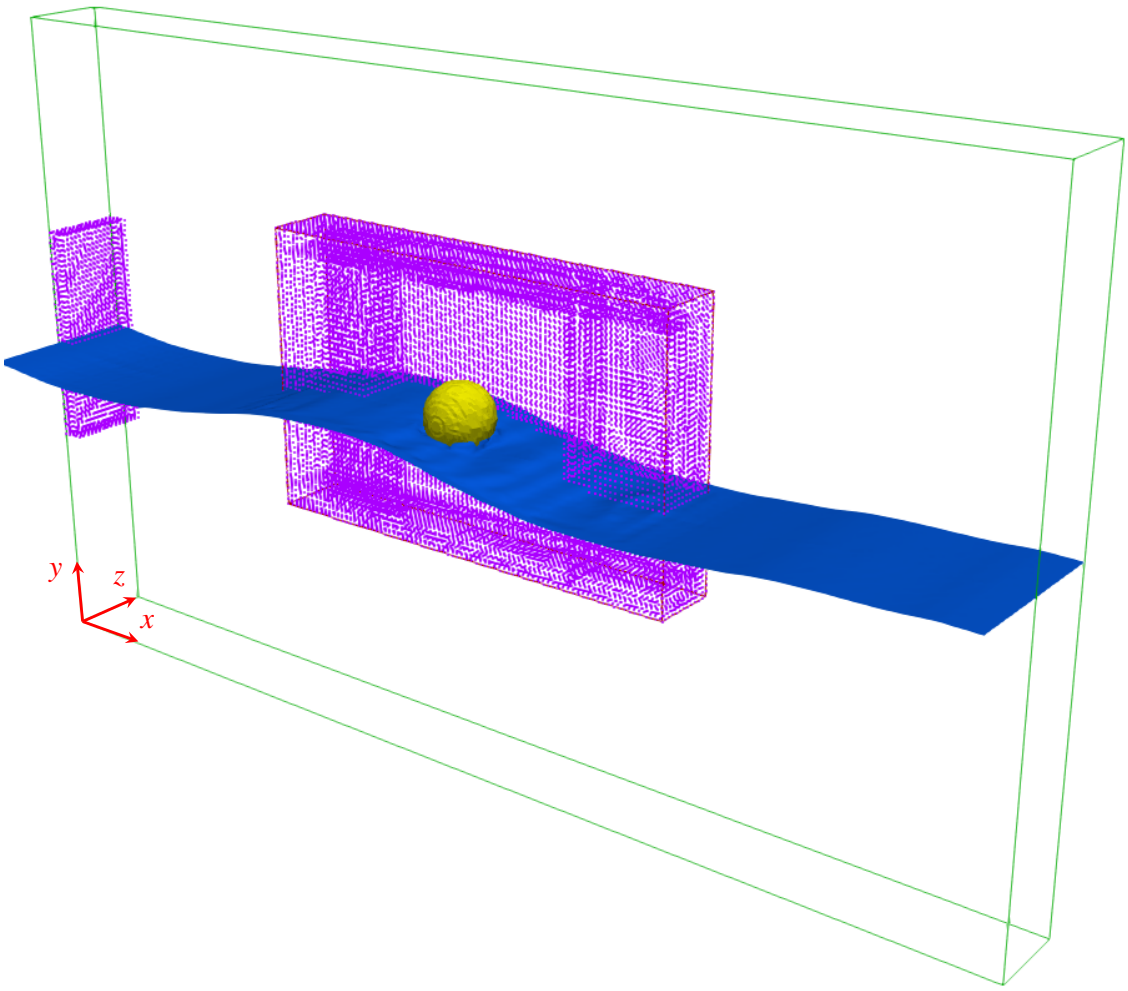

Fig. 4.31 Snapshot of the air-water interface, located at $\alpha = 0.5$, obtained from the coupled model in the out-of-sample test. The green domain represents Ω_{HF}, the violet domains represent the total support of the minimization problem, given by both the overlapping domain (around the sphere) and the sensor locations, here taken over a region close to the inlet boundary (on the left). Only one half of the domain in the z direction is actually computed, the visualization in the whole domain is obtained by symmetry.

For a closer examination and better understanding of the results, snapshots of the velocity and VOF fields, at $T = 1\,\mathrm{s}$ and $T = 5\,\mathrm{s}$, are plotted in Figures 4.32, 4.33, respectively. These results, as also the representation in Figure 4.31, are obtained from the multi-fidelity model for the out-of-sample (OOS) test. Near the Ω_{hf} domain, indicated by a light dotted line, a slight discontinuity in the values is noticeable.

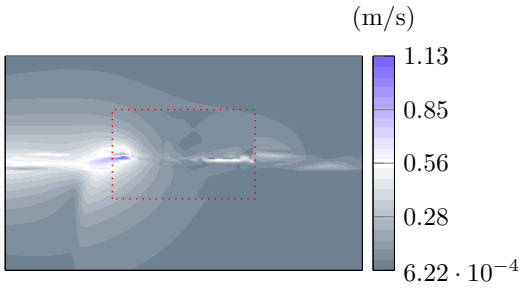

(a) Velocity coupled model solution.

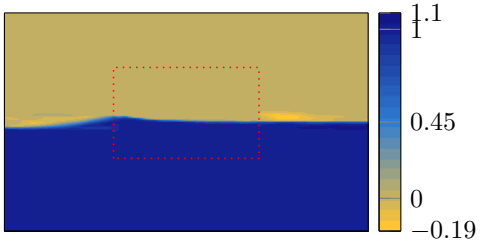

(b) VOF coupled model solution.

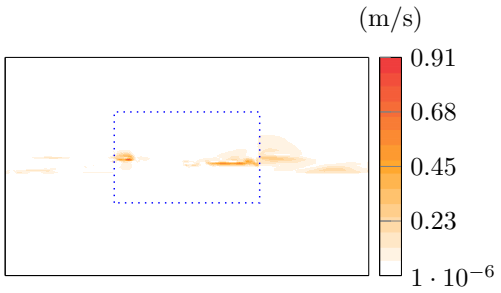

(c) Velocity absolute difference.

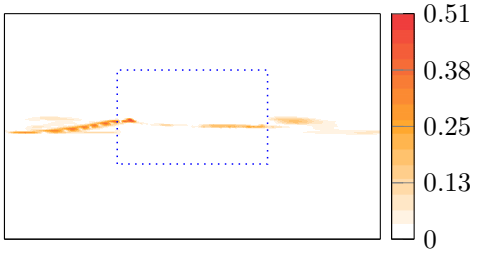

(d) VOF absolute difference.

Fig. 4.32 Snapshot at $T = 1\,\mathrm{s}$. Top: coupled solution for velocity and VOF fields. Bottom: corresponding absolute difference from the FOM solution.

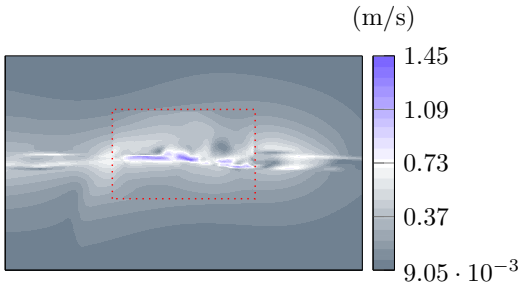

(a) Velocity coupled model solution.

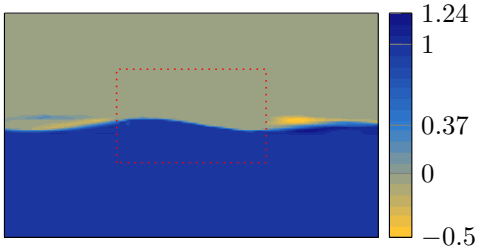

(b) VOF coupled model solution.

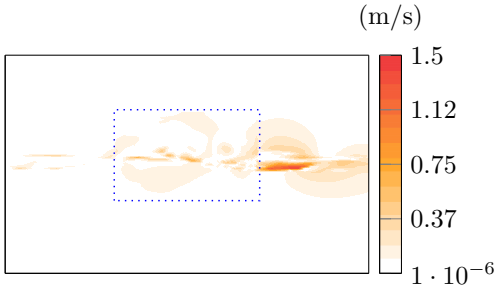

(c) Velocity absolute difference.

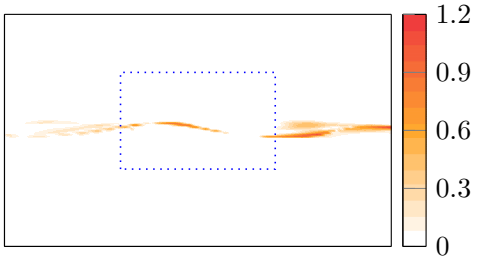

(d) VOF absolute difference.

Fig. 4.33 Snapshot at $T = 5\,\mathrm{s}$. Top: coupled solution for velocity and VOF fields. Bottom: corresponding absolute difference from the FOM solution.

The VOF field snapshots (Figures 4.32b, 4.33b) display a colorbar extension for $\alpha < 0$ and $\alpha > 1$, which are non-physical values confined to the low-fidelity subdomain. While the CFD solver restricts such non-physical values, the approximation in the reconstruction with basis functions permits their occurrence, potentially accumulating over time. An ongoing analysis involves penalizing the reconstruction to mitigate such occurrences, which could also lead to improved boundary conditions for the high-fidelity solver, thereby enhancing the overall solution. Examining the absolute differences in both velocity and VOF fields, in the lower parts of Figures 4.32, 4.33, reveals that, as expected, the primary differences, between the reference and reconstructed solutions, are concentrated around the free surface, where, additionally, the POD model reconstructs a less sharp interface, with some spurious values around $\alpha = 0.5$. Remarkably, within the high-fidelity domain, significant differences are observed at the center of Ω_{hf}, where the body is in motion, hence such values are not representative. While these differences are computed for consistency with the methodology employed throughout the document, a more refined approach to error computation, in such areas, should be considered. As mentioned, the other region exhibiting high absolute difference magnitude is around the free surface, where point-by-point differences are computed. Consequently, due to possible phase shifts, some points may lack the presence of the free surface where it should be, resulting in very large differences. However, this does not necessarily imply poor performance of the coupled model.

Moreover, the absence of spurious reflections is noteworthy. In simulations involving waves, establishing appropriate boundary conditions is a significant challenge [223, 224], often necessitating large domains (as Ω_{sim} here), and forcing or damping models [225, 226]. The computational costs required to solve the Navier-Stokes equations, in such a computational domain, can become prohibitively large. In this section, leveraging POD to provide suitable boundary conditions has proven to be an effective approach, enabling a reduction in the computational domain size. Consequently, there is no need for buffer layers in the coupling methodology, as required in other coupling approaches, since only the values of the variables of interest at the boundary sections of the high-fidelity domain are sufficient.

Finally, one might argue that the floating body utilized in this section does not closely resemble a real WEC, given its smaller dimensions and weight compared to typical WECs. This objection is valid, as WECs generally have, indeed, much larger dimensions and weight. However, this difference does not undermine the

efficacy of the coupling methodology. Numerical simulations are essential not only for real-scale dimensions, but also for describing experimental tests, which are often conducted at reduced scales. The size of the sphere and the simulated waves of this section align with various experimental designs [172, 227–229], where Froude and Reynolds scaling techniques are commonly applied to ensure kinematic and dynamic similarities between the scaled model, and the real-world scenario [230–232]. However, these considerations mainly pertain to the original high-fidelity solver, which generates the snapshots, and resolves fluid-structure interactions. The POD analysis is conducted based on such results. Therefore, as long as the CFD model is validated, and accurately represents the intended problem, the coupling methodology is expected to yield reliable results. This underscores the importance of validating against the high-fidelity solution, and the absence of experimental data validation for the simulations conducted in this thesis.

4.4.3 WEC Farm Coupling Algorithm

As the title of this manuscript suggests, the ultimate aim is the simulation of WEC farms. The presented coupled CFD/POD methodology demonstrates its suitability for simulating a single WEC. The next logical step involves integrating multiple coupled models. The algorithm for this integration should augment the size of the minimization problem, while retaining simplicity as a least squares problem.

To provide a brief overview of the potential algorithm, $n_B = 3$ WECs of the same type are chosen, each with identical setups for high-fidelity, and low-fidelity domains, and simulations. As WECs are typically positioned relatively close together in a farm, Ω_{HF} domains may potentially overlap, as illustrated in Figure 4.34a. In such scenarios, the minimization problem extends from the current support, the overlapping region Ω_o (orange areas in the figure), and the sensor locations $\mathbf{x}^S$, to an additional area, Ω_E, defined by the overlapping regions highlighted in blue in the figure.

Expanding the framework in this manner, slightly increases the complexity of the minimization problem. With information now coming from multiple directions, not only from sensors and from the center of Ω_{HF}, the minimization problem for each body j must be solved over the new region $\Omega_O^j = \Omega_o^j \cup \mathbf{x}_j^S \cup \Omega_E^j$, where Ω_E^j encompasses all overlaps related to the j-th body, and Ω_E is the union of the n_P

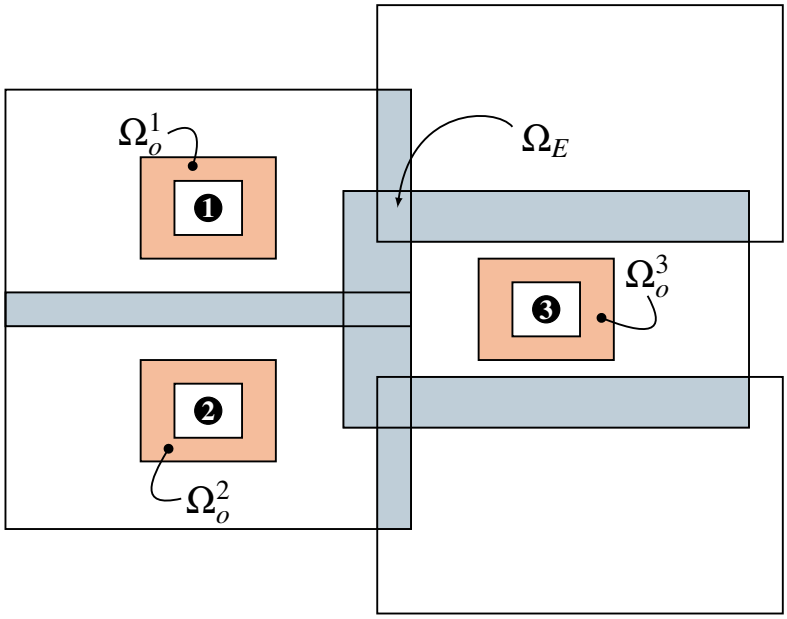

(a) WEC farm with small distances.

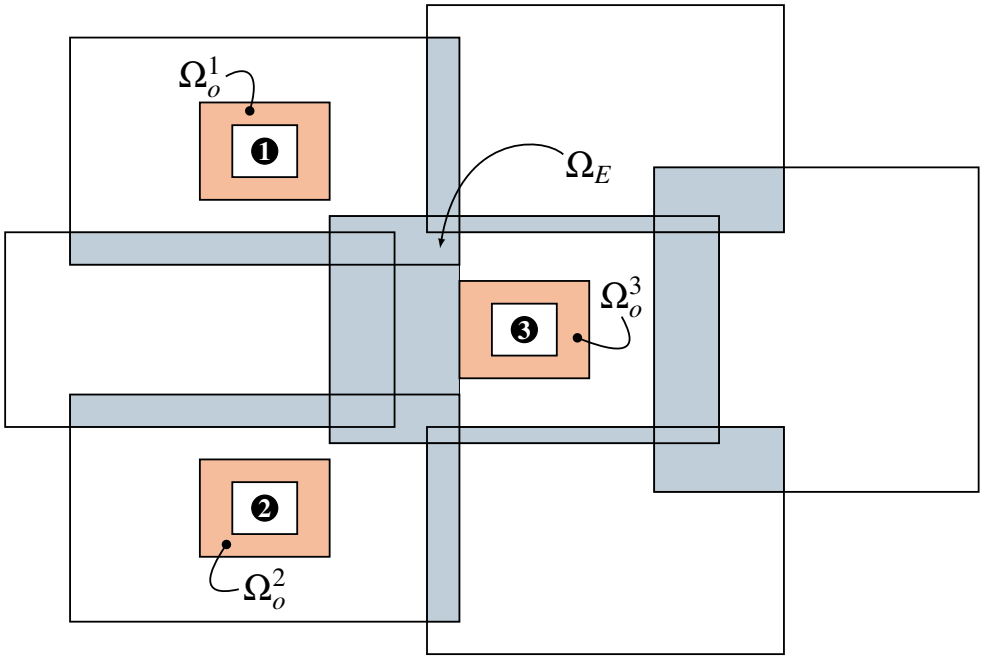

(b) WEC farm with large distances.

Fig. 4.34 Visual representation of the coupling methodology for a WEC farm, considering small (above) and large (below) distances among WECs.

overlapping patches, as depicted in blue in Figure 4.34. The minimization problem is not solved once any more, but with an iterative process, inspired from the Schwarz alternating method [233, 234], which involves solving the least squares problem multiple times, until convergence in the overall $\Omega_O = \bigcup_{j=1}^{n_P} \Omega_O^j$, represented by all the colored regions in Figure 4.34. In this way, the solution for the temporal coefficients accounts for the information coming from all the WECs.

However, the distance between devices, in a farm, may vary, especially in parameter studies, resulting in different forms of overlap. A minimum WEC-WEC spacing may be established, to ensure adequate space for the different Ω_{hf}^j to neither touch, nor overlap. For the maximum distance, a limit may not be strictly related to the coupling methodology, but rather follow conventional farm guidelines. In scenarios where devices are spaced farther apart, the coupled farm model might resemble the configuration depicted in Figure 4.34b, where additional domains without devices are patched in. As a WEC farm simulation should describe both near and far fields, POD basis functions need to be defined also around the farm, including areas without WECs. Training can thus be conducted on various wave characteristics without the presence of moving bodies. These subdomains are then incorporated into the minimization process alongside the other subdomains containing the WECs, following the same principle of overlapping macro-areas. Furthermore, by limiting the size of propagating patches in this manner, the inherent dissipation of a CFD model is also constrained.

The main challenge in this algorithm lies in simulating multiple bodies in different Ω_{hf} domains in StarCCM+. Although the software allows for parallel computations, gathering information from each simulation, or from a single simulation with several computational domains, is necessary at each time step, to solve the minimization problem in the overall overlapping region Ω_O, and provide the respective boundary conditions to each Ω_{hf}^j, for the subsequent time step. This aspect is currently under investigation.

Validating such a farm model with a CFD solution, over a large domain, presents significant challenges. Therefore, validation against experimental data, or another validated model, may be more practical. In such cases, bypassing numerical validation, given its complexity, could be preferable, with direct experimental validation being a viable alternative.

4.5 Conclusion

The primary objective of this chapter is to efficiently model the behavior of WECs under the influence of ocean waves, which presents a complex challenge due to the interaction between the floating structure, and the dynamic fluid environment of real waves. While the solution of the full order model is accurate, it becomes prohibitively costly when applied to large-scale WEC problems. Indeed, accurately modeling real waves necessitates a significantly large computational domain to accurately generate and potentially dampen waves, particularly to prevent reflections. In this framework, POD has proven essential to save computational resources and can be used to provide appropriate information on the boundaries of the simulation domain. A non-intrusive, two-way coupling methodology is proposed, based on domain decomposition, and a Galerkin-free approach. The methodology simplifies to a least squares minimization problem, enabling application to simulations involving moving bodies, including wave energy conversion.

Beginning by considering a simple prototype, a point absorber sphere, the methodology can easily adapt to more complex, and full-scale, WECs, with multiple degrees of freedom. Furthermore, without altering the coupling strategy, additional details such as mooring, or control systems, can be incorporated, thus enhancing realism in the simulations. Parameter tuning, such as adjusting domain sizes or the number of POD modes, is problem-specific, and can be tailored to strike a balance between accuracy and speedups. For the case considered, the volume of the high-fidelity domain is reduced to just 0.015% of the original domain, yielding a huge computational saving, while still maintaining accuracy, as the maximum relative errors stay below 0.2%. The approach yields fitting results for in-sample cases, where the reproduction of the previously simulated problem, also used to obtain the POD modes, is needed to assess the validity of the coupled model. Notably, the method also demonstrates the ability to predict solutions for unseen parameters, in out-of-sample simulations. In this case, the accuracy is conserved, and the significant reduction in CPU costs is pushed even further, enabling intensive simulations, suitable for optimization tasks and multiple-query simulations.

Although the model yields satisfactory results, there is room for improvement. For instance, optimizing sensor locations could enhance accuracy, and computational savings. Additionally, exploring advanced clustering techniques on snapshots could reduce the POD offline stage, while simultaneously improving the online stage by

decreasing the number of POD modes for each cluster. Moreover, the WEC farm simulation is partially addressed, but further development is needed to fully model and optimize such systems.

Chapter 5

Conclusion

This thesis represents a convergence of two distinct domains, typical of a cotutelle programme. On one side, there is a mathematical tool, with a very high potential in simplifying complex numerical simulations, as evidenced by numerous examples in literature, albeit often still distant from real-world scenarios. On the other side, there is the highly applied domain of wave energy, encompassing various aspects, including numerical simulations on actual fluids, and possibly non-idealized cases. The development of WEC farms poses significant challenges, given their multi-scale nature, nonlinearities, numerous degrees of freedom, and the extensive numerical simulations required prior to practical testing and deployment. Despite being less obvious, computationally intensive numerical simulations also contribute to pollution due to the substantial computing resources they demand, in terms of storage, time, energy, hardware, software, and network usage. Therefore, reducing computational costs not only facilitates progress in wave energy, leading to cleaner energy production, but also minimizes the carbon footprint associated with simulations. This further motivates the application of promising mathematical tools to real-world scenarios.

The chapter structure of the document mirrors the sequential progression of the project. An initial assessment of the current state of the art is crucial to delineate the problem and determine the direction of research. Following Chapter 2, the need for a modeling approach capable of addressing the multi-scale nature of WEC farms becomes imperative. Additionally, a multi-fidelity model is preferable to separate different dynamics, and identify the most suitable solver for each one. Typically, a

high-fidelity solver is favored around the WEC, where nonlinearities and viscous effects are concentrated. Conversely, a lower-fidelity solver is employed to propagate solutions across larger domains, and needs to interact effectively with the high-fidelity solver. A model that maintains consistency in variables across both solvers is the most practical solution. Deviating from conventional methods, the use of model order reduction aligns well with all the requirements. However, ROMs based on POD for multiphase flows lack evidence in existing literature. Hence, an initial exploration is necessary to assess the feasibility of applying such a technique to the specific problem at hand. Chapter 3 deals with this aspect. Actually, a POD ROM model is implemented for a biphase flow, showing a good reduction of the problem with the POD, since less than 3% of the modes possess 99% of the information. Moreover, an asymptotic reduced version allows to obtain a dynamical system composed of at most third-order tensors, avoiding the appearing of a fourth-order tensor, which would be cumbersome and against the idea of reduction. However, the dynamical system fails to give a solution, when applied to real water/air flows. Considering the limitations of POD ROM models with highly nonlinear problems, and recalling the multi-fidelity approach, the coupling methodology proposed in Chapter 4 is tested, and validated. The Galerkin-free approach enables the preservation of POD reduction, without the burden of the stability issues. Moreover, coupling the POD with the CFD around the WECs allows for accurate descriptions of nonlinearities in that region, while the wave propagation is handled by the POD across the broader domain. Communication between the two solvers is straightforward, as the variables remain unchanged, eliminating the need for transformations, and preserving accuracy. The only exception is the interpolation, necessary to establish a common framework for information exchange. Additionally, potential dissipation inherent to CFD for wave propagation is mitigated by computing the snapshots for POD training on small patches, thus enabling control over numerical dissipation.

The research conducted in this PhD project raises several unresolved questions, and offers numerous clues for future exploration. Currently, the coupling methodology demonstrates promising results, and significant reduction rates. Beyond the immediate task of modeling WEC farms, including scenarios with hybrid configurations involving additional energy systems, such as wind energy, lies a wide range of potential investigations.
For instance, there is a need to consider sensor placement and data acquisition, as the current assumption is idealized. Presently, numerous sensors are positioned at

the inlet zone of the high-fidelity domain, providing extensive data on the variables of interest. However, in real-world scenarios, such as at sea or in experimental basins, sensors are typically scarce, sparsely distributed, and collect limited data, potentially noisy and incomplete. Addressing this issue is essential to adapt the external information to the numerical simulation, in addition to the fine-tuning of the model to suit the specifics of the case under investigation.
Another area of focus could involve refining the implementation of the algorithm to optimize the code, both in the offline and online steps, enhance information exchange, and suitably tune parameter values related to model, geometry, and training phase. Establishing a user-friendly platform for running multiple simulations, particularly for optimization and parametric studies, could be beneficial, potentially in collaboration with the StarCCM+ support. Alternatively, adapting the model for integration into an open-source CFD code would widen the access to the model. The non-intrusive nature of the approach offers flexibility for implementation. However, while non-intrusiveness is advantageous, exploring an intrusive model, especially in the case of a POD ROM, might be worthwhile, to assess potential improvements in the Galerkin projection and governing equations. The primary objective would be to stabilize the surrogate model, and prevent excessively large temporal coefficients in the dynamical system solution. Further testing could involve assessing uncertainty propagation at different stages of ROM model development, and exploring alternative combinations of variables, to better understand potential crossover effects. Additionally, a shift from linear to nonlinear methods might be considered. Given the focus on tracking free surface evolution, which can exhibit highly nonlinear behavior, linear approximations in a POD ROM model may prove inadequate, even with a high number of modes. Techniques such as optimal transportation [235], or Wasserstein distances [236], could be explored for describing wave front movement, aligning with shock-capturing methods, usually applied for numerical dissipation activation or with error indicators for mesh adaptation and refinement. Nonetheless, a primary challenge would involve defining the correct forward and backward mapping functions, in three dimensions.

In the case of WEC modeling, various factors must be considered. In this study, the focus has been primarily on analyzing the fluid dynamics aspect. However, other components, such as the mooring system or control strategy, may require different approaches, possibly involving reduction techniques. While the methodology proposes a coupling between two solvers for fluid dynamics, there is no restriction

against coupling with other models, potentially including other reduced models. In any case, efforts should be made to prevent the simulation from becoming overly complex. Nevertheless, achieving a comprehensive simulation is desirable, in wave energy applications, to enable policymakers and stakeholders to make well-informed decisions.

Similar considerations may apply to various other application sectors of the methodologies outlined in this document. Specifically, the coupling methodology is inherently versatile, with the high-fidelity solver handling the most intricate aspects, and boundary condition management posing the primary challenge. As the coupling simplifies to a least squares problem, there are no restrictions on the variables of interest, provided that a set (or sets) of basis functions can be associated to them. Hence, while initially developed for a specific domain, the findings of this thesis may have broader applications across multiple domains.

References

[1] Institute E. Statistical Review of World Energy. https://www.energyinst.org/statistical-review. 2023.

[2] International Energy Agency. World Energy Outlook 2023. https://www.iea.org/reports/world-energy-outlook-2023. 2023.

[3] Shaw S. Ocean – A Vast Reserve of Renewable Energy. *Journal of Physics: Conference Series*. 2021;1834(1):012017.

[4] Lehmann M, Karimpour F, Goudey CA, Jacobson PT, Alam MR. Ocean Wave Energy in the United States: Current Status and Future Perspectives. *Renewable and Sustainable Energy Reviews*. 2017;74:1300–1313.

[5] Pelc R, Fujita RM. Renewable Energy from the Ocean. *Marine Policy*. 2002; 26(6):471–479.

[6] López I, Andreu J, Ceballos S, Martínez de Alegría I, Kortabarria I. Review of Wave Energy Technologies and the Necessary Power-equipment. *Renewable and Sustainable Energy Reviews*. 2013;27:413–434.

[7] The European Marine Energy Center (EMEC). Wave Developers. https://www.emec.org.uk/marine-energy/wave-developers/. Accessed: 2024-01-02.

[8] International Renewable Energy Agency (IRENA). Ocean energy: Technology Readiness, Patents, Deployment Status and Outlook. 2014.

[9] CorPower Ocean Website. https://corpowerocean.com. Accessed: 2024-01-28.

[10] Ocean Power Technologies Website. https://oceanpowertechnologies.com/platform/opt-pb3-powerbuoy/. Accessed: 2024-01-28.

[11] Wave Star Website. https://wavestarenergy.com. Accessed: 2024-01-28.

[12] Xu D, Stuhlmeier R, Stiassnie M. Harnessing Wave Power in Open Seas II: Very Large Arrays of Wave-energy Converters for 2D Sea States. *Journal of Ocean Engineering and Marine Energy*. 2017;3:1–10.

[13] Kara F. Time Domain Prediction of Power Absorption from Ocean Waves with Wave Energy Converter Arrays. *Renewable Energy*. 2016;92:30–46.

[14] Winship B, Fleming A, Penesis I, Hemer M, Macfarlane G. Preliminary Investigation on the Use of Tank Wall Reflections to Model WEC Array Effects. *Ocean Engineering*. 2018;164:388–401.

[15] Thomas GP, Evans DV. Arrays of Three-dimensional Wave-energy Absorbers. *Journal of Fluid Mechanics*. 1981;108:67–88.

[16] Devolder B, Stratigaki V, Troch P, Rauwoens P. CFD Simulations of Floating Point Absorber Wave Energy Converter Arrays Subjected to Regular Waves. *Energies*. 2018;11(3).

[17] Pelamis Wave Power Website. https://web.archive.org/web/20140106215458/http://www.pelamiswave.com/. Accessed: 2024-01-28.

[18] Rusu E, Guedes Soares C. Coastal Impact Induced by a Pelamis Wave Farm Operating in the Portuguese Nearshore. *Renewable Energy*. 2013;58:34–49.

[19] Palha A, Sassetti Mendes L, Fortes C, Brito-Melo A, Sarmento A. The Impact of Wave Energy Farms in the Shoreline Wave Climate: Portuguese Pilot Zone Case Study Using Pelamis Energy Wave Devices. *Renewable Energy*. 2010; 35:62–77.

[20] Venugopal V, Smith GH. Wave climate Investigation for an Array of Wave Power Devices. In: *Proceedings of the 7th European Wave and Tidal Energy Conference (EWTEC2007)*. 2007; .

[21] Farley FJM, Rainey RCT, Chaplin JR. Rubber Tubes in the Sea. *Philosophical Transactions: Mathematical, Physical and Engineering Sciences*. 2012; 370(1959):381–402.

[22] Mahmoodian MM. Impact Assessment of a New Wave Energy Converter, Anaconda. Master thesis, University of Southampton. 2009.

[23] Wave for Energy Website. https://www.waveforenergy.com/technologies/iswec/. Accessed: 2024-01-28.

[24] MOREnergyLab Website. http://www.morenergylab.polito.it/pewec/. Accessed: 2024-01-28.

[25] Niosi F, Battisti B, Sirigu SA. Influence of Hydrodynamic Interactions on the Productivity of PeWEC Wave Energy Converter Array. In: *2022 International Conference on Electrical, Computer, Communications and Mechatronics Engineering (ICECCME)*. 2022; pp. 1–6.

[26] Battisti B, Giorgi G, Verao Fernandez G, Troch P. A Multiquery Analysis of a PeWEC Farm. *Proceedings of the European Wave and Tidal Energy Conference*. 2023;15.

[27] Battisti B, Giorgi G, Fernandez GV. Balancing Power Production and Coastal Protection: A Bi-objective Analysis of Wave Energy Converters. *Renewable Energy*. 2024;220:119702.

[28] Wave Dragon. Tethys Website. https://tethys.pnnl.gov/project-sites/wave-dragon-pre-commercial-demonstration-project. Accessed: 2024-01-28.

[29] Nørgaard J, Andersen T. Investigation of Wave Transmission from a Floating Wave Dragon Wave Energy Converter. 2012; .

[30] Beels C, Troch P, De Visch K, Kofoed JP, De Backer G. Application of the Time-dependent Mild-slope Equations for the Simulation of Wake Effects in the Lee of a Farm of Wave Dragon Wave Energy Converters. *Renewable Energy*. 2010;35(8):1644–1661.

[31] Mutriku Wave Energy plant. Power Technology Website. https://www.power-technology.com/projects/mutriku-wave/?cf-view. Accessed: 2024-01-28.

[32] Ahmad I, M'zoughi F, Aboutalebi P, Garrido I, Garrido AJ. Fuzzy logic control of an artificial neural network-based floating offshore wind turbine model integrated with four oscillating water columns. *Ocean Engineering*. 2023;269:113578.

[33] M'zoughi F, Garrido I, Garrido AJ, Sen MDL. Fuzzy Airflow-Based Active Structural Control of Integrated Oscillating Water Columns for the Enhancement of Floating Offshore Wind Turbine Stabilization. *International Journal of Energy Research*. 2023;2023:1–23.

[34] De O Falcão A. Wave-power Absorption by a Periodic Linear Array of Oscillating Water Columns. *Ocean Engineering*. 2002;29(10):1163–1186.

[35] Sarkar D, Renzi E, Dias F. Wave Farm Modelling of Oscillating Wave Surge Converters. *Proceedings of the Royal Society A: Mathematical, Physical and Engineering Sciences*. 2014;470(2167):20140118.

[36] Dias F, Renzi E, Gallagher S, Sarkar D, Wei Y, Abadie T, Cummins C, Rafiee A. Analytical and Computational Modelling for Wave Energy Systems: The Example of Oscillating Wave Surge Converters. *Acta Mechanica Sinica*. 2017; 33:647–662.

[37] AW-Energy Website. https://aw-energy.com/. Accessed: 2024-01-28.

[38] Aquamarine Power. EMEC Website. https://www.emec.org.uk/about-us/wave-clients/aquamarine-power/. Accessed: 2024-01-28.

[39] Balitsky P, Quartier N, Verao Fernandez G, Stratigaki V, Troch P. Analyzing the Near-field Effects and the Power Production of an Array of Heaving Cylindrical WECs and OSWECs Using a Coupled Hydrodynamic-PTO Model. *Energies*. 2018;11(12).

[40] Koca K, Kortenhaus A, Oumeraci H, Zanuttigh B, Angelelli E, Cantù M, Suffredini R, Franceschi G. Recent Advances in the Development of Wave Energy Converters. In: *Proceedings of the 10th European Wave and Tidal Energy Conference (EWTEC2013)*. Aalborg, Denmark. 2013; .

[41] Sundar V, Sannasiraj S, Kaldenhoff H. Directional Spreading of Waves in the Nearshore Zone. *Ocean Engineering*. 1998;26(2):161–188.

[42] Rusu L, Onea F. The Performance of Some State-of-the-art Wave Energy Converters in Locations with the Worldwide Highest Wave Power. *Renewable and Sustainable Energy Reviews*. 2017;75:1348–1362.

[43] European Centre for Medium-Range Weather Forecasts (ECMWF). ERA5 Hourly Data on Single Levels from 1940 to Present. 10.24381/cds.adbb2d47. Accessed: 2024-01-04.

[44] Diaconu S, Rusu E. The Environmental Impact of a Wave Dragon Array Operating in the Black Sea. *The Scientific World Journal*. 2013;.

[45] International Renewable Energy Agency (IRENA). Innovation Outlook: Ocean Energy Technologies. 2020.

[46] Rodriguez-Delgado C, Bergillos RJ, Iglesias G. Dual Wave Farms for Energy Production and Coastal Protection Under Sea Level Rise. *Journal of Cleaner Production*. 2019;222:364–372.

[47] Stratigaki V. Experimental Study and Numerical Modelling of Intra-array Interactions and Extra-array Effects of Wave Energy Converter Arrays. Phd thesis, Ghent University. 2014.

[48] de Andrés A, Guanche R, Meneses L, Vidal C, Losada I. Factors that Influence Array Layout on Wave Energy Farms. *Ocean Engineering*. 2014;82:32–41.

[49] Bozzi S, Giassi M, Moreno Miquel A, Antonini A, Bizzozero F, Gruosso G, Archetti R, Passoni G. Wave Energy Farm Design in Real Wave Climates: the Italian Offshore. *Energy*. 2017;122:378–389.

[50] Babarit A. Impact of Long Separating Distances on the Energy Production of Two Interacting Wave Energy Converters. *Ocean Engineering*. 2010; 37(8):718–729.

[51] Balitsky P, Bacelli G, Ringwood J. Control-influenced Layout Optimization of Arrays of Wave Energy Converters. vol. 9. 2014; .

[52] Garcia Rosa P, Bacelli G, Ringwood J. Control-informed Optimal Array Layout for Wave Farms. *Sustainable Energy, IEEE Transactions on*. 2015; 6:575–582.

[53] Peña-Sanchez Y, García-Violini D, Penalba M, Zarketa A, Nava V, Ringwood J. Spectral Control Co-design of Wave Energy Converter Array Layout. *Proceedings of the European Wave and Tidal Energy Conference*. 2023;15.

[54] Meunier PE, Clément A, Gilloteaux Jc, Kerkeni S. Development of a Methodology for Collaborative Control Within a WEC Array. *International Marine Energy Journal*. 2018;1:51–59.

[55] Li G, Belmont MR. Model Predictive Control of Sea Wave Energy Converters – Part II: The Case of an Array of Devices. *Renewable Energy*. 2014;68:540–549.

[56] McNatt JC, Venugopal V, Forehand D. A Novel Method for Deriving the Diffraction Transfer Matrix and its Application to Multi-body Interactions in Water Waves. *Ocean Engineering*. 2015;94:173–185.

[57] Stratigaki V, Troch P, Stallard T, Forehand D, Folley M, Kofoed JP, Benoit M, Babarit A, Vantorre M, Kirkegaard J. Sea-state Modification and Heaving Float Interaction Factors from Physical Modelling of Arrays of Wave Energy Converters. *Journal of Renewable and Sustainable Energy*. 2015;7(6):061705.

[58] Göteman M, Giassi M, Engström J, Isberg J. Advances and Challenges in Wave Energy Park Optimization - A Review. *Frontiers in Energy Research*. 2020;8.

[59] Abdulkadir H, Ellithy A, Abdelkhalik O. Heterogeneous WEC Array Optimization Using the Hidden Genes Genetic Algorithm. *Proceedings of the European Wave and Tidal Energy Conference*. 2023;15.

[60] Sharp C, DuPont B. Wave Energy Converter Array Optimization: A Genetic Algorithm Approach and Minimum Separation Distance Study. *Ocean Engineering*. 2018;163:148–156.

[61] Child BFM, Venugopal V. Optimal Configurations of Wave Energy Device Arrays. *Ocean Engineering*. 2010;37(16):1402–1417.

[62] Mendoza E, Silva R, Zanuttigh B, Angelelli E, Lykke Andersen T, Martinelli L, Nørgaard JQH, Ruol P. Beach Response to Wave Energy Converter Farms Acting as Coastal Defence. *Coastal Engineering*. 2014;87:97–111.

[63] Foteinis S. Wave Energy Converters in Low Energy Seas: Current State and Opportunities. *Renewable and Sustainable Energy Reviews*. 2022;162:112448.

[64] Berrio Y, Rivillas-Ospina G, Ruiz-Martínez G, Arango-Manrique A, Ricaurte C, Mendoza E, Silva R, Casas D, Bolívar M, Díaz K. Energy Conversion and Beach Protection: Numerical Assessment of a Dual-purpose WEC Farm. *Renewable Energy*. 2023;219:119555.

[65] Kazimierczuk K, Henderson C, Duffy K, Hanif S, Bhattacharya S, Biswas S, Jacroux E, Preziuso D, Wu D, Bhatnagar D, Tarekegne B. A Socio-technical Assessment of Marine Renewable Energy Potential in Coastal Communities. *Energy Research & Social Science*. 2023;100:103098.

[66] Schoonees T, Gijón Mancheño A, Scheres B, Bouma TJ, Silva R, Schlurmann T, Schüttrumpf H. Hard Structures for Coastal Protection, Towards Greener Designs. *Estuaries and Coasts*. 2019;42(7):1709–1729.

[67] Foteinis S, Tsoutsos T. Strategies to Improve Sustainability and Offset the Initial High Capital Expenditure of Wave Energy Converters (WECs). *Renewable and Sustainable Energy Reviews*. 2017;70:775–785.

[68] Michele S, Sammarco P, d'Errico M, Renzi E, Abdolali A, Bellotti G, Dias F. Flap Gate Farm: From Venice Lagoon Defense to Resonating Wave Energy Production. Part 2: Synchronous Response to Incident Waves in Open Sea. *Applied Ocean Research*. 2015;52:43–61.

[69] Joint Research Centre, Institute for Energy and Transport, Uihlein A, Magagna D. *2014 JRC Ocean Energy Status Report – Technology, Market and Economic Aspects of Ocean Energy in Europe*. Publications Office of the European Union. 2015.

[70] Babarit A. On the Park Effect in Arrays of Oscillating Wave Energy Converters. *Renewable Energy*. 2013;58:68–78.

[71] Davidson J, Costello R. Efficient Nonlinear Hydrodynamic Models for Wave Energy Converter Design - A Scoping Study. *Journal of Marine Science and Engineering*. 2020;8(1).

[72] Chowdhury SD, Nader JR, Sanchez AM, Fleming A, Winship B, Illesinghe S, Toffoli A, Babanin A, Penesis I, Manasseh R. A Review of Hydrodynamic Investigations into Arrays of Ocean Wave Energy Converters. 2015.

[73] Folley M, Babarit A, Child B, Forehand D, O'Boyle L, Silverthorne K, Spinneken J, Stratigaki V, Troch P. A Review of Numerical Modelling of Wave Energy Converter Arrays. vol. 7: Ocean Space Utilization; Ocean Renewable Energy of *International Conference on Offshore Mechanics and Arctic Engineering*. 2012; pp. 535–545.

[74] Budal K. Theory for Absorption of Wave Power by a System of Interacting Bodies. *Journal of Ship Research*. 1977;21(04):248–254.

[75] Evans D. Some Theoretical Aspects of Three-dimensional Wave-energy Absorbers. *Proceedings of the 1st Symposium on Wave Energy Utilisation, Gothenburg, Sweden*. 1979;.

[76] Falnes J. Radiation Impedance Matrix and Optimum Power Absorption for Interacting Oscillators in Surface Waves. *Applied Ocean Research*. 1980; 2(2):75–80.

[77] Lee H. Water Wave Generation with Source Function in the Level Set Finite Element Framework. *Journal of Mechanical Science and Technology*. 2015; 29:3699–3706.

[78] Agamloh EB, Wallace AK, von Jouanne A. Application of Fluid–structure Interaction Simulation of an Ocean Wave Energy Extraction Device. *Renewable Energy*. 2008;33(4):748–757.

[79] McCallum PD. Numerical Methods for Modelling the Viscous Effects on the Interactions Between Multiple Wave Energy Converters. Phd thesis, University of Edimburgh. 2017.

[80] Penalba M, Giorgi G, Ringwood JV. Mathematical modelling of wave energy converters: A review of nonlinear approaches. *Renewable and Sustainable Energy Reviews*. 2017;78:1188–1207.

[81] Longuet-Higgins MS, Cokelet ED. The Deformation of Steep Surface Waves on Water. I. A Numerical Method of Computation. *Proceedings of the Royal Society of London Series A, Mathematical and Physical Sciences*. 1976; 350(1660):1–26.

[82] Bosi U, Engsig-Karup AP, Eskilsson C, Ricchiuto M. A Spectral/hp Element Depth-integrated Model for Nonlinear Wave–body Interaction. *Computer Methods in Applied Mechanics and Engineering*. 2019;348:222–249.

[83] Beck G, Lannes D. Freely Floating Objects on a Fluid Governed by the Boussinesq Equations. *Annales de l'Institut Henri Poincaré C, Analyse non linéaire*. 2022;39.

[84] Godlewski E, Parisot M, Sainte-Marie J, Wahl F. Congested Shallow Water Model: on Floating Body. *The SMAI Journal of computational mathematics*. 2020;6:227–251.

[85] Karambas T, Loukogeorgaki E. A Boussinesq-type Model for Nonlinear Wave-Heaving Cylinder Interaction. *Energies*. 2022;15(2).

[86] Forehand DIM, Kiprakis AE, Nambiar AJ, Wallace AR. A Fully Coupled Wave-to-Wire Model of an Array of Wave Energy Converters. *IEEE Transactions on Sustainable Energy*. 2016;7(1):118–128.

[87] Borgarino B, Babarit A, Ferrant P. Impact of Wave Interactions Effects on Energy Absorption in Large Arrays of Wave Energy Converters. *Ocean Engineering*. 2012;41:79–88.

[88] Zhang W, Liu H, Zhang X, Zhang L, Ashraf MA. Optimal Configurations of Wave Energy Converter Arrays with a Floating Body. *Polish Maritime Research*. 2016;23:71–77.

[89] Ancellin M, Dong M, Jean P, Dias F. Far-Field Maximal Power Absorption of a Bulging Cylindrical Wave Energy Converter. *Energies*. 2020;13(20).

[90] Borgarino B, Babarit A, Ferrant P. An Implementation of the Fast Multipole Algorithm for Wave Interaction Problems on Sparse Arrays of Floating Bodies. *Journal of Engineering Mathematics*. 2012;77:51–68.

[91] Penalba M, Touzón I, Lopez-Mendia J, Nava V. A Numerical Study on the Hydrodynamic Impact of Device Slenderness and Array Size in Wave Energy Farms in Realistic Wave Climates. *Ocean Engineering*. 2017;142:224–232.

[92] Beels C, Troch P, De Backer G, Vantorre M, De Rouck J. Numerical Implementation and Sensitivity Analysis of a Wave Energy Converter in a Time-dependent Mild-slope Equation Model. *Coastal Engineering*. 2010;57(5):471–492.

[93] Troch P, Beels C, Rouck J, De Backer G. Wake Effects Behind a Farm of Wave Energy Converters for Irregular Long-crested and Short-crested Waves. In: *Proceedings of the 32nd International Conference on Coastal Engineering*, vol. 1. Shanghai, China. 2010; .

[94] Smith HC, Pearce C, Millar DL. Further Analysis of Change in Nearshore Wave Climate due to an Offshore Wave Farm: An Enhanced Case Study for the Wave Hub Site. *Renewable Energy*. 2012;40(1):51–64.

[95] Atan R, Finnegan W, Nash S, Goggins J. The Effect of Arrays of Wave Energy Converters on the Nearshore Wave Climate. *Ocean Engineering*. 2019;172:373–384.

[96] Porter A, Haller M, Lenee-Bluhm P. Laboratory Observations and Numerical Modeling of the Effects of an Array of Wave Energy Converters. *Coastal Engineering Proceedings*. 2012;1(33).

[97] Bergillos RJ, López-Ruiz A, Medina-López E, Moñino A, Ortega-Sánchez M. The Role of Wave Energy Converter Farms on Coastal Protection in Eroding Deltas, Guadalfeo, Southern Spain. *Journal of Cleaner Production*. 2018; 171:356–367.

[98] McIver P. Wave forces on Arrays of Floating Bodies. *Journal of Engineering Mathematics*. 1984;18:273–285.

[99] Mavrakos S. Hydrodynamic Coefficients for Groups of Interacting Vertical Axisymmetric Bodies. *Ocean Engineering*. 1991;18(5):485–515.

[100] Tokić G, Yue DKP. Hydrodynamics of Periodic Wave Energy Converter Arrays. *Journal of Fluid Mechanics*. 2019;862:34–74.

[101] Mavrakos SA, Kalofonos A. Power Absorption by Arrays of Interacting Vertical Axisymmetric Wave-Energy Devices. *Journal of Offshore Mechanics and Arctic Engineering*. 1997;119(4):244–251.

[102] Mavrakos S, McIver P. Comparison of Methods for Computing Hydrodynamic Characteristics of Arrays of Wave Power Devices. *Applied Ocean Research*. 1997;19(5):283–291.

[103] Simon MJ. Multiple Scattering in Arrays of Axisymmetric Wave-energy Devices. Part 1. A Matrix Method Using a Plane-wave Approximation. *Journal of Fluid Mechanics*. 1982;120:1–25.

[104] Kagemoto H, Yue DKP. Interactions Among Multiple Three-dimensional Bodies in Water Waves: An Exact Algebraic Method. *Journal of Fluid Mechanics*. 1986;166:189–209.

[105] Göteman M. Multiple Cluster Scattering with Applications to Wave Energy Park Optimizations. *Applied Ocean Research*. 2022;125:103256.

[106] Mcnatt C, Venugopal V, Forehand D. The Cylindrical Wave Field of Wave Energy Converters. In: *Proceedings of the 10th European Wave and Tidal Energy Conference (EWTEC2013)*. Aalborg, Denmark. 2013; .

[107] Ruiz PM, Nava V, Topper MBR, Minguela PR, Ferri F, Kofoed JP. Layout Optimisation of Wave Energy Converter Arrays. *Energies*. 2017;10(9).

[108] Topper MB, Nava V, Collin AJ, Bould D, Ferri F, Olson SS, Dallman AR, Roberts JD, Ruiz-Minguela P, Jeffrey HF. Reducing Variability in the Cost of Energy of Ocean Energy Arrays. *Renewable and Sustainable Energy Reviews*. 2019;112:263–279.

[109] Chen J, Pillai AC, Johanning L, Ashton I. Using Machine Learning to Derive Spatial Wave Data: A Case Study for a Marine Energy Site. *Environmental Modelling & Software*. 2021;142:105066.

[110] Cornejo-Bueno L, Garrido-Merchán E, Hernández-Lobato D, Salcedo-Sanz S. Bayesian Optimization of a Hybrid System for Robust Ocean Wave Features Prediction. *Neurocomputing*. 2018;275:818–828.

[111] James SC, Zhang Y, O'Donncha F. A Machine Learning Framework to Forecast Wave Conditions. *Coastal Engineering*. 2018;137:1–10.

[112] Valério D, Mendes MJ, Beirão P, Sá da Costa J. Identification and Control of the AWS Using Neural Network Models. *Applied Ocean Research*. 2008; 30(3):178–188.

[113] Li L, Yuan Z, Gao Y. Maximization of Energy Absorption for a Wave Energy Converter Using the Deep Machine Learning. *Energy*. 2018;165:340–349.

[114] Lu KH, Hong CM, Xu Q. Recurrent Wavelet-based Elman Neural Network with Modified Gravitational Search Algorithm Control for Integrated Offshore Wind and Wave Power Generation Systems. *Energy*. 2019;170:40–52.

[115] Cuadra L, Salcedo-Sanz S, Nieto-Borge J, Alexandre E, Rodríguez G. Computational Intelligence in Wave Energy: Comprehensive Review and Case Study. *Renewable and Sustainable Energy Reviews*. 2016;58:1223–1246.

[116] Sarkar D, Contal E, Vayatis N, Dias F. Prediction and Optimization of Wave Energy Converter Arrays Using a Machine Learning Approach. *Renewable Energy*. 2016;97:504–517.

[117] Dehghan Manshadi M, Mousavi M, Soltani M, Mosavi A, Kovacs L. Deep Learning for Modeling an Offshore Hybrid Wind-wave Energy System. *Energies*. 2022;15(24).

[118] Neshat M, Abbasnejad E, Shi Q, Alexander B, Wagner M. Adaptive Neuro-surrogate-based Optimisation Method for Wave Energy Converters Placement Optimisation. In: *Neural Information Processing*, edited by Gedeon T, Wong KW, Lee M. Cham: Springer International Publishing. 2019; pp. 353–366.

[119] Sampath MK, Dounavis A, Khazaka R. Parameterized Model Order Reduction Techniques for FEM Based Full Wave Analysis. *IEEE Transactions on Advanced Packaging*. 2009;32(1):2–12.

[120] Black F, Schulze P, Unger B. Model Order Reduction with Dynamically Transformed Modes for the Wave Equation. *PAMM*. 2021;20(1):202000321.

[121] Suchithra R, Ezhilsabareesh K, Samad A. Development of a Reduced Order Wave to Wire Model of an OWC Wave Energy Converter for Control System Analysis. *Ocean Engineering*. 2019;172:614–628.

[122] Vertechy R, Papini Rosati GP, Fontana M. Reduced Model and Application of Inflating Circular Diaphragm Dielectric Elastomer Generators for Wave Energy Harvesting. *Journal of Vibration and Acoustics*. 2015;137(1):011004.

[123] Faedo N, Peña-Sanchez Y, Ringwood JV. Parametric Representation of Arrays of Wave Energy Converters for Motion Simulation and Unknown Input Estimation: A Moment-based Approach. *Applied Ocean Research*. 2020; 98:102055.

[124] Faedo N, Piuma F, Giorgi G, Ringwood J. Nonlinear Model Reduction for Wave Energy Systems: a Moment-matching-based Approach. *Nonlinear Dynamics*. 2020;102:1–23.

[125] Sayadi T, Schmid PJ, Richecoeur F, Durox D. Parametrized Data-driven Decomposition for Bifurcation Analysis, with Application to Thermo-acoustically Unstable Systems. *Physics of Fluids*. 2015;27(3):037102.

[126] Lieu T, Farhat C. Adaptation of Aeroelastic Reduced-order Models and Application to an F-16 Configuration. *AIAA Journal*. 2007;45(6):1244–1257.

[127] Roy S, Hua JC, Barnhill W, Gunaratne GH, Gord JR. Deconvolution of Reacting-flow Dynamics Using Proper Orthogonal and Dynamic Mode Decompositions. *Physical Review E*. 2015;91:013001.

[128] Treuille A, Lewis A, Popovic Z. Model Reduction for Real-time Fluids. *ACM Trans Graph*. 2006;25:826–834.

[129] Liu B, Mason G, Hodgson J, Tong Y, Desbrun M. Model-Reduced Variational Fluid Simulation. *ACM Transactions on Graphics*. 2015;34(6).

[130] Rowley CW, Dawson ST. Model Reduction for Flow Analysis and Control. *Annual Review of Fluid Mechanics*. 2017;49(1):387–417.

[131] Lassila T, Manzoni A, Quarteroni A, Rozza G. *Model Order Reduction in Fluid Dynamics: Challenges and Perspectives*, pp. 235–273. Cham: Springer International Publishing. 2014;.

[132] Huang C, Duraisamy K, Merkle CL. Investigations and Improvement of Robustness of Reduced-order Models of Reacting Flow. *AIAA Journal*. 2019; 57(12):5377–5389.

[133] Huang C, Duraisamy K, Merkle C. Component-based Reduced Order Modeling of Large-scale Complex Systems. *Frontiers in Physics*. 2022;10.

[134] Blonigan PJ, Rizzi F, Howard M, Fike JA, Carlberg KT. Model Reduction for Steady Hypersonic Aerodynamics via Conservative Manifold Least-squares Petrov–Galerkin Projection. *AIAA Journal*. 2021;59(4):1296–1312.

[135] Ravindran SS. A Reduced-order Approach for Optimal Control of Fluids Using Proper Orthogonal Decomposition. *International Journal for Numerical Methods in Fluids*. 2000;34(5):425–448.

[136] Illingworth SJ. Model-based Control of Vortex Shedding at Low Reynolds Numbers. *Theoretical and Computational Fluid Dynamics*. 2016;30(5):429–448.

[137] Barbagallo A, Sipp D, Schmid PJ. Closed-loop Control of an Open Cavity Flow Using Reduced-order Models. *Journal of Fluid Mechanics*. 2009; 641:1–50.

[138] Weller J, Camarri S, Iollo A. Feedback Control by Low-order Modelling of the Laminar Flow Past a Bluff Body. *Journal of Fluid Mechanics*. 2009; 634:405–418.

[139] Manzoni A, Quarteroni A, Rozza G. Shape Optimization for Viscous Flows by Reduced Basis Methods and Free-form Deformation. *International Journal for Numerical Methods in Fluids*. 2012;70(5):646–670.

[140] Hay A, Borggaard J, Akhtar I, Pelletier D. Reduced-order Models for Parameter Dependent Geometries Based on Shape Sensitivity Analysis. *Journal of Computational Physics*. 2010;229(4):1327–1352.

[141] Bui-Thanh T, Willcox K, Ghattas O. Parametric Reduced-order Models for Probabilistic Analysis of Unsteady Aerodynamic Applications. *AIAA Journal*. 2008;46(10):2520–2529.

[142] Wang Z, Akhtar I, Borggaard J, Iliescu T. Proper Orthogonal Decomposition Closure Models for Turbulent Flows: A Numerical Comparison. *Computer Methods in Applied Mechanics and Engineering*. 2012;237-240:10–26.

[143] Weller J, Lombardi E, Bergmann M, Iollo A. Numerical Methods for Low-order Modeling of Fluid Flows Based on POD. *International Journal for Numerical Methods in Fluids*. 2010;63(2):249–268.

[144] Cazemier W, Verstappen RWCP, Veldman AEP. Proper Orthogonal Decomposition and Low-dimensional Models for Driven Cavity Flows. *Physics of Fluids*. 1998;10(7):1685–1699.

[145] Ahmed SE, Pawar S, San O, Rasheed A, Iliescu T, Noack BR. On Closures for Reduced Order Models - A Spectrum of First-principle to Machine-learned Avenues. *Physics of Fluids*. 2021;33(9):091301.

[146] Lassila T, Manzoni A, Quarteroni A, Rozza G. A Reduced Computational and Geometrical Framework for Inverse Problems in Hemodynamics. *International Journal for Numerical Methods in Biomedical Engineering*. 2013; 29(7):741–776.

[147] Sarmast S, Dadfar R, Mikkelsen RF, Schlatter P, Ivanell S, Sørensen JN, Henningson DS. Mutual Inductance Instability of the Tip Vortices Behind a Wind Turbine. *Journal of Fluid Mechanics*. 2014;755:705–731.

[148] Xiao D, Lin Z, Fang F, Pain C, Navon I, Salinas P, Muggeridge A. Non-intrusive Reduced Order Modeling for Multiphase Porous Media Flows Using Smolyak Sparse Grids. *International Journal for Numerical Methods in Fluids*. 2016;83.

[149] Botsas T, Pan I, Mason LR, Matar OK. Multiphase Flow Applications of Nonintrusive Reduced-order Models with Gaussian Process Emulation. *Data-Centric Engineering*. 2022;3:20.

[150] Silva WA. Application of Nonlinear Systems Theory to Transonic Unsteady Aerodynamic Responses. *Journal of Aircraft*. 1993;30(5):660–668.

[151] Tromp J, Jenkins J. A Volterra Kernel Identification Scheme Applied to Aerodynamic Reactions. In: *17th Atmospheric Flight Mechanics Conference*. 1990; .

[152] Maple RC. Adaptive Harmonic Balance Method for Unsteady, Nonlinear, One-dimensional Periodic Flows. Phd thesis, Air Force Institute of Technology. 2002.

[153] Lucia DJ, Beran PS, Silva WA. Reduced-order Modeling: New Approaches for Computational Physics. *Progress in Aerospace Sciences*. 2004;40(1):51–117.

[154] Ruhe A. Rational Krylov Sequence Methods for Eigenvalue Computation. *Linear Algebra and its Applications*. 1984;58:391–405.

[155] Moore B. Principal Component Analysis in Linear Systems: Controllability, Observability, and Model Reduction. *IEEE Transactions on Automatic Control*. 1981;26(1):17–32.

[156] Mullis C, Roberts R. Synthesis of Minimum Roundoff Noise Fixed Point Digital Filters. *IEEE Transactions on Circuits and Systems*. 1976;23(9):551–562.

[157] Chinesta F, Ladeveze P, Cueto E. A Short Review on Model Order Reduction Based on Proper Generalized Decomposition. *Archives of Computational Methods in Engineering*. 2011;18:395–404.

[158] Czech C, Lesjak M, Bach C, Duddeck F. Data-driven Models for Crashworthiness Optimisation: Intrusive and Non-intrusive Model Order Reduction Techniques. *Structural and Multidisciplinary Optimization*. 2022;65(190).

[159] Benner P, Gugercin S, Willcox K. A Survey of Projection-based Model Reduction Methods for Parametric Dynamical Systems. *SIAM Review*. 2015; 57(4):483–531.

[160] Barnett J, Farhat C. Quadratic Approximation Manifold for Mitigating the Kolmogorov Barrier in Nonlinear Projection-based Model Order Reduction. *Journal of Computational Physics*. 2022;464:111348.

[161] Barrault M, Maday Y, Nguyen N, Patera A. An 'Empirical Interpolation' Method: Application to Efficient Reduced-basis Discretization of Partial Differential Equations. *Comptes Rendus Mathematique*. 2004;339:667–672.

[162] Barnett J, Farhat C, Maday Y. Neural-network-augmented Projection-based Model Order Reduction for Mitigating the Kolmogorov Barrier to Reducibility. *Journal of Computational Physics*. 2023;492:112420.

[163] Lumley JL. The Structure of Inhomogeneous Turbulent Flows. *Atmospheric Turbulence and Radio Wave Propagation*. 1967;pp. 166–178.

[164] Sirovich L. Turbulence and the Dynamics of Coherent Structures. I - Coherent Structures. II - Symmetries and Transformations. III - Dynamics and Scaling. *Quarterly of Applied Mathematics*. 1987;45:561–571.

[165] Cordier L, Bergmann M. Proper Orthogonal Decomposition: An Overview. In: *Lecture series 2002-04 on post-processing of experimental and numerical data*. Von Kármán Institute for Fluid Dynamics. 2002;.

[166] Luo Z, Chen G. *Proper Orthogonal Decomposition Methods for Partial Differential Equations*. Elsevier. 2008.

[167] Siemens Digital Industries Software. Simcenter STAR-CCM+ User Guide v. 2021.1. Siemens 2021.

[168] Bergmann M. Optimisation Aérodynamique par Réduction de Modèle POD et Contrôle Optimal. Application au Sillage Laminaire d'un Cylindre Circulaire. Phd thesis, Institut National Polytechnique de Lorraine / LEMTA. 2004.

[169] Noack B, Papas P, Monkewitz P. The Need for a Pressure-term Representation in Empirical Galerkin Models of Incompressible Shear Flows. *Journal of Fluid Mechanics*. 2005;523.

[170] Bergmann M, Bruneau CH, Iollo A. Enablers for Robust POD Models. *Journal of Computational Physics*. 2009;228(2):516–538.

[171] Buffoni M, Camarri S, Iollo A, Salvetti MV. Low-dimensional Modelling of a Confined Three-dimensional Wake Flow. *Journal of Fluid Mechanics*. 2006; 569:141–150.

[172] Windt C, Faedo N, García-Violini D, Peña Sanchez Y, Davidson J, Ferri F, Ringwood J. Validation of a CFD-based Numerical Wave Tank Model of the 1/20th Scale Wavestar Wave Energy Converter. *Fluids*. 2020;5(3).

[173] Sirisup S, Karniadakis G. A Spectral Viscosity Method for Correcting the Long-term Behavior of POD Models. *Journal of Computational Physics*. 2004;194(1):92–116.

[174] Pinnau R. Model Reduction via Proper Orthogonal Decomposition. In: *Model Order Reduction: Theory, Research Aspects and Applications*, vol. 13. 2008; pp. 95–109.

[175] Carlberg K, Barone M, Antil H. Galerkin v. Least-squares Petrov-Galerkin Projection in Nonlinear Model Reduction. *Journal of Computational Physics*. 2017;330:693–734.

[176] Azaiez M, Chacón Rebollo T, Oulghelou M, Sánchez Muñoz I. Least-squares Pressure Recovery in Reduced Order Methods for Incompressible Flows. 2024.

[177] Schmid P, Li L, Juniper M, Pust O. Applications of the Dynamic Mode Decomposition. *Theoretical and Computational Fluid Dynamics*. 2010;25:249–259.

[178] Schmid P, Sesterhenn J. Dynamic Mode Decomposition of Numerical and Experimental Data. *Journal of Fluid Mechanics*. 2008;656.

[179] Kutz JN, Brunton SL, Brunton BW, Proctor JL. *Dynamic Mode Decomposition*. Philadelphia, PA: Society for Industrial and Applied Mathematics. 2016.

[180] Rowley C, Mezic I, Bagheri S, Schlatter P, Henningson D. Spectral Analysis of Nonlinear Flows. *Journal of Fluid Mechanics*. 2009;641:115 – 127.

[181] Kutz JN, Fu X, Brunton SL. Multiresolution Dynamic Mode Decomposition. *SIAM Journal on Applied Dynamical Systems*. 2016;15(2):713–735.

[182] Leroux R, Cordier L. Dynamic Mode Decomposition for Non-uniformly Sampled Data. *Experiments in Fluids*. 2016;57(94).

[183] Foias C, Jolly MS, Kevrekidis IG, Titi ES. Dissipativity of Numerical Schemes. *Nonlinearity*. 1991;4(3):591.

[184] Marion M, Temam R. Nonlinear Galerkin Methods. *SIAM Journal on Numerical Analysis*. 1989;26(5):1139–1157.

[185] Feeny B. A complex orthogonal decomposition for wave motion analysis. *Journal of Sound and Vibration*. 2008;310(1):77–90.

[186] Campana E, Mascio AD, Esposito P, Lalli F. Viscous-inviscid Coupling in Free Surface Ship Flows. *International Journal for Numerical Methods in Fluids*. 1995;21:699–722.

[187] Lock R, Williams B. Viscous-inviscid Interactions in External Aerodynamics. *Progress in Aerospace Sciences*. 1987;24(2):51–171.

[188] Tomey-Bozo N, Babarit A, Murphy J, Stratigaki V, Troch P, Lewis T, Thomas G. Wake Effect Assessment of a Flap Type Wave Energy Converter Farm Under Realistic Environmental Conditions by Using a Numerical Coupling Methodology. *Coastal Engineering*. 2019;143:96–112.

[189] Verao Fernandez G, Stratigaki V, Vasarmidis P, Balitsky P, Troch P. Wake Effect Assessment in Long- and Short-crested Seas of Heaving-point Absorber and Oscillating Wave Surge WEC Arrays. *Water*. 2019;11(6).

[190] Balitsky P, Quartier N, Stratigaki V, Fernandez GV, Vasarmidis P, Troch P. Analysing the Near-field Effects and the Power Production of Near-shore WEC Array Using a New Wave-to-wire Model. *Water 2019, Vol 11, Page 1137*. 2019;11(6):1137.

[191] Verao Fernández G, Stratigaki V, Troch P. Irregular Wave Validation of a Coupling Methodology for Numerical Modelling of Near and Far Field Effects of Wave Energy Converter Arrays. *Energies*. 2019;12(3).

[192] Balitsky P, Verao Fernandez G, Stratigaki V, Troch P. Coupling Methodology for Modelling the Near-field and Far-field Effects of a Wave Energy Converter. In: *Proceedings of the 36th International Conference on Ocean, Arctic and Offshore Engineering (OMAE2017)*. Trondheim, Norway. 2017; p. V010T09A029.

[193] Singh J, Babarit A. A Fast Approach Coupling Boundary Element Method and Plane Wave Approximation for Wave Interaction Analysis in Sparse Arrays of Wave Energy Converters. *Ocean Engineering*. 2014;85:12–20.

[194] Charrayre F, Peyrard C, Benoit M, Babarit A. A Coupled Methodology for Wave-body Interactions at the Scale of a Farm of Wave Energy Converters Including Irregular Bathymetry. In: *Proceedings of the International Conference on Offshore Mechanics and Arctic Engineering - OMAE*, vol. 8. San Francisco, California, USA. 2014; p. V08AT06A043.

[195] Belibassakis K, Bonovas M, Rusu E. A Novel Method for Estimating Wave Energy Converter Performance in Variable Bathymetry Regions and Applications. *Energies*. 2018;11(8).

[196] Bingham H. A Hybrid Boussinesq-panel Method for Predicting the Motion of a Moored Ship. *Coastal Engineering*. 2000;40(1):21–38.

[197] Kemper J, Windt C, Graf K, Ringwood J. Development Towards a Nested Hydrodynamic Model for the Numerical Analysis of Ocean Wave Energy Systems. In: *Proceedings of the 13th European Wave and Tidal Energy Conference (EWTEC2019)*, 1414. Naples, Italy. 2019; pp. 1–9.

[198] Verbrugghe T, Stratigaki V, Altomare C, Domínguez JM, Troch P, Kortenhaus A. Implementation of Open Boundaries within a Two-way Coupled SPH Model to Simulate Nonlinear Wave–structure Interactions. *Energies*. 2019; 12(4).

[199] Aliyar S, Ducrozet G, Bouscasse B, Bonnefoy F, Sriram V, Ferrant P. Numerical Coupling Strategy Using HOS-OpenFOAM-MoorDyn for OC3 Hywind SPAR Type Platform. *Ocean Engineering*. 2022;263:112206.

[200] Christensen ED, Bredmose H, Hansen EA. Transfer of Boussinesq Waves to a Navier-Stokes Solver: Application to Wave Loads on an Offshore Wind Turbine Foundation. vol. Volume 4: Ocean Engineering; Ocean Renewable Energy; Ocean Space Utilization, Parts A and B of *International Conference on Offshore Mechanics and Arctic Engineering*. 2009; pp. 917–926.

[201] Li Z, Bouscasse B, Ducrozet G, Gentaz L, Le Touzé D, Ferrant P. Spectral Wave Explicit Navier-Stokes Equations for Wave-structure Interactions Using Two-phase Computational Fluid Dynamics Solvers. *Ocean Engineering*. 2021; 221:108513.

[202] Jacobsen NG, Fuhrman DR, Fredsøe J. A Wave Generation Toolbox for the Open-source CFD Library: OpenFoam. *International Journal for Numerical Methods in Fluids*. 2012;70(9):1073–1088.

[203] Paulsen BT, Bredmose H, Bingham HB. An Efficient Domain Decomposition Strategy for Wave Loads on Surface Piercing Circular Cylinders. *Coastal Engineering*. 2014;86:57–76.

[204] Wei Y, Abadie T, Dias F. A Cost-effective Method for Modelling Wave-OWSC Interaction. *International Journal of Offshore and Polar Engineering*. 2017; 27:366–373.

[205] Quarteroni A, Valli A. *Domain Decomposition Methods for Partial Differential Equations*. Oxford, UK: Oxford University Press. 1999.

[206] Reis T, Stykel T. A Survey on Model Reduction of Coupled Systems. In: *Model Order Reduction: Theory, Research Aspects and Applications*, vol. 13. 2008; pp. 133–155.

[207] Maday Y, Rønquist EM. A Reduced-basis Element Method. *Journal of Scientific Computing*. 2002;17:447–459.

[208] Iapichino L, Quarteroni A, Rozza G. Reduced Basis Method and Domain Decomposition for Elliptic Problems in Networks and Complex Parametrized Geometries. *Computers & Mathematics with Applications*. 2016;71(1):408–430.

[209] Willcox K, Peraire J, Paduano JD. Application of Model Order Reduction to Compressor Aeroelastic Models . *Journal of Engineering for Gas Turbines and Power*. 2002;124(2):332–339.

[210] Iollo A, Sambataro G, Taddei T. A One-shot Overlapping Schwarz Method for Component-based Model Reduction: Application to Nonlinear Elasticity. *Computer Methods in Applied Mechanics and Engineering*. 2023;404:115786.

[211] Sambataro G. Component-based Model Order Reduction Procedure for Large Scales Thermo-hydro-mechanical Systems. Phd thesis, Université de Bordeaux. 2022.

[212] Corigliano A, Dossi M, Mariani S. Model Order Reduction and Domain Decomposition Strategies for the Solution of the Dynamic Elastic–plastic Structural Problem. *Computer Methods in Applied Mechanics and Engineering*. 2015;290:127–155.

[213] Phillips TRF, Heaney CE, Tollit BS, Smith PN, Pain CC. Reduced-order Modelling with Domain Decomposition Applied to Multi-group Neutron Transport. *Energies*. 2021;14(5).

[214] Ahmed SE, San O, Kara K, Younis R, Rasheed A. Multifidelity Computing for Coupling Full and Reduced Order Models. *PloS one*. 2021;16(2).

[215] Buffoni M, Telib H, Iollo A. Iterative Methods for Model Reduction by Domain Decomposition. *Computers & Fluids*. 2009;38(6):1160–1167.

[216] Lucia DJ, King PI, Beran PS. Reduced Order Modeling of a Two-dimensional Flow with Moving Shocks. *Computers & Fluids*. 2003;32(7):917–938.

[217] Baiges J, Codina R, Idelsohn S. A Domain Decomposition Strategy for Reduced Order Models. Application to the Incompressible Navier–Stokes Equations. *Computer Methods in Applied Mechanics and Engineering*. 2013; 267:23–42.

[218] Bergmann M, Ferrero A, Iollo A, Lombardi E, Scardigli A, Telib H. A Zonal Galerkin-free POD Model for Incompressible Flows. *Journal of Computational Physics*. 2018;352:301–325.

[219] Carlino MG. ADER scheme on Overset Grids with Compact Transmission and Hyper-reduction : Application to Incompressible Navier-Stokes Equations. Phd thesis, Université de Bordeaux. 2021.

[220] Freno BA, Cizmas PG. A proper orthogonal decomposition method for nonlinear flows with deforming meshes. *International Journal of Heat and Fluid Flow*. 2014;50:145–159.

[221] Gautam RK, Singh N, Choudhary NK, Narain A. Model Order Reduction Using Factor Division Algorithm and Fuzzy C-means Clustering Technique. *Transactions of the Institute of Measurement and Control*. 2019;41(2):468–475.

[222] Arthur D, Vassilvitskii S. K-means++: The Advantages of Careful Seeding. In: *Proceedings of the Eighteenth Annual ACM-SIAM Symposium on Discrete Algorithms*, SODA '07. USA: Society for Industrial and Applied Mathematics. 2007; p. 1027–1035.

[223] Jin G, Braza M. A Nonreflecting Outlet Boundary Condition for Incompressible Unsteady Navier-Stokes Calculations. *Journal of Computational Physics*. 1993;107(2):239–253.

[224] Bruneau CH, Fabrie P. Effective Downstream Boundary Conditions for Incompressible Navier–Stokes Equations. *International Journal for Numerical Methods in Fluids*. 1994;19(8):693–705.

[225] Choi J, Yoon SB. Numerical Simulations Using Momentum Source Wavemaker Applied to RANS Equation Model. *Coastal Engineering*. 2009; 56(10):1043–1060.

[226] Kim J, O'Sullivan J, Read A. Ringing Analysis of a Vertical Cylinder by Euler Overlay Method. vol. Volume 4: Offshore Geotechnics; Ronald W. Yeung Honoring Symposium on Offshore and Ship Hydrodynamics of *International Conference on Offshore Mechanics and Arctic Engineering*. 2012; pp. 855–866.

[227] Stavropoulou C, Goude A, Katsidoniotaki E, Göteman M. Fast Time-domain Model for the Preliminary Design of a Wave Power Farm. *Renewable Energy*. 2023;219:119482.

[228] Mercadé Ruiz P, Ferri F, Kofoed JP. Experimental Validation of a Wave Energy Converter Array Hydrodynamics Tool. *Sustainability*. 2017;9(1).

[229] Stratigaki V, Troch P, Stallard T, Forehand D, Kofoed JP, Folley M, Benoit M, Babarit A, Kirkegaard J. Wave Basin Experiments with Large Wave Energy Converter Arrays to Study Interactions between the Converters and Effects on Other Users in the Sea and the Coastal Area. *Energies*. 2014;7(2):701–734.

[230] Sheng W, Alcorn R, Lewis T. Physical Modelling of Wave Energy Converters. *Ocean Engineering*. 2014;84:29–36.

[231] Dai S, Day S, Yuan Z, Wang H. Investigation on the hydrodynamic scaling effect of an OWC type wave energy device using experiment and CFD simulation. *Renewable Energy*. 2019;142:184–194.

[232] Schmitt P, Elsäßer B. The application of Froude scaling to model tests of Oscillating Wave Surge Converters. *Ocean Engineering*. 2017;141:108–115.

[233] Barnett J, Tezaur I, Mota A. The Schwarz Alternating Method for the Seamless Coupling of Nonlinear Reduced Order Models and Full Order Models. 2022.

[234] Bjørstad PE, Skogen MD. Domain Decomposition Algorithms of Schwarz Type, Designed for Massively Parallel Computers. In: *Proceedings of the Fifth International Symposium on Domain Decomposition Methods for Partial Differential Equations*. Philadelphia, USA. 1989; pp. 362–375.

[235] Iollo A, Taddei T. Mapping of Coherent Structures in Parameterized Flows by Learning Optimal Transportation with Gaussian Models. *Journal of Computational Physics*. 2022;471:111671.

[236] Battisti B, Blickhan T, Enchery G, Ehrlacher V, Lombardi D, Mula O. Wasserstein Model Reduction Approach for Parametrized Flow Problems in Porous Media. *ESAIM: ProcS*. 2023;73:28–47.

Declaration

I hereby declare that, the contents and organization of this dissertation constitute my own original work and does not compromise in any way the rights of third parties, including those relating to the security of personal data.

Beatrice Battisti
2024

* This dissertation is presented in partial fulfillment of the requirements for **Ph.D. degree** in the Graduate School of Politecnico di Torino (ScuDo).